Introduction

NETWORKS as a framework for analyzing large scale data sets in molecular cell biology and neurobiology and at the same time a challenge for mathematical theory, that was our motivation for organizing the conference and for editing the present volume of lecture notes from that conference. So, why is this of relevance, and what can we contribute here?

It is the basic paradigm of physics that, on the basis of deep and fundamental mathematical structures, general and universal laws can be formulated and experiments can then be devised for unambiguously confirming or rejecting those laws. In contrast to this, in modern biology, we are usually confronted with large data sets in which we need to discern some structure. These structures are not self-evident, nor can they be deduced from general principles. Biological structures are aggregate structures of physico-chemical constituents, and their function emerges from the interaction of many elements. Therefore, we need some guidance for which structures to look and to understand how the biological functions are achieved.

Networks provide such a paradigm. They constitute an organizational principle for biological data sets. We need to identify the basic elements in a given framework. Depending on the biological context, these may be certain types of molecules like specific proteins or RNAs, or whole cells, like neurons. We also need to describe the interactions between them, forming bonds, catalyzing reactions, or exchanging spikes through synapses. On one hand, we need to find out which elements interacts with which specific other ones. On the other hand, we need to understand the dynamics of those interactions. The first aspect leads us to the mathematical structure of a graph. The second aspect brings in the theory of dynamical systems. A dynamical network thus is a graph whose elements dynamically interact according to the structural pattern of the graph. From these local interactions, a collective dynamical pattern emerges that describes the system as a whole. Networks thus link structural and dynamical aspects. In mathematics, often the richest and most interesting patterns emerge from new connections between different theories. The present link between graph theory and dynamical systems in our opinion confirms this and leads to challenging research questions. Its ultimate aim is to contribute to the understanding of the formation of structures in biological and other systems.

Networks as such, however, are too general for reaching profound theories. There are simply too many types of graphs and dynamical systems, and arbitrary combinations of them seem of little use. Therefore, the theory needs

the concrete biological data to identify the structures and dynamical patterns of interest and substance. In contrast to many areas of applied mathematics that simply provide tool boxes for data analysis, like statistics packages or numerical analysis software, here the theory itself is strongly driven by concrete biological findings.

Thus, these proceedings aim at the same time at displaying a mathematical framework for organizing and understanding biological data, at providing a survey of such biological data, and showing the fruitful synthesis, the application of mathematical principles to those data, and the mathematical research stimulated by those data. We hope that these proceedings will be useful for an introduction to the theoretical aspects, as a survey of important biological networks (see for example the contribution by Prohaska, Mosig, and Stadler on regulatory networks in eukaryotic cells), and as a sample of more concrete case studies of molecular and neural networks

Since biological systems are aggregate and composite ones, in each case, we need to decide which are the relevant and crucial aspects, and which ones can be neglected, and perhaps should even be neglected because they obstruct the identification of the principles. In biological systems, often details at some lower level average out at some higher level. This then leads to the question which details should be included in a model and which ones omitted. While network theory agrees that the models are based on interactions between discrete entities, one then has to decide whether only discrete states are possible or whether we should rather admit continuous state values. In the first case, naturally also the update is carried out at discrete time steps only. In the simplest case, there then are only two possible state values, labeled by 0 (rest) and 1 (activity). We then have a so-called Boolean network. Often such a network, even though it obviously represents a very simplified model, can still capture crucial qualitative aspects. Also, in a situation of only sparse data, it is advantageous to have a very simple with as few parameters as possible, to avoid having to estimate such parameters without sufficient data. Some of the contributions in these proceedings show the advantages of this approach. In other situations, one may know more about the temporal dynamics and can build a corresponding model. A prime example are networks of spiking neurons that have a much better correspondence with neurobiological reality than simple spin systems like the Hopfield network. Also, continuous state dynamics even with discrete temporal updating, like the so-called coupled map lattices, show new features like synchronization that are not so meaningful in discrete state systems.

A beautiful example where the question of which details to include in a model can be analyzed are transmission delays in networks. In many formal models they are, and can be, neglected because they do not affect the emerging collective dynamical patterns. In many cases, however, they can also lead to new dynamical phenomena. Atay presents three pertinent case studies, motivated by models in biology and neurobiology. In one of them, it is found that, surprisingly, transmission delays can facilitate synchronization of the individual dynamics in a global network of coupled oscillators. This provides a direct link to synchronization as a proposed mechanism for feature binding in neural systems. The idea, as originally proposed by von der Malsburg, is that a complex percept can be neurally represented by the coincident firing of the neurons responding to its specific features. Since there does not seem to exist a global temporal coordinator in neural systems, such a synchronization must emerge from local interactions between neurons, and the synchronization studies for dynamical systems provide novel insights. Nevertheless, synchronization is only the simplest type of collective dynamics, and non-linear dynamical systems can also find richer global patterns. This is explored from an experimentally driven perspective in the contribution of Eckhorn and his collaborators who identify global dynamical patterns corresponding to specific sensory inputs. The same issue is approached from a theoretical perspective in the contribution of Ritter and his collaborators who construct neural networks that develop global dynamical patterns in response to their input from an interaction between neurons and a competition between neuron layers. This is then connected with the principles of gestalt formation in cognitive psychology. This reflects an important approach for elucidating the relationship between neural processes and cognitive phenomena.

It is a basic insight from the theory of networks, that such a dynamical pattern formation also depends on underlying structural aspects, and the contribution of Jost lays some foundations for the analysis of the interplay between structure and dynamics. A basic set of structural parameters of a graph is provided by its Laplacian spectrum, and this in turn characterizes the synchronizability of so-called coupled map lattice dynamics. This is an important example of the fact that one needs to be careful in isolating the correct parameters that determine the global dynamical features of the network supported by a graph. Since there far too many different graphs even of moderate size to describe all them exhaustively, we need to identify some graph classes that display fundamental qualitative features as observed in real data. At the same time, we should also be attentive to the specific features that distinguish graphs in some concrete biological domain from other ones. Huang et al. investigate protein-protein interaction networks from that perspective, and they found that a hierarchical model captures the qualitative features of some species, but not of others. Also in this regard, Li et al. demonstrate in their contribution that real biological networks (their examples are

the cell-cycle and life-cycle networks of protein-protein and protein-DNA interactions in budding yeast) can have structural and dynamical properties that are profoundly different from the ones of some general graph paradigms like random graphs studied in the literature. In particular, their examples show a dynamical attractor with a large basin of attraction that is reliably attained on a specific pathway. This secures the robust function of the network under perturbations, a crucial aspect for any biological system. While in the work of Li et al., structural and dynamical stability of the important cycles is shown, Zhang and Qian study the same system from a stochastic point of view, and they show that the system is also stable against random perturbations. Finally, Huang et al. examine still another concept of stability, namely the one against experimental errors, and they reach the fortunate conclusion that protein-protein interaction networks are quite stable in that sense as well.

One specific class of graphs that have found important biological applications are trees. They are used for reconstructing and displaying evolutionary histories on the basis of observed similarities between present species. They are also used in other fields, like in linguistics for the reconstruction of historical divergences from common ancestral languages. Often the available data do not allow for the unambiguous reconstruction of such an evolutionary tree, however. Dress then argues that instead of forcibly suppressing those unresolvable ambiguities in a data set X, we should rather work with a class of graphs that is larger than the ones of X-trees. The endpoints of such a tree are the representatives of the data set to be grouped, and the internal nodes are putative common ancestors. Thus, the edges of a tree reflect unambiguous historical descendence relationships, and the lengths encode the degrees of dissimilarity between adjacent nodes. Dress introduces the category of X-nets where the edges of a tree can get replaced by parallelograms that reflect alternative descendence relationships, and the lengths of the sides then describe again degrees of dissimilarity as contained in the data. More precisely, the defining characteristic of an X-net is that for any neighboring nodes u, v in the network and any other node x, one shortest connection from x to one of them (which one depends, of course, on x) has to pass through the other one. This theory constitutes a beautiful example of profound new mathematics developed in response to concrete challenges from biological and other data sets.

From a somewhat different perspective, certain ingredients in real dynamical systems are relegated to the role of noise or random perturbations, and we should then argue for the stability of the system against such perturbations. It is an important insight, however, that noise can also play a constructive role by providing energy that facilitates the distinction between weak signals. This aspect is taken up and further in the contributions of Feng and his collaborations for networks of spiking neurons. They analyze the trade-off

between speed and accuracy in neural decision making. Input correlations and inhibitory input improve the speed, but increase the variability of neuronal output and thereby affect reproducibility of output patterns and thus accuracy of the decision. They develop a mathematical framework for the analysis of higher order statistics in neural networks. Tuckwell and Feng then investigate under which conditions such networks of spiking neurons can sustain spontaneous background activity and determine the neuronal firing rates. As demonstrated in the contribution of Zhang and Qian, stochastic fluctuations may also play useful roles in intracellular and other networks, by allowing for transitions between different metastable states and optimizing the expected time spent in the deepest basin of attraction and following the most robust pathways for transitions between different states.

Sometimes, in molecular biology, network data are not directly available, and one only has sequence data instead. One then needs reliable methods for reconstructing the network from those sequence data. Qian and her collaborators provide Bayesian schemes that can solve that task successfully for protein-protein interaction networks. The basic ingredient to their approach are motifs of polypeptide subsequences of 4 amino acids. In another contribution from the group of Qian, a new method for the identification of transcription factor binding sites in DNA sequences is introduced. Also, the complementary question for protein sequence motifs that can bind at regulatory sites at DNA level can be addressed with their methods.

As already mentioned, Prohaska, Mosig, and Stadler provide a comprehensive state-of-the-art survey of regulatory modes, modules, and motifs in eukaryotic cells, including in particular recent findings about regulation at RNA level as well as indications about deep phylogenies that conserved regulatory sequences can yield. Luo and Jia discover some surprising statistical correlations between RNA copy number or structure and protein structure. For example, the helices and strands in proteins are preferably coded by mRNA stem regions, but the protein coils by mRNA loops. One should notice here that RNA secondary structure can be reliably predicted by available algorithms while protein folding is still a computationally very difficult and theoretically largely unsolved problem. This fact might provide a useful perspective for the results of Luo and Jia. They also find that RNA structure data available from different species show a significant preference for low folding energies when compared to randomized sequences. Moreover, they detect a dichotomy between intraspecific homogeneity and interspecific inhomogeneity of mRNA folding energies. Presumably, such results are just the tip of an iceberg, and many structural relationships in biological await discovery. We hope that the theory of networks will provide a useful framework within which to formulate hypotheses that can guide the conception of experiments and to organize and

understand diverse biological data.

The conference from which these lecture notes result was first conceived in October 2003 when one of us (J.J.) gave a public lecture on "Mathematical perspectives in biology and neurobiology" and got in contact with the other two organizers at the Sino-German Centre in Beijing, a cooperative research institution of the DFG (German Research Foundation) and the NSFC (National Science Foundation of China). We are grateful to Robert Paul Königs and his colleagues from the Sino-German Centre for arranging that initial lecture, for supporting our scientific scheme, and for hosting our conference at the Sino-German Centre. All the lecturers and participants of the conference enjoyed the excellent facilities and the hospitality of the Center's staff. The conference stimulated both concrete cooperations between scientists from China and Germany and long ranging scientific perspectives on which we plan to build in the future.

Warwick/Leipzig/Beijing,
February 2006

Jianfeng Feng,
Jürgen Jost,
Minping Qian

Contents

List of Contributors

Fatihcan M. Atay

Max Planck Institute for Mathematics in the Sciences Inselstr,

22, D-04103 Leipzig, Germany.

atay@member.ams.org

B. Al-Shaikhli

Physics Department, Neurophysics Group,

Philipps-University,

D–35032 Marburg, Germany.

A. Bruns

Physics Department, Neurophysics Group,

Philipps-University,

D–35032 Marburg, Germany.

Hilary Buxton

University of Sussex, United Kingdom

hilaryb@sussex.ac.uk

Minghua Deng

LMAM, School of Mathematical Sciences and Center for Theoretical Biology,

Peking University,

Beijing ,100871, P.R. China.

dengmh@pku.edu.cn

R. Eckhorn

Physics Department,Neurophysics Group,

Philipps-University,

D–35032 Marburg, Germany.

Reinhard.Eckhorn@physik.uni-marburg.de

Jywe-Fei Fang

Department of Digital Content and Technology,

National Taichung Teachers College,

Taichung, 140, Taichung, Taiwan 403.

Jianfeng Feng

Department of Mathematics ,

Hunan Normal University,

chang,410081,P.R.China.

Department of Computer Science and Mathematics,

Warwick University,

Coventry, CV4 7AL, UK.

jianfeng@susex.ac.uk

Xiucheng Feng

Center for Theoretical Biology and School of Mathematical Sciences,

Peking University,

Beijing 100871, P.R. China.

xcfeng@ctb.pku.edu.cn

A. Gabriel

Physics Department, Neurophysics Group,

Philipps-University,

D–35032 Marburg, Germany.

A. Gail

Physics Department, Neurophysics Group,

Philipps-University,

D–35032 Marburg, Germany.

Benoit Gaillard

University of Sussex, United Kingdom

bg22@sussex.ac.uk

Po-Han Lee

The Affiliated Senior High School,

National Taiwan Normal University,

Taipei, Taiwan 106.

Axel Mosig

Bioinformatics Group, Department of Computer Science,

Interdisciplinary Center of Bioinformatics,

University of Leipzig.

Härtelstrasse 16-18, D-04107 Leipzig, Germany

Chien-Hung Huang

Department of Computer Science and Information Engineering,

National Formosa University, Taiwan 632.

zhangyp@ctb.pku.edu.cn

Mengwen Jia

MOE Key Laboratory of Bioinformatics, Department of Automation,

Tsinghua University,

Beijing, 100084,P.R. China.

mwjia@mail.tsinghua.edu.cn

Tao Long

Center for Theoretical Biology and Department of Physics,

Peking University,

Beijing 100871,P.R. China.

Fangting Li

Center for Theoretical Biology and Department of Physics,

Peking University,

Beijing, 100871, P.R.China.

Liaofu Luo

Laboratory of Theoretical Biophysics,

Faculty of Science and Technology,

Inner Mongolia University,

Hohhot, 010021 China.

lfluo@mail.imu.edu.cn

Ying Lu Center

for Theoretical Biology and Department of Physics,

Peking University,

Beijing 100871,P.R. China.

Ka-Lok Ng

Department of Biological Science and Technology,

Asia University,

No.500, Lioufeng Road, Wufeng Shiang,Taichung, Taiwan 413

Jrg Ontrup

Neuroinformatics Group,Faculty of Technology,

Bielefeld University

Qi Ouyang

Center for Theoretical Biology and Department of Physics,

Peking University,

Beijing ,100871, P.R.China.

qi@pku.edu.cn

Sonja J. Prohaska

Bioinformatics Group, Department of Computer Science,

Interdisciplinary Center of Bioinformatics,

University of Leipzig,

Härtelstrasse 16-18, D-04107 Leipzig, Germany.

Minping Qian

Center for Theoretical Biology and School of Mathematical Sciences,

Peking University,

Beijing, 100871, P.R. china

qianmp@math.pku.edu.cn

Helge Ritter

Neuroinformatics Group,Faculty of Technology,

Bielefeld University

M. Saam

Physics Department, Neurophysics Group,

Philipps-University,

D–35032 Marburg, Germany.

Peter F. Stadler

Bioinformatics Group, Department of Computer Science,

Interdisciplinary Center of Bioinformatics,

University of Leipzig,

Härtelstrasse 16-18, D-04107 Leipzig, Germany.

Institute for Theoretical Chemistry,

Wä hringerstrasse 17, A-1090 Wien,

Austria Santa Fe Institute,

1399 Hyde Park Rd., Santa Fe 87501, USA.

Fengzhu Sun

Molecular and Computational Biology Program,

Department of Biological Sciences,

University of Southern California,

Los Angeles, CA 90089 ,USA

fsun@hto.usc.edu

Chao Tang

California Institute for Quantitative Biomedical Research,

Departments of Biopharmaceutical Sciences and Biochemistry andBiophysics QB3,

University of California,

San Francisco, USA.

tang@itsa.ucsf.edu

Henry C. Tuckwell

Max Planck Institute for Mathematics Sciences Inselstr,

22, Leipzig, D-04103 Germany.

tuckwell@mis.mpg.de

Jost

Jochen Steil

Neuroinformatics Group, Faculty of Technology,

Bielefeld University.

Lin Wan

Center for Theoretical Biology and School of Mathematical Sciences,

Peking University,

Beijing 100871, P.R. China

wanlin@ctb.pku.edu.cn

Sebastian Weng

Neuroinformatics Group,Faculty of Technology,

Bielefeld University.

Huan Yu

School of Mathematical Sciences and Center for Theoretical Biology,

Peking University,

Beijing 100871, P.R.China.

Yuping Zhang

Center for Theoretical Biology and School of Mathematical Sciences,

Peking University,

Beijing, 10087, P.R.China.

zhangyp@ctb.pku.edu.cn

Part I

Theory

1

The Category of X-Nets

Andreas Dress

Summary. While, in current discussions, networks are most often described in terms of (more or less ornamented) graphs, in this report, we prefer to describe networks in terms of *metric spaces*. The reason for this is that the concepts and results to be presented here using metric spaces as the basic notion are of some use in the context of phylogenetic analysis where the *lengths* of edges customarily used in pictorial representations of results are not only highly informative as they indicate the presumed time span of evolutionary phases under investigation, they often are already quite essential for deriving such results algorithmically by searching for results that provide edge lengths which are "optimally" adapted to the given data. More specifically, the theory of X-nets described here in terms of metric spaces can be used as a natural framework for taxonomic analysis in terms of *phylogenetic networks* in analogy to the framework offered by the theory of X-trees supporting taxonomic analysis in terms of (the much more familiar) phylogenetic trees.

1.1 Introduction

While, in current discussions, networks are most often described in terms of (more or less ornamented) graphs, in this report on recent work done at the Center for Combinatorics at Nankai University, we prefer to describe networks in terms of *metric spaces*.

The reason for this is that the concepts and results to be presented here using metric spaces as the basic notion are of some use in the context of phylogenetic analysis where the *length* of edges customarily used in pictorial representations of results are not only highly informative as they indicate the presumed time span of evolutionary phases under investigation, they often are already quite essential for *deriving* such results algorithmically by searching for results that provide edge lengths which are "optimally" adapted to the given data.

More specifically, the *category of X-nets* described here in terms of metric spaces can be used as a natural framework for taxonomic analysis in terms of *phylogenetic networks* (cf. [2, 3, 4, 11, 13]) in analogy to the framework offered by the *theory of X-trees* supporting taxonomic analysis in terms of (the much more familiar) *phylogenetic trees* (cf. [5, 14]):

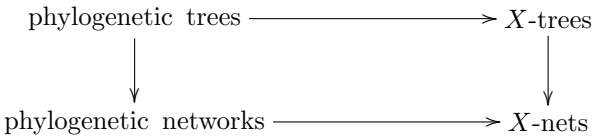

In the next section, we will present some basic terminology. In Section 3, we collect some basic results (whose proofs need still to be written up, in publishable form, jointly with members of the Center for Combinatorics at Nankai University). In Section 4, it will be discussed how X-nets are "classified" by R-valued split systems, and in the last section, some relevant examples are presented, extending from phylogenetic trees and networks to nets related to (i) subjectively perceived similarity of colours, (ii) geographic data from a road atlas, and (iii) the structural relatedness of world languages.

1.2 Basic Terminology

In this note, we consider finite metric spaces $\mathbf{M} = (M, D)$, i.e., pairs consisting of a finite set M and a (proper) metric[1] $D : M \times M \to \mathrm{R} : (u, v) \mapsto uv$ defined on M.

Given any two points u, v in M, we define the interval $[u, v]$ spanned by u and v by

[1] Recall that a metric or, more precisely, a *proper* metric defined on a set M is a bivariate map $D : M \times M \to \mathrm{R} : (u, v) \mapsto uv$ such that $uv = 0 \iff u = v$ and $uv + vw \geq wu$ — and, therefore, also $uv = vu \geq 0$ — holds for all $u, v, w \in M$. Recall also that, according to J. Isbell (cf. [12]), (i) the most appropriate way of defining *The Category of Metric Spaces* denoted by `MET` is to define, for any two metric spaces $\mathbf{M} = (M, D)$ and $\mathbf{M}' = (M', D')$, the set of morphisms from $\mathbf{M}$ into $\mathbf{M}'$ to consist of the set of all *non-expansive* maps from M into M', i.e., all maps $\varphi : M \to M'$ with $D'(\varphi(u), \varphi(v)) \leq D(u, v)$ for all $u, v \in M$, — with composition of morphisms defined in the obvious way, (ii) there is a canonical class of monomorphisms in that category — including all isomorphisms — which are the "isometric embeddings", i.e., the maps $\varphi : M \to M'$ from a metric space $\mathbf{M} = (M, D)$ into a metric space $\mathbf{M}' = (M', D')$ for which $D'(\varphi(u), \varphi(v)) = D(u, v)$ holds for all $u, v \in M$, and that (iii) two metric spaces are called *isometric* if they are isomorphic objects in that category.

$$[u,v] = [u,v]_D := \{w \in M : uv = uw + wv\},$$

we write $u \leq_w v$ for some $w \in M$ whenever $u \in [w,v]$ holds and note that the binary relation "$\leq_u$" is a partial order of M for every $u \in M$, and we define a binary relation "$\|$" on M^2 by putting

$$uu' \| vv' \iff_{\text{def}} u', v \in [u,v'] \text{ and } u, v' \in [u',v]$$

for all pairs $(u,u'),(v,v')$ in M^2.

Next, the L_1-*product* of any two metric spaces $\mathbf{M} = (M,D)$ and $\mathbf{M}' = (M',D')$, denoted by $\mathbf{M} \times \mathbf{M}'$, is defined to be the metric space

$$\mathbf{M} \times \mathbf{M}' := (M \times M', D \oplus D')$$

whose point set is the cartesian product $M \times M'$ of the point sets M and M' of the two given spaces, and whose metric $D \oplus D'$ is defined by putting

$$(D \oplus D')\big((u,u'),(v,v')\big) := D(u,v) + D'(u',v')$$

for all $(u,u'),(v,v') \in M \times M'$ — note that the k-dimensional *standard* L_1-space $\mathbf{L_1}(\mathbf{k}) := (\mathrm{R}^k, L_1^{(k)})$ whose metric $L_1^{(k)} : \mathrm{R}^k \times \mathrm{R}^k \to \mathrm{R}$ is given by

$$L_1^{(k)}(\mathbf{x},\mathbf{y}) := \|\mathbf{x},\mathbf{y}\|_1 := \sum_{i=1}^{k} |x_i - y_i|$$

for all $\mathbf{x} := (x_1,\ldots,x_k), \mathbf{y} := (y_1,\ldots,y_k) \in \mathrm{R}^k$ is nothing but the L_1-product of k copies of the space $\mathbf{L_1}(\mathbf{1})$, that is, the real line (endowed with its standard metric).

Further, given any metric space $\mathbf{M} = (M, D : V \times V \to \mathrm{R} : (u,v) \mapsto uv)$,

(1) we define $\mathbf{M}$ to be an (abstract) L_1-*space* if the relation "$\|$" is an equivalence relation on M^2 — implying that the L_1-product of any two abstract L_1-spaces and, therefore, also (as good sense would require) the standard L_1-spaces $\mathbf{L_1}(\mathbf{k})$ are abstract L_1-spaces (as the real line is easily seen to be one: indeed, one has $uu' \| vv'$ for any two pairs $(u,u'),(v,v')$ of real numbers relative to $L_1^{(1)}$ if and only if either $\#\{u,u'\} = \#\{v,v'\} = 1$ or and $(u,v) = (u',v')$ holds),

(2) we define two elements $u,v \in M$ to be forming a *primitive pair* (in $\mathbf{M}$) if and only if $\#[u,v] = 2$ — or, equivalently, $u \neq v$ and $\{u,v\} = [u,v]$ — holds, and we denote the set of all primitive pairs in $\mathbf{M}$ by $\mathrm{Prim}(\mathbf{M})$, i.e., we put

$$\mathrm{Prim}(\mathbf{M}) := \{\{u,v\} \subseteq M : \#[u,v] = 2\},$$

(3) we define a sequence $a_0, a_1, a_2, \ldots, a_k$ of points in M to be

(i) a *geodesic* sequence (in $\mathbf{M}$) if the identity $a_0a_k = \sum_{i=1}^{k} a_{i-1}a_i$ holds (in which case — even stronger — $a_ia_j = \sum_{\ell=i+1}^{j} a_{\ell-1}a_\ell$ holds for all $i, j \in \{0, 1, 2, \ldots, k\}$ with $i < j$),

(ii) a *path* (in $\mathbf{M}$) if all pairs $\{a_{i-1}, a_i\}$ $(i = 1, 2, \ldots, k)$ are primitive pairs in $\mathbf{M}$,

(iii) and, of course, a *geodesic path* (in $\mathbf{M}$) if it is a geodesic sequence that is, simultaneously, a path in $\mathbf{M}$,

(4) we put

$$\mathbf{M}(u < v) := \{w \in M : u \leq_w v\} \quad (= \{w \in M : u \in [w, v]\})$$

for all $u, v \in M$, we define two elements $u, v \in M$ to be forming a *bipartioning pair* (in $\mathbf{M}$) if $M = \mathbf{M}(u < v) \cup \mathbf{M}(v < u)$ holds — implying that a subset $\{u, v\} \subseteq V$ is a bipartioning pair if and only if $u \neq v$ holds and $\{u, v\}$ is a *gated* subset of $\mathbf{M}$ (i.e., if and only if $\#\{u, v\} = 2$ holds and there exists, for every $x \in M$, some point $y \in \{u, v\}$ — the *gate* of x in $\{u, v\}$ — with $xw = xy + yw$ for each element $w \in \{u, v\}$), and that every bipartioning pair must also be a primitive pair,

(5) we define $\mathbf{M}$ to be *bipartite* if, conversely, every primitive pair in $\mathbf{M}$ is also a bipartioning pair,

(6) and we recall that $\mathbf{M}$ is said to be a *median* space if and only if one has $\#([u, v] \cap [v, w] \cap [w, u]) = 1$ for all $u, v, w \in M$ in which case the single element in $[u, v] \cap [v, w] \cap [w, u]$ is denoted by $\mathrm{med}(u, v, w) = \mathrm{med}_D(u, v, w)$ and dubbed *the* median of u, v, and w — note that the L_1-product of any two median spaces and, therefore, also the standard L_1-spaces $\mathbf{L_1}(\mathbf{k})$ are median spaces (as the real line $\mathbf{L_1}(\mathbf{1})$ is a median space, the median $\mathrm{med}(x, y, z)$ of any three real numbers x, y, z in $\mathbf{L_1}(\mathbf{1})$ being given by $\mathrm{med}(x, y, z) = x + y + z - \max(x, y, z) - \min(x, y, z)$).

Remarks: (R1) Note that the primitive pairs in a finite metric space correspond to the edges in a connected finite graph. More precisely, given any finite metric space $\mathbf{M} = (M, D)$, we can associate to $\mathbf{M}$ the necessarily finite and connected simple graph

$$G_{\mathbf{M}} := (M, \mathrm{Prim}(\mathbf{M}))$$

with vertex set M and edge set $\mathrm{Prim}(\mathbf{M}) \subseteq \binom{M}{2}$ and, conversely, to any finite and connected simple graph $G = (V, E)$ with vertex set V and edge set $E \subseteq \binom{V}{2}$, the finite metric space $\mathbf{M}_G := (V, D_G)$ with point set V whose metric D_G is the standard graph metric on V, i.e., the (well-defined and unique) largest metric D defined on V for which $D(u, v) \leq 1$ holds for every edge $\{u, v\}$ in E.

This yields in particular a canonical one-to-one correspondence between

(i) the isometry classes of finite metric spaces $\mathbf{M}$ for which $D(u, v) = 1$ holds for every primitive pair $\{u, v\}$ in $\mathrm{Prim}(\mathbf{M})$ and

(ii) the isomorphism classes of finite and connected simple graphs.

Recall also that a subgraph $G' = (V', E')$ of a finite and connected simple graph $G = (V, E)$ is called an *isometric* subgraph of G if it is connected and $D_G(u', v') = D'_{G'}(u', v')$ holds for all $u', v' \in V'$.

(R2) More generally, given a *weighted* finite and connected simple graph, i.e., a triple $\mathbf{G} = (V, E; L)$ consisting of a finite and connected simple graph $G = (V, E)$ together with an edge weighting $L : E \to \mathrm{R}_{>0} := \{\rho \in \mathrm{R} : \rho > 0\}$, we may associate to L the unique largest metric $D = D_L$ defined on V for which $D(u, v) \leq L(\{u, v\})$ holds for every edge $\{u, v\}$ in E, this way setting up a canonical one-to-one correspondence between the isometry classes of finite metric spaces $\mathbf{M} = (M, D)$ and the isomorphism classes of weighted finite and connected simple graphs $\mathbf{G} = (V, E; L)$ for which

$$L(\{u, v\}) < \sum_{i=1}^{k} L(\{u_{i-1}, u_i\})$$

holds for every edge $\{u, v\}$ in E and all sequences $u_0, u, \ldots, u_k$ of vertices in V of length $k > 1$ with $u_0 = u, u_k = v$, and $\{u_{i-1}, u_i\} \in E$ for all $i = 1, \ldots, k$ (or, equivalently, for which $D_L(u, v) < D_L(u, w) + D_L(w, v)$ holds for every edge $\{u, v\}$ in E and every $w \in V - \{u, v\}$). Indeed, if $\mathbf{M} = (M, D)$ is a finite metric space, the edge weighting $L = L_{\mathbf{M}}$ defined on the set $\mathrm{Prim}(\mathbf{M})$ of edges of the associated graph $G_{\mathbf{M}}$ by $L_{\mathbf{M}} : \mathrm{Prim}(\mathbf{M}) \to \mathrm{R} : \{u, v\} \mapsto D(u, v)$ satisfies the above condition and one has $D = D_{L_{\mathbf{M}}}$ while conversely, if an edge weighting L defined on the set E of edges of a finite and connected simple graph $G = (V, E)$ satisfies this condition, one has $G = G_{(\mathbf{M}_L)}$ for the associated finite metric space $\mathbf{M}_L = \mathbf{M}_{(G,L)} := (V, D_L)$ while L coincides with the corresponding edge weighting $L_{(\mathbf{M}_L)}$.

(R3) Note that, given a finite and connected simple graph $G = (V, E)$, the above condition holds for *every* edge weighting $L : E \to \mathrm{R}_{>0}$ if and only if G is a tree. The resulting metrics D_L will be called T-metrics, and the

resulting metric spaces $\mathbf{M}_L$ will be called T-spaces. Consequently, a finite metric space $\mathbf{M} = (M, D)$ is a T-space if and only if the associated graph $G_{\mathbf{M}} = (M, \mathrm{Prim}(\mathbf{M}))$ is a tree in which case the metric D_L induced by the edge weighting

$$L := L_{\mathbf{M}} : \mathrm{Prim}(\mathbf{M}) \to \mathrm{R} : \{u, v\} \mapsto D(u, v)$$

coincides with D.

(R4) Note also that a connected finite simple graph G is a bipartite or a median graph if and only if the associated metric space $\mathbf{M}_G$ is a bipartite or a median metric space, respectively, and that every T-space is a bipartite as well as a median metric space.

Finally, we'll need the following definitions:

(7) A finite metric space $\mathbf{H}$ is called a *hypercuboid* if it is isometric to the L_1-product $\mathbf{M}_1, \mathbf{M}_2, \ldots, \mathbf{M}_k$ of a finite number of metric spaces all of whose point sets have cardinality 2 — implying that every hypercuboid is a median L_1-space (as any metric space of cardinality 2 is such a space), that any hypercuboid derived from k factors can be embedded isometrically into the k-dimensional standard L_1-space $\mathbf{L_1}(\mathbf{k})$, and that the graph $G_{\mathbf{H}}$ associated to a hypercuboid $\mathbf{H}$ is a hypercube, i.e., it is isomorphic to a graph of the form $(\{0,1\}^k, E^{(k)})$ with $E^{(k)}$ defined by

$$E^{(k)} := \{\{(x_1, \ldots, x_k), (y_1, \ldots, y_k)\} \subseteq \{0,1\}^k : \sum_{i=1}^{k} |x_i - y_i| = 1\},$$

i.e., the graph associated to the subspace of the standard L_1-space $\mathbf{L_1}(\mathbf{k})$ whose point set is $\{0,1\}^k$.

(8) Another, yet equivalent way to describe hypercuboids is to associate, to any weighted set $\mathbf{E}$, i.e., to a pair $\mathbf{E} := (E, L)$ consisting of a finite set E and a map $L : E \to \mathrm{R}_{>0}$, the metric space $\mathbf{M}^{\mathbf{E}} := (\mathcal{P}(E), D^{\mathbf{E}})$ whose point set is the power set $\mathcal{P}(E)$ of E while its metric $D^{\mathbf{E}}$ is given by the map

$$D^{\mathbf{E}} : \mathcal{P}(E) \times \mathcal{P}(E) \to \mathrm{R} : (F, F') \mapsto L_+(F \triangle F')$$

(where, as usual, $F \triangle F'$ denotes the *symmetric difference* $(F - F') \cup (F' - F)$ of the two subsets F and F' of E, and $L_+(F)$ denotes, for a weighted set $\mathbf{E} = (E, L)$ and a subset F of E, the sum $L_+(F) := \sum_{e \in F} L(e)$), and then to define a finite metric space $\mathbf{H}$ to be a hypercuboid if it is isometric to a metric space of that form, i.e., if a weighted set $\mathbf{E}$ as above exists so that $\mathbf{H}$ is isometric to $\mathbf{M}^{\mathbf{E}}$ (as $\mathbf{M}^{\mathbf{E}}$ is apparently isometric to the L_1-product $\Pi_{e \in E}(\{0,1\}, D_e)$ where $D_e : \{0,1\} \times \{0,1\} \to \mathrm{R}$ is, of course,

defined by $D_e(0,1) = D_e(1,0) := L(e)$ and $D_e(0,0) = D_e(1,1) := 0$). So, $\mathbf{M}^{\mathbf{E}} = (\mathcal{P}(E), D^{\mathbf{E}})$ must, in particular, be a median space — and it is indeed also easily verified directly that the median of any three subsets F, F', F'' of E, considered as points in the point set $\mathcal{P}(E)$ of $\mathbf{M}^{\mathbf{E}}$, always exists, and always coincides with the subset $(F \cap F') \cup (F' \cap F'') \cup (F'' \cap F)$, independently of the choice of L.

(9) A *net* $\mathbf{N}$ is a metric space $\mathbf{N} = (N, D)$ with point set N and metric D that can be embedded into a hypercuboid $\mathbf{M}$ so that any two points in $\mathbf{N}$ can be connected by a geodesic path $a_0, a_1, a_2, \ldots, a_k$ in $\mathbf{M}$ all of whose points are points in $\mathbf{N}$.

(10) We define *the category* `NET` *of nets* to be the category whose objects are the nets while the morphisms from one net $\mathbf{N} = (N, D)$ into another net $\mathbf{N}' = (N', D')$ are defined to be exactly those morphisms from $\mathbf{N}$ into another net $\mathbf{N}'$ in the category `MET` (i.e., those non-expansive maps φ from N into N') that are *additive*, i.e., one has

$$D'(\varphi(u), \varphi(v)) + D'(\varphi(v), \varphi(w)) = D'(\varphi(u), \varphi(w))$$

for all $u, v, w \in V$ with $uv + vw = uw$ (or, equivalently, $\varphi(w) \in [\varphi(u), \varphi(v)]$ holds for all $u, v, w \in N$ with $w \in [u, v]$), and for which

$$\{\varphi(u), \varphi(v)\} \in \mathrm{Prim}(V', D')$$

holds for every primitive pair $\{u, v\}$ in $\mathrm{Prim}(V, D)$ with $\varphi(u) \neq \varphi(v)$. And any such morphism φ is called an *isometric embedding* if φ, considered as a morphism in `MET`, is an isometric embedding, i.e., if $D'(\varphi(u), \varphi(v)) = D(u, v)$ holds for all $u, v \in N$.

(11) Given a finite set X, we define an X-net $\mathcal{N}$ to be a pair $\mathcal{N} := (\mathbf{N}, \psi)$ consisting of a net $\mathbf{N} = (N, D)$ together with a map $\psi : X \to N$ such that

$$\psi(X) \cap \mathbf{N}(u < v) \cap \mathbf{N}(u' < v') \neq \emptyset$$

holds for all primitive pairs $\{u, v\}, \{u', v'\}$ in $\mathbf{N}$ for which the intersection $\mathbf{N}(u < v) \cap \mathbf{N}(u' < v')$ is non-empty.

(12) And we define *the category* `X–NET` *of* X*-nets* to be the category whose objects are the X-nets while the morphisms from one X-net $\mathcal{N} = (\mathbf{N}, \psi)$ into another X-net $\mathcal{N}' = (\mathbf{N}', \psi')$ are those morphisms φ from $\mathbf{N}$ into $\mathbf{N}'$ in `NET` for which $\psi' = \varphi \circ \psi$ holds. As above, any such morphism will also be called an *isometric embedding* if it is one, considered as a morphism in `NET` (or, equivalently, in `MET`).

1.3 Some Basic Results

Clearly, the definition of a net given above is rather a "descriptive" or "constructive" than a structural or "intrinsic" definition. However, the other definitions collected above allow us to present the following seven characterizations of nets two of which are "intrinsic":

Theorem 1. *Given a finite metric space* $\mathbf{M} = (M, D)$*, the following assertions all are equivalent:*

(i) $\mathbf{M}$ *is a net,*

(ii) $\mathbf{M}$ *is a bipartite* L_1*-space,*

(iii) $\mathbf{M}$ *is bipartite and the relation* "$\|$" *defined — by abuse of notation — on* $\mathrm{Prim}(\mathbf{M})$ *by putting*

$$\{u,u'\}\|\{v,v'\} \iff_{\mathrm{def}} uu'\|vv' \text{ or } uu'\|v'v$$

for all $\{u,u'\},\{v,v'\} \in \mathrm{Prim}(\mathbf{M})$ *is an equivalence relation on* $\mathrm{Prim}(\mathbf{M})$*,*

(iv) *the graph* $G_{\mathbf{M}} = (M, \mathrm{Prim}(\mathbf{M}))$ *is an isometric subgraph of a hypercube, and* $uu' = vv'$ *holds for all* u,u',v,v' *in* M *for which* $\{u,u'\},\{v,v'\}$ *are parallel edges in that hypercube,*

(v) *there exists a pair* $(\mathbf{E}, \Delta)$ *consisting of a weighted finite set* $\mathbf{E} = (E, L)$ *and a map* $\Delta : M^2 \to \mathcal{P}(E)$ *with*

$$\mathrm{Prim}(\mathbf{M}) = \{\{u,v\} \subseteq M : \#\Delta(u,v) = 1\}$$

such that

$$\Delta(u,v) = \Delta(u,w) \triangle \Delta(w,v)$$

and

$$D(u,v) = L_+(\Delta(u,v))$$

holds for all $u,v,w \in M$ *in which case*

(a) *the map*

$$\psi_v : M \to \mathcal{P}(E) : u \mapsto \Delta(u,v)$$

is an isometry from $\mathbf{M}$ *into the metric space* $\mathbf{M}^{\mathbf{E}}$ *for given any point* $v \in M$*,*

(b) $\Delta(u,v) = \Delta(v,u)$ *and* "$\Delta(u,v) = \emptyset \iff u = v$" *holds for all* u,v *in* M*,*

(c) *and* $uu' \| vv'$ *holds for some* u, u', v, v' *in* M *if and only if*

$$\Delta(u,u') = \Delta(v,v') \text{ and } \Delta(u,u') \cap \Delta(u',v') = \emptyset$$

and, hence, also

$$\Delta(u,v) = \Delta(u,v') \triangle \Delta(v',v) = \Delta(v',u) \triangle \Delta(u,u') = \Delta(u',v')$$

as well as

$$\Delta(u,v') = \Delta(u,u') \cup \Delta(u',v') = \Delta(u',u) \cup \Delta(u,v) = \Delta(u',v)$$

holds,

(vi) *there exists some* $k \in \mathrm{N}$ *and an isometric embedding* φ *of* $\mathbf{M}$ *into the standard* k*-dimensional* L_1*-space* $\mathbf{L_1(k)}$ *such that*

$$\mathrm{med}_{\mathbf{L_1(k)}}(\varphi(u), \varphi(v), \varphi(w)) \in \{\varphi(u), \varphi(v)\}$$

holds for all $u, v, w \in M$ *with* $\{u, v\} \in \mathrm{Prim}(\mathbf{M})$*,*

(vii) *there exists an isometric embedding* φ *of* $\mathbf{M}$ *into some median* L_1*-space* $\mathbf{M'}$ *with such that* $\mathrm{med}_{\mathbf{M'}}(\varphi(u), \varphi(v), \varphi(w)) \in \{\varphi(u), \varphi(v)\}$ *holds for all* $u, v, w \in M$ *with* $\{u, v\}$ *in* $\mathrm{Prim}(\mathbf{M})$*.*

To establish Theorem 3.58, the following more detailed results are required:

Theorem 2. *A path* $a_0, a_1, \ldots, a_k$ *in a finite bipartite metric space* $\mathbf{M}$ *is a geodesic path if and only if* $\{a_{i-1}, a_i\} \| \{a_{j-1}, a_j\}$ *implies* $i = j$ *for all* $i, j = 1, \ldots, k$*. Furthermore, if* $a_0, a_1, \ldots, a_k$ *is a geodesic path in* $\mathbf{M}$*, one has* $k' \geq k$ *for any other path* $a'_0, a'_1, \ldots, a'_{k'}$ *of points in* $\mathbf{M}$ *with* $a_0 = a'_0$ *and* $a_k = a'_{k'}$ *while equality* $k = k'$ *holds if and only if the path* $a'_0, a'_1, \ldots, a'_{k'}$ *is also a geodesic path in which case there exists a permutation* π *of the index set* $\{1, \ldots, k\}$ *such that* $a_{i-1}a_i = a'_{\pi(i)-1}a'_{\pi(i)}$ *holds for all* $i = 1, \ldots, k$*.*

Theorem 3. *If* $\mathbf{M} = (M, D)$ *is a finite bipartite metric space for which the binary relation "*$\|$*" defined above on* $\mathrm{Prim}(\mathbf{M})$ *is an equivalence relation on* $\mathrm{Prim}(\mathbf{M})$*, one has* $\{u, v\} \| \{u', v'\}$ *for two primitive pairs* $\{u, v\}, \{u', v'\}$ *in* $\mathrm{Prim}(\mathbf{M})$ *if and only if the two bipartitions* $\{\mathbf{M}(u < v), \mathbf{M}(v < u)\}$ *and* $\{\mathbf{M}(u' < v'), \mathbf{M}(v' < u')\}$ *of the point set* M *of* $\mathbf{M}$ *associated with* $\{u, v\}$ *and* $\{u', v'\}$ *coincide.*

Thus, denoting the set of "$\|$"-equivalence classes in $\mathrm{Prim}(\mathbf{M})$ by $\mathrm{E}(\mathbf{M})$ and associating to any path $a_0, a_1, \ldots, a_k$ in $\mathbf{M}$ the set

$$\Delta(a_0, a_1, \ldots, a_k) := \{e \in \mathrm{E}(\mathbf{M}) : \#\{i \in \{1, \ldots, k\} : \{a_{i-1}, a_i\} \in e\} \equiv 1 \mod 2\}$$

of "$\|$"-equivalence classes e in $\mathrm{E}(\mathbf{M})$ represented by an odd number of pairs of the form $\{a_{i-1}, a_i\}$ $(i = 1, \ldots, k)$, the following can be established:

Theorem 4. *If* $\mathbf{M}$ *is a finite bipartite metric space for which the binary relation "*$\|$*" defined above on* $\mathrm{Prim}(\mathbf{M})$ *is an equivalence relation on* $\mathrm{Prim}(\mathbf{M})$*, a path* $a_0, a_1, \ldots, a_k$ *in* $\mathbf{M}$ *is a geodesic path in* $\mathbf{M}$ *if and only if the cardinality of set* $\Delta(a_0, a_1, \ldots, a_k)$ *coincides with* k *in which case one has* $\Delta(a_0, a_1, \ldots, a_k) = \Delta(a'_0, a'_1, \ldots, a'_{k'})$ *for any other path* $a'_0, a'_1, \ldots, a'_{k'}$ *in* $\mathbf{M}$ *with* $a_0 = a'_0$ *if and only if* $a_k = a'_{k'}$ *holds — allowing us to (well-)define the map* $\Delta : V^2 \to \mathcal{P}(\mathrm{E}(\mathbf{M}))$ *as described in* Theorem 3.58 (v) *by letting* $\Delta(u, v)$ *denote the set* $\Delta(a_0, a_1, \ldots, a_k)$ *for one — or, as well, for all — paths* $a_0 := u, a_1, \ldots, a_k; = v$ *from* u *to* v *in* $\mathbf{M}$

Together, these results can be used to establish

Theorem 5. (i) *For any two* X*-nets* $\mathcal{N}$ *and* $\mathcal{N}'$*, there exists at most one morphism in* X–NET *from* $\mathcal{N}$ *into* $\mathcal{N}'$*.*
(ii) *Whenever a (necessarily unique) morphism* φ *from an* X*-net* $\mathcal{N} = (\mathbf{N}, \psi)$ *into an* X*-net* $\mathcal{N}' = (\mathbf{N}', \psi')$ *exists, this morphism is an isometric embedding if and only if* ψ *and* ψ' *induce the same metric on* X*, i.e., if and only if*

$$D(\psi(x), \psi(y)) = D'(\psi'(x), \psi'(y))$$

holds for all $x, y \in X$*.*
(iii) *For every* X*-net* $\mathcal{N}$*, there exists an* X*-net* $\mathcal{N}^*$*, also called the* injective hull *of* $\mathcal{N}$*, together with an isometric embedding* $\varphi_{\mathcal{N}}$ *from* $\mathcal{N}$ *into* $\mathcal{N}^*$ *such that, for every isometric embedding* φ *of* $\mathcal{N}$ *into another* X*-net* $\mathcal{N}'$*, there exists a (necessarily unique) isometric embedding* φ' *from* $\mathcal{N}'$ *into* $\mathcal{N}^*$ *with* $\varphi_{\mathcal{N}} = \varphi' \circ \varphi$ *(implying, as usual, that both,* $\mathcal{N}^*$ *and* $\varphi_{\mathcal{N}}$ *are uniquely determined up to canonical isomorphism by* $\mathcal{N}$*, and that* $\mathcal{N}^*$ *is also the injective hull of every* X*-net* $\mathcal{N}'$ *for which an isometric embedding from* $\mathcal{N}$ *into* $\mathcal{N}'$ *exists).*
Moreover, any morphism φ *in* X–NET *from an* X*-net* $\mathcal{N}_1$ *into an* X*-net* $\mathcal{N}_2$ *induces a morphism* φ^* *in* X–NET *from the injective hull* $\mathcal{N}_1^*$ *of* $\mathcal{N}_1$ *into the injective hull* $\mathcal{N}_2^*$ *of* $\mathcal{N}_2$*.*
(iv) *And, given an* X*-net* $\mathcal{N} = (\mathbf{N}, \psi)$*, the underlying metric space* N *of* $\mathcal{N}$ *is a median metric space if and only if every isometric embedding from* $\mathcal{N}$ *into any other* X*-net* $\mathcal{N}'$ *is an isomorphism if and only if the morphism* $\varphi_{\mathcal{N}} : \mathcal{N} \to \mathcal{N}^*$ *is an isomorphism, that is, if and only if* $\mathcal{N}$ *is its own injective hull (implying that the underlying metric space of the injective hull* $\mathcal{N}^*$ *of any* X*-net* $\mathcal{N}$ *is a median metric space).*

Corollary 1. *Every* T*-space is a net while a pair* $(\mathbf{N}, \psi)$ *consisting of* T*-space* $\mathbf{N} = (N, D)$ *and a map* $\psi : X \to N$ *from* X *into the point set* N *of* $\mathbf{N}$ *is an* X*-net if and only if the tree* $G_{\mathbf{N}}$ *together with the map* ψ *from* X *into its vertex set* N *is an* X*-tree, i.e., if and only if every vertex in the graph*

$$G_{\mathbf{N}} = (N, \mathrm{Prim}(\mathbf{N}))$$

of degree less than 3 *is contained in the image of* ψ*.*

1.4 X-nets and Split Systems over X

Now, recall that given any finite set X, one denotes

- by $\mathcal{S}(X)$ the collection
$$\mathcal{S}(X) := \{\{A, B\} : A, B \subseteq X, A \cup B = X, A \cap B = \emptyset\}$$
of all *X-splits*,
- by $S(x)$, for every X-split $S = \{A, B\} \in \mathcal{S}(X)$ and every element $x \in X$, that subset, A or B, in S that contains x,
- by $\mathcal{S}^*(X)$ the collection
$$\mathcal{S}^*(X) := \{\{A, B\} : A, B \subseteq X, A \cup B = X, A \cap B = \emptyset \neq A, B\}$$
of all *bipartitions* of X, or *proper X-splits*,
- and by $\mathcal{S}^*(X|\,\mathrm{R})$ the R-vectorspace consisting of all maps μ from $\mathcal{S}(X)$ into R with $\mu(\{X, \emptyset\} = 0$, that is, all maps μ from $\mathcal{S}(X)$ into R whose support
$$\mathrm{supp}(\mu) := \{S \in \mathcal{S}(X) : \mu(S) \neq 0\}$$
is contained in $\mathcal{S}^*(X)$.

Any such map μ will also be called an (R-weighted) split system over X, and it will be called an $\mathrm{R}_{\geq 0}$-weighted split system over X if $\mu(S) \geq 0$ holds for all $S \in \mathcal{S}(X)$.

There is a close connection between X-nets and $\mathrm{R}_{\geq 0}$-weighted split systems over X. To explicate this, note first that, given a finite set X and an X-net $\mathcal{N} = (\mathbf{N}, \psi)$, one can associate, to any primitive pair $\{u, v\} \in \mathrm{Prim}(\mathbf{N})$, the corresponding X-split
$$S_{u,v} = S^{\mathcal{N}}_{u,v} := \{X(u < v), X(v < u)\}$$
whose two parts $X(u < v)$ and $X(v < u)$ are the pre-images (relative to ψ) of the two parts of the split $\{\mathbf{N}(u < v), \mathbf{N}(v < u)\}$ associated to the pair $\{u, v\}$ in $\mathrm{Prim}(\mathbf{N})$, i.e., the two subsets
$$X(u < v) = X^{\mathcal{N}}(u < v) := \{x \in X : \psi(x) \in \mathbf{N}(u < v)\}$$
and
$$X(v < u) = X^{\mathcal{N}}(v < u) := \{x \in X : \psi(x) \in \mathbf{N}(v < u)\}$$
of X. The following is a simple corollary of the definitions and results collected above:

Corollary 2. *Given a finite set X, an X-net $\mathcal{N} = (\mathbf{N}, \psi)$, and two primitive pairs $\{u, v\}\{u', v'\} \in \mathrm{Prim}(\mathbf{N})$, one has $\{u, v\} \| \{u', v'\}$ if and only if $S_{u,v} = S_{u',v'}$ holds. In particular, one has $uv = u'v'$ for any two primitive pairs $\{u, v\}, \{u', v'\}$ in $\mathrm{Prim}(\mathbf{N})$ with $S_{u,v} = S_{u',v'}$.*

In consequence, one can associate, to any X-net $\mathcal{N} = (\mathbf{N}, \psi)$, a corresponding $\mathrm{R}_{\geq 0}$-weighted split system $\mu = \mu_{\mathcal{N}}$ over X that maps any split $S \in \mathcal{S}(X)$ of the form $S = S_{u,v}$ for some primitive pair $\{u, v\} \in \mathrm{Prim}(\mathbf{N})$, onto the positive real number uv, and all other splits $S \in \mathcal{S}(X)$ (including the split $\{X, \emptyset\}$) onto 0.

Conversely, given any $\mathrm{R}_{\geq 0}$-weighted split system μ over X, one can associate to μ the X-net $\mathcal{N} = \mathcal{N}_\mu = (\mathbf{N}_\mu, \psi_\mu) = ((N_\mu, D_\mu), \psi_\mu)$ for which $\mu = \mu_{\mathcal{N}}$ holds that is defined as follows: One defines N_μ to consist of all maps $v : X \to \mathcal{P}(\mathrm{supp}(\mu))$ with

$$\binom{\mathrm{supp}(\mu)}{2} = \bigcup_{x \in X} \binom{\mathrm{supp}(\mu) - v(x)}{2} \tag{1.1}$$

for which

$$v(x) \triangle v(y) = \Delta_\mu(x, y) := \{S \in \mathrm{supp}(\mu) : S(x) \neq S(y)\} \tag{1.2}$$

or, equivalently,

$$v(x) = v(y) \triangle \Delta_\mu(x, y)$$

holds for all $x, y \in X$ — Condition (1.1) just requiring that there exists, for any two splits $S_1, S_2 \in \mathrm{supp}(\mu)$, some $x \in X$ such that $S_1, S_2 \notin v(x)$ holds.

Next, one defines

$$\Delta_\mu(u, v) := \bigcup_{x \in X} u(x) \triangle v(x)$$

and

$$D_\mu(u, v) := \mu_+(\Delta_\mu(u, v))$$

for all maps $u, v : X \to \mathcal{P}(\mathrm{supp}(\mu))$ and, noting that

$$u(x) \triangle v(x) = (\Delta_\mu(x, y) \triangle u(y)) \triangle (\Delta_\mu(x, y) \triangle v(y)) = u(y) \triangle v(y)$$

holds for all $x, y \in X$ and $u, v \in N_\mu$, one sees that

$$\Delta_\mu(u, v) := u(x) \triangle v(x)$$

and

$$D_\mu(u, v) := \mu_+(u(x) \triangle v(x)) = \sum_{S \in u(x) \triangle v(x)} \mu(S)$$

holds for every $x \in X$ and any two maps $v, u \in N_\mu$. And one defines $\psi_\mu : X \to N_\mu$ by associating, to any $x \in X$, the map

$$\psi_\mu(x)(S) : X \to \mathrm{supp}(\mu) : y \mapsto \Delta_\mu(x, y).$$

Using these constructions, it can be shown that the $\mathrm{R}_{\geq 0}$-weighted split systems over X "classify" the *injective objects* in X–NET, i.e., the X-nets $\mathcal{N}$ that "coincide" with their injective hull. More precisely, the following holds for any finite set X:

Theorem 6. (i) *Given any two* $\mathrm{R}_{\geq 0}$*-weighted split systems* μ *and* μ' *over* X*, there exists a morphism* φ *from* $\mathcal{N}_\mu$ *into* $\mathcal{N}_{\mu'}$ *in* X–NET *if and only if* $\mu' \leq \mu$ *holds (i.e., if and only if* $\mu'(S) \leq \mu(S)$ *holds for every* X*-split* S *in* $\mathcal{S}^*(X)$*); in particular, two* X*-nets of the form* $\mathcal{N}_\mu$ *and* $\mathcal{N}_{\mu'}$ *are isomorphic if and only if* $\mu = \mu'$ *holds.*

(ii) *Given any* X*-net* $\mathcal{N}$*, its injective hull* $\mathcal{N}^*$ *is canonically isomorphic to the* X*-net* $\mathcal{N}_\mu$ *for the* $\mathrm{R}_{\geq 0}$*-weighted split systems* $\mu := \mu_{\mathcal{N}}$ *; in particular,* $\mathcal{N}$ *is an injective object in* X–NET *if and only if it is isomorphic to an* X*-net of the form* $\mathcal{N}_\mu$ *for some* $\mathrm{R}_{\geq 0}$*-weighted split system* μ *over* X *in which case there is only one such* $\mathrm{R}_{\geq 0}$*-weighted split system* μ*,* viz.*, the* $\mathrm{R}_{\geq 0}$*-weighted split system* $\mu_{\mathcal{N}}$*; in particular,*

(1) *given any* X*-net* $\mathcal{N}$*, its injective hull* $\mathcal{N}^*$ *is canonically isomorphic to the* X*-net* $\mathcal{N}_{\mu_{\mathcal{N}}}$*,*

(2) *two* X*-nets* $\mathcal{N}$ *and* $\mathcal{N}'$ *have isomorphic injective hulls if and only if* $\mu_{\mathcal{N}} = \mu_{\mathcal{N}'}$ *holds,*

(3) *there exists a morphism from an* X*-net* $\mathcal{N}$ *into the injective hull of an* X*-net* $\mathcal{N}'$ *if and only if* $\mu_{\mathcal{N}} \leq \mu_{\mathcal{N}'}$ *holds.*

(ii) *Given any* X*-net* $\mathcal{N}$*, its injective hull* $\mathcal{N}^*$ *is canonically isomorphic to the* X*-net* $\mathcal{N}_\mu$ *for the* $\mathrm{R}_{\geq 0}$*-weighted split systems* $\mu := \mu_{\mathcal{N}}$*; in particular,* $\mathcal{N}$ *is an injective object in* X–NET *if and only if it is isomorphic to an* X*-net of the form* $\mathcal{N}_\mu$ *for some* $\mathrm{R}_{\geq 0}$*-weighted split system* μ *over* X *in which case there is only one such* $\mathrm{R}_{\geq 0}$*-weighted split system* μ*,* viz.*, the* $\mathrm{R}_{\geq 0}$*-weighted split system* $\mu := \mu_{\mathcal{N}}$*; in particular,*

(1) *given any* X*-net* $\mathcal{N}$*, its injective hull* $\mathcal{N}^*$ *is canonically isomorphic to the* X*-net* $\mathcal{N}_{\mu_{\mathcal{N}}}$*,*

(2) *two* X*-nets* $\mathcal{N}$ *and* $\mathcal{N}'$ *have isomorphic injective hulls if and only if* $\mu_{\mathcal{N}} = \mu_{\mathcal{N}'}$ *holds,*

(3) *there exists a morphism from an X-net $\mathcal{N}$ into the injective hull of an X-net $\mathcal{N}'$ if and only if $\mu_{\mathcal{N}} \leq \mu_{\mathcal{N}'}$ holds.*

1.5 Examples

Here are some "real-life" examples of X-nets. Fig. 1.1 belong to the group of altogether more than 10 phylogenetic trees ever published. They were carefully drawn by Ernst Haeckel who published his work on XXX in 1866, just 7 years after Charles Darwin published "The Origin of Species".

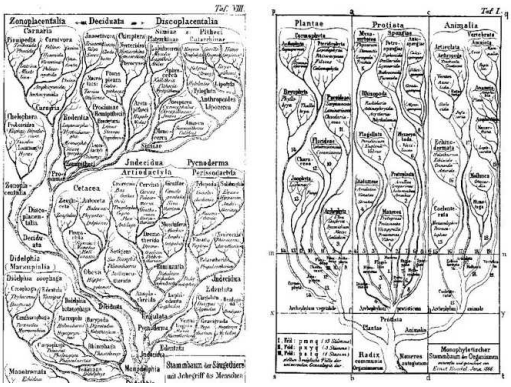

Fig. 1.1. Two phylogenetic trees from Ernst Haeckel's book on XXX.

Fig. 1.2 and Fig. 1.3present *proper* networks, constructed using the program *SplitsTrees* based on data provided by XXX Helms in his thesis on the perception of colour similarity, Hamburg, 1980.

Fig. 1.4-Fig. 1.6 present networks that do not refer to a biological context (even though manuscript copying has a number of interesting analogies with sequence evolution).

Fig. 1.7-Fig. 1.10 deal with proper biological data. Figure 7 deals with 16S rRNA sequences from all three *Kingdoms of Life*, the Eucariots, the Procariots, and the Archeae. Figures 8 and 9 deal with data regarding various variants of the AIDS virus, including HIV1, HIV2, and HIV sequences discovered in other primates. The same data have been analysed in two distinct ways, the first figure being based on (dis)similarity taking into account the first position, only, from each coding triple, the second one taking into account all positions, yet registering only the difference between purins and purimidins, neglecting

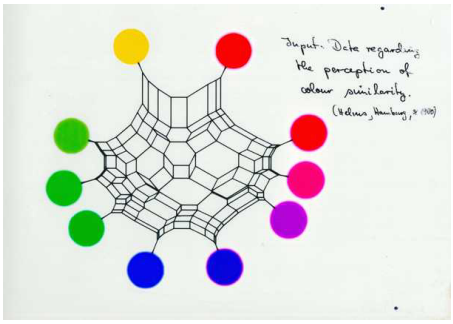

Fig. 1.2. An X-net constructed by applying the program *SplitsTrees* to data regarding the perception of colour similarity (Helms XXX, Hamburg, 1980). The set X consists of 10 distinct colours.

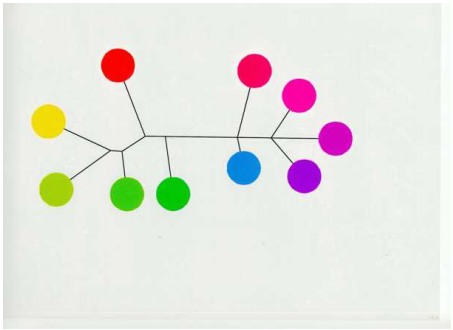

Fig. 1.3. Using data from the same source, now regarding a colour-blind subject's perception of colour similarity (also from data published by Helms XXX, Hamburg, 1980): The X-net constructed by *SplitsTrees* now degenerates into an X-tree.

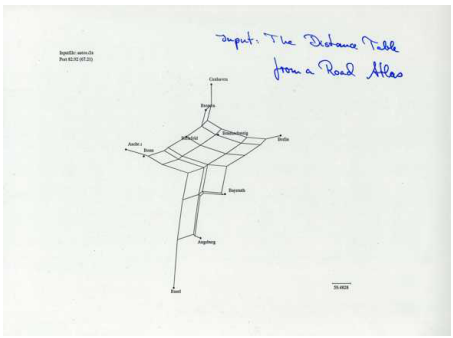

Fig. 1.4. An X-net constructed by applying *SplitsTrees* to data from a German Road Atlas. The set X consists of 10 distinct German cities.

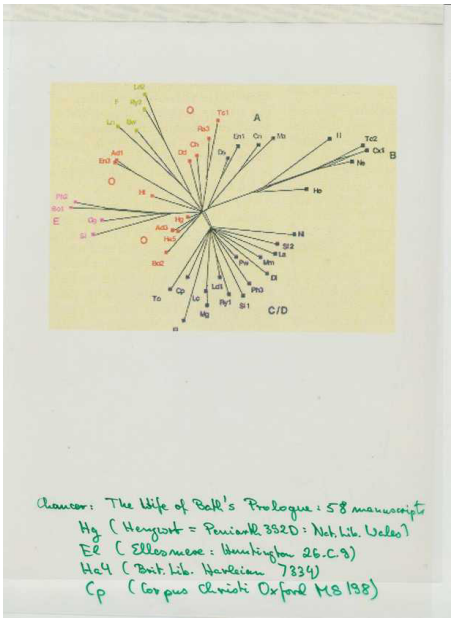

Fig. 1.5. An X-net constructed by Peter Robinson et al by applying *SplitsTrees* to data that he derived by comparing distinct hand-written copies of the Prologue of XXX Chaucer's "The Wife of Bath". The set X consists of more than 40 such manuscripts. And the resulting X-net is, not unexpectedly, rather "tree-ish".

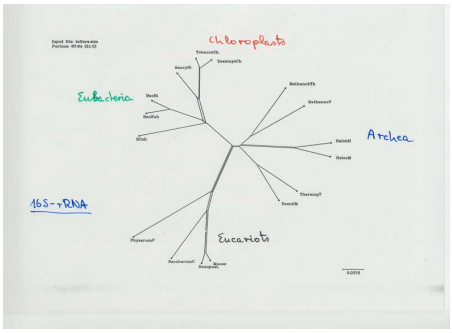

Fig. 1.6. An X-net constructed by Mihai Albu by applying *Neighbour Net* to data from *The World Atlas of Language Structure* depicting the overall structural (dis)similarity of 20 world languages.

transitions between nucleotides. The resulting, rather tree-ish structures are surprisingly similar, corroborating each other, and demonstrating that it is very unlikely that they both are just artefacts of the respective methods of quantifying (dis)similarity applied for deriving these two X-nets. Figure 10 deals with Human mitochondrial DNA data, and the resulting X-net clearly supports Allan Wilson's "Out of Africa" hypothesis (as African sequences can be found all over in that net while all other groups are clearly localized).

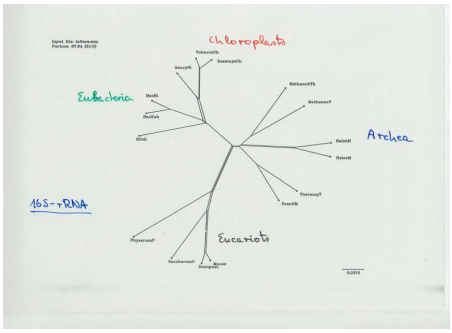

Fig. 1.7. An X-net constructed by applying the program *SplitsTrees* to data regarding the (dis)similarity of 16 distinct 16S rRNA sequences from Eucariots, Procariots, and Archeae. A proper net, though almost a tree as the length of edges not fitting in the "obvious" underlying tree structure is negligibly small. The underlying tree structure clearly supports Karl Woese's thesis claiming the existence of one common ancestor for all currently existing forms of Archeae.

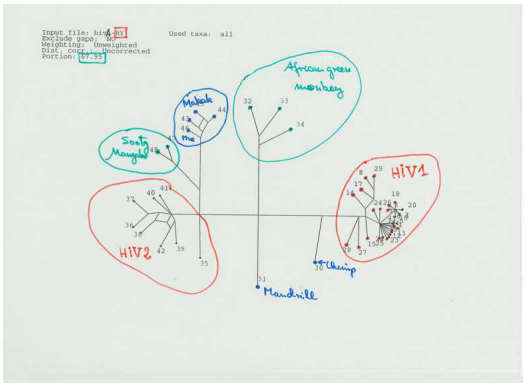

Fig. 1.8. An X-net constructed by applying the program *SplitsTrees* to data regarding the (dis)similarity of HIV sequences, taking into account the first position, only, from each coding triple.

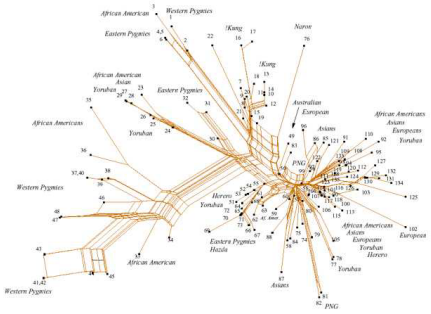

Fig. 1.9. An X-net constructed by applying the program *SplitsTrees* to data regarding the (dis)similarity of HIV sequences, taking into account the difference between purins and purimidins, only, neglecting all *transitions* between nucleotides.

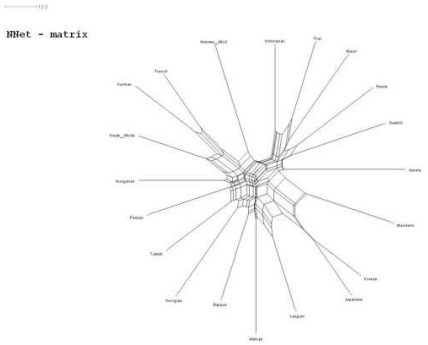

Fig. 1.10. An X-net constructed by applying the program *Neighbour-Net* to data regarding the (dis)similarity of Human mitochondrial DNA sequences. The resulting X-net clearly supports Allan Wilson's "Out of Africa" hypothesis as African sequences can be found all over in that net while all other groups are clearly localized.

References

1. H.-J. Bandelt, Recognition of tree metrics, *SIAM J. Disc. Math.* **3** (1990) 1-6.
2. H.-J. Bandelt, A. Dress, Weak hierarchies associated with similarity measures – an additive clustering technique, *Bul. Math. Biol.* **51** (1989) 133-166.
3. H.-J. Bandelt, A. Dress, A canonical split decomposition theory for metrics on a finite set, *Adv. Math.* **92** (1992) 47-105.
4. H .-J. Bandelt, A. Dress, Split decomposition: a new and useful approach to phylogenetic analysis of distance data, Molecular Phylogenetics and Evolution **1**(3) (1992b) 242-252.
5. J.-P. Barthélemy and A. Guénoche, Trees and proximity representations (Wiley, 1991).

6. P. Buneman, The recovery of trees from measures of dissimilarity. In F. Hodson et al., Mathematics in the Archeological and Historical Sciences, Edinburgh University Press, 1971, pp. 387-395.
7. A. Dress, Trees, tight extensions of metric spaces, and the cohomological dimension of certain groups: A note on combinatorial properties of metric spaces, Adv. in Math. **53** (1984) 321-402.
8. A. Dress, K.T. Huber and V. Moulton, Some variations on a theme by Buneman, Ann. Combin. **1** (1997) 339-352.
9. A. Dress, K.T. Huber and V. Moulton, An explicit computation of the injective hull of certain finite metric spaces in terms of their associated Buneman complex, Adv. in Math. **168** (2002) 1-28.
10. A. Dress, V. Moulton and W. Terhalle, T-theory: An overview, Europ. J. Combinatorics 17 (1996) 161-175.
11. D. Huson, SplitsTree: a program for analyzing and visualizing evolutionary data, *Bioinformatics* **14** (1998) 68-73; see also *http://www-ab.informatik.uni-tuebingen.de/software/splits/welcome_en.h tml*.
12. J. Isbell, Six theorems about metric spaces, *Comment. Math. Helv.* **39** (1964) 65-74.
13. P. J. Lockhart, A. E. Meyer, D. Penny, Testing the phylogeny of Swordtail fishes using Split Decomposition and Spectral Analysis, J. Mol. Evol. **41** (1995) 666-674.
14. C. Semple, M. Steel, Phylogenetics, Oxford University Press, 2003.

2

Networks with Delays

Fatihcan M. Atay

2.1 Introduction

In any collection of interacting dynamical systems, the information flow between the individual units is constrained by the laws of nature. The information may be transmitted by chemical agents in biological systems, by the motion of electrons in electronic devices, and by light in optical equipment. In all cases, it is never conveyed instantaneously, but only after some time delay, across space. Indeed, it is a fundamental law of nature that the speed of light, about 299,792,458 m/s in vacuum, is an upper bound for the speed of mass and energy (and thus of information) flow in any system. Consequently, time delays are a fundamental reality for physical systems.

The description of physical reality, however, cannot and does not (and perhaps need not) include all the details. Mathematical models inevitably contain simplifications in order to be amenable to solution methods. The treatment of time delays is no exception, and it is usual that models of dynamical networks ignore the delays resulting from finite transmission speeds. This does not necessarily mean that such models are not useful. The situation can be compared to the role of Newtonian mechanics which has been used to build most of our existing technology, although the theory of relativity tells us it is not the correct description of the universe. The important thing is to know when relativistic effects need to be included in our formulas, at the expense of making them more complicated. In a similar fashion, it is important to be aware of the possible effects of time delays so that a useful mathematical model can be chosen for the description of dynamical behavior in a particular application.

While the speed of light is an upper limit for information transmission speed, many systems encountered in practice are considerably slower. In a

spectrum of applications ranging from biology to optics, the range of time delays differ by orders of magnitude. The question then is, when to take delays into consideration and when to ignore them. One may be tempted to assume that delays might be more important for the slower biological systems, while they can be safely ignored in faster systems such as lasers or electro-optical devices. Upon more careful study it becomes apparent that the answer also depends on the particular dynamics being studied. Indeed, one sees that delays can only be neglected when they are of a smaller order of magnitude than the characteristic time scales of the system.

Several examples of should be convincing that information transmission even near the speed of light may not be fast enough to ignore the effects of delays. For instance, signals from the earth station reaches a satellites in low earth orbit after about 0.2 s, which implies a round-trip feedback delay of 0.4 s [1]. This round-trip delay is about 3 s for spacecraft near the moon. It may be argued that these are extreme examples because of the astronomical distances involved. However, the effects can be significant also at the distance scales of biological entities. Consider, for instance, a pair of coupled lasers placed 1 m apart . At the speed of light, the information from one laser reaches the other in about 10^{-8} s. Is this a small delay? Considering that the period of a typical laser operating in the nanometer range is on the order of 10^{-14} s, the transmission delay between the lasers is about a million times larger, and certainly significant! (See e.g. [2] for some effects of delays in coupled lasers.) In biological systems delays are generally larger: The delays involved in neuro-muscular action are typically on the order of 0.1 s, which can have important consequences for the dynamics, e.g. in the pupil light reflex [3, 4]. Similarly, the relatively slow speed of neural signal propagation along axons (0.1-10 m/s) gives rise to distance-dependent delays in the neural field, some of whose consequences will be briefly mentioned in Section 2.4.

What is it, then, that might be missed by neglecting delays in network models? Certainly there is a *quantitative* loss which manifests itself in decreased numerical accuracy of the results, which may or may not be significant for the particular application. More importantly, there is also the possibility of a *qualitative* loss, in the sense that the delays may cause a completely different type of behavior which is absent in the undelayed model. The importance of qualitative discrepancies between the data and the model can hardly be over-emphasized, as they bring into question the validity of experimental techniques, data analysis methods, and the assumptions underlying the model. It is thus important to know when the model can be reconciled with data by taking the time delays into account.

In the following sections we give an overview of the qualitatively different dynamics that may emerge in networks as a result of time delays. We focus on three prototypical examples of dynamical networks, each with a different

character, that are often used to model physical and biological systems. We will see how delays enhance synchrony in coupled map lattices, suppress oscillations in coupled oscillators, and lead to traveling waves in coupled neural field models.

2.2 Coupled map lattices

A map, or a function, f on a suitable space (here $\mathbb{R}$) induces a discrete-time dynamical system by the iteration rule

$$x(t+1) = f(x(t))$$

where the iteration step $t \in \mathbb{Z}$ plays the role of discrete time. A coupled map lattice [5] is a collection of such systems which interact with each other in some specified way. A model of such a network where the interaction has a diffusive form is given by

$$x_i(t+1) = f(x_i(t)) + \kappa \frac{1}{d_i} \sum_{\substack{j \\ j \sim i}} (f(x_j(t-\tau)) - f(x_i(t))) \tag{2.1}$$

Here, $i = 1, \ldots, N$ indexes the units, $\kappa \in \mathbb{R}$ is the coupling strength, and $\tau \in \mathbb{Z}^+$ is the delay in information transmission. Thus the i-th unit x_i interacts with its d_i neighbors, and the symbol $\sim$ denotes the neighborhood relation, i.e., $i \sim j$ means that the i-th and j-th units are neighbors of each other. The neighborhood relation casts the system as one defined on a graph, and the diffusive nature of interaction is reflected in the *Laplacian* operator

$$\mathcal{L} = I - D^{-1}A,$$

where $A = [a_{ij}]$ is the adjacency matrix

$$a_{ij} = \begin{cases} 1 & \text{if } i \sim j \\ 0 & \text{otherwise} \end{cases}$$

and $D = \text{diag}\{d_1, \ldots, d_N\}$ is the diagonal matrix of vertex degrees, i.e. number of neighbors of the units. The operator $\mathcal{L}$ encapsulates the information about the connection structure of the units.

A natural question is how the dynamics of (2.1) are related to the underlying graph structure. A particularly interesting type of dynamics is *synchronization*, whereby all units tend to behave identically regardless of initial conditions and external disturbances. Even chaotic units, which show sensitive dependence on initial conditions, can exhibit synchronous behavior under

appropriate conditions [6]. In the absence of delays ($\tau = 0$), synchronization is related to the network structure through the eigenvalues of the Laplacian operator, which encapsulates the connection structure of the network [7]. With nonzero delays, the relation between the two becomes more complicated. Figure 2.1 shows the parameter regions where chaotic logistic maps given by

$$f(x) = 4x(1 - x)$$

exhibit synchrony when coupled.

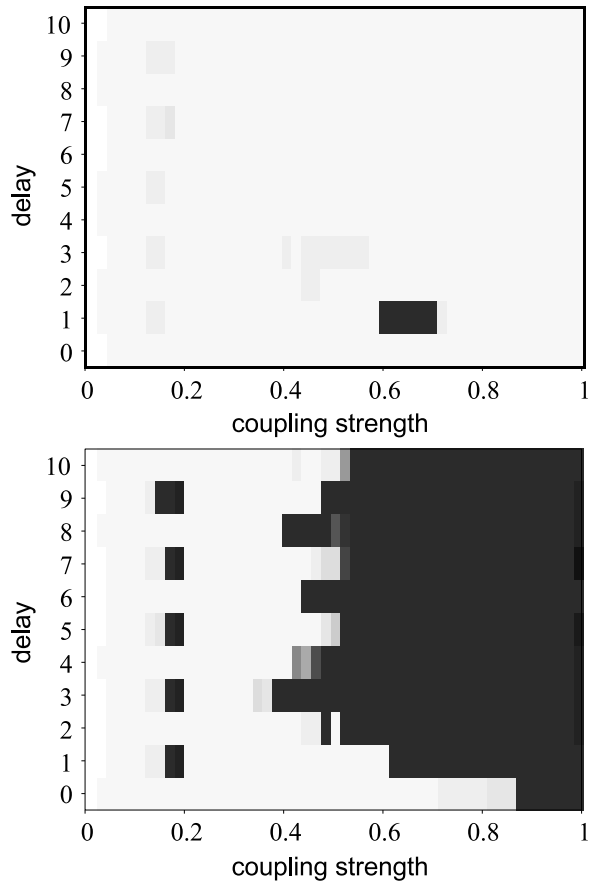

Fig. 2.1. Synchronization of coupled maps. The gray scale codes the degree of synchrony, black corresponding to complete synchronization. The upper graph corresponds a small-world network obtained from a regular one by randomly reconnecting a few edges, and the lower graph is a random network, both having the same number of nodes and links.

It is apparent that delays and the network topology interact in a nontrivial way to determine synchronization. Interestingly, it can be seen from the figure that the delays can enhance synchronization. For instance, in the random network, for the range of coupling strengths $0.6 < \kappa < 0.85$ the system synchronizes only when the delay τ is nonzero. The fact that the delayed system can manage to act in unison at all is a bit surprising in view of the fact that each unit is unaware of the present state of the others. Hence it is all the more surprising when synchrony occurs *only* with delays. Furthermore, it turns out that the synchronous behavior itself can exhibit a wide range of dynamics in the presence of delays, including periodic and quasi-periodic oscilations, chaos with a different Lyapunov exponent than the original map, and hyperchaos (two or more positive Lyapunov exponents) [8, 9]. Even more possibilities arise if the delays in (2.1) are allowed to vary between pairs of units. When the delays are chosen from a random distribution with a sufficiently large variance, the coupled system can tend to a stable fixed point [10]. Thus, the delays can induce a very rich set of new behavior into the network (2.1).

2.3 Coupled oscillators

The coupled map model of the previous section assumes that the units update their states at the same instant, namely at integer values of time. In some cases it is more realistic to consider a continuous update mechanism. Such systems can be described by differential equations in continuous time, which may take the form

$$\dot{x}(t) = f(x(t); \varepsilon) \tag{2.2}$$

with $x \in \mathbb{R}^n$ and $\varepsilon \in \mathbb{R}$ is a parameter. A common example is the modeling of limit cycle oscillators that arise in biology, population dynamics, electronic circuits, etc. One way such stable oscillations can arise is through a supercritical Hopf bifurcation, where the system has a stable fixed point for $\varepsilon < 0$, which loses its stability when ε is increased as a pair of complex conjugate eigenvalues of the linearized system crosses to the right half complex plane at the bifurcation value $\varepsilon = 0$. It can then be shown that under quite general conditions an attracting periodic solution exists for $0 < \varepsilon \ll 1$. We assume this to be the case so that (2.2) models an oscillator. Analogous to (2.1), a coupled system of such oscillators may be represented by

$$\dot{x}_i(t) = f(x_i(t); \varepsilon) + \varepsilon\kappa \frac{1}{d_i} \sum_{\substack{j \\ j \sim i}} (x_j(t - \tau) - x_i(t)) \,. \tag{2.3}$$

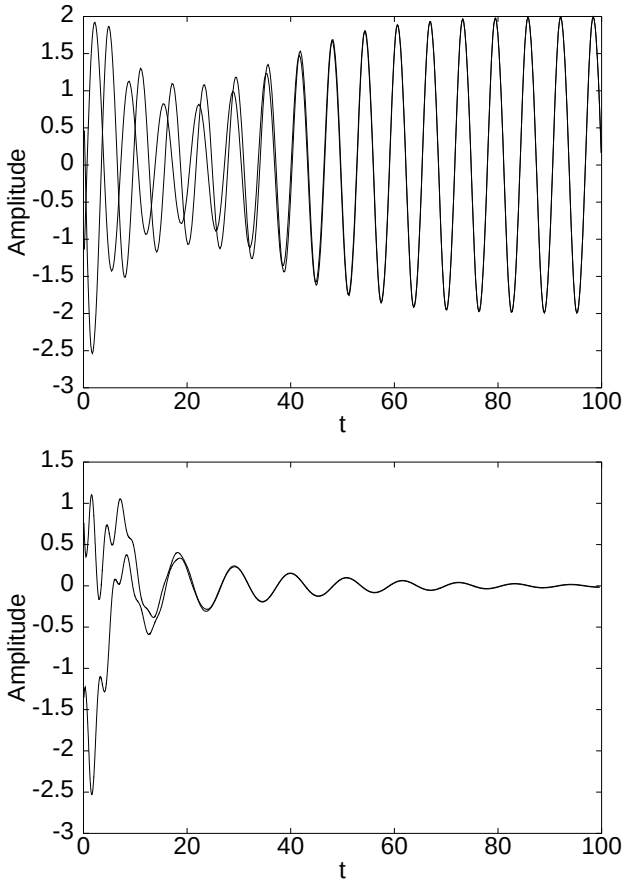

Fig. 2.2. Two coupled van der Pol oscillations. The upper graph shows the behavior when there are no coupling delays ($\tau = 0$), where the system synchronizes. In the lower graph $\tau = 1$, and the oscillations are quenched.

As before, synchrony is again a possible behavior for the coupled system, but we focus on another interesting behavior which emerges in the presence of delays—the so-called *amplitude death* or *oscillator death*. The term refers to the quenching of oscillations as the system is attracted to the fixed point which was unstable for the isolated system (2.2). We illustrate this behavior for the familiar van der Pol oscillator, whose dynamics are described by

$$\ddot{y} + \varepsilon(y^2 - 1)\dot{y} + y = 0 \tag{2.4}$$

For (2.4), the zero solution is stable for negative values of ε, and undergoes a supercritical Hopf bifurcation at $\varepsilon = 0$ as a pair of complex conjugate eigenvalues of the linearized equation migrate to the right half of the complex

plane. For small positive values of ε, there is a stable limit cycle with amplitude near 2, which attracts all initial conditions, except the unstable equilibrium at zero. We couple a pair of such oscillators through their velocities, obtaining the system

$$\begin{aligned} \ddot{y}_1 + \varepsilon(y_1^2 - 1)\dot{y}_1 + y_1 &= \varepsilon\kappa(\dot{y}_2(t-\tau) - \dot{y}_1(t)) \\ \ddot{y}_2 + \varepsilon(y_2^2 - 1)\dot{y}_2 + y_2 &= \varepsilon\kappa(\dot{y}_1(t-\tau) - \dot{y}_2(t)) \end{aligned} \tag{2.5}$$

Figure 2.2 illustrates delay-induced death for (2.5). When there are no delays in the coupling, the oscillators fall into step after starting from arbitrary initial conditions. For positive coupling delay and an appropriate range of coupling strengths, the oscilations are suppressed and replaced by an equilibrium solution.

Interestingly, in a network such as (2.3) where the oscillators are identical, amplitude death is possible only in the presence of delays [11, 12], and for non-identical oscillators, delays make amplitude death easier to occur [13]. This is clearly an important phenomenon since oscillations form a crucial function of many biological systems, such as cardiac cells, neurons, etc., which once again underscores the importance of delays. For systems near Hopf bifurcation, the role of the network topology can be expressed in terms of the largest eigenvalue of the Laplacian operator [14]. Hence, there is again an intimate relation between the delays and the network structure in shaping the dynamics of the system.

2.4 Neural field model

The coarse-grained activity of neural ensembles are often modeled by integro-differential equations of the form [15]

$$L(\partial/\partial t)V(x,t) = \kappa \int_\Omega K(|x-y|)S\left(V\left(y, t - \frac{|x-y|}{v}\right)\right)\, dy + E(x,t). \tag{2.6}$$

Here, $V(x,t)$ denotes the mean postsynaptic potential at time t and location x inside the spatial domain Ω (here $\mathbb{R}$), L is a first or second order temporal differential operator, $\kappa \geq 0$ is the coupling strength, S is a nonlinear transfer function, v is the axonal transmission speed, K is the connectivity kernel, and E is the external input. At first sight, (2.6) has little resemblance to the networks mentioned in the previous sections; but in fact it can be considered as a dynamical network over a continuum of nodes, labeled by the coordinate system in Ω. The propagation delay between two locations (or nodes) x and y is given by $|x-y|/v$. Thus, the delays in the model (2.6) are distributed over an interval, in contrast to the fixed delays of previous examples. Many

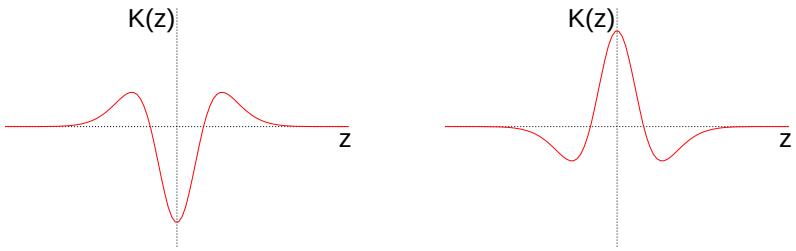

Fig. 2.3. Typical connectivity kernels K for the neural field model: The graph on the left corresponds to local inhibition-lateral excitation, while the one on the right gives local excitation-lateral inhibition.

studies ignore these delays by taking $v = \infty$. The function K describes the connection structure and plays a role similar to the Laplacian operator of (2.1) and (2.3). If K is a positive (respectively, negative) function, then the connections are excitatory (respectively, inhibitory). On the other hand, a kernel K with mixed signs allows the modeling of more general connectivity, such as local inhibition and lateral excitation or vice versa, as depicted in Figure 2.3.

A systematic analysis of (2.6) can proceed by finding spatially uniform equilibrium solutions for constant input level, and study their stability as parameters are varied. By following the behavior near bifurcation values, one can discover such phenomena as spatial patterns (Turing patterns), oscillations, or traveling waves [16, 17]. The bifurcations can be classified as temporally constant or oscillatory, which can further be relegated as spatially constant or varying. Temporally constant bifurcations may lead to spatially uniform equilibria or spatial patterns, while oscillatory bifurcations may yield spatially uniform oscillations or traveling waves. Figure 2.4 summarizes the four basic possibilities for bifurcations. For the system (2.6) it turns out that oscillatory solutions can bifurcate from spatially homogeneous equilibria *only when* delays are present. We make this statement precise by the following theorem.

Theorem 1. *Suppose* $L(\frac{\partial}{\partial t}) = \eta \frac{\partial^2}{\partial t^2} + \gamma \frac{\partial}{\partial t} + \rho$, *where* $\eta = 0$ *or* 1 *and* $\gamma, \rho > 0$. *If*

$$\kappa \int_\Omega |zK(z)|\, dz < |\gamma| v \tag{2.7}$$

then there are no oscillatory bifurcations of spatially homogeneous equilibria.

Clearly, (2.7) is satisfied for instantaneous or very fast signal transmission, so in these cases only stationary solutions can bifurcate from equilibria. Stated

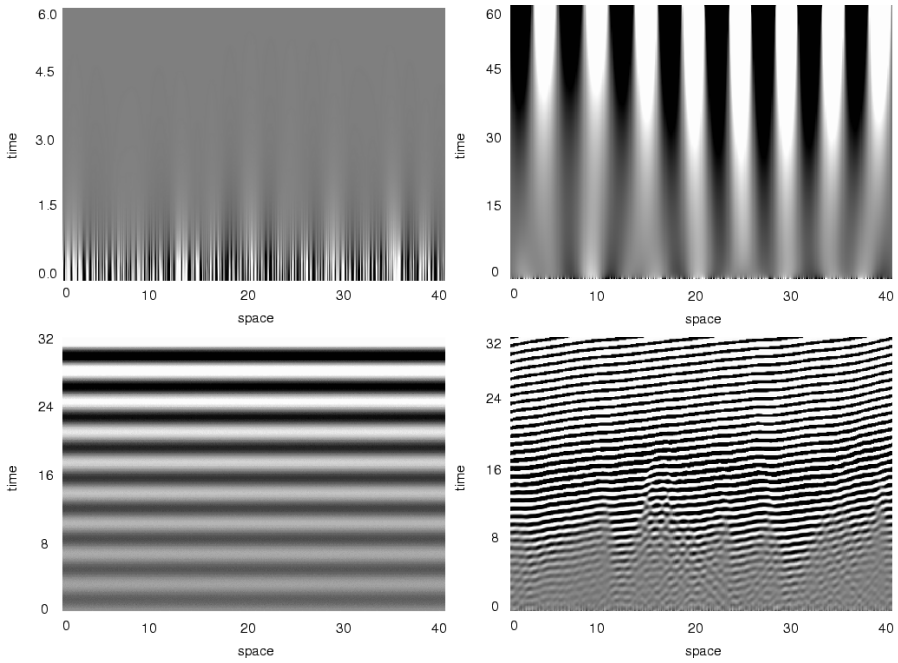

Fig. 2.4. Possible bifurcations from a spatially homogeneous equilibrium of the neural field. In the upper row are the stationary bifurcations leading to a new spatially constant equilibrium (left) or a Turing pattern (right). In the lower row are the oscillatory bifurcations yielding uniform oscillations (left) and traveling waves (right). In each graph, the vertical axis is the time and the horizontal axis is space.

differently, the two possibilities shown in the lower row of Figure 2.4 can only occur in the presence of (sufficiently large) delays. This once again shows the rich dynamics introduced by delayed interaction in the network.

2.5 Conclusion

We have looked at three examples of common networks arising from models of biological and physical systems. Each network is a dynamical system with a different character with respect to space and time, as summarized in Table 2.1. Each one can display quite a rich spectrum of dynamics, depending on the particular nonlinearities, system size, initial conditions, and the like. In each case we have seen that the introduction of transmission delays into the network enables the emergence of completely new behavior, which is not possible in the absence of delays.

Table 2.1. Summary of example networks.

System	Space	Time
Coupled maps	Discrete	Discrete
Coupled differential equations	Discrete	Continuous
Field models	Continuous	Continuous

We have also noted that there is a non-trivial interaction between the delays and the network topology, or connectivity, which turns out to be an important factor in shaping the dynamical features of the system. In our examples of discrete networks, the connectivity is described by the Laplacian operator (which can be derived from the adjacency matrix), which supposes that the interaction between the units is of diffusive type. Similarly, in the continuous neural field (2.6), the connectivity given by the kernel K assumes a homogeneous and isotropic field, since it depends only on the absolute value of the distance betwen two locations. Of course more general interaction types may arise in different application areas. On the other hand, in many applications, such as real neural networks, the precise form of the connectivity is not known. This underlines the fact that it is essential to have a theoretical understanding of the network dynamics for general connectivities, delays, and nonlinearities.

Realistic models of dynamical networks increasingly demand the inclusion of transmission delays for proper analysis, design, and control of their dynamics. As we have seen, novel dynamical behavior can emerge as a result of delays, even though the undelayed network may itself be sufficiently complex. Note that we did not assume any particular form for the nonlinearities in the models considered. Hence, the observations are quite general and applicable to dynamical networks arising in diverse disciplines, showing that the effects of delays are not peculiar to a particular system. A mathematical theory of complex dynamical networks is therefore important for obtaining general results relevant for interacting cells, neurons, proteins, infectious agents, lasers, stock markets, and so on.

References

1. Kolmanovskii V, Myshkis A (1992) Applied Theory of Functional Differential Equations. Kluwer Academic Publishers, Dordrecht
2. Kuntsevich BF, Pisarchik AN (2001) Synchronization effects in a dual-wavelength class-B laser with modulated losses. Phys Rev E 64:046221
3. Longtin A, Milton J (1988) Complex oscillations in the human pupil light reflex with 'mixed' and delayed feedback. Math Biosci 90:183–199

4. Atay FM, Mallet-Paret J (1998) Modeling reflex asymmetries with implicit delay differential equations. Bull Math Biol 60:999–1015
5. Kaneko K (ed) (1993) Theory and applications of coupled map lattices. Wiley, New York
6. Pecora LM, Carroll TL (1990) Synchronization in chaotic systems. Phys Rev Lett 64:821–824
7. Jost J, Joy MP (2002) Spectral properties and synchronization in coupled map lattices. Phys Rev E 65:016201
8. Atay FM, Jost J, Wende A (2004) Delays, connection topology, and synchronization of coupled chaotic maps. Phys Rev Lett 92:144101
9. Atay FM, Jost J (2004) On the emergence of complex systems on the basis of the coordination of complex behaviors of their elements: Synchronization and complexity. Complexity, 10:17–22
10. Masoller C, Marti AC (2005) Random delays and the synchronization of chaotic maps. Phys Rev Lett 94:134102
11. Ramana Reddy DV, Sen A, Johnston GL (1998) Time delay induced death in coupled limit cycle oscillators. Phys Rev Lett 80:5109–5112
12. Atay FM (2003) Total and partial amplitude death in networks of diffusively coupled oscillators. Physica D 183:1–18
13. Atay FM (2003) Distributed delays facilitate amplitude death of coupled oscillators. Phys Rev Lett 91:094101
14. Atay FM (2005) Oscillator death in coupled functional differential equations near hopf bifurcation. J. Differential Equations, to appear.
15. Wilson HR, Cowan JD (1972) Excitatory and inhibitory interactions in localized populations of model neurons. Biophys. J. 12:1–24
16. Atay FM, Hutt A (2005) Stability and bifurcations in neural fields with finite propagation speed and general connectivity. SIAM J. Appl. Math. 65:644–666
17. Hutt A, Atay FM (2005) Analysis of nonlocal neural fields for both general and gamma-distributed connectivities. Physica D 203:30–54

3

Dynamical networks

Jürgen Jost

3.1 Introduction

The theory of dynamical networks is a combination of graph theory and nonlinear dynamics. It is concerned with elements or agents whose states are dynamical quantities, following some dynamical rule, and that dynamical rule includes interactions with neighboring elements. These elements are considered as the nodes or vertices of a graph, and the edges connecting them with other vertices in the graph specify with which other elements they interact. Thus, from the point of view of dynamical systems, we have a coupled system of dynamical equations, and the emphasis is on the resulting global dynamics of the system emerging from the interactions between the local dynamics of the individual elements. Graph theory then analyzes the coupling structure and its influence on those emerging global patterns. Here, one thinks about dynamical nodes, but a fixed topology. In contrast to this, one may also consider how evolution rules shape the dynamics of a network, that is, admitting a dynamical topology. In that scenario, the underlying graph is not fixed, but changing, possibly in response to the dynamics supported by it.
Thus, the emphasis can be put either on the interplay between the local and the global dynamics or on the dynamically evolving topology. Most interesting is a combination of both. Typically, such a combination involves a coupling between two different time scales, a fast one on which the individual dynamic takes place and a slow one on which the networks responds to that dynamic and evolves. In neural networks, for example, one has a fast activity dynamic of the nodes, called neurons in this context, and a slow learning dynamic that changes the weights of the connections, called synapses, in response to the activity correlations between neurons.
While, as discussed the interplay between dynamic and structure is of ultimate interest, for the exposition, we first need to describe the two aspects separately. We start with the theory of the underlying structure, that is, with

graph theory, with a view towards dynamical patterns. In particular, we shall introduce and analyze the graph Laplacian and its spectrum. This will also provide a link with dynamical aspects. Namely, we shall consider dynamics at the nodes of the graph that are coupled via that graph Laplacian, or some generalizations thereof. We shall then conclude this survey by discussing the question of synchronization, that is, when the coupling is strong enough to make the dynamics at the nodes identical to each other.

3.2 Qualitative properties of graphs

As described in the introduction, we consider networks of interacting discrete agents or elements. Usually, these interactions not only follow some dynamical rule, but also some underlying structural pattern that encodes which elements interacts with which other one. This is typically specific, in the sense that the interaction partners of each element are specific, selected other elements. This structure may itself evolve in time, but if it does, then it will do so rather slowly in most situations.

This interaction pattern or structure is usually formalized as a graph. The nodes or vertices of the graph are the original elements themselves whereas the edges or links encode the interaction pattern. In the simplest case, the graph is symmetric and without weights, and there is a link between the elements i and j when they interact. In a dynamical evolution, the influences need not be symmetric, however. That is, the state of i may be an input for the computation of the next state of j, but not conversely. In that case, we should represent this by a directed edge from i to j. Thus, we shall construct a directed graph. Also, the interaction or influence may occur with a certain strength w_{ji}, and we may also encode this by assigning the weight w_{ji} to the edge from i to j. We thus obtain a weighted graph; it is symmetric if always $w_{ji} = w_{ij}$.

Examples of unweighted, symmetric graphs are the ones that describe reciprocal social relationships like acquaintance, friendship, scientific collaboration, or the ones that describe infrastructures (roads, train or flight connections between cities, power lines, internet connections between servers etc). Directed graphs occur for such diverse patterns as web links, gene regulatory networks, food webs, flows of payments. Extreme cases are hierarchical or dependency, descendence structures and the like where links can only go in one direction. Weighted graphs occur, for example, as structures of neural networks.

A graph can be represented by its adjacency matrix. That matrix carries an entry 1 (or w_{ji} in the weighted case) at the intersection of the ith row and the jth column if there is a link from i to j. When there is no link, the entry will be 0.

We are interested in qualitative properties of the interaction graph and in quantities whose values can encode the significant such properties. Let us try to develop some of those. We consider the symmetric case without weights. We assume that the graph Γ is connected and finite. We say that two vertices are neighbors if they are connected by an edge. An extreme case is the complete graph of N vertices where each vertex is connected to every other one. Excluding self-connections, we thus have $\frac{N(N-1)}{2}$ links. That graph is said to be fully connected. In particular when N is large, this becomes unwieldy. Typically, large graphs are rather sparsely connected, that is, most entries in the adjacency matrix will be 0.

Another prototype that is a natural starting point is a regular graph. We consider some regular tessellation of Euclidean space, for example by unit cubes or simplices. We take all the corner points of this tessellation, for example all points in Euclidean space with integer coordinates in the case of a unit cube tessellation. We then select a regular connectivity pattern, that is, connect any such points with all the nearest other ones, and perhaps also with the second, third,..., nearest ones. In order to obtain a finite graph, we can identify points that are obtained from each other through a shift of some fixed size in any of the coordinate directions. Such a regular graph then possesses a transitive[1] symmetry group because the connectivity pattern of all the nodes is the same. While such a graph may describe the structure of certain crystals, in most other cases we do not encounter so much homogeneity, but rather some diversity and differences between the connectivity patterns of the various nodes. In order to provide a pattern that is opposite to the one of a regular graph, Erdös and Rényi introduced random graphs. Here, one starts with, say, N nodes and each pair of nodes gets a link with some fixed probability p. That is, we start with a fully connected graph of N nodes and delete any individual edge with probability $1-p$, of course treating all edges independently of each other. Since this is a stochastic constructions, it then makes sense to consider the class of all such random graphs with fixed parameters N, p and derive typical properties, that is, properties that hold almost surely as N tends to ∞, with respect to some obvious natural measure on the space of all such random graphs.

For nodes i, j of a graph Γ, we let $d(i, j)$ denote their distance, that is, the smallest number of edges that establish a connection between them. In a regular graph, the distance between randomly drawn nodes grows like a power of the total number N of nodes. In most graphs occurring in applications, however, the average or maximal distance between nodes is much smaller. This has been called the small-world phenomenon, and Watts and Strogatz[31] proposed a simple algorithm for converting a regular graph into a small-world graph. Namely, given a regular graph and some p between 0 and 1, for any node i, select with probability p a random partner j somewhere in the graph and add a link from i to j. One variant of the construction then deletes one

[1] on the set of nodes

of the original links from i so as to keep the total number of edges constant. When p exceeds some critical threshold, the small-world phenomenon sets in, that is, the average distance between two nodes jumps to a much smaller value than for the original regular graph.

Another class of graphs that recently found much interest are the so-called scale-free graphs. Here, the number of nodes of degree k, that is, those that possess k links, behaves like a power $k^{-\beta}$. That is, the number of nodes of degree k does not decay exponentially as a function of k as many examples of graphs might lead one to expect, but rather only polynomially. Graphs modeling web links, internet connections between servers, airline connections between cities, and also biological networks like gene regulatory networks seem to exhibit this type of structure. Simon[29] and Barabasi and Albert[4] proposed a construction scheme for such scale-free graphs. One starts with some small graph and then adds new nodes successively. Any new node is allowed to make k links while any node already established has a probability proportional to the number of links it already possesses for becoming the recipient of one of those k new links. As the network grows it exhibits this type of scale-free behavior. However, a scale-free structure can also be generated by completely different mechanisms, with different qualitative properties with regard to other aspects.

One such important network aspect is the clustering behavior, both on the local and on the global scale. We start with the local aspect. For an Erdös-Rényi random graph, given a node i_0 and two of its neighbors i_1, i_2, the probability that they are connected, that is, that there exists an edge between i_1 and i_2, is given by the fixed number p underlying the construction and is not influenced at all by the fact that they possess a common neighbor, namely i_0. In many networks arising in applications, this is different, however. Namely, two nodes with a common neighbor have a higher probability of being directly connected than two arbitrary ones. Of course, it may also happen that that probability is lower. For example, for the regular graph formed from the points in Euclidean space with integer coordinates, connected when precisely one of these coordinates differs by 1 between them while the other ones coincide, that probability is 0 as the neighbors of a vertex are never directly connected. Likewise, two neighbors of a vertex are never connected for trees, that is, for graphs without cycles (loops), in other words, for simply connected graphs.

The average probability for two neighbors of some vertex to be directly connected is given by the clustering coefficient C of the graph Γ, defined as 3 times the ratio between the number of triangles in the graph (that is triples of vertices for which each is connected to the other two) and the number of connected triples (that is triples where one is connected to the other two). The factor 3 arises because each triangle contains three connected triples.

One can then also consider other graph motives that are larger than triangles, for example complete subgraphs of k vertices, that is, subgraphs in which any two vertices are connected by an edge, for some $k > 3$ (for $k = 3$, we have the triangles just discussed). Two such complete k-subgraphs are called adjacent

when they share a complete $(k-1)$-subgraph. One can then search for clusters defined as maximal subgraphs consisting of uninterrupted chains of adjacent complete k-subgraph (see [12]). That means that each vertex is contained in a complete k-subgraph, and for any two vertices i, j inside such a cluster, we find a sequence $i_1 = i, i_2, ..., i_n = j$ of vertices inside the cluster such that i_ν and $i_{\nu+1}$ are always contained in adjacent complete k-subgraphs.
This was the local aspect of clustering. The global one is what is also called community structure. Here, one looks for groups of vertices with many connections within a group, but considerably fewer between groups. Perhaps this aspect is best understood by describing methods for breaking a network up into such subgroups or communities. We shall exhibit two methods that are kind of dual to each other. The first one is based on a quantity that is analogous to one introduced by Cheeger in Riemannian geometry. Letting n_i denote the degree of the node i (the number of its neighbors) and $|E|$ the number of edges contained in an edge set E, that quantity is

$$h(\Gamma) := \inf\{\frac{|E_0|}{\min(\sum_{i\in V_1} n_i, \sum_{i\in V_2} n_i)}\} \tag{3.1}$$

where removing E_0 disconnects Γ into the components V_1, V_2. Thus, we try to break the graph up into two large components by removing only few edges. We may then repeat the process within those components to break them further up until we are no longer able to realize a small value of h. The other method was introduced by Girvan and Newman[14]. They define the betweenness of an edge as the number of shortest paths between vertices that contain it, that is, run through it. The underlying intuition is that severing an edge with a high value of that betweenness cuts many shortest paths between vertices on different sides and therefore is conducive to breaking up the graph. Their algorithm for breaking up a graph efficiently into communities then consists in the iterative removal of the (or an) edge with the highest betweenness where of course the value of that betweenness has to be recomputed after each removal.
Rather obvious network parameters are the maximal and the average distance between nodes. As already mentioned, the values of those parameters are high for regular graphs and small for small-world ones. Random graphs also tend to have relatively small values.
So far, we have discussed qualitative features that can be simply described. In the next section, we shall turn to a more a technical set of invariants, the eigenvalues of the graph Laplacian. That will then enable us in subsequent sections to discuss the former qualitative aspects in a more profound manner.

3.3 The graph Laplacian and its spectrum

So far, we have considered quantities that can be directly evaluated from an inspection of the graph. We now turn to constructions that depend on

the choice of additional data. These data are functions on the set of vertices of the graph Γ. Of course, any such function can be extended to the edges by linear interpolation, and we shall occasionally assume that interpolation implicitly. For analyzing such functions, it is in turn useful to have a basis of that function space. For that purpose, we introduce the L^2-product for functions on Γ:

$$(u, v) := \sum_{i\in\Gamma} n_i u(i)v(i) \tag{3.2}$$

where n_i is the degree of the vertex i. For purposes of normalization, one might wish to put an additional factor $\frac{1}{|\Gamma|}$ in front where $|\Gamma|$ is the number of elements of the graph, but we have decided to omit that factor in our conventions. We may then choose an orthonormal base of that space $L^2(\Gamma)$. In order to find such a basis that is also well adapted to dynamical aspects, we introduce the graph Laplacian

$$\Delta : L^2(\Gamma) \to L^2(\Gamma)$$

$$\Delta v(i) := \frac{1}{n_i} \sum_{j,j\sim i} v(j) - v(i) \tag{3.3}$$

where $j \sim i$ means that j is a neighbor of i. [2] The idea behind this operator is the comparison of the value of a function v at a vertex i with the average of the values at the neighbors of i. Thus, Δv detects local inhomogeneities in the values of the function v. In particular, since we assume that our graph is connected

- $$\Delta v \equiv 0 \text{iff} v \equiv \text{const.} \tag{3.4}$$

  (If the graph is not connected, then $\Delta v \equiv 0$ when v is constant on each component.)

Other important properties of Δ are the following ones:

- Δ is selfadjoint w.r.t. $(.,.)$:

[2] There are several different definitions of the graph Laplacian in the literature. Some of them are equivalent to ours inasmuch as the yield the same spectrum, but others are not. In the monograph [8], the operator $\mathcal{L}v(i) := v(i) - \sum_{j,j\sim i} \frac{1}{\sqrt{n_i}\sqrt{n_j}} v(j)$ is employed. Apart from the minus sign, it has the same eigenvalues as Δ: if $\Delta v(i) = \mu v(i)$, then $w(i) = \sqrt{n_i} v(i)$ satisfies $\mathcal{L}w(i) = -\mu w(i)$. While our operator Δ is symmetric w.r.t. the product $(u, v) = \sum_{i\in\Gamma} n_i u(i)v(i)$, $\mathcal{L}$ is symmetric w.r.t. $\langle u, v\rangle := \sum_{i\in\Gamma} u(i)v(i)$. – The operator $Lv(i) := n_i v(i) - \sum_{j,j\sim i} v(j)$ that is also often employed in the literature, however, has a spectrum different from Δ for general graphs.

$$(u, \Delta v) = (\Delta u, v) \tag{3.5}$$

for all $u, v \in L^2(\Gamma)$.[3] This holds because the neighborhood relation is symmetric.

- Δ is nonpositive:
$$(\Delta u, u) \leq 0 \tag{3.6}$$
for all u. This follows from the Cauchy-Schwarz inequality.

The preceding properties have consequences for the eigenvalues of Δ:

- By (3.5), the eigenvalues are real.
- By (3.6), they are nonpositive. We write them as $-\lambda_k$ so that the eigenvalue equation becomes
$$\Delta u_k + \lambda_k u_k = 0. \tag{3.7}$$
- By (3.4), the smallest eigenvalue then is $\lambda_0 = 0$. Since we assume that Γ is connected, this eigenvalue is simple (see (3.4)), that is
$$\lambda_k > 0 \tag{3.8}$$
for $k > 0$ where we order the eigenvalues as
$$\lambda_0 < \lambda_1 \leq ... \leq \lambda_K$$
($K = |\Gamma| - 1$).

We next consider, for neighbors i, j

$$Du(i, j) := u(i) - u(j) \tag{3.9}$$

(Du can be considered as a function defined on the edges of Γ. Thus, D maps functions on the vertices to functions on the edges.) We also introduce the product

$$(Du, Dv) := (\sum_{j \sim i} (u(i) - u(j))(v(i) - v(j)) \tag{3.10}$$

where the sum is over edges[4] (note that here, in contrast to (3.2), we do not use any weights). We have

[3] An operator $A = (A_{ij})$ is symmetric w.r.t. a product $\langle v, w \rangle := \sum_i b_i v(i) w(i)$, that is, $\langle Av, w \rangle = \langle v, Aw \rangle$ if $b_i A_{ij} = b_j A_{ji}$ for all indices i, j. The b_i are often called multipliers in the literature.

[4] If we summed over pairs of vertices (i, j) with $i \sim j$, then each edge would be counted twice, and we would have to introduce a factor $1/2$ in front of the sum.

$$\begin{aligned}(Du, Dv) &= \frac{1}{2}(\sum_i n_i u(i)v(i) + \sum_j n_j u(j)v(j) - 2\sum_{j\sim i} u(i)v(j)) \\ &= -\sum_i u(i)\sum_{j\sim i}(v(j) - v(i)) \\ &= -(u, \Delta v). \end{aligned} \tag{3.11}$$

We may find an orthonormal basis of $L^2(\Gamma)$ consisting of eigenfunctions of Δ,

$$u_k,\ k = 1, ..., K.$$

This is achieved as follows. We iteratively define, with $H_0 := H := L^2(\Gamma)$ being the Hilbert space of all real-valued functions on Γ with the scalar product $(.,.)$,

$$H_k := \{v \in H : (v, u_i) = 0 \text{ for } i \leq k-1\}, \tag{3.12}$$

starting with a constant function u_0 as the eigenfunction for the eigenvalue $\lambda_0 = 0$. Also

$$\lambda_k := \inf_{u \in H_k - \{0\}} \frac{(Du, Du)}{(u, u)}, \tag{3.13}$$

that is, we claim that the eigenvalues can be obtained as those infima. First of all, since $H_k \subset H_{k-1}$, we have

$$\lambda_k \geq \lambda_{k-1}. \tag{3.14}$$

Secondly, since the expression in (3.13) remains unchanged when a function u is multiplied by a nonzero constant, it suffices to consider those functions that satisfy the normalization.

$$(u, u) = 1 \tag{3.15}$$

whenever convenient.
We may find a function u_k that realizes the infimum in (3.13), that is

$$\lambda_k = \frac{(Du_k, Du_k)}{(u_k, u_k)}. \tag{3.16}$$

Since then for every $\varphi \in H_k, t \in \mathbb{R}$

$$\frac{(D(u_k + t\varphi), D(u_k + t\varphi))}{(u_k + t\varphi, u_k + t\varphi)} \geq \lambda_k, \tag{3.17}$$

the derivative of that expression w.r.t. t vanishes at $t = 0$, and we obtain, using (3.11)

$$0 = (Du_k, D\varphi) - \lambda_k(u_k, \varphi) = -(\Delta u_k, \varphi) - \lambda_k(u_k, \varphi) \tag{3.18}$$

for all $\varphi \in H_k$; in fact, this even holds for all $\varphi \in H$, and not only for those in the subspace H_k, since for $i \leq k-1$

$$(u_k, u_i) = 0 \tag{3.19}$$

and

$$(Du_k, Du_i) = (Du_i, Du_k) = -(\Delta u_i, u_k) = \lambda_i(u_i, u_k) = 0 \tag{3.20}$$

since $u_k \in H_i$. Thus, if we also recall (3.11),

$$(\Delta u_k, \varphi) + \lambda_k(u_k, \varphi) = 0 \tag{3.21}$$

for all $\varphi \in H$ whence

$$\Delta u_k + \lambda_k u_k = 0. \tag{3.22}$$

Since, as noted in (3.15), we may require

$$(u_k, u_k) = 1 \tag{3.23}$$

for $k = 0, 1, ..., K$ and since the u_k are mutually orthogonal by construction, we have constructed an orthonormal basis of H consisting of eigenfunctions of Δ. Thus we may expand any function f on Γ as

$$f(i) = \sum_k (f, u_k) u_k(i). \tag{3.24}$$

We then also have

$$(f, f) = \sum_k (f, u_k)^2 \tag{3.25}$$

since the u_k satisfy

$$(u_j, u_k) = \delta_{jk}, \tag{3.26}$$

the condition for being an orthonormal basis. Finally, using (3.25) and (3.11), we obtain

$$(Df, Df) = \sum_k \lambda_k (f, u_k)^2. \tag{3.27}$$

We next derive **Courant's minimax principle**:
Let P^k be the collection of all k-dimensional linear subspaces of H. We have

$$\lambda_k = \max_{L \in P^k} \min \{ \frac{(Du, Du)}{(u, u)} : u \neq 0,\ (u, v) = 0 \text{ for all } v \in L \} \tag{3.28}$$

and dually

$$\lambda_k = \min_{L \in P^{k+1}} \max \{ \frac{(Du, Du)}{(u, u)} : u \in L \backslash \{0\} \}. \tag{3.29}$$

To verify these relations, we recall (3.13)

$$\lambda_k = \min\{\frac{(Du, Du)}{(u, u)} : \ u \neq 0, (u, u_j) = 0 \text{ for } j = 1, ..., k-1\}. \tag{3.30}$$

Dually, we have

$$\lambda_k = \max\{\frac{(Du, Du)}{(u, u)} : \ u \neq 0 \text{ linear combination of } u_j \text{ with } j \leq k\}. \tag{3.31}$$

The latter maximum is realized when u is a multiple of the kth eigenfunction, and so is the minimum in (3.30). If now L is any $k+1$-dimensional subspace, we may find some v in L that satisfies the k conditions

$$(v, u_j) = 0 \text{ for } j = 0, ..., k-1. \tag{3.32}$$

From (3.25) and (3.27), we then obtain

$$\frac{(Dv, Dv)}{(v, v)} = \frac{\sum_{j \geq k} \lambda_j (v, u_j)^2}{\sum_{j \geq k} (v, u_j)^2} \geq \lambda_k. \tag{3.33}$$

This implies

$$\max_{v \in L \setminus \{0\}} \frac{(Dv, Dv)}{(v, v)} \geq \lambda_k. \tag{3.34}$$

We then obtain (3.29). (3.28) follows in a dual manner.

For linking the function theory on Γ with the underlying topological structure of Γ, it is important to understand how the eigenvalues of Δ depend on the properties of Γ. Again, we start with some extreme cases that are easy to analyze.
For a fully connected graph, we have

$$\lambda_1 = ... = \lambda_K = \frac{|\Gamma|}{|\Gamma| - 1} \tag{3.35}$$

since

$$\Delta v = -v \tag{3.36}$$

for any v that is orthogonal to the constants, that is

$$\frac{1}{|\Gamma|} \sum_{i \in \Gamma} n_i v(i) = 0. \tag{3.37}$$

We also recall that since Γ is connected, the trivial eigenvalue $\lambda_0 = 0$ is simple. If Γ had two components, then the next eigenvalue λ_1 would also become 0. A corresponding eigenfunction would be equal to a constant on each component, the two values chosen such (3.37) is satisfied; in particular, one of the two would be positive, the other one negative. We therefore expect

that for graphs with a pronounced community structure, that is, for ones that can be broken up into two large components by deleting only few edges as discussed above, the eigenvalue λ_1 should be close to 0. Formally, this is easily seen from the variational characterization

$$\lambda_1 = \min\{\frac{\sum_{j\sim i}(v(i)-v(j))^2}{\sum_i n_i v(i)^2} : \sum_i n_i v(i) = 0\} \tag{3.38}$$

(see (3.13) and observe that $\sum_i n_i v(i) = 0$ is equivalent to $(v, u_0) = 0$ as the eigenfunction u_0 is constant). Namely, if two large components of Γ are only connected by few edges, then one can make v constant on either side, with opposite signs so as to respect the normalization (3.37) with only a small contribution from the numerator.
The strategy for obtaining an eigenfunction for the first eigenvalue λ_1 is, according to (3.38), to do the same as one's neighbors. Because of the constraint $\sum_i n_i v(i) = 0$, this is not globally possible, however. The first eigenfunction thus exhibits oscillations with the lowest possible frequency .
By way of contrast, according to (3.29), the highest eigenvalue is given by

$$\lambda_K = \max_{u\neq 0} \frac{(Du, Du)}{(u, u)}. \tag{3.39}$$

Thus, the strategy for obtaining an eigenfunction for the highest eigenvalue is to do the opposite what one's neighbors are doing, for example to assume the value 1 when the neighbors have the value -1. Thus, the corresponding eigenfunction will exhibit oscillations with the highest possible frequency. Here, the obstacle can be local. Namely, any triangle, that is, a triple of three mutually connected nodes, presents such an obstacle. More generally, any cycle of odd length makes an alternation of the values 1 and -1 impossible. The optimal situation here is represented by a bipartite graph, that is, a graph that consists of two sets Γ_+, Γ_- of nodes without any links between nodes in the same such subset. Thus, one can put $u_m = \pm 1$ on $\Gamma_\pm$. The highest eigenvalue λ_K becomes smallest on a fully connected graph, namely

$$\lambda_K = \frac{|\Gamma|}{|\Gamma| - 1} \tag{3.40}$$

according to (3.37). For graphs that are neither bipartite nor fully connected, this eigenvalue lies strictly between those two extremal possibilities.
Perhaps the following caricature can summarize the preceding: For minimizing λ_1 – the minimal value being 0 – one needs two subsets that can internally be arbitrarily connected, but that do not admit any connection between each other. For maximizing λ_K – the maximal value being 2 – one needs two subsets without any internal connections, but allowing arbitrary connections between them. In either situation, the worst case – that is the one of a maximal value for λ_1 and a minimal value for λ_K – is represented by a fully connected graph.

In fact, in that case, λ_1 and λ_K coincide.

We also have the following version of Courant's nodal domain theorem of Gladwell-Davies-Leydold-Stadler [15]:

Lemma 1. *Let u_k be an eigenfunction for the eigenvalue λ_k, with our above ordering, $0 = \lambda_0 < \lambda_1 \leq \lambda_2 \leq .... \leq \lambda_K$. Delete from Γ all edges that connect points on which the values of u_k have opposite signs. This divides Γ into connected components $\Gamma_1, ..., \Gamma_l$. Then $l \leq k+1$, where we need to order the eigenvalues appropriately when they are not simple.*

Systematic questions:

- What is the relationship between global properties or quantities (diameter, clustering coefficient, Cheeger constant, community structure,...), local quantities (pointwise clustering, upper and lower bounds for vertex degrees,...) and eigenvalues?

- How do operations on graphs affect eigenvalues, in particular (in the case of a connected graph) λ_1 as given in (3.38)? Let us consider some examples for the latter question:

  1. We add a new node, labeled j_0, with a single edge to some existing node i_0 in the graph Γ. This does not increase λ_1. This is seen as follows: Let $u = u_1$ be a first eigenfunction; thus, u realizes the infimum in (3.38) and satisfies the constraint $\sum_i n_i u(i) = 0$. However, on the new graph Γ' obtained by adding the node j_0, this constraint is no longer satisfied, even if we put $u(j_0) = 0$, because the degree of i_0 has been increased by 1 by the new edge from j_0 to i_0. We therefore construct a new function u' by putting $u'(i) = u(i) + \eta$ for all nodes $i \in \Gamma$ and $u'(j_0) = u'(i_0)$, for some constant η to be determined by the constraint which now becomes $\sum_{j\in\Gamma'} n'_j u'(j) = 0$ where n'_j of course denotes the vertex degrees in Γ'. This becomes

$$\sum_{i\in\Gamma} n_i(u(i)+\eta) + 2(u(i_0)+\eta) \tag{3.41}$$

  where the last term arises from the increase in n_{i_0} by 1 and the presence of the additional node j_0. This yields $\eta = -\frac{2u(i_0)}{\sum n_i + 2}$. Since we are changing u by a global additive constant and since $u'(i_0) = u'(j_0)$, the numerator in (3.38) is the same for u' on Γ' as it was for u on Γ. We now compute the denominator as

$$\sum_{i\in\Gamma} n_i(u(i)+\eta)^2 + 2(u(i_0)+\eta)^2 > \sum_{i\in\Gamma} n_i u(i)^2$$

since $\sum_{i\in\Gamma} n_i \eta u(i) = 0$ by the constraint condition for u and the additional contributions are squares and therefore positive (unless $u(i_0) = 0$ in which case they vanish).

2. We add an edge between existing nodes. Here, however, the effect on λ_1 depends on the structure of Γ and where the edge is added. If Γ has two connected components, then $\lambda_1 = 0$ as noted above, and if we add an edge that connects those two components, then λ_1 becomes positive, and so, it increases. Also, we may find graphs that are almost disconnected and have small λ_1 and if we add more and more edges the graph eventually approaches a fully connected graph for which all eigenvalues except λ_0 are $=1$. Thus, again, during this process of adding edges, we expect λ_1 to increase. However, in certain situations, adding an edge may decrease λ_1 instead. Namely, if there exist nodes i_1, i_2 that are not linked, but for which the first eigenfunction satisfies $u_1(i_1) = u_1(i_2)$, then linking them decreases λ_1 by the same computation as in 1. The same then of course also holds when $u_1(i_1)$ and $u_1(i_2)$ are not quite equal, but their difference is sufficiently small.

3. We rewire the graph: We choose nodes i_1, i_2, j_1, j_2 with $i_1 \sim i_2$ and $j_1 \sim j_2$, but with no further neighboring relation, that is neither i_1 nor i_2 is a neighbor of j_1 or j_2. We then delete the two edges that is, the one between i_1 and i_2 and the one between j_1 and j_2 and insert new edges between i_1 and j_1 and between i_2 and j_2. Obviously, since this is a reversible process, in general this will not have a systematic effect on λ_1. However, we may try to find such pairs i_1, i_2 and j_1, j_2 to influence certain characteristic properties of the graph like its clustering through systematic such rewirings, and we may then study the influence on λ_1 as well.

We now derive elementary estimates for λ_1 from above and below in terms of the constant $h(\Gamma)$ introduced in (3.1). Our reference here is [8] (that monograph also contains many other spectral estimates for graphs, as well as the original references). We start with the estimate from above and use the variational characterization (3.38). Let the edge set E divide the graph into the two disjoint sets V_1, V_2 of nodes, and let V_1 be the one with the smaller vertex sum $\sum n_i$. We consider a function v that is $=1$ on all the nodes in V_1 and $= -\alpha$ for some positive α on V_2. α is chosen so that the normalization $\sum_\Gamma n_i v(i) = 0$ holds, that is, $\sum_{i\in V_1} n_i - \sum_{i\in V_2} n_i\alpha = 0$. Since V_2 is the subset with the larger $\sum n_i$, we have $\alpha \le 1$. Thus, for our choice of v, the quotient in (3.38) becomes $\le \frac{(1+\alpha)^2|E|}{\sum_{i\in V_1} n_i + \sum_{i\in V_2} n_i\alpha^2} = \frac{(\alpha+1)|E|}{\sum_{V_1} n_i} \le 2\frac{|E|}{\sum_{V_1} n_i}$. Since this holds for all such splittings of our graph Γ, we obtain from (3.1) and (3.38)

$$\lambda_1 \le 2h(\Gamma). \tag{3.42}$$

The estimate from below is slightly more subtle. We consider the first eigenfunction u_1. Like all functions on our graph, we consider it to be defined on the nodes. We then interpolate it linearly on the edges of Γ. Since u_1 is orthogonal to the constants (recall $\sum_i n_i u(i) = 0$), it has to change sign, and the zero set of our extension then divides Γ into two parts Γ' and Γ''. W.l.o.g., Γ' is the part with fewer nodes. The points where (the extension of) $u_1 = 0$ are called boundary points. We now consider any function φ that is linear on the edges, 0 on the boundary, and positive elsewhere on the nodes and edges of Γ'. We also put $h'(\Gamma') := \inf\{\frac{|E|}{\sum_{i\in\Omega} n_i}\}$ where removing the edges in E cuts out a subset Ω that is disjoint from the boundary. We then have

$$\begin{aligned}
\sum_{i\sim j} |\varphi(i) - \varphi(j)| &= \int_\sigma \sharp_e(\varphi = \sigma) d\sigma \\
&= \int_\sigma \frac{\sharp_e(\varphi = \sigma)}{\sum_{i:\varphi(i)\geq\sigma} n_i} \sum_{i:\varphi(i)\geq\sigma} n_i \; d\sigma \\
&\geq \inf_\sigma \frac{\sharp_e(\varphi = \sigma)}{\sum_{i:\varphi(i)\geq\sigma} n_i} \int_s \sum_{i:\varphi(i)\geq s} n_i \; ds \\
&= \inf_\sigma \frac{\sharp_e(\varphi = \sigma)}{\sum_{i:\varphi(i)\geq\sigma} n_i} \sum_i n_i |\varphi(i)| \\
&\geq h'(\Gamma') \sum_i n_i |\varphi(i)|
\end{aligned}$$

when the sets $\varphi = \sigma$ and $\varphi \geq \sigma$ satisfy the conditions in the definition of $h'(\Gamma)$; that is, the infimum has to be taken over those $\sigma < \max\varphi$. Here, $\sharp_e(\varphi = \sigma)$ denotes the number of edges on which φ attains the value σ. Applying this to $\varphi = v^2$ for some function v on Γ' that vanishes on the boundary, we obtain

$$\begin{aligned}
h(\Gamma') \sum_i n_i |v(i)|^2 &\leq \sum_{i\sim j} |v(i)^2 - v(j)^2| \\
&\leq \sum_{i\sim j} (|v(i)| + |v(j)|)|v(i) - v(j)| \\
&\leq 2(\sum_i n_i |v(i)|^2)^{1/2} (\sum_{i\sim j} |v(i) - v(j)|^2)^{1/2}
\end{aligned}$$

from which

$$\frac{1}{4} h(\Gamma')^2 \sum_i n_i |v(i)|^2 \leq \sum_{i\sim j} |v(i) - v(j)|^2. \tag{3.43}$$

We now apply this to $v = u_1$, the first eigenfunction of our graph Γ. We have $h'(\Gamma') \geq h(\Gamma)$, since Γ' is the component with fewer nodes. We also have

$$\lambda_1 \sum_{i\in\Gamma'} n_i u_1(i)^2 = \frac{1}{2}\sum_{i\in\Gamma'}\sum_{j\sim i}(u_1(i)-u_1(j))^2,^5 \tag{3.44}$$

cf. (3.16) (this relation holds on both Γ' and Γ'' because u_1 vanishes on their common boundary)[6]. (3.43) and (3.44) yield the desired estimate

$$\lambda_1 \geq \frac{1}{2}h(\Gamma)^2. \tag{3.45}$$

From (3.42) and (3.45), we also observe the inequality

$$h(\Gamma) \leq 4 \tag{3.46}$$

for any connected graph.

3.4 Other graph parameters

One set of useful parameters that encode important qualitative properties comes from the metric on the graph generated by assigning every edge the length 1, that is, letting neighbors in the graph have distance 1. The diameter of the graph (assumed to be connected, as always) then is the maximal distance between any two of its nodes. Most graphs of N nodes have a diameter of order $\log N$. More precisely, there exists a constant c with the property that the fraction of all graphs with N nodes having diameter exceeding $c\log N$ tends to 0 for $N\to\infty$. Of course, a fully connected graph has diameter 1. However, one can realize a small diameter already with much fewer edges; namely, one selects one central node to which every other node is connected. In that manner, one obtains a graph of N nodes with $N-1$ edges and diameter 2. Of course, the central node then has a very large degree, namely $N-1$. It is a big hub. Similarly, one can construct graphs with a few hubs, so that none of them has to be quite that big, efficiently distributed so that the diameter is still rather small. Such graphs can be realized as so-called scale free graphs to be discussed below. Another useful quantity is the average distance between nodes in the graph. The property of having a small diameter or average distance has been called the small-world effect.

[5] We obtain the factor 1/2 because we are now summing over vertices so that each edge gets counted twice.

[6] To see this, one adds nodes at the points where the edges have been cut, and extends functions by 0 on those nodes. These extended functions then satisfy the analogue of (3.11) on either part, as one sees by looking at the derivation of that relation and using the fact that the functions under consideration vanish at those new "boundary" nodes.

A rather different quantity that was already described in the introduction is the clustering coefficient that measures how many connections there exist between the neighbors of a node. Formally, it is defined as

$$C := \frac{3 \times \text{ number of triangles}}{\text{number of connected triples of nodes}}. \tag{3.47}$$

The normalization is that C becomes one for a fully connected graph. It vanishes for trees and other bipartite graphs.
A triangle is a cycle of length 3. One may then also count the number of cycles of length k, for integers > 3. A different generalization consists in considering complete subgraphs of order k. For example, for $k = 4$, we would have a subset of 4 nodes that are all mutually connected. One may then associate a simplicial complex to our graph by assigning a k-simplex to every such complete subgraph, with obvious incidence relations. This is the basis of topological combinatorics, enabling one to apply tools from simplicial topology to graph theory.

3.5 Generalized random graphs

A generalized random graph is characterized by its number N of nodes or vertices and real numbers $0 \leq p_{ij} \leq 1$ (with the symmetry $p_{ij} = p_{ji}$) that assign to each pair i, j of nodes the probability for finding an edge between them. Self-connections of the node i are excluded when $p_{ii} = 0$. The expected degree of i then is

$$\nu_i = \sum_j p_{ij}. \tag{3.48}$$

This construction generalizes the random graphs introduced by Erdös and Rényi[13]; their important idea was not to specify a graph explicitly, but rather only its generic type by selecting edges between nodes randomly. In their construction, for any pair of nodes, there was a uniform probability p for an edge between them. If the network has N nodes, then, if we do not allow self-links, each node has $N - 1$ possible recipients for an edge, while if self-links are permitted, there are N of them. Thus, the average degree of a node is

$$z := (N - 1)p \text{ or } Np, \tag{3.49}$$

and this difference of course becomes insignificant for large N. Moreover, the probability that a given node has degree k in an Erdös-Rényi graph is

$$p_k = \binom{N-1}{k} p^k (1-p)^{N-1-k} \tag{3.50}$$

because the degree happens to be k when precisely p out of the $N-1$ possible edges from the given node are chosen, and each of them is chosen with probability p and not chosen with probability $1-p$. Thus, the degree distribution is binomial, and for $N \gg kz$, this is approximated by the Poisson distribution

$$p_k = \frac{z^k e^{-z}}{k!}. \tag{3.51}$$

(and so $z = \langle k \rangle = \sum_k k p_k$.)
For an Erdös-Rényi graph, one can also compute the distribution of the number of second neighbors of a given node, that is, the number of neighbors of its neighbors, discarding of course the original node itself as well as all its direct neighbors that also happen to be connected with another neighbor. However, since there is no tendency to clustering in the construction, the probability that a second neighbor is also a first neighbor behaves like $1/N$ and so becomes negligible for large N. Now, however, the degree distribution of first order neighbors of some node is different from the degree distribution of all the nodes in the random graph, because the probability that an edge leads to a particular node is proportional to that node's degree so that a node of degree k has a k-fold increased chance of receiving an edge. Therefore, the probability distribution of our first neighbors is proportional to kp_k, that is, given by $\frac{kp_k}{\sum_l lp_l}$, instead of p_k, the one for all the nodes in the graph. Such a first neighbor of degree k has $k-1$ edges leading away from the original node. Therefore, when we shift the index by 1, the distribution for having k second neighbors via one particular one of its neighbors is then given by

$$q_k = \frac{(k+1)p_{k+1}}{\sum_l lp_l}. \tag{3.52}$$

Thus, to obtain the number of second neighbors, we need to sum over the first neighbors, since, as argued, we can neglect clustering in this model. So, the mean number of second neighbors is obtained by multiplying the expected number of second neighbors via a particular first neighbor, that is, $\sum kq_k$, by the expected number of first neighbors, $z = \sum kp_k$. So, we obtain for that number

$$\sum_l lp_l \sum_k kq_k = \sum_{k=0}^{\infty} k(k+1)p_{k+1} = \sum_{k=0}^{\infty}(k-1)kp_k = \langle k^2 \rangle - \langle k \rangle. \tag{3.53}$$

Following the exposition in [24], such probability distributions can be encoded in probability generating functions. If we have a probability distribution p_k as above on the non-negative integers, we have the generating function

$$G_p(x) := \sum_{k=0}^{\infty} p_k x^k. \tag{3.54}$$

Likewise, the above distribution for the number of second neighbors then is encoded by

$$G_q(x) = \sum_{k=0}^{\infty} q_k x^k = \frac{\sum_k (k+1)p_{k+1}}{\sum_l lp_l} = \frac{G_p'(x)}{z}. \tag{3.55}$$

When we insert the Poisson distribution (3.51), we obtain

$$G_p(x) = e^{-z} \sum_{k=0}^{\infty} \frac{z^k}{k!} x^k = e^{z(x-1)} \tag{3.56}$$

and from (3.55) then also

$$G_q(x) = e^{z(x-1)} \tag{3.57}$$

Thus, for an Erdös-Rényi graph, the two generating functions agree. This is quite useful for deriving analytical results.

In order to also include scale-free graphs, [5] introduced the following generalization of this procedure. One starts with an N-tuple $\nu = (\nu_1, ..., \nu_N)$ of positive numbers satisfying

$$\max_i \nu_i^2 \leq \sum_j \nu_j; \tag{3.58}$$

when the ν_i are positive integers, this is the necessary and sufficient for the existence of a graph with nodes i of degree ν_i, $i = 1, ..., N$. When putting $\gamma := \frac{1}{\sum_i \nu_i}$ and $p_{ij} := \gamma \nu_i \nu_j$, then $0 \leq p_{ij} \leq 1$ for all i, j. We then insert an edge between the nodes i and j with probability p_{ij} to construct the (generalized) random graph Γ. By (3.48), the expected degree of node i in such a graph is ν_i. When all the ν_i are equal, we obtain an Erdös-Rényi graph. For other types, the number of nodes i with $\nu_i = k$ will decay as a function of k, at least for large k, for example exponentially. When that number behaves like a power $k^{-\beta}$ instead, we obtain a so-called scale free graph.
Scale-free graphs were apparently first considered by H.Simon[29]; they have been popularized more recently by Barabasi-Albert[4]. Their construction can be simply described: Prescribe some positive integer $m \geq 2$ and start with some (small) connected graph. Add each iteration step, add a new node that can make connections to m nodes already existing in the network. The probability for each of those nodes to be a recipient of a connection from the new node is proportional to the number of connections it already has. By this scheme, those nodes that already possess many connections are favored to become recipients of further connections, and in this manner, many hubs are generated in the network, and in the final network, the number of nodes with degree k decays like a power of k, instead of exponentially as is the case for random graphs. It should be pointed out that the construction just described is not the only one that can generate graphs with such a power law behavior. For example, Kleinberg et al.[19] introduced a copying model that in contrast to the preceding, but like the subsequently mentioned models needs only local information for deciding the connections of new nodes. In [30] and [26],

a local exploration model is introduced. Jost-Joy[18] constructed graphs by the make-friends-with-the-friends-of-your-friends principle. According to that principle, new nodes added to the network that are again allowed to make a specified number m of connections make their first connection at random and then preferentially make connections with neighbors of those nodes they are already connected with. Since the probability of a node i of being a neighbor of another node the new node is already connected is proportional to the degree of i, this principle again favors highly connected nodes and leads to a power law degree sequence. With respect to important graph parameters, however, the graphs so constructed are rather different from the ones produced by the Barabasi-Albert scheme. For example, their diameter tends to be much larger, and their first eigenvalue significantly smaller than the corresponding quantities for the latter. For a more systematic analysis of the spectral properties, see [1]. See also the discussion below. More generally, [18] discuss attachment rules where the preference for a node to become a recipient of a new connection depends on the distance to the node forming those connections.
One can also consider networks where not only new nodes are added, but where also rewiring takes place. For example, Klemm and Eguíluz [20, 21] consider a growing network model based on the scale free paradigm, with the distinctive feature that older nodes become inactive at the same rate that new ones are introduced. This is interpreted as a finite memory effect, in the sense that older contributions tend to be forgotten when they are not frequently enough employed. This results in networks that are even more highly clustered than regular ones. Davidsen et al. [11] consider a network that rewires itself through triangle formation. Nodes together with all their links are randomly removed and replaced by new ones with one random link. The resulting network again is highly clustered, has small average distance, and can be tuned towards a scale free behavior.

In the construction of [10], the probability to find a connection between i and j depends only on a property intrinsic to i and j, namely their expected degrees. In the more general construction we should like to propose here, that probability rather encodes a relationship between i and j that may well be special to them. This seems to capture the essential aspect underlying most constructions of graphs in specific applications where they are supposed to represent a particular structure of relations between individual elements. Each element can form relations with selective other elements, and whether another element is chosen need not only depend on a property intrinsic to the latter, but also on some affinity, similarity or dissimilarity to the former. In this regard, see also the Cameo principle of Blanchard-Krüger[6].
The appropriate approach to analyzing properties of random graphs of course is not to consider an individual such graph, but rather to derive properties that hold for all or almost all such graphs for a given collection p_{ij} or class of such collections with specified properties, at least perhaps asymptotically for $N \to \infty$. This applies in particular to the eigenvalues of the graph Laplacian.

Such properties, in general, will not only depend on the N-tuple ν above. Two graphs with the same ν can have rather different geometric properties, as for example encoded by the clustering coefficient or the average distance between nodes, and also their spectrum can be rather different. For instance, we can apply the rewiring rule 3 from Section 3.3 to change some of those quantities in a systematic manner without affecting the degrees of nodes. In particular, since we can affect the constant $h(\Gamma)$ in that manner, for instance making it arbitrarily small, we cannot expect non-trivial estimates for the first eigenvalue λ_1 that hold uniformly for all graphs with given ν. This is systematically investigated in [1].

3.6 Interactions

Above, we have considered the graph Laplacian Δ. It can be considered as the prototype of an interaction operator. We consider a function f representing the dynamics of the individual elements. This means that an element i in isolation obeys the dynamical rule

$$u(i, n+1) = f(u(i, n)); \tag{3.59}$$

here, $n \in \mathbb{N}$ stands for the discrete time. $u(i, n)$ is the state of element i at time n. Prototypes of such reaction functions f are

$$f_1(x) = \rho x(1-x) \tag{3.60}$$

with $0 < \rho \leq 4$ which, for sufficiently large ρ generates chaotic dynamics, see e.g. [16] for details (in our investigations, we have mostly considered the value $\rho = 4$), and

$$f_2(x) = \frac{1}{1+e^{-\kappa(x-\theta)}}, \text{ with } \kappa > 0, \tag{3.61}$$

the so-called sigmoid function in neural networks, which in contrast to f_1 is monotonically increasing and leads to a regular, non-chaotic behavior , and which has 1 or 3 fixed points (depending on κ, θ).
When considering networks of interacting elements, we need to add an interaction term to (3.59):

$$u(i, n+1) = f(u(i, n)) + \epsilon\mu_i(\sum_j c_{ji} g(u(j, n)) - \sum_k c_{ik} g(u(i, n))) \tag{3.62}$$

for a network with nodes i, with multipliers μ_i, coupling strengths c_{jk} from j to k and global interaction strength ϵ, for some function g. For simplicity of presentation, we restrict ourselves here to the case $g = f$, even though the general case can be treated by the same type of analysis. Thus, we shall consider

$$u(i,n+1) = f(u(i,n)) + \epsilon\mu_i(\sum_j c_{ji} f(u(j,n)) - \sum_k c_{ik} f(u(i,n))). \quad (3.63)$$

A question that we shall discuss is under which conditions the solution u synchronizes, that is when $\lim_{n\to\infty} |u(i,n) - u(j,n)| = 0$ for all vertices i, j (in computer simulations, when synchronization occurs, it can be seen already at finite values of n, that is, $u(i,n) = u(j,n)$ for all n larger than some $N \in \mathbb{N}$). The fundamental reference on this topic that we shall also use in the sequel is [27].
When we put $\mu_i = \frac{1}{n_i}$ and $c_{jk} = 1$ when j and k are neighbors and 0 otherwise, the interaction operator becomes our graph Laplacian Δ studied above. In fact, that operator serves as a prototype for the interaction, and we now derive conditions that allows us to generalize the key features of Δ to some larger class of interaction operators. There are three types of conditions that we shall now discuss in turn:

1. A balancing condition

$$\sum_j c_{ji} = \sum_k c_{ik} \quad \text{for all } i. \quad (3.64)$$

This condition states that what comes in at a node is balanced by what is flowing out of that node.
For simplicity, we also assume

$$c_{ii} = 0 \quad \text{for all } i. \quad (3.65)$$

This condition is not essential for the formal analysis, but notationally convenient in the sequel. It excludes a self-interaction term from the interaction operator, and this is easily justified by declaring that any self-interaction is already contained in the reaction term, the first term on the right hand side of (3.62).
The balancing condition can be rewritten as a zero-row-sum condition when we define an operator $L = (l_{xy})$ by putting

$$l_{ik} := \mu_i c_{ki} \quad \text{for } i \neq k \quad (3.66)$$

(note the reversal of the indices), and

$$l_{ii} := -\mu_i \sum_j c_{ji} = -\mu_i \sum_k c_{ik}. \quad (3.67)$$

The balancing condition (3.64) then is equivalent to

$$\sum_j l_{ij} = 0 \quad \text{for all } i. \quad (3.68)$$

In terms of the operator L, our dynamics (3.63) becomes

$$u(i,n+1) = f(u(i,n)) + \epsilon \sum_j l_{ij} f(u(j,n)). \tag{3.69}$$

or, more abstractly,

$$u(.,n+1) = f(u(.,n)) + \epsilon L f(u(.,n)). \tag{3.70}$$

The important point of the balancing condition (3.64) or the equivalent zero-row-sum condition (3.68) is that the synchronized solutions, that is,

$$u(i,n) = u(j,n) \quad \text{for all } i,j,n, \tag{3.71}$$

satisfying the individual equation (3.59) are also solutions of the collective equation (3.63) (or, equivalently, (3.69), (3.70)).

2. Another useful condition is a non-negativity condition: Let the coupling matrix $C = (c_{xy})$ have **non-negative entries**, that is,

$$c_{ij} \geq 0 \quad \text{for all } i,j. \tag{3.72}$$

We shall **not** assume this condition in most of the sequel, but we discuss it here because it allows us to derive some kind of asymptotic stability condition for the globally synchronized solution. We consider the adjoint operator L^* with coefficients

$$l^*_{ik} = \frac{\mu_i}{\mu_k} l_{ki} \ (= \mu_i c_{ik} \quad \text{for } i \neq k), \tag{3.73}$$

assuming, of course, that the multipliers $\mu_i \neq 0$. We then have, from (3.68),

$$\sum_k l^*_{ik} = 0. \tag{3.74}$$

The crucial quantity that will be seen as a Lyapunov function then is

$$\begin{aligned} &-\sum_i \frac{1}{\mu_i} L^* u(i,n+1) u(i,n+1) \qquad (3.75)\\ &= -\sum_i \frac{1}{\mu_i} L^*((1+\epsilon L) f(u(i,n)))(1+\epsilon L) f(u(i,n)). \end{aligned}$$

We have

$$\begin{aligned} &-\sum_i (\sum_k \frac{1}{\mu_i} l^*_{ik}((1+\epsilon L) f(u(k,n))))(1+\epsilon L) f(u(i,n)) \\ &= \frac{1}{2} \sum_{i \neq k} \frac{1}{\mu_i} l^*_{ik} (1+\epsilon L)(f(u(i,n)) - f(u(k,n)))(1+\epsilon L)(f(u(i,n)) - f(u(k,n))) \\ &\leq -\sup |f'|^2 \|1+\epsilon L\|^2 \sum_i \frac{1}{\mu_i} L^* u(i,n) u(i,n) \qquad (3.76) \end{aligned}$$

by (3.74) and since the non-diagonal entries of L are non-negative. Here, the norm of the operator $1 + \epsilon L$ is evaluated on those functions that are orthogonal to the constants as the difference in the preceding formula vanishes on the constants. Therefore, when this norm is smaller than $|f'|^{-1}$, that is, when we have the global stability condition,

$$\sup |f'|^2 \|1 + \epsilon L\|^2 < 1, \tag{3.77}$$

$$-\sum_i \frac{1}{\mu_i} L^* u(i,n) u(i,n) \tag{3.78}$$

is exponentially decreasing as a function of n under our dynamical iteration (3.63). Thus, for $n \to \infty$, it goes to 0. Thus, the limit $u(i) := \lim_{n\to\infty} u(i,n)$ (or, more precisely, the limit of any subsequence) satisfies

$$\sum_i (\sum_j c_{ji} u(j) - \sum_j c_{ik} u(i)) u(i) = 0 \tag{3.79}$$

which, by (3.72), (3.64), and the Schwarz inequality, implies that $u(i)$ is constant, that is, independent of i. This means that under dynamical iteration (3.63) synchronizes as $n \to \infty$.
In the symmetric case to be discussed below, such an estimate had been derived in [17]. In the general case, similar conditions have been obtained by Wu[32] and Chen-Lu[23]. For recnt work in this direction, see [22].

3. A symmetry condition on the the operator L will guarantee that its spectrum is real, and then, when also the non-negativity condition (3.72) will be assumed, that it is non-negative. In order to obtain such a condition, we need a scalar product on the space of functions on Γ, to make it into an L^2-space. Such a product is given by

$$(u, v) := \sum_{i,j} a_{ij} u(i) v(j). \tag{3.80}$$

Here, $A := (a_{ij})$ should be positive definite and symmetric:

$$a_{ij} = a_{ji} \quad \text{for all } i, j. \tag{3.81}$$

L is symmetric with respect to this product if

$$(Lu, v) = (u, Lv) \quad \text{for all } u, v, \tag{3.82}$$

that is, if

$$\sum_{i,j,k} a_{ij} l_{ik} u(k) v(j) = \sum_{i,j,k} a_{ij} u(i) l_{jk} v(k). \tag{3.83}$$

This requires

$$a_{ij} l_{ik} = a_{ik} l_{ij}, \tag{3.84}$$

using the symmetry (3.81). (3.84) is the condition yielding the symmetry of L, that is, we can infer that L has a real spectrum when we can find a symmetric matrix $A := (a_{ij})$ satisfying (3.84).
If we want to have a scalar product that is more intimately tied to the graph structure, we should require that it admits an orthonormal basis of functions of the form u_i with $u_i(j) = 0$ for $j \neq i$. In that case, the scalar product has to be of the form already given in (3.2)

$$(u, v) = \sum_i n_i u(i) v(i) \tag{3.85}$$

where, however, the n_i can be arbitrary positive numbers, not necessarily the vertex degrees. In that situation, the symmetry condition for L becomes

$$n_i l_{ik} = n_k l_{ki} \quad \text{for all } i, k. \tag{3.86}$$

When we have

$$n_i = \frac{1}{\mu_i} \tag{3.87}$$

for the above multipliers μ_i, this simply becomes the symmetry of the interaction matrix,

$$c_{ik} = c_{ki} \quad \text{for all } i, k, \tag{3.88}$$

see (3.66). In that case, that is, when L is self-adjoint with respect to the product (3.85) with (3.87), coincides with the operator L^* defined in (3.73), as the latter is the adjoint of L with respect to this product.

3.7 Local stability of the synchronized solution

In the preceding, we have derived a global stability condition, (3.77). We now discuss the local stability of a synchronized solution with the help of the eigenvalue expansion obtained in Section 3.3, following the presentation in [17]. A similar analysis has been carried out and related to the Gershgorin disk theorem in [28, 7]. We shall only consider the case of the graph Laplacian as our interaction operator, although the subsequent analysis readily extends to other symmetric operators that are negative definite on the subspace orthogonal to the constant functions.
We consider a solution $\bar{u}(n)$ of the uncoupled equation (3.59),

$$\bar{u}(n+1) = f(\bar{u}(n)). \tag{3.89}$$

$u(i, n) = \bar{u}(n)$ then is a synchronized solution of the coupled equation

$$u(i, n+1) = f(u(i, n) + \frac{\epsilon}{n_i} \sum_{j, j\sim i} (f(u(j, n)) - f(u(i, n))). \tag{3.90}$$

The local stability question then is whether a perturbation

$$u(i,n) = \bar{u}(n) + \delta\alpha_k(n)u_k(i) \tag{3.91}$$

by an eigenmode u_k for some $k \geq 1$, and small enough δ, $\alpha_k(n)$ goes to 0 for $n \to \infty$, if $u(i,n)$ solves (3.90). We now perform a linear stability analysis. We insert (3.3) into (3.2) and expand about $\delta = 0$. This yields

$$\alpha_k(n+1) = (1 - \epsilon\lambda_k)f'(\bar{u}(n))\alpha_k(n). \tag{3.92}$$

The sufficient local stability condition[7]

$$\lim_{N\to\infty} \frac{1}{N} \log \frac{\alpha_k(N)}{\alpha_k(0)} = \lim_{N\to\infty} \frac{1}{N} \log \prod_{n=0}^{N-1} \frac{\alpha_k(n+1)}{\alpha_k(n)} < 0 \tag{3.93}$$

therefore becomes

$$\log|1 - \epsilon\lambda_k| + \lim_{N\to\infty} \frac{1}{N} \sum_{n=0}^{N-1} \log|f'(\bar{u}(n))| < 0. \tag{3.94}$$

Here,

$$\mu_0 = \lim_{N\to\infty} \frac{1}{N} \sum_{n=0}^{N-1} \log|f'(\bar{u}(n))|$$

is the Lyapunov exponent of f. Therefore, the stability condition (3.94) is

$$|e^{\mu_0}(1 - \epsilon\lambda_K)| < 1. \tag{3.95}$$

The fundamental observation is that we may find synchronization, that is, may have (3.95) for all $k \geq 1$, even in the presence of temporal instability, that is,

$$\mu_0 > 0. \tag{3.96}$$

In that case, the individual, and therefore also the synchronized global dynamics, may exhibit chaotic behavior. Synchronization then means that the chaotic dynamics of the individual nodes are identical. We shall now investigate this issue further. By our ordering convention for the eigenvalues, (3.95) holds for all $k \geq 1$ if

$$\frac{1 - e^{-\mu_0}}{\lambda_1} < \epsilon < \frac{1 + e^{-\mu_0}}{\lambda_K}. \tag{3.97}$$

For that condition, we need

$$\frac{\lambda_K}{\lambda_1} < \frac{e^{\mu_0} + 1}{e^{\mu_0} - 1}. \tag{3.98}$$

[7] Stability is understood here in the sense of Milnor. See [27] for a detailed analysis.

When (3.98) holds, from the local stability analysis, we expect the following behavior of the coupled system as ϵ increases. For very small values of ϵ, the solution is not synchronized because the positive Lyapunov exponent of the individual dynamics is not compensated by a sufficiently strong diffusive interaction. As ϵ increases, first the highest modes become stabilized until at some critical value of ϵ, all spatially inhomogeneous modes become stable directions, and global synchronization sets in. When ϵ is further increased, first the highest mode becomes unstable, and then others follow, and the solution gets desynchronized again. The important point here is that a unidirectional variation of the coupling strength parameter leads from a desynchronized to a synchronized state and then back to a – different – desynchronized state. We now describe this process in some more detail, following again [17]. For very small values of $\epsilon > 0$, as we assume (3.97)

$$e^{\mu_0}(1 - \epsilon\lambda_k) > 1,$$

and so, all spatial modes $u_k, k \geq 1$, are unstable, and no synchronization occurs. Unless we have a global all-to-all coupling (see Section 3.3) λ_1 is smaller than λ_K. Let ϵ_k be the solution of

$$e^{\mu_0}(1 - \epsilon_k\lambda_k) = 1.$$

The smallest among these values is ϵ_K, the largest ϵ_1. If then, for $k_1 < k_2$,

$$\epsilon_{k_2} < \epsilon < \epsilon_{k_1}$$

the modes $u_{k_2}, u_{k_2+1}, ..., u_K$ are stable, but the modes $u_1, u_2, ..., u_{k_1}$ are unstable. Recalling Lemma 1, we see that desynchronization can lead to at most $k_2 + 1$ subdomains on which the dynamics is either advanced or retarded.

In particular, if ϵ increases, first the highest modes, i.e., the ones with most spatial oscillations, become stabilized, and the mode u_1 becomes stabilized the last. So if $\epsilon_2 < \epsilon < \epsilon_1$, then any desynchronized state consists of two subdomains.

We then let $\bar{\epsilon_k}$ be the solution of

$$e^{\mu_0}(\bar{\epsilon_k}\lambda_k - 1) = 1$$

Again,

$$\bar{\epsilon_k} \leq \bar{\epsilon}_{k-1}.$$

Because of (3.97),

$$\epsilon_1 < \bar{\epsilon}_K.$$

If

$$\epsilon_1 < \epsilon < \bar{\epsilon}_K,$$

then all modes $u_k, k = 1, 2, ..., K$, are stable, and the dynamics synchronizes.

If ϵ increases beyond $\bar{\epsilon}_K$, then the highest frequency mode u_K becomes unstable and we predict spatial oscillations of high frequency of a solution of the dynamics. If ϵ increases further then more and more spatial modes become destabilized.

References

1. F.Atay, T.Biyikoglu, J.Jost, On the synchronization of networks with prescribed degree distributions,
2. F.Atay, J.Jost, On the emergence of complex systems on the basis of the coordination of complex behaviors of their elements: Synchronization and complexity, Complexity 10, 17-22, 2004
3. F.Atay, J.Jost, A.Wende, Delays, connection topology, and synchronization of coupled chaotic maps, Phys.Rev.Lett.92, 144101-144104, 2004
4. A.-L.Barabasi, R.Albert, Emergence of scaling in random networks, Science 286, 509-512, 1999
5. E.Bender, E.Canfield, The asymptotic number of labeled graphs with given degree sequences, J.Comb.Th.A 24, 296-307, 1978
6. P.Blanchard, T.Krüger, The "Cameo" principle and the origin of scale-free graphs in social networks, J.Stat.Phys.114, 1399-1416, 2004
7. Y.H.Chen, G.Rangarajan, M.Z.Ding, General stability analysis of synchronized dynamics in coupled systems, Phys.Rev.E 67, 26209-26212, 2003
8. F.Chung, Spectral graph theory, AMS, 1997
9. F.Chung, Discrete isoperimetric inequalities
10. F.Chung, L.Lu, V.Vu, The spectra of random graphs with expected degrees
11. J. Davidsen, H. Ebel, and S. Bornholdt, Emergence of a small world from local interaction: Modeling acquaintance networks, Phys. Rev. Lett. **88**, 128701 (2002)
12. I.Derényi, G.Palla, T.Vicsek, Clique percolation in random networks, Phys.Rev.Lett.94, 160202, 2005
13. P.Erdös, A.Rényi, On random graphs.I, Publ.Math.Debrecen 6, 290-291, 1959
14. M.Girvan, M.Newman, Community structure in social and biological networks, Proc.Nat.Acad.Sc.99, 7021-7026, 2002
15. G. Gladwell, E. B. Davies, J. Leydold, and P. F. Stadler, Discrete nodal domain theorems, Lin.Alg.Appl.336, 2001, 51-60
16. J.Jost, Dynamical systems, Springer, 2005
17. J.Jost, Joy, Spectral properties and synchronization in coupled map lattices, Phys.Rev.E 65, 16201-16209, 2001
18. J.Jost, Joy, Evolving networks with distance preferences, Phys.Rev.E 66, 36126-36132, 2002
19. J.Kleinberg, The web as a graph: Measurements, methods, and models, Lecture Notes in Computer Science, Chapter 1, Springer, 1999
20. K. Klemm, V. M. Eguíluz, Growing scale-free networks with small-world behavior, Phys. Rev. E **65**, 057102 (2002)
21. K. Klemm, V. M. Eguíluz, Highly clustered scale-free networks, Phys. Rev. E **65**, 036123 (2002)

22. W.L.Lu, Chaos synchronization in coupled map networks via time varying topology, Preprint, MPIMIS, 2005
23. W.L.Lu, T.P.Chen, Synchronization analysis of linearly coupled map networks with discrete time systems, Physica D, 198, 148-168, 2004
24. M.Newman, Random graphs as models of networks, in: S.Bornholdt, H.G.Schuster (eds.), Handbook of graphs and networks, Wiley-VCH, Berlin, 2002
25. M.Newman, The structure and function of complex networks, cond-mat/0303516, 2003
26. R.Pastor-Satorras, A.Vazquez, A.Vespignani, Dynamical and correlation properties of the internet, Phys.Rev.Lett.87, 258701-4, 2001
27. A.Pikovsky, M.Rosenblum, J.Kurths, Synchronization, Cambridge Univ.Press, 2001
28. G.Rangarajan, M.Z.Ding, Stability of synchronized chaos in coupled dynamical systems, Phys.Lett.A 296, 204-212, 2002
29. H.Simon, On a class of skew distribution functions, Biometrika 42, 425-440, 1955
30. A.Vázquez, Growing networks with local rules: Preferential attachment, clustering hierarchy and degree correlations, cond-mat/0211528, 2002
31. D.Watts, S.Strogatz, Collective dynamics of 'small-world' networks, Nature 393, 440-442, 1998
32. C.W.Wu, Synchronization in networks of nonlinear dynamical systems coupled via a directed graph

Part II

Applications in Neuroscience

4

Neuronal Computation Using High Order Statistics

Jianfeng Feng

Summary. Neuron is a stochastic unit: it receives and sends out random spikes. Usually the second order statistics is thought of as noise: useless and harmful. Here we first review some results in the literature and point out that in fact the second order statistics plays an important role in computation. Both positive and negative correlations are observed in *in vivo* recorded data. Positive correlation (∼synchronization) has been extensively discussed in the literature, we mainly focus on some functional roles of negative correlations. Based upon these results, a novel way of neuronal computation: moment neuronal networks, is proposed and some applications are included.

4.1 Introduction

During the past 20 years, we have witnessed the development of the *artificial neural networks (ANN)* and its impact on Neuroscience. In comparison with the development of ANN in 50's where a neuron takes two states only, we have used a continuous input-output relationship (sigmoidal function) to describe the activity of a neuron. Obviously with a simple sigmoidal function to characterize the complex input-output activity of a neuron is oversimplified and such an approach never really brings us to anywhere near to a biological reality.

It is clear from the past few years of research that a neuron activity will be decided not only by its mean input activity (mean firing rate), but also by its higher order statistics of inputs. For example, in the scenario of balanced inhibitory and excitatory inputs, the mean input to a neuron is zero and in the ANN approach the neuron will be simply silent (higher order statistics are not taken into account). Can we develop a theory which will naturally include the mean (first order statistics), the second order statistics and so on to compute? In other words, can we develop a theory of moments neuronal network

(MNN)? The advantage of such an approach over the ANN is obvious. For example, we all know that synchronized neuronal activity might play an important role in information processing in the nervous systems. In the MNN, we can naturally include the synchronized firing case since it corresponds to the fully correlated activity, i.e. with a correlation coefficient being unity. There are other advantages of the MNN over the ANN. First, since our theory is developed based upon spiking neurons, we can related all of our parameters to biologically measurable quantities. We can always test our theory in biological experiments. Second, from purely theoretical point of view, we know that in a stochastic system, any computation based upon mean is somewhat similar to the law of large numbers in probability theory. To have a complete description of a stochastic system, we need the central limit theorem (second order statistics calculations). MNN is equivalent to the development of the central limit theory in probability. Third, although our theory is developed in terms of spiking neuronal networks, the learning theory developed in ANN will be mostly applicable and hence MNN will serve as a bridge between ANN theory and neurobiology.

In the current paper, we aim to develop a theory of moment computation. Before doing it, we first present a few examples to emphasize the importance of the second order statistics. The examples include the input and output surfaces of a single neuron (the integrate-and-fire model and the Hodgkin-Huxley model), optimal control models, discrimination with correlated inputs, noise reductions and storage capacity with negative correlations.

Our general setup is as following. In section 2, the input-output surfaces of a single neuron are discussed. In section 3, we discuss an optimal control model based upon the second order statistics. In section 4, we address the issue of discrimination among mixed input signals. In section 5, the importance of negative correlations is presented. In section 6, we then develop the moment neural networks. The exact relationship of input and output of an integrate-and-fire neuron is known. The renewal theorem is applied to the integrate-and-fire model which enables us to have complete equations to describe the input and output relationship of spiking neuronal networks. The similar idea to investigate the input-output relationship of spiking neuronal networks has been widely investigated in the literature [2], however, to the best of our knowledge, our approach is novel. In fact, as pointed out in [71] at page 435, final paragraph, all approaches before are based upon two key assumptions: the output of the integrate-and-fire model is again a Poisson process, which is only approximately true in a very limit parameter regions; the input is independent. Our general theory requires neither of the assumptions.

In the current paper we confine ourselves to neuronal computation with the first and the second order statistics. The reason is that to completely describe a random system the first and the second order statistics are enough

in most cases. We can of course generalize our approach to general cases: including the third, the fourth etc. order statistics. Furthermore we only consider feedforward networks and it is easy to generalize our results to recurrent networks.

4.2 Single Neuron Activity: Variance

Let us consider a neuron activity. Traditionally, an $F - I$ curve is used to *fully* characterize its behaviour, where F means its out frequency and I is the input current. The $F - I$ curve usually takes the form of a sigmoidal function, which serves as the basis of classical neural computation theory.

The simplest model of a spiking neuronal network, leaky integrate-and-fire model[71], is defined by

$$dV_t = -\frac{V_t}{\gamma} + I$$

where V_t is the membrane potential (in mV), γ is the decay time (in msec) and I is the external input. The firing time is then given by

$$T = \gamma \log\left(1 - \frac{V_{thre}}{I\gamma}\right)$$

where V_{thre} is the threshold. The output frequency F (Hz) is

$$F = \frac{1000}{T + T_{ref}}$$

it shows a typical sigmoidal shape, where T_{ref} is the refractory time.

If we agree that a neuron is a stochastic unit, then the output of a single neuron could be totally different from the above scenario. Now the membrane potential of a neuron takes the following form

$$dV_t = -\frac{V_t}{\gamma} + dS_t$$

where S_t could be pulsed synaptic inputs, or its approximation taking the form $\mu dt + \sigma dB_t$ with μ, σ being constants and B_t the noise. In Fig. 4.1, we plot the output firing rate and CV (standard deviation/mean) of interspike intervals for the integrate-and-fire neuron (upper panel) and the Hodgkin-Huxley neuron (bottom panel). It is clearly seen, not surprisingly, that the output firing rate depends on not only the input firing rate μ, but also the input variance σ. In fact, with different neuron models, the surfaces are quite different and we refer the reader to [23] for more details.

To further illustrate the importance of the second statistics, we turn out attention to a high-level model: a model on movement control.

4.3 Control Tasks

The experimental study of movements in humans and other mammals has shown that voluntary reaching movements obey two fundamental psychophysical principles from the point of view of trajectory formation, and of the dependence of movement time upon relative accuracy, as reviewed in [72].

1. **Trajectory formation**: it is found that the trajectory of arm (hand) movement from a starting point to an end point is almost a straight line and the velocity profile is bell-shaped.

2. **Fitts Law [70]**: the longer the time to take for a reaching movement, the more accurate the hand to arrive at the end point.

These principles are of paramount importance and of great interests both in theory and in applications. In theory, how our brain controls our daily movements remains illusive, despite a century long of intensive research in Neuroscience. In comparison with an open loop approach where we try to directly understand how a brain works, a close loop approach to connect sensory inputs with motor outputs (for example, voluntary movements) might be the only way to make genuine progresses in the area. In engineering applications, if we can unravel the mechanisms underlying these principles, we could apply them to the control of (humanoid) robots. Due to these reasons, there are considerable interests devoting to investigating these principles (see [71] for a most recent review, [73, 75]). However, as far as we are aware, no rigorous results are available in the literature and many issues remain illusive.

In the current section, we present an analytical and rigorous approach to tackle the problem. Within the framework of optimal stochastic control principles and in three dimensional space [74], it is shown that the straight line trajectory is a natural consequence of optimal stochastic control principles, under the condition that we have a non-degenerate optimal control signal. Numerically we conclude that the bell-shaped velocity profile follows as well. Furthermore, we also numerically demonstrate that the optimal variance is proportional to the time interval in which the movements are performed, i.e. Fitts law is verified.

4.3.1 The Model

We consider a simple model of (arm) movements. Let $X(t) = (x(t), y(t), z(t))'$ be the position of the hand at time t, we then have

$$\ddot{X} = -\frac{1}{\tau_1\tau_2}X - \frac{\tau_1+\tau_2}{\tau_1\tau_2}\dot{X} + \frac{1}{\tau_1\tau_2}\left[\Lambda(t)dt + \Lambda(\alpha,t)d\mathbf{B}(t)\right] \tag{4.1}$$

where $\tau_1, \tau_2, \alpha > 0$ are parameters, $\Lambda(t) = (\lambda_x(t), \lambda_y(t), \lambda_z(t))'$ is the control signal, $\Lambda(\alpha, t)$ is a 3×3 diagonal matrix with diagonal elements as $\lambda_x^\alpha(t), \lambda_y^\alpha(t), \lambda_z^\alpha(t)$ respectively, $\mathbf{B}_t = (B_x(t), B_y(t), B_z(t))'$ is the standard Brownian motion. In Physics, we know that Eq. (4.1) is the well-known Kramers' equation. In Neuroscience, it is observed in all *in vivo* experiments that the noise strength is proportional to the signal strength $\Lambda(t)$ and hence the signals received by muscle take the form of Eq. (4.1) (see for example, [57, 71, 67]).

For a point $D = (d_x, d_y, d_z)' \in I\!R^3$ and two positive numbers T, R, we intend to find a control signal $\Lambda^*(t)$ which satisfies

$$\langle X(t) \rangle = D, \text{ for } t \in [T, T+R] \tag{4.2}$$

and

$$\begin{aligned} I(\Lambda^*) &= \min_{\Lambda \in \mathcal{L}^{2\alpha}[0,T+R]} I(\Lambda) = \min_{\Lambda \in \mathcal{L}^{2\alpha}[0,T+R]} \int_T^{T+R} \text{var}(X(t)) dt \\ &= \min_{\Lambda \in \mathcal{L}^{2\alpha}[0,T+R]} \int_T^{T+R} [\text{var}(x(t)) + \text{var}(y(t)) + \text{var}(z(t))] dt \end{aligned} \tag{4.3}$$

where $\Lambda \in \mathcal{L}^{2\alpha}[0, T+R]$ means that each component of it is in $\mathcal{L}^{2\alpha}[0, T+R]$. To stablize the hand, we further require that the hand will stay at D for a while, i.e., in time interval $[T, T+R]$, which also naturally requires that the velocity should be zero at the end of movement. The physical meaning of the problem we considered here is clear: *at time T the hand will reach the position D (Eq. (4.2)), and as precisely as possible (Eq. (4.3)).* Without loss of generality we assume that $d_x > 0, d_y > 0$ and $d_z > 0$.

4.3.2 Optimal control

The optimal control problem posed in the previous section, is a highly nonlinear problem, as we are going to show below.

Solving Eq. (4.1) we obtain that

$$\begin{aligned} (x(t), \dot{x}(t))' = &\left(\int_0^t \frac{b_{12}(t-s)}{\tau_1 \tau_2} \lambda_x(s) ds, \int_0^t \frac{b_{22}(t-s)}{\tau_1 \tau_2} \lambda_x(s) ds \right)' \\ &+ \left(\int_0^t \frac{b_{12}(t-s)}{\tau_1 \tau_2} \lambda_x^\alpha(s) dB_x(s), \int_0^t \frac{b_{22}(t-s)}{\tau_1 \tau_2} \lambda_x^\alpha(s) dB_x(s) \right)' \end{aligned} \tag{4.4}$$

where

$$b_{12}(t) = \frac{\tau_1\tau_2}{\tau_2-\tau_1}\left[\exp\left(-\frac{t}{\tau_2}\right) - \exp\left(-\frac{t}{\tau_1}\right)\right]$$
$$b_{22}(t) = \frac{\tau_1\tau_2}{\tau_2-\tau_1}\left[\frac{1}{\tau_1}\exp\left(-\frac{t}{\tau_1}\right) - \frac{1}{\tau_2}\exp\left(-\frac{t}{\tau_2}\right)\right].$$

The similar equation holds true for $y(t)$ and $z(t)$.

Note that

$$\begin{aligned}\int_T^{T+R} \mathrm{var}(x(t))dt &= \langle \int_T^{T+R}\left[\int_0^t b_{12}(t-s)\lambda_x(s)^\alpha dB_x(s)\right]^2 dt\rangle \\ &= \int_T^{T+R}\left[\int_0^t b_{12}^2(t-s)|\lambda_x(s)|^{2\alpha}ds\right]dt \end{aligned} \tag{4.5}$$

The original control problem defined by Eq. (4.2) and (4.3) is reduced to the following optimization problem.

Find $\Lambda^*(s) \in \mathcal{L}^{2\alpha}[0, T+R]$ which minimizes

$$\int_T^{T+R}\left[\int_0^t b_{12}^2(t-s)[|\lambda_x(s)|^{2\alpha} + |\lambda_y(s)|^{2\alpha} + |\lambda_z(s)|^{2\alpha}]ds\right]dt \tag{4.6}$$

subject to the constraint

$$\int_0^t b_{12}(t-s)\Lambda(s)ds = \tau_1\tau_2 D, \text{ for } t \in [T, T+R]. \tag{4.7}$$

Since $R > 0$, by differentiating (4.7), we obtain

$$-\frac{1}{\tau_2}\exp\left(-\frac{t}{\tau_2}\right)\int_0^t \exp\left(\frac{s}{\tau_2}\right)\Lambda(s)ds + \frac{1}{\tau_1}\exp\left(-\frac{t}{\tau_1}\right)\int_0^t \exp\left(\frac{s}{\tau_1}\right)\Lambda(s)ds = 0 \tag{4.8}$$

for $t \in (T, T+R)$. Solving Eq. (4.7) and Eq. (4.8) we see that

$$\begin{cases} \int_0^t \exp\left(\frac{s}{\tau_2}\right)\Lambda(s)ds = D\tau_2\exp\left(\frac{t}{\tau_2}\right) \\ \int_0^t \exp\left(\frac{s}{\tau_1}\right)\Lambda(s)ds = D\tau_1\exp\left(\frac{t}{\tau_1}\right) \end{cases} \tag{4.9}$$

for $t \in [T, T+R]$, which implies that $\Lambda(t) = D$ and in particular

$$\begin{cases} \int_0^T \exp\left(\frac{s}{\tau_2}\right)\Lambda(s)ds = D\tau_2\exp\left(\frac{T}{\tau_2}\right) \\ \int_0^T \exp\left(\frac{s}{\tau_1}\right)\Lambda(s)ds = D\tau_1\exp\left(\frac{T}{\tau_1}\right). \end{cases} \tag{4.10}$$

Now let us find the optimal signal $\Lambda^*(t)$ for $t \in [0, T]$.

It is easily seen that

$$I(\Lambda) = I_x(\lambda_x) + I_y(\lambda_y) + I_z(\lambda_z) \tag{4.11}$$

$$= \int_0^T \left[\int_T^{T+R} b_{12}^2(t-s)dt\right] [|\lambda_x|^{2\alpha}(s) + |\lambda_y|^{2\alpha}(s) + |\lambda_z|^{2\alpha}(s)]ds$$

$$+ \int_T^{T+R} \left[\int_T^s b_{12}^2(t-s)dt\right] [|\lambda_x|^{2\alpha}(s) + |\lambda_y|^{2\alpha}(s) + |\lambda_z|^{2\alpha}(s)]ds \tag{4.12}$$

Since to minimize each term in Eq. (4.12) implies to minimize $I(\Lambda)$, we apply the calculus of variations to the first term in Eq. (4.12), as the second term is a constant (for $t \in [T, T+R]$ $\Lambda(t) = D$, see Eq. (4.10).) To this end, let us define

$$\left\{\lambda_x, \int_0^T b_{12}(T-s)\lambda_x(s)ds = \tau_1\tau_2 d_x, \lambda_x(t) = d_x, t \in [T, T+R]\right\} = \mathcal{U}_D.$$

For a small τ, consider $\lambda_x + \tau\phi \in \mathcal{U}_D$, i.e.

$$\phi \in \{\phi, \int_0^T \exp(s/\tau_1)\phi(s)ds = 0,$$

$$\int_0^T \exp(s/\tau_2)\phi(s)ds = 0, \phi(t) = 0, \text{ for } t \in [T, T+R]\} = \mathcal{U}_D^0.$$

The first two constraints in $\mathcal{U}_D^0$ are from Eq. (4.10). We then have

$$\frac{dI_x(\lambda_x + \tau\phi)}{d\tau}|_{\tau=0} = 0$$

which gives

$$\int_0^T \left\{\left[\int_T^{T+R} b_{12}^2(t-s)dt\right] |\lambda_x(s)|^{2\alpha-1}\text{sgn}(\lambda_x(s))\phi(s)\right\} ds = 0. \tag{4.13}$$

Comparing Eq. (4.13) with the first two constraints in $\mathcal{U}_D^0$, we conclude that

$$\left[\int_T^{T+R} b_{12}^2(t-s)dt\right] |\lambda_x(s)|^{2\alpha-1}\text{sgn}(\lambda_x(s)) = \xi_x \exp\left(\frac{s}{\tau_1}\right) + \eta_x \exp\left(\frac{s}{\tau_2}\right) \tag{4.14}$$

almost surely for $s \in [0, T]$ with two parameters $\xi_x, \eta_x \in R$. Hence the solution of the original problem is

$$\lambda_x^*(s) = \frac{\left|\xi_x \exp\left(\frac{s}{\tau_1}\right) + \eta_x \exp\left(\frac{s}{\tau_2}\right)\right|^{1/(2\alpha-1)} \text{sgn}\left[\xi_x \exp\left(\frac{s}{\tau_1}\right) + \eta_x \exp\left(\frac{s}{\tau_2}\right)\right]}{\left(\int_T^{T+R} b_{12}^2(t-s)dt\right)^{1/(2\alpha-1)}} \tag{4.15}$$

with ξ_x, η_x being given by

$$\begin{cases} d_x\tau_2 \exp\left(\frac{T}{\tau_2}\right) = \int_0^T \exp\left(\frac{s}{\tau_2}\right) \\ \cdot \frac{\left|\xi_x \exp\left(\frac{s}{\tau_1}\right) + \eta_x \exp\left(\frac{s}{\tau_2}\right)\right|^{1/(2\alpha-1)} \operatorname{sgn}\left[\xi_x \exp\left(\frac{s}{\tau_1}\right) + \eta_x \exp\left(\frac{s}{\tau_2}\right)\right]}{\left(\int_T^{T+R} b_{12}^2(t-s)dt\right)^{1/(2\alpha-1)}} ds \\ d_x\tau_1 \exp\left(\frac{T}{\tau_1}\right) = \int_0^T \exp\left(\frac{s}{\tau_1}\right) \\ \cdot \frac{\left|\xi_x \exp\left(\frac{s}{\tau_1}\right) + \eta_x \exp\left(\frac{s}{\tau_2}\right)\right|^{1/(2\alpha-1)} \operatorname{sgn}\left[\xi_x \exp\left(\frac{s}{\tau_1}\right) + \eta_x \exp\left(\frac{s}{\tau_2}\right)\right]}{\left(\int_T^{T+R} b_{12}^2(t-s)dt\right)^{1/(2\alpha-1)}} ds. \end{cases} \tag{4.16}$$

The similar equation is true for λ_y and λ_z.

From the results above, we see that the optimal problem is in general a highly nonlinear problem. However, we arrive at the following surprising conclusions.

Theorem 1 *Under the optimal control framework as we set up here and $\alpha > 1/2$, the optimal mean trajectory is a straight line. When $\alpha \leq 1/2$ the optimal control problem is degenerate, i.e. the optimal control signal is a delta function. Eq. (4.12) with $\Lambda = \Lambda^*$ gives us an exact relationship between time T and variance.*

Proof We only need to show that if, say $d_x = kd_y$, we then have $\langle x(t)\rangle = k\langle y(t)\rangle$ with a positive constant k. Let us assume that for $\alpha > 1/2$, (ξ_x, η_x) is the solution of Eq. (4.16). It is easily seen that $k^{2\alpha-1}(\xi_x, \eta_x)$ is the solution of Eq. (4.16) with d_x being replaced by kd_y. From Eq. (4.15), together with the fact above, we have $\lambda_y(s) = k\lambda_x(s)$. From Eq. (4.4), we finally conclude that $\langle x(t)\rangle = k\langle y(t)\rangle$ holds true. The proof of the second part of Theorem 1 is easy and is left to the reader.

For a deterministic problem similar to the optimal control problem defined by Eq. (4.2) and (4.3), i.e. $\alpha \to 0$, the optimal signal is a delta function. The results in Theorem 1 tell us that when the noise is not strong enough $\alpha \leq 1/2$, the optimal control signal is still degenerate. Nevertheless, when $\alpha > 1/2$, i.e. the noise is strong enough, the solution of the optimal control problem turns out to be non-degenerate. This is different from our usual intuition that any tiny noise could smooth an action, i.e. any tiny noise ensures that the system is ergodic.

A straight line trajectory indicates that the travelling distance between the starting point and the end point is the shortest. In other words, the shortest distance principle is the consequence the optimal control problem defined by Eq. (4.2) and (4.3), provided that $\alpha > 1/2$.

In Fig. 4.2 [68], we plot $\langle y(t)\rangle$, the optimal trajectory $\langle x(t)\rangle, \langle y(t)\rangle$, velocity profile and variance for fixed $R = 0.2T$, $\tau_1 = 5, \tau_2 = 15$ and various D and T as shown in the figure for $\alpha = 0.75, 1, 1.5$ [69]. As we proved in Theorem 1, $(\langle x(t)\rangle, \langle y(t)\rangle)$ shows a straight line trajectory starting from (0,0) in Fig. 4.2) and arriving at an end point (indicated by arrow in Fig. 4.2 right Upper trace). It is worthwhile pointing out that $\langle x(t)\rangle$ and $\langle y(t)\rangle$ (Fig. 4.2 upper left) are highly nonlinear function of time t. Fig. 4.2 middle left shows the velocity profiles vs. distance. The bell-shaped is obvious. In fact, this might not be surprising in comparison with the trajectory formation which is a consequence of a highly nonlinear optimal control problem. The optimal control problem we considered here requires that the velocity is zero at the beginning and the end point of the movement, i.e. $(\langle x(t)\rangle, \langle y(t)\rangle)$ is a constant for $t \in [T, T + R]$. We would then expect that a bell-shaped velocity profile will be the most natural outcome, provided that the velocity is continuous. In Fig. 4.2 middle trace right, we also depict the optimal variance $I_x(\lambda_x^*) + I_y(\lambda_y^*)$ vs. distance. We see that the optimal variance is an increasing function of distance, as one would naturally expect. To compare our results with Fitts law, we plot $I_x(\lambda_x^*) + I_y(\lambda_y^*)$ vs. time T in Fig. 4.2, bottom right. It is easily seen that the longer the time is, the smaller the variance. In fact, from our results, we could also assess the exactly relation between the optimal variance and the time. Finally Bottom left, we show the optimal control signals vs. t for various time T.

It is clear now that the second order statistics plays an important role in neuronal computation, but we have not taken into account another important second order statistics here: the correlation between neuronal activity. In the next few sections, we will concentrate on it.

4.4 Discrimination

In this section we present a study on the discrimination capacity of the simplest neuron model: the integrate-and-fire model. Suppose that a neuron receives two sets of signal. Both of them are contaminated by noise, as shown in Fig. 4.3. After neuronal transformations, we want to know whether the signals become more mixed or more separated. This is a typical scenario in decision theory.

We conclude that without correlation between signals, the output histograms are separable if and only if the input histograms are separable. With positively correlated input signals, the output histograms become more separable than input histograms. With negatively correlated input signals, the output histograms are more mixed than input histograms. This is a clear-cut and interesting result. In fact, in recent years, there are many publications devoted to exploring the functional role of correlated neuronal activity. For example, synchronization is a special case of correlated neuronal activity[77, 30, 35]. People have extensively investigated the functional roles of correlations in neurons from information theoretic approaches[47, 48, 8], from experimental approaches[53, 52] and from modelling approaches [1, 54, 51, 15].

In the classical theory of neural networks, we only take into account the excitatory inputs. However, in recent years, we have found many intriguing functional roles of inhibitory inputs, ranging from linearizing input-output relationship of a neuron[38], to synchronizing a group of neurons[58] and to actually increasing neuron firing rates[19]. In particular, neuronal and neuronal network models with an exactly balanced inhibitory and excitatory input are intensively studied in the literature[59, 55]. For these two most interesting cases, independent input case and exactly balanced input case, we are able to find out the exact value of neuronal discrimination capacity. Roughly speaking, here discrimination capacity is the minimal number of synapses carrying signals so that the output histograms of the neuron are separable, provided that input signals are different (see Section 3 for the definition). Interestingly, the obtained analytical discrimination capacity is *universal* for the model. It is independent of the decay rate, the threshold, the magnitude of EPSP and IPSP, and the input signal distributions.

The section is organized as follows. In subsection 4.2, the model is exactly defined. In subsection 4.3, we consider the worst case and the exact value of discrimination capacity is obtained. In subsection 4.4, we generalize results in subsection 4.3. In subsection 4.5, some numerical results are included. We have presented numerical results for the integrate-and-fire model and the IF-FHN model [19] in a meeting report[21]. In subsection 4.6, we briefly discuss related issues. Detailed theoretical proofs are omitted and can be found in [14].

4.4.1 The Models

The neuron model we use here is the classical integrate-and-fire model [10, 18, 28, 57]. When the membrane potential $V_t^{(k)}$ is below the threshold V_{thre}, it is given by

$$dV_t^{(k)} = -L(V_t^{(k)} - V_{rest})dt + dI_{syn}^{(k)}(t) \tag{4.17}$$

where $L = 1/\gamma$ (Section 2) is the decay coefficient and the synaptic input is

$$I_{syn}^{(k)}(t) = a\sum_{i=1}^{p} E_i^{(k)}(t) - b\sum_{j=1}^{q} I_j^{(k)}(t)$$

with $E_i^{(k)}(t), I_i^{(k)}(t)$ as Poisson processes with rates $\lambda_{i,E}^{(k)}$ and $\lambda_{i,I}^{(k)}$ respectively, $a > 0, b > 0$ are the magnitudes of each EPSP and IPSP, p and q are the total number of active excitatory and inhibitory synapses, $k = 1, 2$ represent different input signals and we aim at discriminating between them in terms of an observation of efferent firing rates. Once $V_t^{(k)}$ crosses V_{thre} from below a spike is generated and $V_t^{(k)}$ is reset to V_{rest}, the resting potential. This model is termed the intergrate and fire (IF) model. The interspike interval of efferent spikes is

$$T^{(k)} = \inf\{t : V_t^{(k)} \geq V_{thre}\}.$$

For simplicity of notation we assume that $q = p$ and $\lambda_{i,I}^{(k)} = r\lambda_{i,E}^{(k)}$, where $0 \leq r \leq 1$ is the ratio between inhibitory and excitatory inputs.

Furthermore we suppose that p_c out of p synapses carry the true signal and the rest $p - p_c$ synapses are noise (or distorted signals). Synapses which code true signals are correlated, but synapses which code noise are independent. For simplicity of notation we assume that the correlation coefficient between the ith excitatory (inhibitory) synapse and the jth excitatory (inhibitory) synapse is a constant c, where $i, j = 1, \cdots, p_c$. The correlation considered here reflects the correlation of activity of different synapses, as discussed and explored in [19, 78]. More specifically, synaptic inputs take the following form ($p = q$)

$$\begin{aligned} I_{syn}^{(k)}(t) &= a\sum_{i=1}^{p} E_i^{(k)}(t) - b\sum_{j=1}^{p} I_j^{(k)}(t) \\ &= a\sum_{i=1}^{p_c} E_i^{(k)}(t) + a\sum_{i=p_c+1}^{p} E_i^{(k)}(t) - b\sum_{i=1}^{p_c} I_i^{(k)}(t) - b\sum_{i=p_c+1}^{p} I_i^{(k)}(t) \end{aligned}$$

where $E_i^{(k)}(t), i = 1, \cdots, p_c$ are correlated Poisson processes with an identical rate $\lambda^{(k)}$ (signal), $E_i^{(k)}(t), i = p_c + 1, \cdots, p$ are Poisson processes with a firing rate λ_i independently and identically distributed random variables from $[0, \lambda_{max}]$Hz (noise), $I_i^{(k)}(t), i = 1, \cdots, p$ have the same properties as $E_i^{(k)}(t)$, but with a firing rate of $r\lambda^{(k)}$ or $r\lambda_i$ for $r \in [0, 1]$ representing the ratio between inhibitory and excitatory inputs. It was pointed out in [55] that the ratio of inhibitory and excitatory synapses is around 15/85. Of course, in general, inhibitory inputs are larger than excitatory inputs. All conclusions below can be easily extended to the case of $r > 1$. On the other hand, for the simplicity of notation, we have introduced a single parameter r to describe the relationship between inhibitory and excitatory inputs. From the proofs

below, we can see that this assumption can be easily relaxed. Without loss of generality we simply assume that $\lambda^{(1)}, \lambda^{(2)} \in [0, \lambda_{max}]$Hz.

Hence the neuron model receives two set of inputs: one is

$$a\sum_{i=1}^{p_c} E_i^{(1)}(t) + a\sum_{i=p_c+1}^{p} E_i^{(1)}(t) - b\sum_{i=1}^{p_c} I_i^{(1)}(t) - b\sum_{i=p_c+1}^{p} I_i^{(1)}(t)$$

where the signal term

$$a\sum_{i=1}^{p_c} E_i^{(1)}(t) - b\sum_{i=1}^{p_c} I_i^{(1)}(t)$$

is masked by the noise term

$$a\sum_{i=p_c+1}^{p} E_i^{(1)}(t) - b\sum_{i=p_c+1}^{p} I_i^{(1)}(t);$$

the other is

$$a\sum_{i=1}^{p_c} E_i^{(2)}(t) + a\sum_{i=p_c+1}^{p} E_i^{(2)}(t) - b\sum_{i=1}^{p_c} I_i^{(2)}(t) - b\sum_{i=p_c+1}^{p} I_i^{(2)}(t)$$

where the signal term

$$a\sum_{i=1}^{p_c} E_i^{(2)}(t) - b\sum_{i=1}^{p_c} I_i^{(2)}(t)$$

is masked by the noise term

$$a\sum_{i=p_c+1}^{p} E_i^{(2)}(t) - b\sum_{i=p_c+1}^{p} I_i^{(2)}(t).$$

In the following, we further use diffusion approximations to approximate synaptic inputs [57] and assume $a = b$

$$\begin{aligned} i_{syn}^{(k)}(t) &= ap_c\lambda^{(k)}t + a\sum_{i=p_c+1}^{p}\lambda_i t - bp_c r\lambda^{(k)}t - b\sum_{i=p_c+1}^{p} r\lambda_i t \\ &\quad + \sqrt{(a^2+b^2r)\lambda^{(k)}p_c(1+c(p_c-1)) + (a^2+b^2r)\sum_{i=p_c+1}^{p}\lambda_i}\cdot B_t \\ &= a(1-r)t\left[p_c\lambda^{(k)} + \sum_{i=p_c+1}^{p}\lambda_i\right] \\ &\quad + a\sqrt{(1+r)[\lambda^{(k)}p_c(1+c(p_c-1)) + \sum_{i=p_c+1}^{p}\lambda_i]}\cdot B_t \end{aligned} \tag{4.18}$$

where B_t is the standard Brownian motion.

Therefore the term

$$a(1-r)t\left[p_c\lambda^{(k)}+\sum_{i=p_c+1}^{p}\lambda_i\right], \qquad k=1,2 \tag{4.19}$$

in Eq. (4.18) is the mean input signal to the cell. Without loss of generality, we always assume that $\lambda^{(1)}<\lambda^{(2)}$. Denote $p_k^{(in)}(\lambda)$ as the distribution density of random variables (ignore the constants $a(1-r)t$ in Eq. (4.19)).

$$p_c\lambda^{(k)}+\sum_{i=p_c+1}^{p}\lambda_i. \tag{4.20}$$

In summary, we consider the case that a neuron receives p synaptic inputs, with p_c out of p carrying the signals and $p-p_c$ being noise (distorted signals). The setup here roughly corresponds to the experiments of Newsome and his colleagues. We will explore this aspect in further publications [26].

4.4.2 Discrimination Capacity: The Worst Case

For a fixed $\lambda^{(1)}<\lambda^{(2)}$ we have corresponding two histograms $p_1^{(out)}(\lambda)$ and $p_2^{(out)}(\lambda)$ of output firing rates as shown in Fig. 4.4. Let

$$R_{\min}^{(out)}(\lambda^{(2)})=\min\{\lambda : p_2^{(out)}(\lambda)>0\}$$

and

$$R_{\max}^{(out)}(\lambda^{(1)})=\max\{\lambda : p_1^{(out)}(\lambda)>0\}$$

and denote

$$\alpha(\lambda^{(1)},\lambda^{(2)},c,r)=\{p_c : R_{\min}^{(out)}(\lambda^{(2)})=R_{\max}^{(out)}(\lambda^{(1)})\}. \tag{4.21}$$

Hence for fixed $(\lambda^{(1)},\lambda^{(2)},c,r)$, $\alpha(\lambda^{(1)},\lambda^{(2)},c,r)$ gives us the critical value of p_c: when $p_c>\alpha(\lambda^{(1)},\lambda^{(2)},c,r)$ the input patterns are perfectly separable in the sense that the the output firing rate histograms are not mixed; when $p_c<\alpha(\lambda^{(1)},\lambda^{(2)},c,r)$ the input patterns might not be separable. For fixed $(\lambda^{(1)},\lambda^{(2)},c,r)$, α is termed the *(worst) discrimination capacity* of the neuron.

For input signals let us introduce more notation. Define

$$R_{\min}^{(in)}(\lambda^{(2)})=\min\{\lambda : p_2^{(in)}(\lambda)>0\}$$

and

$$R^{(in)}_{\max}(\lambda^{(1)}) = \max\{\lambda : p^{(in)}_1(\lambda) > 0\}.$$

Therefore as soon as $R^{(in)}_{\min}(\lambda^{(2)}) > R^{(in)}_{\max}(\lambda^{(1)})$ the two masked inputs are perfectly separable. Otherwise the two masked inputs are mixed. Hence the relationship between $R^{(in)}_{\min}(\lambda^{(2)}) - R^{(in)}_{\max}(\lambda^{(1)})$ and $R^{(out)}_{\min}(\lambda^{(2)}) - R^{(out)}_{\max}(\lambda^{(1)})$ characterizes the input-output relationship of signals.

Behaviour of $\alpha(\lambda^{(1)}, \lambda^{(2)}, c, r)$

First of all, we note that the output firing rate is given by [57]

$$\langle T^{(k)} \rangle = \frac{2}{L} \int_{A(V_{rest}, \sum_{j=p_c+1}^{p} \lambda_j)}^{A(V_{thre}, \sum_{j=p_c+1}^{p} \lambda_j)} g(x)dx, \tag{4.22}$$

where

$$A(x,y) = \frac{xL - a[p_c\lambda^{(k)} + y](1-r)}{a\sqrt{[\lambda^{(k)}p_c(1+c(p_c-1)) + y](1+r)}}$$

and

$$g(x) = \left[\exp(x^2)\int_{-\infty}^{x} \exp(-u^2)du\right].$$

Let us define

$$\tilde{T}^{(k)}(x) = \frac{2}{L} \int_{A(V_{rest},x)}^{A(V_{thre},x)} g(u)du. \tag{4.23}$$

We know that the output firing rate is calculated via

$$1000/(\langle T^{(k)} \rangle + T_{ref})$$

where T_{ref} is the refractory period. It is obvious to see that $\tilde{T}(x)$ is a monotonic function of input $x \geq 0$, i.e. the output firing rate of a neuron is an increasing function of input. We conclude that $\alpha(\lambda^{(1)}, \lambda^{(2)}, c, r)$ is the solution of the following equation about p_c.

$$\begin{aligned}
&\int_0^{V_{thre}L} g\left(\frac{y - a[p_c\lambda^{(1)} + (p-p_c)\lambda_{\max}](1-r)}{a\sqrt{[\lambda^{(1)}p_c(1+c(p_c-1)) + (p-p_c)\lambda_{\max}](1+r)}}\right)dy \\
&= \frac{\sqrt{[\lambda^{(1)}p_c(1+c(p_c-1)) + (p-p_c)\lambda_{\max}]}}{\sqrt{[\lambda^{(2)}p_c(1+c(p_c-1))]}} \\
&\quad \cdot \int_0^{V_{thre}L} g\left(\frac{y - a(p_c\lambda^{(2)})(1-r)}{a\sqrt{[\lambda^{(2)}p_c(1+c(p_c-1))](1+r)}}\right)dy.
\end{aligned} \tag{4.24}$$

The critical value $\alpha(\lambda^{(1)}, \lambda^{(2)}, c, r)$ can be found analytically in the two most interesting cases: $c = 0$ and $r = 1$. Define

$$0 \leq \Lambda = \frac{\lambda^{(2)} - \lambda^{(1)}}{\lambda_{max}} \leq 1$$

we then have the following conclusions

Theorem 2 *We assume* $\Lambda > 0, 0 < r < 1$,

- *When* $c > 0$ *we have*

$$\alpha(\lambda^{(1)}, \lambda^{(2)}, c, 1) < \alpha(\lambda^{(1)}, \lambda^{(2)}, 0, r) \tag{4.25}$$

and furthermore

$$\alpha(\lambda^{(1)}, \lambda^{(2)}, c, 1) = \frac{\sqrt{[\Lambda(1-c)+1]^2 + 4pc\Lambda} - (1-c)\Lambda - 1}{2c\Lambda}. \tag{4.26}$$

- *When* $c = 0$ *we have*

$$\alpha(\lambda^{(1)}, \lambda^{(2)}, 0, r) = \frac{p}{1+\Lambda} \tag{4.27}$$

independent of r.

- *When* $c < 0$ *we have*

$$\alpha(\lambda^{(1)}, \lambda^{(2)}, c, 1) > \alpha(\lambda^{(1)}, \lambda^{(2)}, 0, r). \tag{4.28}$$

The proof of Theorem 2 is quite tricky and we postpone it to the Appendix. In fact, from all our numerical results (see Fig. 4.6, bottom panel), we have the following stronger conclusions than Theorem 2 (Eq. (4.25) and Eq. (4.28)).

- When $c > 0$ we have

$$\alpha(\lambda^{(1)}, \lambda^{(2)}, c, r_2) < \alpha(\lambda^{(1)}, \lambda^{(2)}, c, r_1) \tag{4.29}$$

where $1 \geq r_2 > r_1 > 0$.

- When $c < 0$ we have

$$\alpha(\lambda^{(1)}, \lambda^{(2)}, c, r_2) > \alpha(\lambda^{(1)}, \lambda^{(2)}, c, r_1) \tag{4.30}$$

where $1 \geq r_2 > r_1 > 0$.

However, we are not able to theoretically prove the stronger conclusions (Eq. (4.29) and Eq. (4.30)).

It is very interesting to note that Eq. (4.27) and Eq. (4.26) are independent of a, V_{thre} and L, three essential parameters in the integrate-and-fire model. In other words, the results of Eq. (4.27) and Eq. (4.26) of the integrate-and-fire model are *universal*. In Fig. 4.5 we plot α vs. Λ for $c = 0$ and $c = 0.1$. according to Eq. (4.27) and Eq. (4.26). For a given Λ and $c = 0.1$, the solid line in Fig. 4.5 gives us the smallest number of coherently synaptic inputs for an integrate-and-fire model to discriminate between input signals if we assume that $r \in [0, 1]$. Hence the solid line in Fig. 4.5 is the smallest discrimination capacity of an integrate-and-fire model with $c = 0.1$. It is worth pointing out that the lowest limit of α is about $\alpha = 23$. Finally we want to emphasize that our results are independent of input distributions. No matter what the input distribution is, as soon as p_c is greater than 40, the input signal can be perfectly separated from an observation of efferent spike trains provided that $\Lambda = 0.5$. The improvement of discrimination capacity from $r = 0$ to $r = 1$ is remarkable, almost halving in most cases.

A universal result as in equation (4.26) and (4.27) above is illuminating since it is independent of model parameters and then widely applicable. However, the downside of such a result is that neurons modify their connections to improve their performance. Therefore we would argue that learning plays no role in improving its discrimination capacity, or discrimination tasks are not a primary computational task for a neuronal system. However, we want to point out that Eq. (4.26) is obtained for $r = 1$, the case with exactly balanced inhibitory and excitatory inputs. In a biologically realistic situation, neuron systems might operate in a region with $r < 1$. In the circumstances, α could depend on various model parameters and so learning might be important to improve the integrate-and-fire model discrimination capacity. Certainly to find a learning rule to improve neuronal discrimination capacity would be an interesting topic.

Input-Output Relationship

We first want to asses that whether $R_{\min}^{(out)}(\lambda^{(2)}) - R_{\max}^{(out)}(\lambda^{(1)}) > 0$ even when $R_{\min}^{(in)}(\lambda^{(2)}) - R_{\max}^{(in)}(\lambda^{(1)}) < 0$, i.e. the input signal is mixed, but the output signal is separated. In Fig. 4.6 we plot $R_{\min}^{(out)}(\lambda^{(2)}) - R_{\max}^{(out)}(\lambda^{(1)})$ vs $R_{\min}^{(in)}(\lambda^{(2)}) - R_{\max}^{(in)}(\lambda^{(1)})$. It is easily seen that after neuronal transformation, mixed signals are better separated when $c > 0$. For example, when $c = 0.1, r = 1$ and $R_{\min}^{(in)}(\lambda^{(2)}) - R_{\max}^{(in)}(\lambda^{(1)}) = -5000$ Hz (mixed), but $R_{\min}^{(out)}(\lambda^{(2)}) - R_{\max}^{(out)}(\lambda^{(1)}) > 0$ (separated). The conclusion is not true for $c = 0$, but the separation is not worse after neuronal transformation. In Fig. 4.6, it is clearly seen that when $r < 1$ and $c \neq 0$, the discrimination capacity depends on model parameters.

We can prove the following conclusions.

Theorem 3 *For the integrate-and-fire model*

- *if* $c > 0$ *we have*

$$R_{\min}^{(out)}(\lambda^{(2)}) - R_{\max}^{(out)}(\lambda^{(1)}) > 0 \qquad when \qquad R_{\min}^{(in)}(\lambda^{(2)}) - R_{\max}^{(in)}(\lambda^{(1)}) = 0.$$

- *if* $c = 0$ *we have*

$$R_{\min}^{(out)}(\lambda^{(2)}) - R_{\max}^{(out)}(\lambda^{(1)}) = 0 \qquad when \qquad R_{\min}^{(in)}(\lambda^{(2)}) - R_{\max}^{(in)}(\lambda^{(1)}) = 0.$$

- *if* $c < 0$ *we have*

$$R_{\min}^{(out)}(\lambda^{(2)}) - R_{\max}^{(out)}(\lambda^{(1)}) < 0 \qquad when \qquad R_{\min}^{(in)}(\lambda^{(2)}) - R_{\max}^{(in)}(\lambda^{(1)}) = 0.$$

The conclusions above completely answer the question raised in the Introduction. When $c > 0$, the output histograms become more separated than input histograms; when $c < 0$, the output histograms are more mixed than input histograms. $c = 0$ is the critical case.

4.4.3 Discrimination Capacity: The Distribution Dependent Case

Consider the random variable $(\sum_{i=p_c+1}^{p} \lambda_i)$ in Eq. (4.20) and let us denote $(\sum_{i=p_c+1}^{p} \lambda_i)_j$ as its jth sampling. We see that after m times of sampling, the smallest input signal would be

$$p_c\lambda^{(k)} + \left(\sum_{i=p_c+1}^{p} \lambda_i\right)_{(m)} \tag{4.31}$$

and the largest would be

$$p_c\lambda^{(k)} + \left(\sum_{i=p_c+1}^{p} \lambda_i\right)^{(m)} \tag{4.32}$$

where $(\sum_{i=p_c+1}^{p} \lambda_i)^{(m)}$ and $(\sum_{i=p_c+1}^{p} \lambda_i)_{(m)}$ are the largest and smallest extreme value of the random variable $(\sum_{i=p_c+1}^{p} \lambda_i)$. Note that in subsection 4.4.2, we consider the worst cases and use 0 as its smallest input signal and $(p - p_c)\lambda_{max}$ as its largest input signal.

We can carry out a rigorous analysis on the behaviour of the extreme values of the random variable $(\sum_{i=p_c+1}^{p}\lambda_i)$. However, the conclusion obtained will then depend on the actual distribution of λ_i. To avoid this, we then assume that $p >> p_c$, $\lambda_i, i = p_c+1, \cdots, p$ are an identically and independently distributed random sequence (only for a technical convenience) and we have

$$\left(\sum_{i=p_c+1}^{p}\lambda_i - (p-p_c)\langle\lambda_p\rangle\right)/(\sqrt{p-p_c}\sigma(\lambda_p)) \sim N(0,1)$$

where $\sigma(\lambda_p) = \sqrt{\langle\lambda_p^2\rangle - \langle\lambda_p\rangle^2}$.

We need the following lemma [37]

Lemma 1 *For ξ_n being an identically and independently distributed normal sequence of random variables, then*

$$P(a_m((\xi)^{(m)} - b_m) \le x) \to \exp(-\exp(-x)) \tag{4.33}$$

where

$$\begin{cases} a_m = (2\log m)^{1/2} \\ b_m = (2\log m)^{1/2} - \dfrac{1}{2}(2\log m)^{-1/2}(\log\log m + \log(4\pi)). \end{cases} \tag{4.34}$$

Basically Lemma 1 tells us that approximately $(\xi)_{(m)}$ diverges to positive (negative) infinity at a speed of b_m $(-b_m)$. We thus conclude that

$$\left(\sum_{i=p_c+1}^{p}\lambda_i\right)^{(m)} \sim \min\left\{[(p-p_c)\langle\lambda_p\rangle + \sqrt{p-p_c}\sigma(\lambda_p)(b_m)], (p-p_c)\lambda_{max}\right\} \tag{4.35}$$

and

$$\left(\sum_{i=p_c+1}^{p}\lambda_i\right)_{(m)} \sim \max\left\{[(p-p_c)\langle\lambda_p\rangle - \sqrt{p-p_c}\sigma(\lambda_p)(b_m)], 0\right\}. \tag{4.36}$$

We see that when $m \to \infty$, $\left(\sum_{i=p_c+1}^{p}\lambda_i\right)^{(m)} \to (p-p_c)\lambda_{max}$ and $(\sum_{i=p_c+1}^{p}\lambda_i)_{(m)} \to 0$, which is the worst case we considered in the previous subsection.

For fixed $\lambda^{(1)} < \lambda^{(2)}$ and m, as before, we have two corresponding emperical histograms $p_1^{(out)}(\lambda, m)$ and $p_2^{(out)}(\lambda, m)$ of output firing rates. Let

$$R_{\min}^{(out)}(\lambda^{(2)}, m) = \min\{\lambda, p_2^{(out)}(\lambda, m) > 0\}$$

and

$$R_{\max}^{(out)}(\lambda^{(1)}, m) = \max\{\lambda, p_1^{(out)}(\lambda, m) > 0\}$$

and denote

$$\beta(\lambda^{(1)}, \lambda^{(2)}, c, r, m) = \{p_c : R_{\min}^{(out)}(\lambda^{(2)}, m) = R_{\max}^{(out)}(\lambda^{(1)}, m)\}. \tag{4.37}$$

Hence for fixed $(\lambda^{(1)}, \lambda^{(2)}, c, r, m)$, $\beta(\lambda^{(1)}, \lambda^{(2)}, c, r, m)$ gives us the critical value of p_c and we call it the discrimination capacity of the neuron (under m samplings).

Behaviour of $\beta(\lambda^{(1)}, \lambda^{(2)}, c, r, m)$

As in the previous subsection, we conclude that $\beta(\lambda^{(1)}, \lambda^{(2)}, c, r, m)$ is the solution of the following equation (p_c).

$$\begin{aligned}
&\int_0^{V_{thre}L} g\left(\frac{y - a[p_c\lambda^{(1)} + (\sum_{i=p_c+1}^{p}\lambda_i)^{(m)}](1-r)}{a\sqrt{[\lambda^{(1)}p_c(1+c(p_c-1)) + (\sum_{i=p_c+1}^{p}\lambda_i)^{(m)}](1+r)}}\right) dy \\
&= \frac{\sqrt{[\lambda^{(1)}p_c(1+c(p_c-1)) + (\sum_{i=p_c+1}^{p}\lambda_i)^{(m)}]}}{\sqrt{[\lambda^{(2)}p_c(1+c(p_c-1)) + (\sum_{i=p_c+1}^{p}\lambda_i)_{(m)}]}} \\
&\quad \cdot \int_0^{V_{thre}L} g\left(\frac{y - a[p_c\lambda^{(2)} + (\sum_{i=p_c+1}^{p}\lambda_i)_{(m)}](1-r)}{a\sqrt{[\lambda^{(2)}p_c(1+c(p_c-1)) + (\sum_{i=p_c+1}^{p}\lambda_i)_{(m)}](1+r)}}\right) dy.
\end{aligned} \tag{4.38}$$

The critical value $\beta(\lambda^{(1)}, \lambda^{(2)}, c, r, m)$ can be analytically found in the two most interesting cases: $c = 0$ and $r = 1$. Define

$$0 \le \Theta = \frac{\lambda^{(2)} - \lambda^{(1)}}{\sigma(\lambda_p)}.$$

This corresponds to the parameter Λ defined in the previous subsection.

Theorem 4 *For $\Theta > 0$*

- *when $c > 0$ we have*

$$\beta(\lambda^{(1)}, \lambda^{(2)}, c, 1, m) < \beta(\lambda^{(1)}, \lambda^{(2)}, 0, r, m) \tag{4.39}$$

and furthermore $\beta = \beta(\lambda^{(1)}, \lambda^{(2)}, c, 1, m)$ is the solution of the following equation

$$\Theta\beta(1 + c(\beta - 1)) = 2\sqrt{p - \beta}\, b_m \tag{4.40}$$

provided that the approximation Eq. (4.35) and Eq. (4.36) are used.

- *When $c = 0$ we have*

$$\beta(\lambda^{(1)}, \lambda^{(2)}, 0, r, m) = \frac{2b_m \left[\sqrt{b_m^2 + p\Theta^2} - b_m\right]}{\Theta^2} \tag{4.41}$$

independent of r, provided that the approximation Eq. (4.35) and Eq. (4.36) are used.

- *When $c < 0$ we have*

$$\beta(\lambda^{(1)}, \lambda^{(2)}, c, 1, m) > \beta(\lambda^{(1)}, \lambda^{(2)}, 0, r, m). \tag{4.42}$$

Again from numerical simulations (see Fig. 4.8 and Fig. 4.10) we conclude

- When $c > 0$ we have

$$\beta(\lambda^{(1)}, \lambda^{(2)}, c, r_2, m) < \beta(\lambda^{(1)}, \lambda^{(2)}, c, r_1, m) \tag{4.43}$$

where $1 \geq r_2 > r_1 > 0$.

- When $c < 0$ we have

$$\beta(\lambda^{(1)}, \lambda^{(2)}, c, r_2, m) > \beta(\lambda^{(1)}, \lambda^{(2)}, c, r_1, m) \tag{4.44}$$

where $1 \geq r_2 > r_1 > 0$

Again it is interesting to note that Eq. (4.41) and Eq. (4.40) are independent of a, V_{thre} and L, three essential parameters in the integrate-and-fire model. In other words, the results of Eq. (4.41) and Eq. (4.40) of the integrate-and-fire model are *universal*. In Fig. 4.7 we plot β vs. Θ for $c = 0$ and $c = .1$ according to Eq. (4.41) and Eq. (4.40). For a given Θ and $c = 0.1$, the solid line in Fig. 4.7 gives us the smallest number of coherently synaptic inputs for an integrate-and-fire model to discriminate between input signals for $r \in [0, 1]$. Hence the solid line in Fig. 4.7 is the smallest discrimination capacity of an integrate-and-fire model with $c = 0.1$ if we assume that $r \in [0, 1]$. It is worth pointing out that the lowest limit of β is about $\beta = 14$.

Input-Output Relationship

As before, we can assess the relationship between input and output histograms.

We can prove the following conclusions.

Theorem 5 *For the integrate-and-fire model,*

- *if* $c > 0$ *we have*

$$R_{\min}^{(out)}(\lambda^{(2)}, m) - R_{\max}^{(out)}(\lambda^{(1)}, m) > 0 \qquad when \qquad R_{\min}^{(in)}(\lambda^{(2)}, m) - R_{\max}^{(in)}(\lambda^{(1)}, m) = 0.$$

- *if* $c = 0$ *we have*

$$R_{\min}^{(out)}(\lambda^{(2)}, m) - R_{\max}^{(out)}(\lambda^{(1)}, m) = 0 \qquad when \qquad R_{\min}^{(in)}(\lambda^{(2)}, m) - R_{\max}^{(in)}(\lambda^{(1)}, m) = 0.$$

- *if* $c < 0$ *we have*

$$R_{\min}^{(out)}(\lambda^{(2)}, m) - R_{\max}^{(out)}(\lambda^{(1)}, m) < 0 \qquad when \qquad R_{\min}^{(in)}(\lambda^{(2)}, m) - R_{\max}^{(in)}(\lambda^{(1)}, m) = 0.$$

4.4.4 Numerical Results

Let us now consider the minimum total probability of misclassification (TPM) defined by

$$\text{TPM} = \frac{1}{2}P(\text{ misclassfied as } \lambda^{(2)} \text{ |input is } \lambda^{(1)}) + \frac{1}{2}P(\text{ misclassfied as } \lambda^{(1)} \text{ |input is } \lambda^{(2)}).$$

For example, in Fig. 4.8, we see that TPM (in percentile) for the left upper panel is about 13.5% and for the right upper panel is 5.5%. Therefore adding inhibitory inputs to the neuron considerably improves its discrimination capability, reducing TPM from 13.5% to 5.5%.

The parameters used in simulating the IF model are $V_{thre} = 20mV$, $V_{rest} = 0mV$, $L = 1/20$, $a = b = 1mV$, $p = 100$, $\lambda^{(1)} = 25$ Hz and $\lambda^{(2)} = 75$ Hz. A refractory period of 5msec is added for all numerical results of efferent firing frequency. For each fixed set of parameters of the model, 100 spikes are generated to calculate each mean, standard deviation etc. The histograms are obtained using 100 firing rates, i.e. $m = 100$.

It is interesting to compare numerical results with theoretical results in the previous subsections. From previous subsections we have

$$\alpha(25, 75, 0.1, 1) = 32.5133.$$

and

$$\beta(25, 75, 0.1, 1, 100) = 12.1251 \qquad \beta(0, 100, 0.1, 1, 100) = 7.8058.$$

From Fig. 4.10 (right) we conclude that the discrimination capacity would be between 15 and 20. The discrimination capacity from actual numerical simulations for $r = 1$ closes to $\beta(25, 75, 0.1, 1, 100)$.

Numerical simulations have been extensively carried out for the integrate-and-fire model and the IF-FHN model. All results are in agreement with our theoretical results in the previous subsections and were reported in a meeting [21].

4.4.5 Discussion

We have considered the problem of discriminating between input signals in terms of an observation of efferent spike trains of a single integrate-and-fire neuron. We have demonstrated, both theoretically and numerically, that two key mechanisms to improve the discrimination capability of the model neuron are to increase inhibitory inputs and increase correlation between coherent inputs. Analytical results for two most interesting cases $c = 0$ and $r = 1$ are obtained and the results are independent of model parameters.

Our results offer answers to a few issues which were extensively discussed in the literature. We simply summarize two of them.

Increasing inhibitory inputs and increasing correlations between coherent inputs can enhance discrimination capacity of a neuron. However, on the other hand we all know that increasing inhibitory inputs and correlations between inputs increase its output variability of efferent spike trains, which will simply broaden the efferent firing rate histograms and so reduce the discrimination capacity of a neuron. It seems our results in the current paper simply contradict this. Nevertheless, we must note that all theoretical results in Section 4.4.3 and Section 4.4.2 are obtained under the assumption that the efferent firing rates are exactly obtained. Results in Section 4.4.4 clearly demonstrate that theoretical results in Section 4.4.3 and Section 4.4.2 are true even when the number of spikes used to obtained the firing rates histogram is small (100 spikes). In general our results reveal that a neuron system faces two opposite requirements: to obtain the mean firing rates as exact as possible by reducing the variability of output spike trains (reducing inhibitory inputs and input correlations), to increase the discrimination capacity by increasing inhibitory inputs and input correlations. To elucidate our points further, in Fig. 4.9, we plot the firing rate histograms, using the identical parameters as in Fig. 4.8 (middle panel, right), but with 10 spikes to estimate the mean, rather than 100 spikes. It is clearly shown that the firing rate histograms in Fig. 4.9 are less widely separated than in Fig. 4.8, middle panel (right), and it is impossible to perfectly distinguish between two inputs. A neuronal system must

find a compromise way to resolve the issue. How to find an optimal trade off between the two requirements is an interesting research topic.

Secondly, there are many publications arguing that there is an optimal value of noise at which a neuronal system can optimally extract information. Nevertheless, our results indicate that the optimal point is simply the one at which the neuron's output is most variable. We thus conclude that the larger the noise, the better for the neuron system (see the paragraph above and Fig. 4.10) to separate masked signals. This confirms the fact that noise is useful in a neural system, but not via the form of stochastic resonance.

The only assumption we introduced in the model is that coherent signals are more correlated than random signals. This seems a quite natural assumption given the structured cortical areas. Fig. 4.11 illustrates the point. Coherent signals are transmitted by neurons grouping together (cortical columns) and neurons in the same column are bound to fire with a correlation. On the contrary, noisy (distorted) signals are less correlated.

The integrate-and-fire model is the simplest model in theoretical neuroscience. One might easily argue that the model is too simple to be true for a realistic biological neuron. Nevertheless, we have seen in the past few years that the integrate-and-fire model fits well with many experimental data (see for example, [3, 38, 29]) and still serves as a canonical model of neurons. On the other hand, we have tested results in the current paper on other models as well ([21]. It would be very interesting to investigate the impact of adaptation and dynamical synapses [29] on discrimination tasks.

Currently we are also working on building up a system which mimics experiments carried out in [56, 44] etc. with random dot stimuli and making judgements on dot moving directions[26].

4.5 Multi-Neuron Activity: Correlation

In the past decade, we have witnessed the prevailing of the synchronization theory in nervous systems. Certainly two (partially) synchronized spike trains are positively correlated. Are two spike trains recorded in *in vivo* experiments exclusively positively correlated? This is a question asked by many experimentlists. Here we first present some of our recent data from *in vivo* multi-electrode array recording in rat olfactory bulb.

Noise observed in all in vivo experiments in the nervous system is one of the main curbs for us to reveal the computational principles employed by the brain, despite a century long of research. If individual neuron behaves

unreliably, how we can recognise a face, react to a stimulus, and catch a ball in such an accurate way. One might argue that the noise in the nervous system can be averaged out if a population coding strategy is implemented. In fact, it is early pointed out in the literature [78] that increasing the number of neurons can not enhance the signal to noise ratio without limitations, if neurons are positively correlated. Of course, a pair of positively correlated spike trains imply that they are synchronized in a certain degree and synchronization assumption is very popular in the literature in the past decades.

However, we have found evidence confirming the existence of a negative correlation rather positive correlations in *in vivo* experiments on the rat's olfactory bulb[60]. What is the functional meaning of our findings[22, 17]? To answer the question, we run a few simulations here. Assume there are one hundred neurons and the ith neuron sends out a spike train with an instantaneous rate

$$\xi_i = \sqrt{\sin(2\pi t) + 1.5}\eta_i + \sin(2\pi t) + 1.5$$

where η_i is noise(normally distributed random variable with mean zero and variance one). Note that the firing rate takes the form of Poisson processes: its noise magnitude is proportional to the signal term[57]. In Fig. 4.12 (left), we depict the summation of all $N = 65$ neurons firing rates with various correlation between η_i. The correlation between ith and jth neuron is $-c^n$ (positive) when $i, j < N^p, N^p = 1, , 65$ and otherwise is negative as specified in the figure. It is clearly seen that the noise level is significantly reduced when the correlation becomes more negative, i.e. N^p decreases. When the correlation between neurons is around $c^n = -0.015$ and $N^p = 0$, the obtained signal is almost perfect.

The mechanism behind the observed phenomenon in Fig. 4.12 is essentially due to the central limit theorem. Suppose that we have N normally distributed random variables ((instantaneous) firing rate of N neurons) $\xi_i, i = 1, , N$ with mean and covariance matrix

$$\sigma_{ij} = \begin{cases} (\sin(2\pi t) + 1.5)(\delta_{ij} - c^n(1 - \delta_{ij})), & i, j = 1, \cdots, N^p, \\ (\sin(2\pi t) + 1.5)(\delta_{ij} + c^n(1 - \delta_{ij})), & i, j \notin \{1, , N^p\} \end{cases}$$

From the central limit theorem we know that

$$\frac{\xi_1 + \cdots \xi_N - N(\sin(2\pi t) + 1.5)}{\sqrt{N}} \to N\left(0, \frac{\sum \sigma_{ij}}{N}\right)$$

where $N(\cdot, \cdot)$ is the normal distribution. Note that the variance term can be decomposed into two terms: the first is $i = 1, \cdots, N, \sigma_{ii}$ which is always positive, the remaining term could be positive or negative depending on the correlation between neuronal activity. With a positive correlation, the variance will increase rather than reduce. In other words, the noise level is increased. But

with a negative correlation, the variance could be dramatically reduced. In Fig. 2, right, we plot the variance term with $N^p = 0, 1, , 65$. When $N^p = 0$, all neurons are negatively correlated. When $N^p = 65$, all neurons are positively correlated; and N^p is around 45, the variances is 1, i.e. all neurons are independent. Corresponding to Fig. 4.12 left, we see that when $N^p = 0$, the variance is almost zero with $c^n = -0.015$. From Fig. 4.12 left, we see that the difference between $N^p = 30$ and $N^p = 45$ is not easy to visually detect. However, theoretical results (right) tell us that there is a difference around 0.4.

Hence the negatively correlated terms contribute to reduce the variance, while positively correlated terms result in an increase of the variance. Our results above tell us that even a single neuron is very unreliable: it could behave as a Poisson process (the noise magnitude is proportional to the signal as we used here), the obtained signal in terms of a group of neurons could be almost perfect. In other words, an almost perfect signal can be extracted, as long as the neuronal activity is negatively correlated, as reported in our biological data[60].

In the literature, the redundancy reduction principle is widely regarded as one of the operation principles in the brain[6]. However, recently it is agreed that the principle has difficulty to explain the experimental data such as the number of cells in V1 is much larger than the number of cells in LGN. In fact, the negatively correlated computation principle is a step further than the redundancy reduction principle and is not in contradiction with the known facts and the functional meaning is clear. In Fig. 4.13, we plot 65 random numbers generated with mean zero and variance 16 with correlation -0.015 and 0.8. With a negative correlation, the space is more completely and symmetrically explored, resulting in a mean of -.0080. With a positive correlation, the situation is worst, only a portion of the whole space is covered by the points and the mean is -0.72. The figure also demonstrates another possible role of a negative correlated neuronal activity in discrimination tasks. We all know that the further away the distance between patterns to be discriminated, the easier the discrimination task is. Obviously negative correlation is a mechanism to push each pattern to the corner of its feature space and so make the discrimination task easier, in comparison with independent case, i.e. the redundancy reduction principle.

It might be not surprising to observe the negatively correlated activity in the nervous system. It is known that the interaction between neurons in the olfactory bulb is lateral inhibitory which is the natural cause of negative correlation between neuronal activity.

In the previous sections, we have presented several examples to explain the importance of the second order statistics: both variances and correlations.

Can we develop a general theory to describe network activity including both the first and second order statistics? In the next section, we develop such a theory.

4.6 Moment Neural Networks

We confine ourselves to feedforward networks (see Fig. 4.14) only, although it is readily seen that we can easily generalize our results below to feedback and recurrent networks.

For two given quantities V_{thre} (threshold) $> V_{rest}$ (resting potential) and when $v_i^{(k+1)}(t) < V_{thre}$, the membrane potential of the ith neuron in the $(k+1)$th layer $v_i^{(k+1)}(t)$ satisfies the following dynamics:

$$\begin{cases} dv_i^{(k+1)}(t) = -L(v_i^{(k+1)}(t) - V_{rest})dt + dI_{i,syn}^{(k+1)}(t) \\ v_i^{(k+1)}(0) = V_{rest} \end{cases} \tag{4.45}$$

where L is the decay rate, $I_{i,syn}^{(k+1)}(t)$ is the synaptic input given by

$$dI_{i,syn}^{(k+1)}(t) = \sum_{j=1}^{p^{(k)}} w_{ij}^{E,(k)} dN_j^{E,(k)}(t) - \sum_{j=1}^{q^{(k)}} w_{ij}^{I,(k)} dN_j^{I,(k)}(t) \tag{4.46}$$

here $w_{ij}^{E,(k)}$ is the magnitude of EPSPs (excitatory postsynaptic potentials), $w_{ij}^{I,(k)}$ is the magnitude of IPSPs (inhibitory postsynaptic potentials), $N_i^{E,(k)}$ and $N_j^{I,(k)}$ are renewal processes (EPSPs and IPSPs) arriving from the ith and jth synapse with interspike intervals $T_{im}^{E,(k)}, m = 1, 2, \cdots$, and $T_{jm}^{I,(k)}, m = 1, 2, \cdots$, $p^{(k)}$ and $q^{(k)}$ are the total number of active excitatory and inhibitory synapses in the kth layer. Once $v_i^{(k+1)}(t)$ is greater than V_{thre}, it is reset to V_{rest}. The model defined by Eq. (4.45) is called the (leaky) integrate-and-fire model [57]. In the sequel, we define $T_0 = 0$ and

$$T_{ij}^{(k+1)} = \inf\{t : v_i^{(k+1)}(t) \geq V_{thre}, t > T_{i(j-1)}^{(k+1)}\}, \qquad j = 1, 2, \cdots \tag{4.47}$$

as the firing time (interspike intervals), see Fig. 4.14 right.

According to the renewal theorem, we have

$$\frac{dN_i^E(t)}{dt} \to N\left(\frac{1}{\langle T_{ij}^{E,(k)}\rangle}, \frac{[\langle (T_{ij}^{E,(k)})^2\rangle - \langle T_{ij}^{E,(k)}\rangle^2]}{\langle T_{ij}^{E,(k)}\rangle^3}\right)$$

where $N(\cdot,\cdot)$ is the normal distribution.

In fact, a more detailed calculation tells us that

$$\begin{cases} \langle N_i^{E,(k)}\rangle = \dfrac{t}{\langle T_{ij}^{E,(k)}\rangle} + \dfrac{\mathrm{var}(T_{ij}^{E,(k)}) - (\langle T_{ij}^{E,(k)}\rangle)^2}{2(\langle T_{ij}^{E,(k)}\rangle)^2} + o(1) \\ \mathrm{var}(T_{ij}^{E,(k)}) = \dfrac{[\langle (T_{ij}^{E,(k)})^2\rangle - \langle T_{ij}^{E,(k)}\rangle^2]t}{\langle T_{ij}^{E,(k)}\rangle^3} + c \end{cases} \tag{4.48}$$

where c is a constant depending on the first, second and the third order statistics of $T_{ij}^{E,(k)}$. Hence N_t^E is in general not a Markov process due to the constant term independent of t in Eq. (4.48).

Let us introduce more notation here. Define

$$\mu_{ij}^{E,(k)} = \frac{1}{\langle T_{ij}^{E,(k)}\rangle + T_{ref}}, \qquad (\sigma_{ij}^{E,(k)})^2 = \frac{[\langle (T_{ij}^{E,(k)})^2\rangle - \langle T_{ij}^{E,(k)}\rangle^2]}{\langle T_{ij}^{E,(k)}\rangle^3}$$

where T_{ref} is the refractory period. For the ith neuron in the kth layer, we have

$$dN_i^{E,(k)}(t) \sim \mu_{i1}^{E,(k)}dt + \sigma_{i1}^{E,(k)}dB_i^{E,(k)}(t) \tag{4.49}$$

where $B_i^{E,(k)}(t)$ is the standard Brownian motion with a correlation coefficient $\rho_{ij}^{(k)}, i,j = 1,\cdots,N^{(k)}$. Of course, Eq. (4.54) is an approximation: the so-called usual approximation [57] to Poisson process is a special case[1]. The essential idea behind the approximation is the central limit theorem, i.e., to approximate the input pulses which are a summation of independent random variables by their mean and variance. To the best of our knowledge, such an approximation to the renewal process has not be introduced in the literature and we expect our approach could be quite significant and open upon many new problems to be further addressed. We also stress here that in the literature, there are many papers devoted to investigating the network activity of spiking neurons. However, all of them confined to the case of Poisson inputs, which is of course not satisfactory since the output of an integrate-and-fire model is no longer a Poisson process (hence the self-consistence issue has to be checked) but is surely a renewal process. Summarizing the results above, we obtain

$$\sum_{j=1}^{p^{(k)}} w_{ij}^{E,(k)}dN_j^{E,(k)}(t) = \sum_j w_{ij}^{E,(k)}\mu_{j1}^{E,(k)}dt + \sum_j w_{ij}^{E,(k)}(t)\sigma_{j1}^{E,(k)}dB_j^{E,(k)}(t)$$

Let us further suppose that $p^{(k)} = q^{(k)}$ and for the simplicity of notation

[1] To have a more accurate approximation, we have to resort to the similar idea employed in [20]. For the IF model which is linear before resetting, the approximation developed above without the constant term is quite accurate already (not shown here).

$$\begin{array}{ll} \mu_j^{E,(k)} = \mu_{j1}^{E,(k)}, & \sigma_j^{E,(k)} = \sigma_{j1}^{E,(k)}, \\ r\mu_i^{(k)} = r\mu_i^{E,(k)} = \mu_i^{I,(k)}, & w_{ij}^{(k)} = w_{ij}^{E,(k)} = w_{ij}^{I,(k)} \end{array} \tag{4.50}$$

and

$$r\sigma_i^{(k)} = r\sigma_i^{E,(k)} = \sigma_i^{I,(k)} \tag{4.51}$$

where $i = 1, \cdots, p^{(k+1)}, j = 1, \cdots, p^{(k)}$, r is the ratio between inhibitory inputs and excitatory inputs. In particular, when $r = 0$ the neuron exclusively receives excitatory inputs; when $r = 1$ the inhibitory and excitatory input is exactly balanced. Note that Eq. (4.51) is a quite strong assumption. Now we have

$$dI_{i,syn}^{(k+1)} = \sum_j w_{ij}^{(k)} \mu_j^{(k)} (1-r)dt + \sum_j w_{ij}^{(k)}(t)\sigma_j^{(k)} \sqrt{1+r} dB_j^{(k)}(t) \tag{4.52}$$

where $B_i^{(k)}(t), i = 1, \cdots, p^{(k)}$ are correlated Brownian motion with correlation coefficient $\rho_{ij}^{(k)}$.

In terms of Siegert's expression, we have the expression of all moments of the output firing rate of the model. For the mean we have

$$\langle T_i^{(k+1)} \rangle = \frac{2}{L} \int_{A_i^{(k)}(0))}^{A_i^{(k)}(V_{thre})} g(x)dx, \qquad A_i^{(k)}(y) = \frac{yL - \bar{\mu}_i^{(k)}}{\bar{\sigma}_i^{(k)} \sqrt{L}} \tag{4.53}$$

where

$$\bar{\mu}_i^{(k)} = \sum_j w_{ij} \mu_j^{(k)} (1-r), \qquad (\bar{\sigma}_i^{(k)})^2 = \sum_{m,n} w_{im} w_{in} \sigma_m^{(k)} \sigma_n^{(k)} \rho_{mn}^{(k)} (1+r) \tag{4.54}$$

and

$$g(x) = \left[\exp(x^2) \int_{-\infty}^{x} \exp(-u^2) du \right] = \begin{cases} D_-(x) + \exp(x^2) \dfrac{\sqrt{\pi}}{2} & \text{if } x \geq 0 \\ -D_-(-x) + \exp(x^2) \dfrac{\sqrt{\pi}}{2} & \text{otherwise} \end{cases}$$

with Dawson integral $D_-(x), x \geq 0$.

For the second order moments, variance, we know that

$$\mathrm{Var}(T_i^{(k+1)}) = \frac{4}{L^2} \int_{A_i^{(k)}(0)}^{A_i^{(k)}(V_{thre})} \exp(x^2) \cdot \left\{ \int_{-\infty}^{x} \exp(-u^2) g^2(u) du \right\} dx. \tag{4.55}$$

Finally we have to consider the correlation relationships between neuronal activity. In the literature, there are many publications investigating the functional role of correlations. Unfortunately, it turns out that to find a rigorous relationship between input correlation and output correlation is not an easy task. To this end, we simulate two IF neurons with synaptic inputs

$$\mu(1-r)+\sqrt{\mu(1+r)}dB^{(i)}, i=1,2$$

where $B^{(i)}$ are correlated Brownian motion with a correlation coefficient ρ_{in}, μ is a constant. It is found from Fig. 4.15 that the input correlation ρ_{in} and output correlation ρ_{out} is almost identical, independent of r and μ.

Hence we have the following *Heuristic* relationship between the input and output correlation in the network.

$$\rho_{ij}^{(k+1)}=\frac{\sum_{m,n} w_{im}^{(k)}\sigma_m^{(k)}w_{jn}^{(k)}\sigma_n^{(k)}\rho_{mn}^{(k)}}{\sqrt{\sum_{m,n} w_{im}^{(k)}\sigma_m^{(k)}w_{in}^{(k)}\sigma_n^{(k)}\rho_{mn}^{(k)}}\cdot\sqrt{\sum_{m,n} w_{jm}^{(k)}\sigma_m^{(k)}w_{jn}^{(k)}\sigma_n^{(k)}\rho_{mn}^{(k)}}} \tag{4.56}$$

Note that the right hand side of Eq. 4.56 is the input correlation to the ith and the jth neuron in the (k+1)th layer.

Let us have a few words on the implications of Eq. (4.56). Assume that $w_{im}^{(k)}=w>0$, $\sigma_m^{(k)}=\sigma>0$ and $\rho_{mn}(k)=\rho, m\neq n$, then we have

$$\rho_{ij}^{(k+1)}=\frac{p^{(k)}+(p^{(k)}-1)^2\rho}{p^{(k)}+(p^{(k)}-1)^2\rho}=1$$

In words, the neuronal activity is correlated (synchronized). The synchronized spike trains in a feedforward network as we discussed here have been observed early in the literature for a feedforward spiking network. In the general case where $w_{ij}^{(k)}, \sigma_m^{(k)}$ and $\rho_{ij}^{(k)}$ are not homogeneous and the output correlation is slightly higher or lower than the input correlation, $\rho_{ij}^{(k)}$ will not be unity.

Another extremal case is that we have $w_i^{(k)}=\{w_{im}^{(k)}, m=1,\cdots,p^{(k)}\}\perp w_j^{(k)}=\{w_{jm}^{(k)}, m=1,\cdots,p^{(k)}\}$ (orthogonal). Since we require that $w_{im}^{(k)}\geq 0$, we conclude that $\sum_{m,n} w_{im}^{(k)}\sigma_m^{(k)}w_{jn}^{(k)}\sigma_n^{(k)}\rho_{mn}^{(k)}=0$ and therefore $\rho_{ij}^{(k)}=0$. For $A,B\subset\{1,\cdots,p^{(k+1)}\}$, $A\cap B=\phi$, and $w_i^{(k)}\perp w_j^{(k)}$ for $i\in A, j\in B$, then the neuronal activity in A and B is independent, i.e. patched neuronal activity is observed in this case.

In summary, from Eq. (4.22), Eq. (4.55) and Eq. (4.56), we have the following relationship between inputs and outputs

$$(\boldsymbol{\mu}^{(k+1)},\boldsymbol{\sigma}^{(k+1)},\rho^{(k+1)})=\mathcal{M}(\boldsymbol{\mu}^{(k)},\boldsymbol{\sigma}^{(k)},\rho^{(k)}) \tag{4.57}$$

where $\boldsymbol{\mu}^{(k)} = \{\mu_i^{(k)}, i = 1, \cdots, p^{(k)}\}, \boldsymbol{\sigma}^{(k)} = \{\sigma_i^{(k)} i = 1, \cdots, p^{(k)}\}$ and $\mathcal{M}$ is the mapping defined by Eq. (4.22), Eq. (4.55) and Eq. (4.56). Eq. (4.57) gives us the relationship of the first and the second order moment in a spiking neuronal network and is called *moment mapping*, which is one of the central results in MNN.

4.6.1 Application: Spontaneous Activity

The first question we intend to address here is: how can spontaneous activity be maintained in a feed-forward network? In our simulation typical parameters used are $V_{rest} = 0mV, L = 1/20msec^{-1}$ and $V_{th} = 20mV$, in agreement with most published results [55, 39]. The simulations are carried out with Matlab [61].

Clamped Correlation

We first consider an ideal case: all weights, afferent mean and variance are identical, i.e. the network is homogeneous. Eq. (4.57) is now reduced to

$$(\boldsymbol{\mu}^{(k+1)}, \boldsymbol{\sigma}^{(k+1)}, \rho^{(k+1)}) = \mathcal{M}(\boldsymbol{\mu}^{(k)}, \boldsymbol{\sigma}^{(k)}, \rho^{(k)}) \tag{4.58}$$

with $\mu_1^{(k)} = \mu_j^{(k)}, \sigma_1^{(k)} = \sigma_j^{(k)}, \rho_{12}^{(k)} = \rho_{mn}^{(k)}, m \neq n$. As we discussed before, now the propagation of correlation becomes trivial: it will simply reach one. To prevent it from happening, we clamp the correlation coefficient in the current subsection. From experimental data, we know that correlation coefficient has a mean around 0.1. In all simulation below, we also fixed $w = w_i = 0.5$.

In Fig. 4.16, we plot simulation results for various $\mu^{(1)}$ and $\sigma^{(1)}$ ($C_i^{(k)} = \sigma_i^{(k)}/\mu_i^{(k)}$, the coefficient of variation (CV), is used) with $p^{(k)} = 100, \rho_{ij}^{(k)} = 0, 0.1, i \neq j$. For example, in the upper panel left, for the left branch, we simulate the model with initial state as specified in the figure. From left to right, the ratio r is 0.4, 0.3,0.2,0.1,0.0. Each data point is $(\mu^{(k)}, \sigma^{(k)})$ and we connect $(\mu^{(k)}, \sigma^{(k)})$ with $(\mu^{(k+1)}, \sigma^{(k+1)})$ by a straight line. From Fig. 4.16, upper panel and bottom left $\rho_{ij}^{(k)} = 0$, we see that there are only two possibilities: either the cell becomes completely silent[2] or fires with a relatively high frequency. In all of our simulations, we have never found that values of r between 0 and 1 lead to a system which is stable with a firing rate in accordance with experimental observations, i.e. with a firing rate below 10 Hz.

[2] We stop the simulation if the simulation time is exceedively long which implies that the cell is silent. For example, In Fig. 4.16 upper trace left, for the left branch, with $r = 0.3$, the next point should be with a firing rate being zero

To confirm our conclusions, in Fig. 4.16 bottom right, we carry out a more detailed simulation with $\rho_{ij}^{(k)} = 0.1, r = 0.25, 0.26, 0.27, 0.29, 0.3$. It is easily see that the network activity converges to either a highly firing frequency or completely silent state.

Having observed this difficulty: the network becomes either too active or completely silent, we then try to explore wider parameter regions. From Fig. 4.17, upper panel left, it is concluded that the ratio r must be significantly higher than for exactly balanced input to make the network become stable. When $r = 2.3$, the network settles down to a state with a firing rate below 10 Hz and a coefficient of variation around 1.2. This also validates our approach since the output process is surely not a Poisson process, but a renewal process.

The reason why such a high inhibitory is needed in a network is clear. The input-output firing rate relationship of a neuron takes the shape of a sigmoidal function or a skew bell shape function starting from the origin (see Fig. 8.13 at page 310, middle panel in [28]). Hence there are always three or one fixed points when the output is sigmoidal. When there are three fixed points, two of them are stable. When the initial input is high, the firing rate will become stable at a point with a positive firing rate. Otherwise, it becomes silent. To make sure that the network operates at a low but positive firing rate region, we need a strong excitatory input (see Fig. 4.17 bottom panel). A strong excitatory input implies a high frequency of stable point (see Fig. 4.17, bottom panel left with $r = 0$ and $r = 1$). To get a low frequency of stable firing then a significant inhibitory input is needed. In fact, from Fig. 4.17, we conclude that to obtain a stable, low firing rate the input-output relationship should be a skewed bell shape, rather than the usual sigmoidal function. When $r = 1$, we see that the output firing rate is an increasing function of input firing rate and hence the input-output relationship is still sigmoidal. To have a skewed bell shape input-output relationship requires $r > 1$ since the output firing rate is no longer an increasing function of the input firing rate. For a bell shape input-output function, we know that there might be two fixed points and the positive fixed point could be stable. Of course, a bell shaped input-output relationship possibly leads to a more complicated dynamics such as limit cycle or chaotic activity.

Furthermore, with a larger $p^{(k)}$ (for example, $p^{(k)} > 250$ in Fig. 4.17), we can have a wider encoding and decoding region. When $p^{(k)} = 200$, the output firing rate is either greater than 40Hz or silent, but when $p^{(k)} > 250$, the output firing rate is continuous. We have also tested our results for extreme parameters for example $V_{thre} = 10$ [39] and with refractory periods. Our conclusions all remain true (not shown).

In the literature, the exactly balanced spiking neuronal network assumption is widely accepted (see for example [55, 59, 39]). However, with biolog-

ically reasonable parameters [55], we found that a feedforward spiking neuronal network can not maintain a low frequency spontaneous activity. Hence a *much* strong inhibitory input is needed. It is recently estimated that the magnitude of IPSP is around fives times larger than EPSP, i.e. $b/a = 5$ (see also [28] page 239).

Finally we have to emphasize here that all results are obtained for homogeneous networks.

Due to the space limit we will present our detailed results in the full paper [24].

4.7 Conclusion

In the current paper, we first presented some examples to show the importance of high order statistics in neuronal computations. The examples include simple input and output surfaces, optimal control models, noise reductions and storage capacity. Moment neuronal networks (first order statistics and second order statistics) are developed and some simple applications are included.

Our approach is reminiscent of the hydrodynamics limit in dealing with fluid dynamics, where the Navier-Stokes equation is the ultimate description of fluid dynamics. Of course, our development is more complex than the derivation of the Navier-Stokes equation where only the first order statistics is considered.

Acknowledgement. Partially supported by grants from UK EPSRC(GR/R54569), (GR/S20574), and (GR/S30443).

References

1. Abbott L.F., and Dayan P. (1999), The effect of correlated variability on the accuracy of a population code *Neural Comput* **11**: 91-101.
2. L. F. Abbott and C. van Vreeswijk (1993), Asychronous states in networks of pulse-coupled oscillators *Phys. Rev. E,* **48**: 1483-1490.
3. Abbott L.F., Varela J.A., Sen K., and Nelson S.B.(1997). Synaptic depression and cortical gain control, *Science* **275**, 220-223.
4. D. J. Amit and M. V. Tsodyks (1991), Quantitative study of attractor neural networks retrieving at low spike rates *Network*, **2**: 259-274.

5. D. J. Amit and N. Brunel (1997),Model of global spontaneous activity and local structured activity during delay periods in the cerebral cortex *Cerebral Cortex*, **7**: 237-252.
6. Barlow H. (2001) Redundancy reduction revisited *Network-Comp Neural* **12**: 241-253.
7. Bell, A.J. and Sejnowski, T.J. (1995): An information maximization algorithm that performs blind separation. *Advances in Neural Information Processing Systems* 7:456-474 (MIT Press)
8. Bezzi M., Diamond M.E., and Treves A. (2002) Reduncancy and synergy arising from pariwise correlations in neuronal ensembles *J. Computational Neurosci.* **12** 165-174.
9. Britten K.H., Shadlen M.N., Newsome, W.T., Celebrini S., and Movshon J.A. (1992). The analysis of visual motion: a comparison of neuronal and psychophysical performance. *J. Neurosci.* **12** 4745-4765.
10. Brown D., Feng J., and Feerick, S. (1999) Variability of firing of Hodgkin-Huxley and FitzHugh-Nagumo neurons with stochastic synaptic input. *Phys. Rev. Letts.* **82**, 4731-4734.
11. N. Brunel (2000), Dynamics of sparsely connected networks of excitatory and inhibitory spiking neurons *J. Comput. Neurosci.,* **8**: 183-208.
12. N. Brunel and F. Chance and N. Fourcaud and L. Abbott (2001), Effects of synaptic noise and filtering on the frequency response of spiking neurons *Phys. Rev. Lett.,* **86**: 2186-2189.
13. N. Brunel and V. Hakim (1999), Fast global oscillations in networks of integrate-and-fire neurons with low firing rates *Neural Computation,* **11**: 1621-1671.
14. Deng YC, Williams P, Liu F, et al. (2003) Neuronal discrimination capacity *J PHYS A-MATH GEN* **36**, 12379-12398.
15. Destexhe A., Rudolph M., Fellous J.M., and Sejnowski T.J. (2001) Fluctuating synaptic conductances recreate in-vivo-like activity in neocortical neurons *Neuroscience* **107**: 13-24.
16. Fairhall AL, Lewen GD, Bialek W, et al (2002). Efficiency and ambiguity in an adaptive neural code *Nature* **412**: 787-792.
17. Feng J.F., (2002) Coorelated Neuronal Computation *Unsolved Problems Of Noise and Fluctuations In Physics, Biology and High Technology*, AIP conference proceedings, S.M. Bezrukov (ed.), 208-215.
18. Feng, J.(1997), Behaviours of spike output jitter in the integrate-and-fire model. *Phys. Rev. Lett.* **79** 4505-4508.
19. Feng J. (2001) Is the integrate-and-fire model good enough? –a review *Neural Networks* **14** 955-975.
20. Feng JF, Li GB(2001) Integrate-and-fire and Hodgkin-Huxley models with current inputs *J PHYS A-MATH GEN* **34** (8): 1649-1664.
21. Feng J., Liu F. (2002)A modelling study on discrimination tasks, *Biosystems* **67** 67-73.
22. Feng, J., and Tirozzi B. (2000) Stochastic resonance tuned by correlations in neuronal models. *Phys. Rev. E.* **61**, 4207-4211.
23. Feng JF, Zhang P(2001) Behavior of integrate-and-fire and Hodgkin-Huxley models with correlated inputs *PHYS REV E* **63** 051902.
24. Feng JF, Deng YC, and Rossoni E.(2006) Dynamics of moment neuronal networks *Phys Rre E* (in press).
25. Gammaitoni L., Hänggi P., Jung P. and Marchesoni F. (1998) Stochastic resonance *Reviews of Modern Physics* **70** 224-287.

26. Gaillared B. (2002) *Moving dots discrimination* Master Thesis, Sussex University.
27. W. Gerstner (2000), Population dynamics of spiking neurons: Fast transients, asynchronous states, and locking *Neural Computation* **12**: 43-89.
28. Gerstner W., and Kistler W. (2002) *Spiking Neuron Models: Single Neurons, Populations, Plasticity* Cambridge University Press: Cambridge, UK.
29. Goldman MS, Maldonado P, Abbott LF(2002) Redundancy reduction and sustained firing with stochastic depressing synapses, *J Neurosci.* **22**: 584-591.
30. Gray C.M., Koenig P., Engel A.K., and Singer W. (1989) Oscillatory responses in cat visual cortex exhibit inter-columnar synchronization which reflects global stimulus properties *Nature* **338**: 334-337.
31. Hyvärinen, A., Karhunen, J. and Oja, E. (2001): *Independent Component Analysis* (Wiley)
32. Hyvärinen, A. and Hoyer, P.O. (2000): Emergence of phase- and shift- invariant features by decomposition of natural images into independent feature subspaces. *Neural Computation* 12:1705-1720 23
33. Hyvärinen, A. and Oja, E. (1997): A fast fixed-point algorithm for independent component analysis. *Neural Computation* 9,7:1483-1492
34. Kast B. (2001) Decisions, decisions ... *Nature* **411** 126-128.
35. Kreiter A.K., Singer W. (1996) Stimulus-dependent synchronizaiton of neuronal responses in the visual cortes of the awake macaque monkey *J. Neurosci* **16**: 2381-2396.
36. Laughlin S.B. (1981) Laughlin S.B. (1981) A simple coding rpocedure enhances a neuron's information capacity, *Z. Naturforsch* **36c**: 910-912.
37. Leadbetter M.R., Lindgren, G, and Rootzén H. (1983), *Extremes and Related Properties of Random Sequences and Processes*, Springer-Verlag, New York.
38. Leng G. et al. (2001) Responses of magnocellular neurons to osmotic stimulation involves co-activation of excitatory and inhibitory input: an experimental and theoretical analysis *J. Neurosci.* **21** 6967-6977.
39. Litvak V., Sompolinsky H., Segev I., and Abeles M. (2003), On the transmission of rate code in long feedforward networks with excitatory-inhibitory balance*J. Neurosci.* 3006-3015.
40. Longtin, A., Moss, F., and Bulsara, A. (1991) Time interval sequences in bistable systems and noise induced transmission of neural information. *Phys. Rev. Lett.* **67**, 656-659.
41. M. Mattia and P. Del Giudice (2002),Population dynamics of interacting spiking neurons *Phys. Rev. E*, **66**: 051917.
42. D. Q. Nykamp and D. Tranchina (2000), A population density approach that facilitates large-scale modeling of neural networks: Analysis and an application to orientation tuning*J. Comp. Neurosci.,* **8:** 19-30.
43. Olshausen, B.A. and Field, D.J. (1997): Sparse coding with an overcomplete basis set: A strategy employed by V1? *Vision Research* 37:3311-3325
44. Parker A.J., and Newsome W.T. (1998) Sense and the single neuron: probing the physiology of perception *Annu. Rev. Neurosci.* **21** 227-277.
45. Rudolph M., and Destexhe A. (2001) Do neocortical pyramidal neurons display stochastic resonance? *Journal of Computational Neuroscience* **11**: 19-42.
46. Rudolph M., and Destexhe A. (2001) Correlation detection and resonance in neural systems with distributed noise sources, *Physical Review Letters* **86**: 3662-3665.

47. Petersen,R.S., Panzeri,S., and Diamond,M.E. (2001). Population coding of stimulus location in rat somatosensory cortex. *Neuron* **32**, 503-514.
48. Petersen,R.S., Panzeri,S., and Diamond,M.E. (2002a). Population coding in somatosensory cortex. *Curr Opin Neurobiol.* In press.
49. Rieke, F., Warland, D., de Ruyter van Steveninck, R., and Bialek W. (1997) *Spikes*. The MIT Press.
50. Romo R., and Salinas E.(2001) Touch and go: decision mechanisms in somatosensation. *Annu Rev. Neurosci.* **24** 107-137.
51. Sompolinsky H., Yoon H., Kang K.J., et al (2001). Population coding in neuronal systems with correlated noise *Phys Rev E* **64**: 051904.
52. Stevens CF, and Zador AM(1998) Input synchrony and the irregular firing of cortical neurons *Nat Neurosci* **1**: 210-217.
53. Salinas E, Sejnowski TJ (2001), Correlated neuronal activity and the flow of neural information *Nat Rev Neurosci* **2**: 539-550
54. Salinas E., and Sejnowski T.J. (2000) Impact of correlated synaptic input on output firing rate and variability in simple neuronal models *J Neurosci.* **20**: 6193-6209.
55. Shadlen M.N., and Newsome W.T.(1994). Noise, neural codes and cortical organization, *Curr. Opin. Neurobiol.* **4**, 569-579.
56. Shadlen M.N, and Newsome W.T. (1996) Motion perception: seeing and deciding *PNAS* **93** 628-633.
57. Tuckwell H. C. (1988), *Introduction to Theoretical Neurobiology* Vol 2, Cambridge University Press.
58. van Vereeswijk C., Abbott L.F., and Ermentrout G.B. (1994), When inhibition not excitation synchronizes neural firing. *Jour. Computat. Neurosci.* **1** 313-321.
59. van Vreeswijk C, and Sompolinsky H (1996) Chaos in neuronal networks with balanced excitatory and inhibitory activity *Science* **274** (5293): 1724-1726.
60. Nicol, A., Feng, J. and Kendrick, K. (in preparation): Negative Correlation Yields Computational Vigour in a Mammalian Sensory System.
61. The programs are available at http://www.cogs.susx.ac.uk/users/jianfeng/publications, and we thank to Nicolas Brunel for providing us the matlab code.
62. Gaussel N., Legra, J. (1999) *Black-Sholes... What's next?*, Quants no 35.
63. Dupuis P., Kushner, H. J. (2002) *Stochastic Control Problems in Mobile Communications*, USA gov. rep. no. A071214.
64. Harris CM, Wolpert DM, (1998)Signal-dependent noise determines motor planning *Nature***394**: 780-784.
65. Kistler W., Gerstner W., and van Hemmen J.L. (1997), Reduction of the Hodgkin-Huxley equations to a single-variable threshold model *Neural Computation*, **9**, 1069-1110.
66. Oksendal B. (1989) *Stochastic Differential Equations* (second edition), Springer-Verlag: Berlin.
67. A. Renart et. al. (2003), Ch. 15, in *Computainal Neuroscience* Feng J.F. (ed.). Shadlen M.N., and Newsome W.T.(1994). *Curr. Opin. Neurobiol.* **4**: 569. Livak V. et. al. (2003), *J. Neurosci.* 3006. Leng G. et. al. (2002) *J. Neurosci.* **21**: 6967. Matthews, P.B.C. (1996) *J. Physiology* **492**: 597.
68. Due to the difficulty to plot three dimensional figures, we will simply consider two dimensional case. However, it is readily seen that all conclusions below are true for movements in three dimensional space.

69. Note that we do not want to fit our results with experimental data (such a fitting would be straightforward), but intend to present a general theory. All quantities are unitless.
70. Fitts, P.M. (1954) *J. Experimental Psychology* **47**: 381.
71. *Computational Neuroscience: A Comprehensive Approach* Feng J.F. (ed.) Chapman and Hall/CRC Press: London, UK.
72. Morasso P.G., Sangujineti V. (2003) Ch. 17 in *Computational Neuroscience: A Comprehensive Approach* Feng J.F. (ed.) Chapman and Hall/CRC Press: London, UK.
73. Korman M et al. (2003) *P Natl Acad Sci USA* 100 (21): 12492. Richardson MJE, Flash T (2002) *J Neurosci* **22**: 8201. Vetter P et. al. (2002) *Curr Biol* **12**: 488. Feng J.F. et. al. (2003), *J. Phys. A.* **36**: 7469. Feng J.F. et. al. (2002) *J. Phys. A* **35**: 7287.
74. Fleming W.H., and Rishel R.W. (1975), *Deterministic and Stochastic Optimal Control*, Springer-Verlag: New York. Bensoussan A. (1992) *Stochastic Control of Partially Observable Systems*, Cambridge Univ. Press: Cambridge, UK.
75. Csete M.E., and Doyle J.(2002), *Science*, **295**: 1664. Todorov E. (2002), *Neural Comput* **14**: 1233.
76. Joshi P., and Maass W. (2003) Movement generation and control with generic neural microcircuits (submitted). Kawato M. (1999). *Current Opinion in Neurobiology* **9**: 718.
77. Usrey W.M., and Reid R.C. (1999) Synchronous activity in the visual system *Annu Rev. Physiol.* **61**: 435-456.
78. Zohary E., and Shadlen M.N., and Newsome W.T. (1994) Correlated neuronal discharge rate and its implications for psychophysical performance *Nature* **370** 140-143.

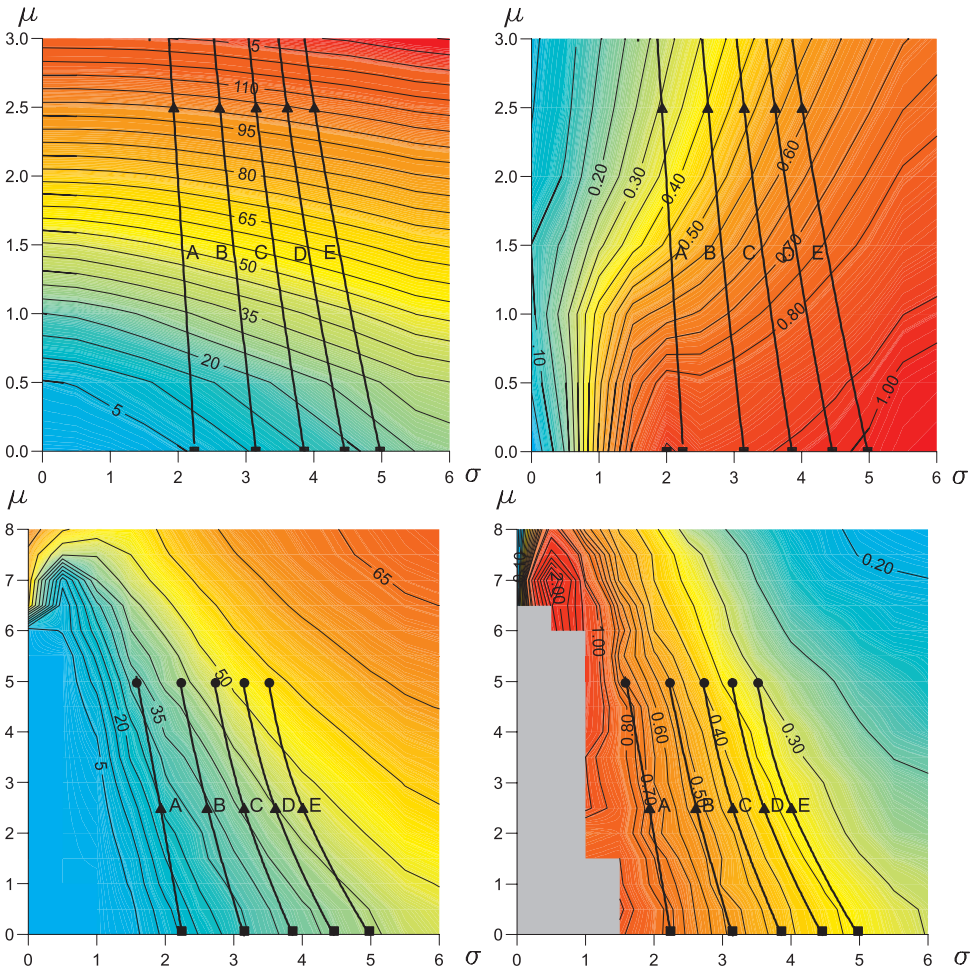

Fig. 4.1. Top panel: the response surface of the integrate-and-fire model, left, contour of the output firing rate, right, contour of the CV. Bottom panel: the response surface of the Hodgkin-Huxley model, left, contour of the output firing rate, right, contour of the CV. We refer the reader to [23] for details of simulations.

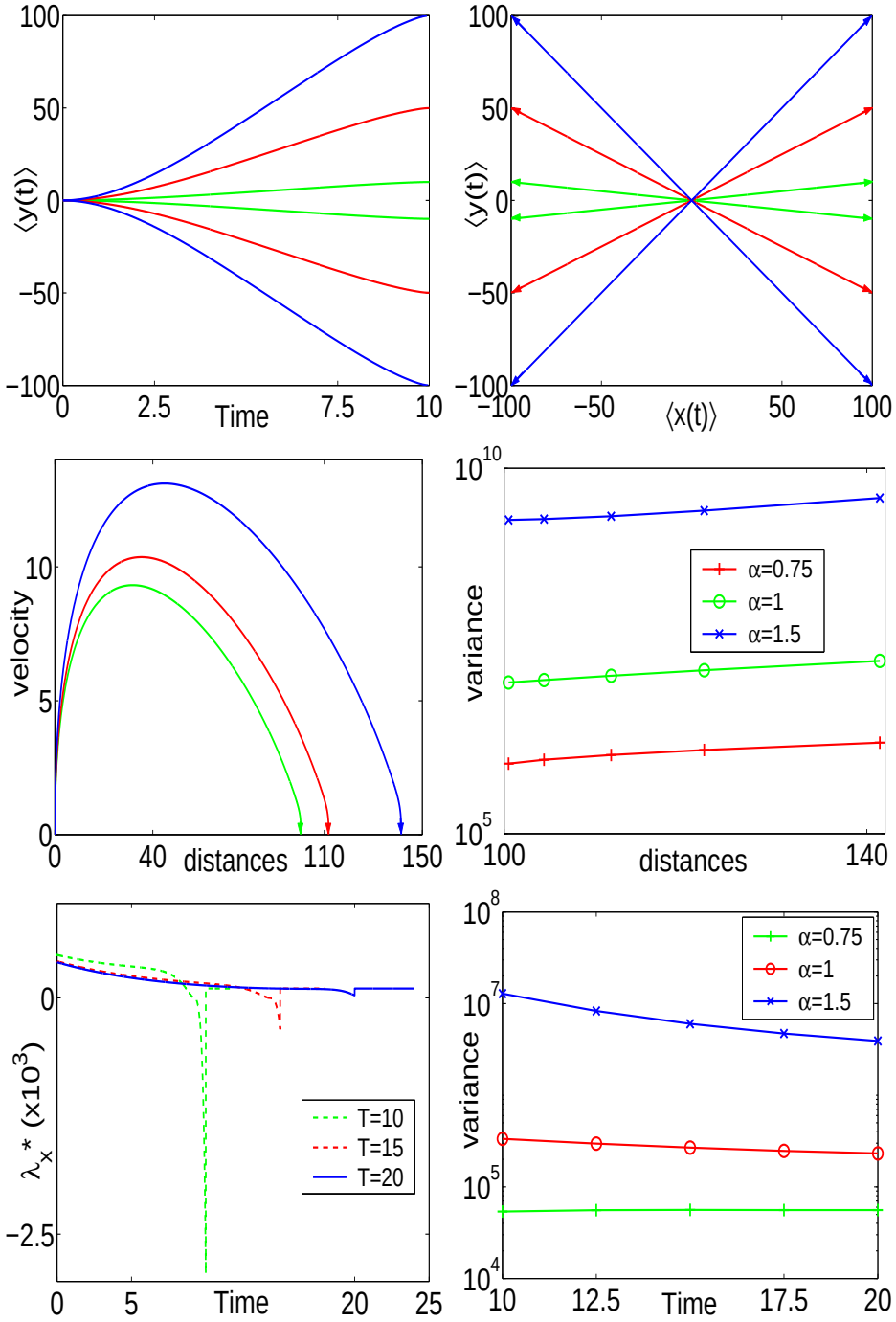

Fig. 4.2. Upper left, $\langle y(t)\rangle$ vs. t with $d_y = 10$ (green),50 (red) and 100 (blue). Upper right, $(\langle y(t)\rangle, \langle x(t)\rangle)$ for $t \in [0,T]$ with $T = 10, \alpha = 0.75$. It is easily seen that the trajectory is a straight line. Middle left, velocity $(\langle \dot{x}(t)\rangle\langle x(t)\rangle + \langle \dot{y}(t)\rangle\langle y(t)\rangle)/\sqrt{(\langle x(t)\rangle)^2 + (\langle y(t)\rangle)^2}$ vs. distance $\sqrt{(\langle x(t)\rangle)^2 + (\langle y(t)\rangle)^2}$ with $\alpha = 0.75, T = 20$. Middle right the optimal variance $I_x(\lambda_x^*) + I_y(\lambda_y^*)$ vs. distance with $T = 20$. Bottom left, λ_x^* vs. time t for fixed $d_x = d_y = 100$ with $\alpha = 0.75$. Bottom right the optimal variance $I_x(\lambda_x^*) + I_y(\lambda_y^*)$ vs. time T with $d_x = d_y = 10$.

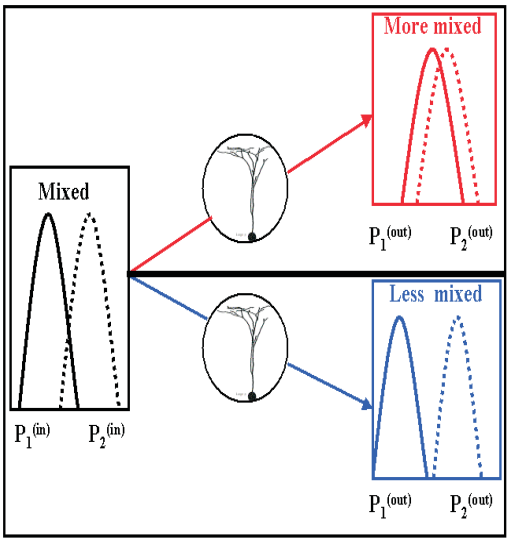

Fig. 4.3. For two possibly mixed input signals, after neuronal transformation, will they become more separated or mixed?

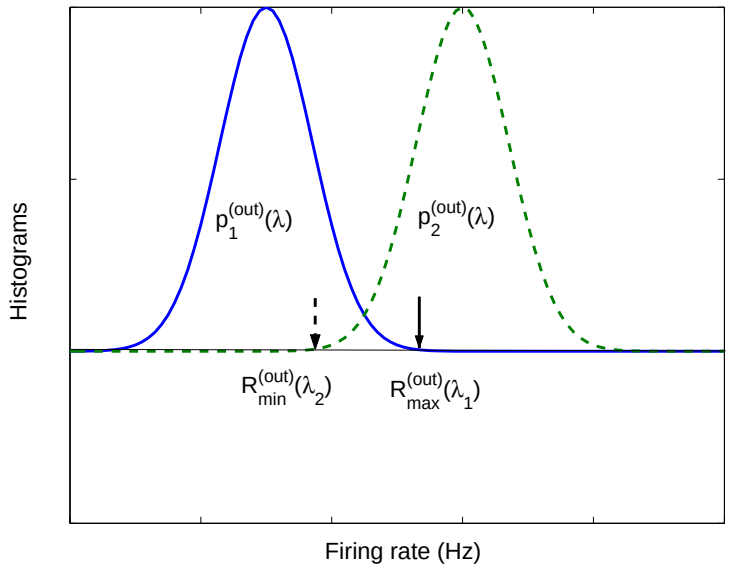

Fig. 4.4. A schematic plot of two output histograms, $R_{\min}^{(out)}(\lambda_2)$ and $R_{\max}^{(out)}(\lambda^{(1)})$. As soon as $R_{\min}^{(out)}(\lambda_2) - R_{\max}^{(out)}(\lambda^{(1)}) > 0$, the two histograms are separable.

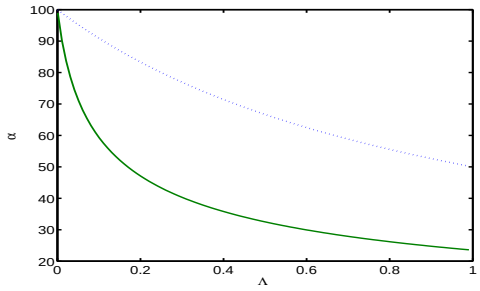

Fig. 4.5. α vs. Λ for $c = 0, r = 0$ (dotted line, independent of r according to Theorem 1) and $c = 0.1, r = 1$ (solid line).

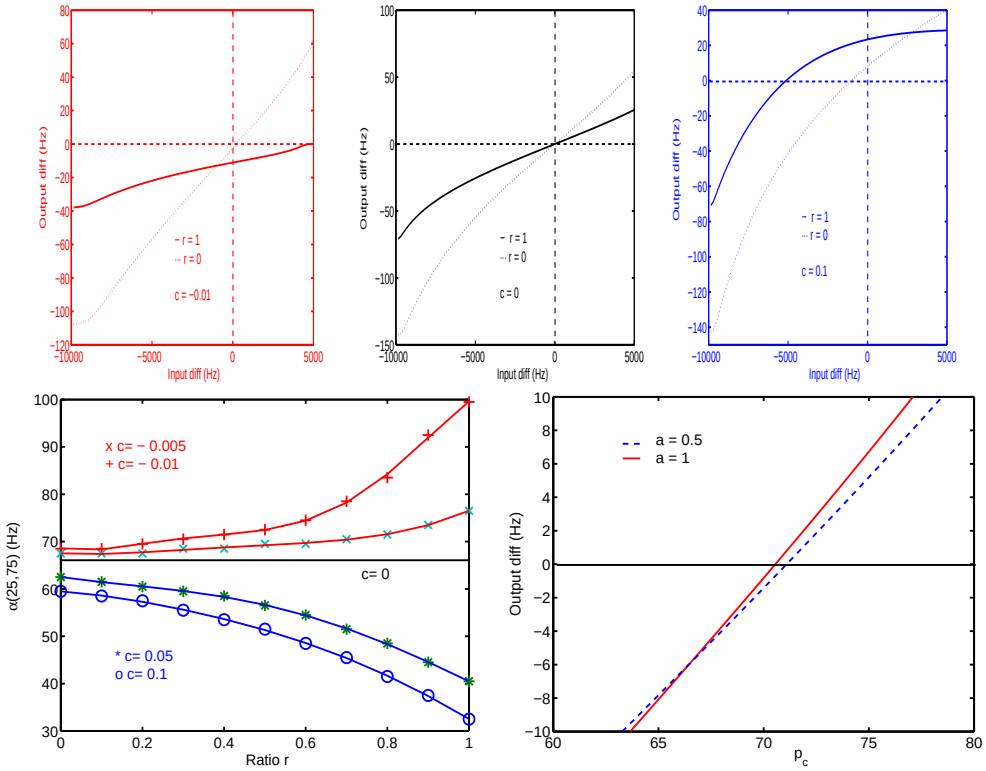

Fig. 4.6. Upper panel, input difference $R^{(in)}_{\min}(\lambda^{(2)}) - R^{(in)}_{\max}(\lambda^{(1)})$ and output difference $R^{(out)}_{\min}(\lambda^{(2)}) - R^{(out)}_{\max}(\lambda^{(1)})$ for $c < 0$ (left), $c = 0$ (middle) and $c > 0$ (right). Output firing rates are equal to $1000/(\langle T^{(k)} \rangle + T_{ref})$ with $T_{ref} = 5$ msec. Bottom panel (left), numerical values are obtained by directly solving Eq. (4.24). Bottom panel (right), the dependence of the discrimination capacity on a with $r = 0.4, c = -0.01$.

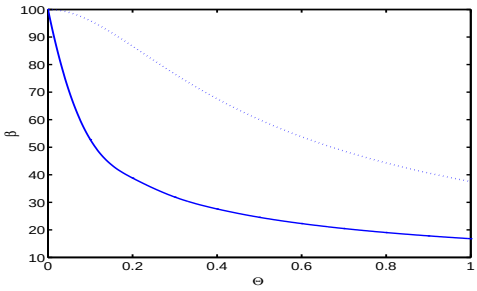

Fig. 4.7. β vs. Θ for $c = 0, r = 0$ (dotted line, independent of r according to Theorem 3) and $c = 0.1, r = 1$ (solid line) with $m = 100$.

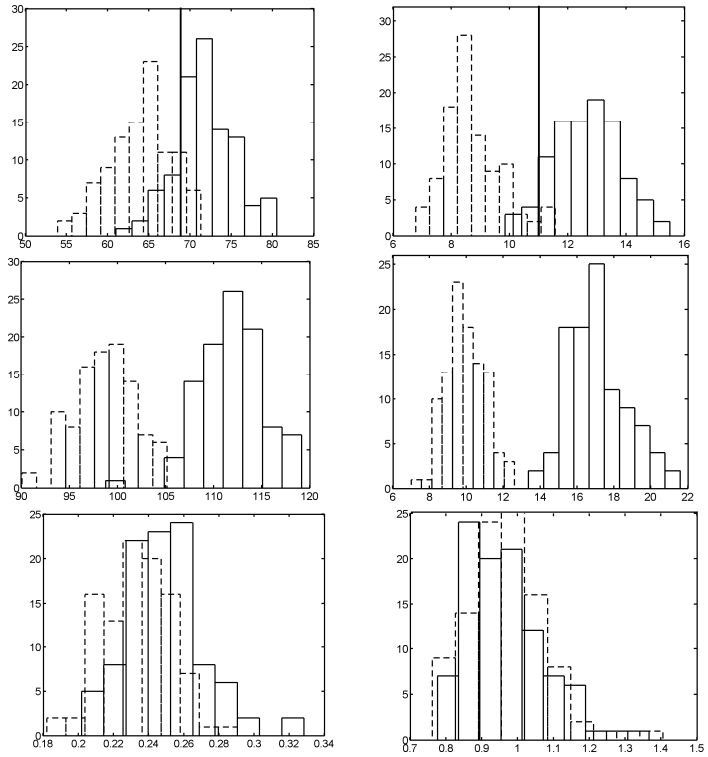

Fig. 4.8. Upper and middle panel, histogram of firing rates (Hz) with $c = 0.1$ for the IF model. Left, exclusively excitatory inputs $r = 0$. Right, $r = 0.95$. Upper panel: $p_c = 15$. The minimum TPM is calculated according to the thick vertical lines (the optimal discrimination line). Middle panel: $p_c = 25$. Bottom panel: histograms of coefficient of variation (CV) for $p_c = 25$ and left with $r = 0$, right with $r = 0.95$, corresponding to middle panel.

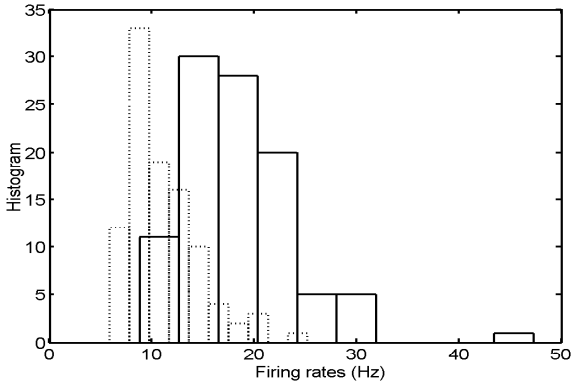

Fig. 4.9. Histogram of firing rates (Hz) with $c = 0.1$ for the IF model, with identical parameters as in Fig. 4.8, bottom panel (right), but only 10 spikes are used for estimating mean firing rates.

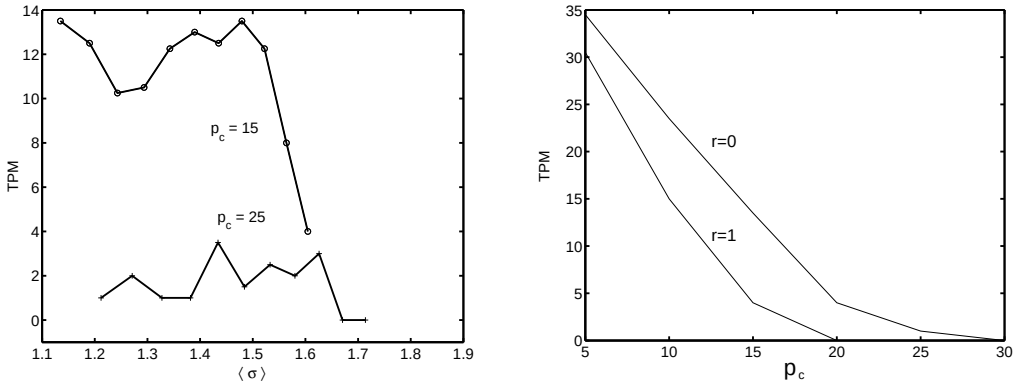

Fig. 4.10. TPM % vs. $\langle\sigma\rangle = \sqrt{a^2(1+r)\lambda^{(1)}p_c(1+c(p_c-1)) + a^2(1+r)\sum_{i=p_c+1}^{p}\langle\lambda_i\rangle}$ with $\langle\lambda_i\rangle = 50$ Hz (left) and TPM vs. p_c (right) for the IF model, $r \in [0,1], c = 0.1, \lambda^{(1)} = 25$Hz. When $p_c = 15$ (left), it is clearly shown that TPM attains its optimal value at $r = 1$, i.e. the larger the noise, the better the discrimination (see the right figure as well). All other parameters are the same as in subsection 4.4.4.

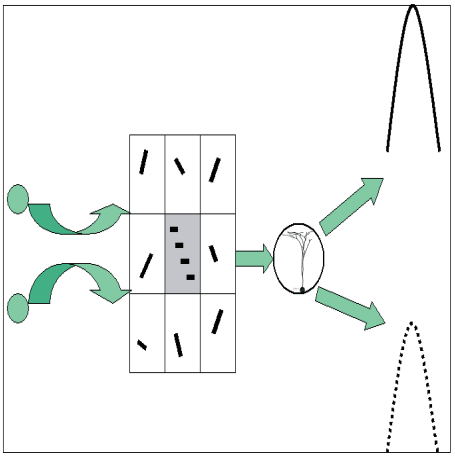

Fig. 4.11. Correlations between coherent signals can be naturally introduced via neuronal pathways.

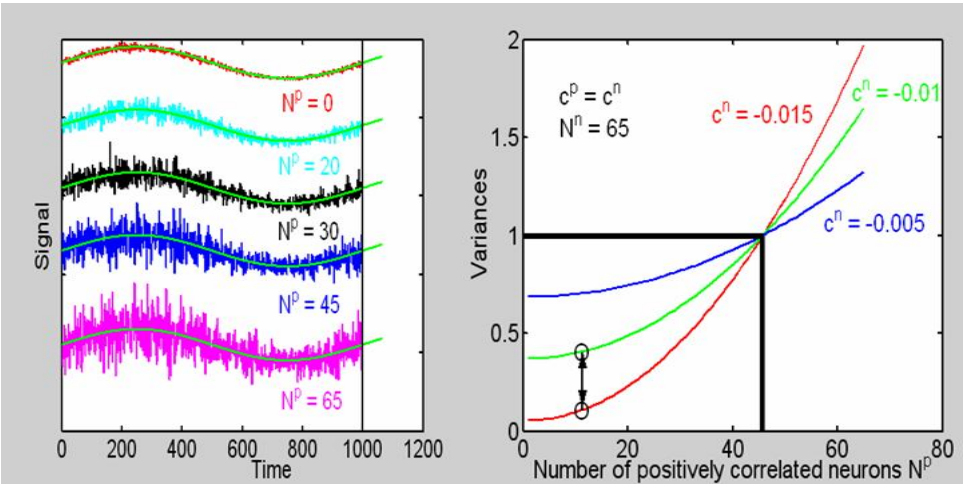

Fig. 4.12. Left, green lines are the true signals, jagged lines are averaged signals with various correlation levels as indicated in the figure. It is easily seen that an almost perfect signal is obtained when the neuron is negatively correlated with a correlation coefficient of -0.015. Right, theoretically calculated variance vs. number of positively correlated neurons N^p. Curves in the left figure correspond to marked points of the red curve. For example, when $N^p = 0$, it is the lowest point of the red curve, $N^p = 45$ is the point where two thick black lines meet. From our experimental data, if we assume that there are 10 neurons are positively correlated (indicated by circles), i.e. there are 100 positive correlations, the improvement of signal to noise ratio is considerably significant.

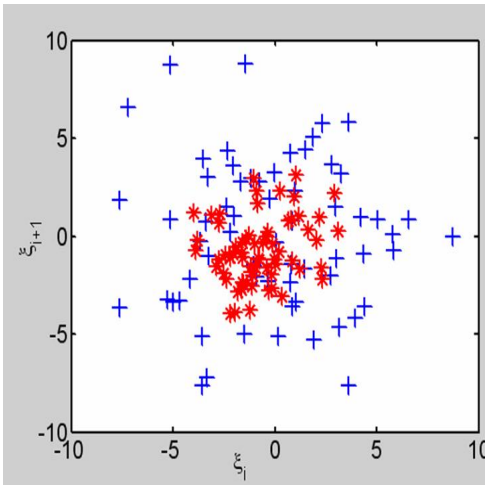

Fig. 4.13. Returning map of 65 random numbers, $(\xi_i, \xi_{i+1})i = 1, 2, \cdots, 64$.'+' is points with a negative correlation of -0.015, and '*' is random numbers with a positive correlation of .8.

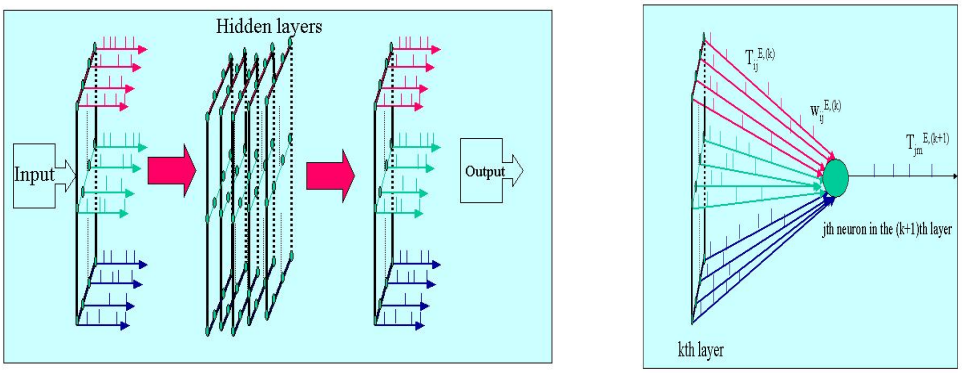

Fig. 4.14. Schematic plot of a feedforward spiking network (left). Right, a single neuron in the (k+1) layer receives inputs from the ith layer with weights (EPSP size) $w_{ij}^{E,(k)}, i = 1, \cdots, p^{(k)}, j = 1, \cdots, p^{(k+1)}, k = 1, 2, \cdots$.

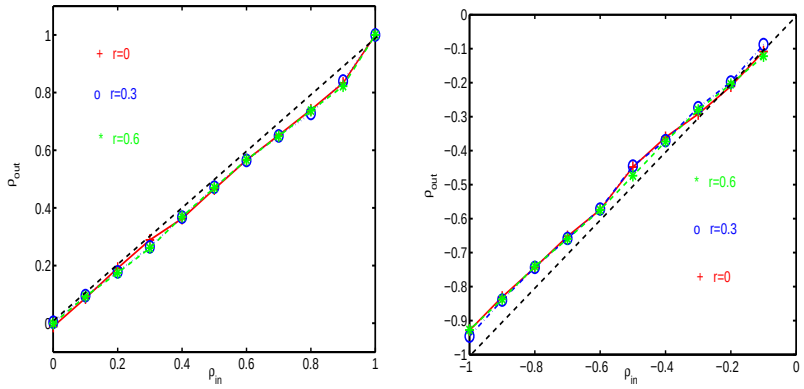

Fig. 4.15. Left, the curve of ρ_{out} vs. ρ_{in} for $r = 0$ (+), $r = 0.3$ (o) and $r = 0.6$ (*) with 5000 interspike intervals. The relationship between the input correlation coefficient and the output correlation coefficient is almost linear and independent of r. Right, ρ_{out} vs. $\rho_{in} \leq 0$. Each point is obtained with 5,000 spikes.

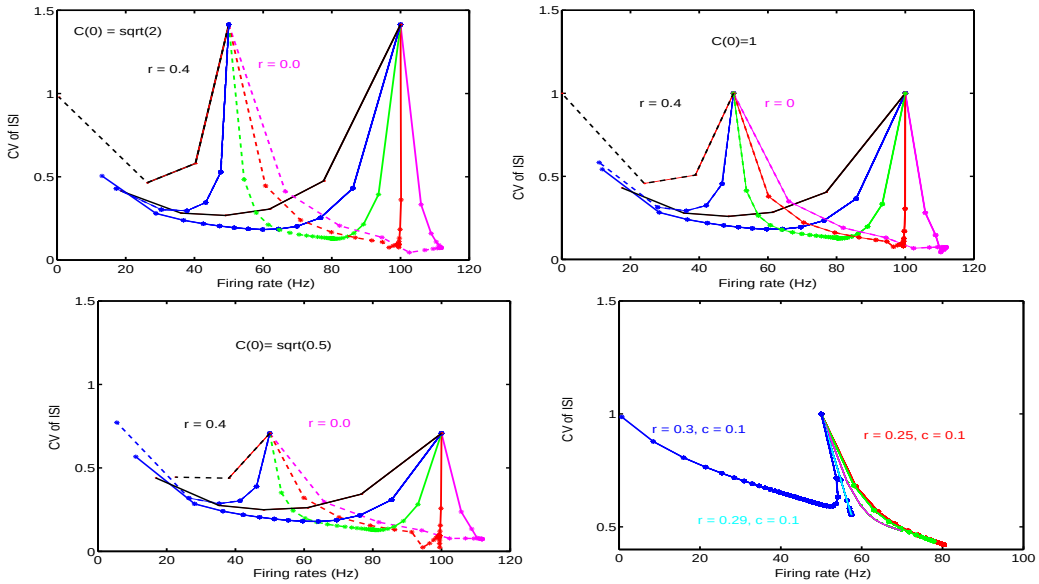

Fig. 4.16. Upper panel and bottom (left) $p^{(k)} = 100, \rho_{ij} = 0.$ with $C_1^{(1)} = \sqrt{0.5}, 1, \sqrt{2}$ and $\mu_1^{(1)} = 100$ Hz (solid lines), 50 Hz (dashed lines). When $r \geq 0.3$, the neuron becomes silent (simulations stop when $\langle T \rangle$ is too large). Bottom panel (right) with $r = 0.25, 0.26, 0.27, 0.29, 0.3$, $\rho_{ij}^{(k)} = 0.1$ and $C_i^{(1)} = 1, \mu_i^{(1)} = 50$ Hz.

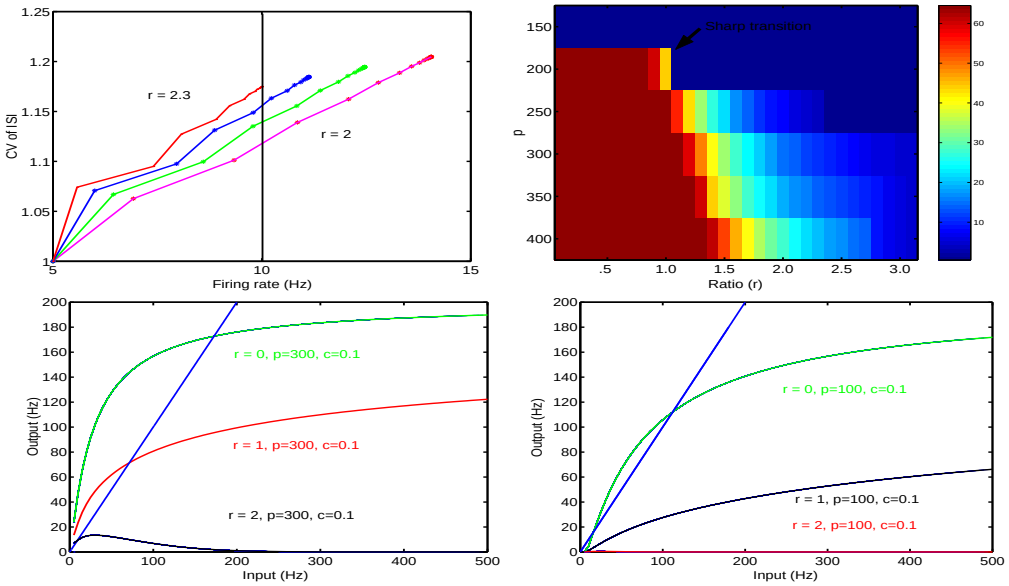

Fig. 4.17. Upper panel, left, $(\mu_i^{(k)}, C_i^{(k)})$ for $k = 1, 2, \cdots$ with $\mu_i^{(1)} = 5$Hz, $C_i^{(i)} = 1$ and $p^{(k)} = 300, \rho_{ij} = 0.1, r = 2., 2.1, 2.2, 2.3$. Upper panel, right, output firing rate (Hz) indicated by color bar with $\mu_i^{(1)} = 5$ Hz and $C_i^{(1)} = 1$. Bottom panel, input-output relationship for $p^{(k)} = 300$ and $p^{(k)} = 100$.

5

Neuronal Model of Decision Making

Benoit Gaillard, Jianfeng Feng, Hilary Buxton

Summary. We have built a neuronal model of decision making. Our model performs a decision based on an imperfect discrimination between highly mixed stimuli, and expresses it with a saccadic eye movement, like real living beings. We use populations of Integrate-and-Fire neurons.

In order to take a decision that depends on imperfectly separated stimuli, we use a model inspired by the principle of accumulation of evidence. More precisely, this accumulation of evidence is performed by a competition between groups of neurons that model a visual column in the Lateral IntraParietal area (area LIP) of the brain. In this column, we have groups of neurons that are sensitive to specific stimuli on which the decision is based. They inhibit each other through groups of inhibitory neurons. Simultaneously, they recursively excite themselves through recurrent synaptic excitation, and all the neurons receive a steady low level excitation from the rest of the brain. The competition is generated by these reccurent inhibitory and excitatory loops. We study this structure within the framework of dynamical systems. The variables we use are the activities of each group of neurons. This dynamical system has several stable states: one of them occurs when all activities are weak, and other ones when one local group of neurons has a higher activity and dominates the others through lateral inhibition. The convergence to one of these stable states models decision making, guided by sensory evidence: The group of neurons sensitive to the specific stimulus has a comparative advantage on the others during the competition. This structure is not a new idea, but we use it to test our hypothesis on the way the brain controls the dynamics of decision making. Our hypothesis is that the statistical signature of the low level activity of the brain modifies the stability of the attractors of our model, and thus changes the dynamics of the competition that models decision making.

The criterium by which we judge that a decision is taken is more realistic than just looking at the decisive neurons' activities. We model a saccadic eye movement directed by the activities of our LIP neurons, and we read the decision from the position of the eye. This experimental set up is comparable to biophysical experiments

in which living beings express their decisions by saccadic eye movements.

The neurons of the LIP column in which the decisions take place are modelled as neurons in a real brain: besides the stimuli and the recurrent interactions, they receive significant inputs from the rest of the brain. It is well known that neurons in the brain are highly influenced by this activity, called low-level background activity.

We study how the dynamics of the decision making change as a function of the first order tatistics (mean) and second-order statistics (variance) of this global low-level background activity or noise. By studying its influence on Reaction Time and Error Rate, we show that this background activity may be used to control the dynamics of decision making. We compare the performance of such a model (Error Rate as a function of Reaction Time) to the performance of living beings during psychophysical experiments. By doing so, we assess the plausibility of the hypothesis that decisions be controlled by the statistical signature of the low level background activity of the brain.

5.1 Introduction

The study of the Reaction Time (RT) and Error Rate (ER) of animals and humans asked to perform simple two-choice perceptual discrimination task has a long history. One of the first approaches to model such decision processes was developed by psychologists and is known as the accumulation of evidence models. Typically, these models consider two variables that measure the quantity of evidence for each of the two decisions, and the first variable that reaches a decision boundary determines the decision. Those models were introduced by, for example Townsend and Ashby(1983) [17]. The diffusion model is often used to explain relations between RT, accuracy, error trials and clarity of the input. Thanks to successful neural recording during decision making (For example Shadlen and Gold (2004) [14], Platt and Glimcher (1999) [12]), experimental evidence confirmed that the diffusion model can account for the accumuluation of evidence, but also inspired more precise models of the neural dynamics involved. In particular, accumulation of evidence through neural competition has been modelled by Wang (2002), [20] and by Brunel (Amitt and Brunel, 1997, [1]). Glimcher [9] has made a review on stochastic decision making. According to Glimcher, who tested this claim by experimenting on monkeys, the tendency to make a choice is implemented in the FR of area LIP and the uncertainty about this decision could be implemented by what we call input noise in area LIP. However, decision making is also controlled by our context, our motivations, and our history. This idea has been addressed by Salinas, 2003 [13]. He uses, as well, background synaptic activity as a switch

between dynamical states in a network. We propose a model in which sensory inputs do not automatically trigger a decision. The decision making is dependent on the characteristics of the low level background neuronal activity of the brain. This background activity does not only control if a decision is taken, but controls the trade off between speed and accuracy as well: In urgent situations, we tend to take less accurate decisions.

We restrict ourselves to a very simple decision in the case of very simple and well studied sensory evidence set up. We use moving dots kinematograms as stimuli, and the model has to decide in which direction to move its eye, signifying if it thinks that the dots generally move downwards or upwards. This experimental set up has been extensively studied on alive monkeys and on humans by Newsome and colleagues ([2, 16, 15, 21]. Our moving dots kinematograms are composed of a hundred dots. A percentage of them move coherently in one direction. This percentage will be called Coherence in the rest of the article. The rest of them move randomly in any direction. In our experimetal set ups, they don't even have consistent directions. This set up is the same as in previous studies [3, 5, 6], and as in many of Newsome's experimental set ups.

We currently treat this stimuli in a very crude way. We suppose that the retina and the early parts of the visual system evaluate the direction of each dot during successive short time steps. Authors have argued for such a discretization of time in the visual system (VanRullen and Koch (2003) [19]). We suppose that each dot moving in a given direction triggers the activity of specific motion detectors. There are more detailed models that support this idea: It has been proved that in the visual system, we find columnns of neurons that detects specific directions of movement (Mountcastle, 1957, [11] Hubel and Wiesel, 1962, [10]). So we suppose that the first detailed neurons of our model receive a hundred different synaptic inputs, each of these inputs corresponding to the direction of one dot. These neurons are detectors of the global direction of the dots in the kinematogram: They react strongly to a given general direction and weakly to its opposite direction. To implement that, we set their synaptic input to be inversely proportional to the difference between their preferred direction and the direction of the corresponding dot.

These global direction detectors and the rest of the model will be described more precisely in the rest of the paper.

5.2 Model

5.2.1 Overview

Our model can be divided into three different parts, illustrated in Fig. 5.1. First we have the global direction detectors. They are made of populations of Integrate and Fire (IF) neurons whose Firing Rates (FR) depend on the global direction of the dots in the stimulus. They are a very simple generalisation of the model we studied in earlier publications [6, 7]. Using the ouptput of the direction detectors, we have our LIP decisive column. Internal recursive loops and global inputs from the brain determine the activities of the neurons in the column. Specific patterns of activity of this column can generate an eye mouvement. The generation of this eye movement is the third part of the model.

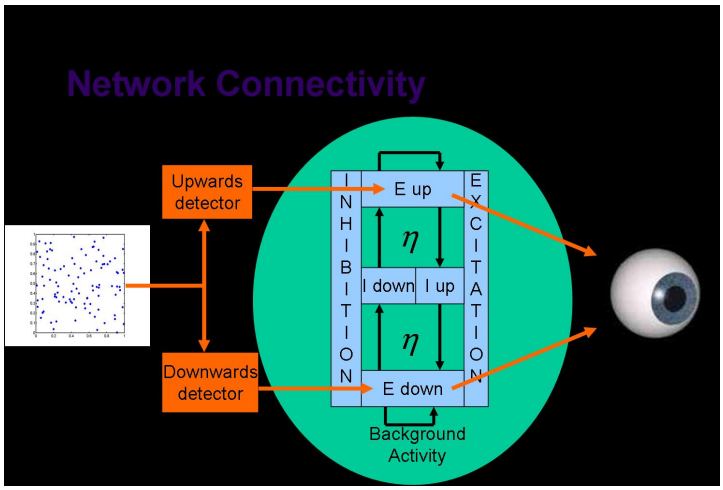

Fig. 5.1. The left panel represents the stimulus: Normaly all those dots are moving, most of them randomly. The middle panel is an illustration of the neuronal activities in the decision column of area LIP. In the middle panel, we see the low level background activity of the brain (represented by the green colour) that surrounds the column. All the represented subpopulations of neurons are connected to themselves and to each other, but the arrows represent hebbian learning potentiated connections. When the eye on the right has turned to one side, a decision has been taken.

The neuron model used here is the classical Leaky Integrate and Fire (IF) model [4, 8, 18]. The dynamics of the membrane potential below threshold are defined as follows:

$$dV = -\frac{1}{\tau}(V - V_{rest})dt + dI_{syn}(t) \tag{5.1}$$

where τ is the time constant of the neuron and the synaptic input is

$$I_{syn}(t) = \sum_{i=1}^{N_s} a_i E_i(t) \tag{5.2}$$

where $E_i(t)$ is the instantaneous frequency of incoming spikes to the i^{th} synapse, a_i is the positive or negative magnitudes of the EPSP and IPSP respectively, N_s the number of synapses. When the membrane potential reaches V_θ, the threshold potential, the neuron emits a spike and the potential is reset to V_{rest}. Then, the neuron goes through a refractory period τ_{ref} during which its membrane potential remains close to V_{rest}. We assume that large groups of incoming synapses receive the activity of large populations of neurons that have a similar activity, and that this activity is small. In that case, as shown by Tuckwell (1988) [18], we can use the diffusion appoximation. So we can rewrite equation 5.2 as:

$$I_{syn}(t) = J \sum_{i=1, w_i>0}^{N_g} w_i \nu_i(t) - J_{inh} \sum_{i=1, w_i<0}^{N_g} w_i \nu_i(t)$$

- N_g is the number of groups of similar incoming synapses to the neuron.
- w_i is the normalized synaptic weight. It is negative for inhibitory synapses.
- ν_i is the rate of the Poisson process coming to the synapses of the group i.
- J is the global excitatory synaptic strength.
- J_{inh} is the global inhibitory synaptic strength.

Then we reach the following expression for the output FR:

$$\nu_{out} = \left[\tau_{ref} + \tau \int_{\frac{V_{rest}-\mu}{\sigma}}^{\frac{V_\theta-\mu}{\sigma}} \phi(u)du \right]^{-1} \tag{5.3}$$

where

$$\phi(u) = \sqrt{\pi} e^{u^2} (1 + erf(u))$$

$$\mu = J \sum_{i=1}^{N_g} w_i \nu_i$$

$$\sigma^2 = J^2 \sum_{i=1}^{N_g} w_i^2 \nu_i + J^2 \sum_{i,j=1, i \neq j}^{N_g} c_{i,j} w_i w_j \sqrt{\nu_i \nu_j}$$

- $c_{i,j}$ is the correlation coefficient between synapse group i and synapse group j. We assume that the correlation coefficient between inhibitory and excitatory synapse is zero.
- The resting membrane potential: $V_{rest} = 0mV$.
- The threshold membrane potential: $V_\theta = 20mV$.
- τ_{ref} is the refractory period of the Leaky Integrate and Fire neuron.
- τ is the time constant of the Leaky Integrate and Fire Neuron.

5.2.2 Global Direction Detectors

The Global Direction Detectors are constituted of populations of Leaky Integrate and Fire Neurons described in the previous section. Each detector is made of a hundred of such neurons, that are not laterally connected, and that receive the same input. The discrimination of such a population is quicker and more accurate, as shown in previous publications (Gaillard et al., (2005, 2006) [6, 7]. We do not evaluate statistically the output FR of the neuron, as in eq. 5.3, but we simulate the production of spikes. For one time window t, the population produces N spikes, and the Firing Rate is $\frac{N}{100t}$.

The synaptic excitation is basically inversely proportional to the distance between the preferred angle of the group and the stimulus angle. Keeping the paradigm of one group of synapses for one dot, synaptic excitation for the upwards detector will be π for a dot moving upwards, 0 for a dot moving downwards, and $\frac{\pi}{2}$ for a dot moving horizontally.

$$\nu_i = k \, \|(\|Angle - Direction_i\| + \pi)[2\pi] - pi\|$$

ν_i is the incoming rate corresponding to i^{th}dot number. $Angle$ is the preferred direction of the detector. $Direction_i$ is the moving dot's direction. k is a normalizing parameter, so that the excitation stays in the range of rates

used in our experimental models. This equation is justified by the idea that the direction detector has more synaptic connections to the motion detector of its preferred direction. We assume as well that the incoming activity corresponding to dots having a coherent direction is correlated. n_c is the number of dots moving coherently, and c is the correlation coefficient. For simplicity,we assume that the detector's synaptic characteristics are as follows: the magnitude (a_i) of an EPSP is the exact opposite of the magnitude of an IPSP, and has the same absolute value for all synapses: a. r is the ratio between the number of excitatory and inhibitory synapses of the Direction Detector. Thus, as shown by Tuckwell (1988) [18], we can simplify Eq. 5.1 into:

$$dV = -\frac{1}{\tau}(V - Vrest)dt + \mu dt + \mathcal{N}\sigma\sqrt{dt}$$

where:

$$\mu = a\sum_{j=1}^{p}(1-r)\nu_j;$$

$$\sigma^2 = a^2\left[\sum_{j=1}^{p}(1+r)\nu_j + \sum_{i,j=1,i\neq j}^{n_c} c(1+r)\sqrt{\nu_i\nu_j}\right] \tag{5.4}$$

- r is the ratio between inhibitory synapses and excitatory synapses.
- $p = 100$ is the number of groups of synapses that receive inputs corresponding to the direction of one dot.
- $\nu(j)$ is the incoming rate corresponding to the direction of the j^{th} dot.
- The time constant of the neuron: $\tau = 20ms$.
- The time step for the integration: $dt = 0.01ms$.
- The correlation coefficient between inputs from dots that have a coherent motion: $c = 0.1$.
- The number of coherent inputs: $n_c \leq p$. Coherent inputs are dots that move consistently in one direction.
- The resting membrane potential: $V_{rest} = 0mV$.
- The threshold membrane potential: $V_{threshold} = 20mV$.

- $\mathcal{N}$ is a normally distributed random variable (mean 0, variance 1); in the formal IF model, $\mathcal{N}\sqrt{dt}$ is the standard Brownian motion.

Characteristics of this model

We previously studied this model (Gaillard et al., (2005, 2006) [6, 7]. We showed that the discrimination accuracy is better when the ratio r between excitatory and inhibitory inputs is closer to $r = 1$. We showed that the population coding reduces a lot the time needed to evaluate the Firing Rate, and increases the discrimination accuracy. The FR decreases with r. However, in order to obtain a reliable measure of the FR, we need to produce at least 100 spikes. Thus, in our model, in order to take decisions faster, we use $r = 0$.

The output FR of the is Direction Detector is used as the specific inputs of the competing groups of neurons in area LIP. These competing groups of neurons form the column that is described in the next subsection.

Fig. 5.2 shows that the mean FR increases linearly with the coherence, as assumed in Wang, 2002 [20]. the output of our detectors actually fits his assumption of a Gaussian distribution of rates very well. We used this approximation to measure the TPM in our previous paper.

5.2.3 LIP Column: Where the decision is taken

Column organisation

If we have p specific stimuli, then our column is described by $2p + 2$ subpopulations of neurons:

- p subpopulations of excitatory neurons specifically sensitive to the specific stimuli.
- one subpopulation of non specific excitatory neurons.
- one subpopulation of non specific inhibitory neurons.
- p subpopulations of specific inhibitory neurons. They are specifically connected to the specific excitatory neurons, and specifically inhibit populations of neurons.

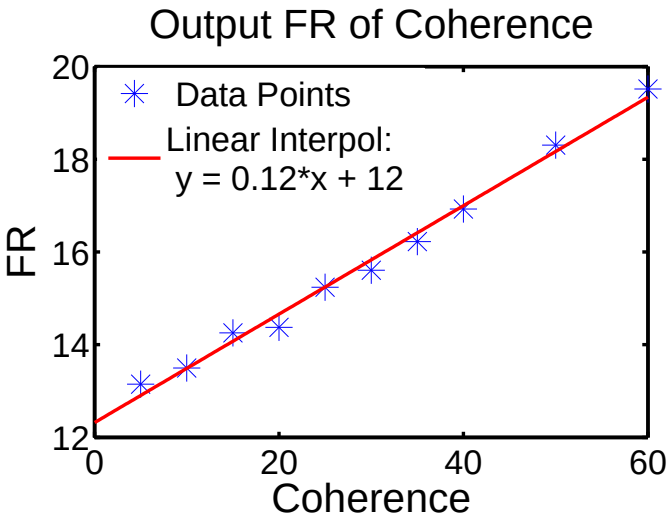

Fig. 5.2. The Firing Rate of a motion detector as a function of the coherence of the stimulus. The global direction of the stimulus is the preferred one of the detector. It is a linear relation.

The specific connections between neurons are modelled to have arisen through hebbian learning, η being the learning coefficient, or Long Term Potentiation coefficient. The rest of the synapses are depressed, in order to keep a normalized synaptic strentgh.

This leads us to the following parameters:

- $x(= 0.8)$:the fraction of local module synapses relatively to external input.
- $J(= 11)$: synaptic excitatory unstructured strength to one neuron.
- $C(= 1.01)$: inhibitory synaptic strength is slighty stronger than excitatory, this is a stability condition. (I have the formal proof of it in one dimension, Amit and Brunel(97) showed it as well).
- $\eta(= 9)$: learning coefficient;
- $f(= 0.01)$: proportion of neurons specifically sensitive to a specific stimulus.
- $p(= 2)$: number of specific stimuli.
- $f_i(= 0.1/p)$: proportion of inhibitory neurons specifically sensitive to subpopulation of excitatory neurons.

- $\eta^- = max(0, \frac{1-\eta\times f}{1-f})$: The synaptic depression.
- $C^- = max(0, \frac{C*(1-\eta\times f_i)}{1-f_i})$, Synaptic depression of inhibitory synapses to an excitatory neuron.
- ξ Standart deviation of the external background activity. This standart deviation varies spatially and temporally.
- $f_b(= 2/3)$: relative strentgh of the background activity in comparison to the whole external input.
- $f_1 = f_2 = ...f_p = \frac{1-f_b}{p}$: relative strentgh of each specific input in comparison to the whole external input.

The Learning rule is expressed as follows: Since neurons that are more sensitive to a specific stimulus will more often fire together, then their connextion will be strengthened. We express it : $J^+ = \eta\times J$, where J is the average unstructured synaptic strength. The rest of the synapses will be depressed, so that the mean synaptic strength remains J. Thus, in our case, we have: $\eta^- = max(0, \frac{1-\eta\times f}{1-f})$. We troncated the synaptic strength so that it can not be a negative strength, as seen in biology. We also suppose learning between inhibitory neurons. Our assumption is that some inhibitory neurons will show self organisation properties, strengthen their incoming synapses from subpopulations of excitatory neurons, and fire correlatively. This learning parameter will be the same, η and the synaptic depression will be similar.

We can concisely represent the structure of the column with the following matrix A. Each element $A_{i,j}$ of the matrix represents the strength of the influence of the neurons of group j on the neurons of group i. This is the synaptic strentgh of each synapse, multiplied by the number of synapses.

$$A = (M, N)$$

Where

$$M = \begin{pmatrix} xf\eta & xf\eta^- & -xf_iC^- & -xf_i\eta C & -x(1-pf_i)C & x(1-pf)\eta^- \\ xf\eta^- & xf\eta & -xf_i\eta C & -xf_iC^- & -x(1-pf_i)C & x(1-pf)\eta^- \\ xf\eta & xf\eta^- & -xf_iC & -xf_iC & -x(1-pf_i)C & x(1-pf)\eta^- \\ xf\eta^- & xf\eta & -xf_iC & -xf_iC & -x(1-pf_i)C & x(1-pf)\eta^- \\ xf & xf & -xf_iC & -xf_iC & -x(1-pf_i)C & x(1-pf) \\ xf & xf & -xf_iC & -xf_iC & -x(1-pf_i)C & x(1-pf) \end{pmatrix}$$

$$N = \begin{pmatrix} (1-x)f_b(1+\xi\mathcal{N}) & (1-x)f_1 & 0 \\ (1-x)f_b(1+\xi\mathcal{N}) & 0 & (1-x)f_2 \\ (1-x)f_b(1+\xi\mathcal{N}) & 0 & 0 \\ (1-x)f_b(1+\xi\mathcal{N}) & 0 & 0 \\ (1-x)f_b(1+\xi\mathcal{N}) & 0 & 0 \\ (1-x)f_b(1+\xi\mathcal{N}) & 0 & 0 \end{pmatrix}$$

System Equation

We use a discrete formalism. At each timestep, we reevaluate the variables of the system (Rates of the output poisson processes), as a function of their value at the previous timestep, and of the value of the contextual variables. The contextual variables are the external inputs: global activity of the brain, Direction Detectors activity.

$$\nu_{n+1}^{int} = F(\nu_n^{int}, \nu_n^{ext}) \tag{5.5}$$

where

$$F(\nu_n^{int}, \nu_n^{ext}) = \left[\tau_{ref} + \tau \int_{\frac{V_{rest}-\mu}{\sigma}}^{\frac{V_\theta-\mu}{\sigma}} \phi(u)du\right]^{-1}$$

where

- $\phi(u) = \sqrt{\pi}e^{u^2}(1+erf(u))$
- $\mu = \mu(\nu_n^{int}, \nu_n^{ext})$is described in the next subsections.
- $\sigma = \sigma(\nu_n^{int}, \nu_n^{ext})$ is described in the next subsections.
- ν^{int} is the vector representing the output Rates of the neurons in the column.

$$\nu^{int} = \begin{pmatrix} \nu_{up} \\ \nu_{down} \\ \nu_{i,up} \\ \nu_{i,down} \\ \nu_i \\ \nu_0 \end{pmatrix}$$

- ν^{ext} is the vector representing the output Rates of the neurons in the brain and the direction detectors.

$$\nu^{ext} = \begin{pmatrix} \nu_{global} \\ \nu_{ext,up} \\ \nu_{ext,down} \end{pmatrix}$$

- $\tau_{ref} = 0.0005$ refractory period in seconds
- $\tau = 0.05$ neuronal time constant in seconds

The variable μ

In equation eq. 5.2, the relation between μ and the incoming poisson rate is linear. So we can write this $(2p + 5)$ linear equation:

$$\mu = J \times A \times \nu \tag{5.6}$$

μ is a vector of size $(2p + 2)$, representing the various subpopulations of neurons in the LIP column. ν_n is a vector of size $(2p+5)$, representing the rate of the poisson processes received from the various subpopulations of neurons.ν is the combination of ν^{ext} and ν^{int}.A is a matrix of size $(2p+2) \times (2p+5)$. If we take the example of $p = 2$, for the two choices dots direction decision task (upwards or downwards), we have: $\mu = \begin{pmatrix} \mu_{up} \\ \mu_{down} \\ \mu_{i,up} \\ \mu_{i,down} \\ \mu_i \\ \mu_0 \end{pmatrix}$, $\nu = \begin{pmatrix} \nu_{up} \\ \nu_{down} \\ \nu_{i,up} \\ \nu_{i,down} \\ \nu_i \\ \nu_0 \\ \nu_{global} \\ \nu_{ext,up} \\ \nu_{ext,down} \end{pmatrix}$

The variable σ

Currently, we suppose that the correlation between neurons that belong to the same group of neurons (for example, the group of excitatory neurons that is especially sensitive to the upwards direction detector) is $c = 0.1$.The correlation between neurons of two different groups is $c = 0.01$. The correlation between inhibitory and excitatory neurons is $c = 0$. So, in the particular case that we study here ($p = 2$), we obtain the following correlation matrix:

$$c = \begin{pmatrix} 0.1 & 0.01 & 0 & 0 & 0 & 0.01 & 0.01 & 0.01 & 0.01 \\ 0.01 & 0.1 & 0 & 0 & 0 & 0.01 & 0.01 & 0.01 & 0.01 \\ 0 & 0 & 0.1 & 0.01 & 0.01 & 0 & 0 & 0 & 0 \\ 0 & 0 & 0.01 & 0.1 & 0.01 & 0 & 0 & 0 & 0 \\ 0 & 0 & 0.01 & 0.01 & 0.1 & 0 & 0 & 0 & 0 \\ 0.01 & 0.01 & 0 & 0 & 0 & 0.1 & 0.01 & 0.01 & 0.01 \\ 0.01 & 0.01 & 0 & 0 & 0 & 0.01 & 0.1 & 0.01 & 0.01 \\ 0.01 & 0.01 & 0 & 0 & 0 & 0.01 & 0.01 & 0.1 & 0.01 \\ 0.01 & 0.01 & 0 & 0 & 0 & 0.01 & 0.01 & 0.01 & 0.1 \end{pmatrix}$$

Consequently, for a neuron belonging to group n, we have:

$$\sigma_n^2 = \frac{1}{2} J^2 \left(\sum_{i=1}^{N_g} A_{n,i}^2 \nu_i + \sum_{i,j=1, i \neq j}^{N_g} c_{i,j} A_{n,i} A_{n,j} \sqrt{\nu_i \nu_j} \right) \tag{5.7}$$

With

- N_g: Number of group of neurons.
- A: is the matrix seen before.
- $c_{i,j}$: Correlation coefficient between the i^{th} and the j^{th} synpapse.

5.2.4 Saccadic Eye Movement

In order to express the decision, we model a Saccadic Eye Movement (SEM). This is the paradigm that is used in Newsome's lab to evaluate the decisions of monkeys during the same task. In our model, the eye position is governed by the following equation:

$$\frac{\partial^2 x}{\partial t^2} = k \times R - l \times tan(x)$$

- x represents the angular position of the eye.
- k and l are parameters. In our recent experiments: $k = l = 3$.

- R is the input that comes from the LIP column. In the two-dimensional case ($p = 2$), $R = \nu_{up} - \nu_{down}$.

The term $tan(x)$ models an elastic force that tends to bring the eye in its central position if no specific comand is sent, and that also prevents the eye angular position from diverging. In fact, when x tends to $\frac{pi}{2}$, the force modelled by $tan(x)$ tends to ∞, thus the moving span of the eye is limited. The position of the eye gives us a natural criterium to measure ER and RT. At the moment, we consider that a decision is taken when $x = 0.95\frac{\pi}{2}$.

5.3 Results/Predictions

5.3.1 Methods

We ran a set of experiments, covering the parameter space that follows: The mean of the global background activity varied from 3 to 10 Hz, and the Standart Deviation varied from 0 to 5 Hz. We measured the Reaction Time and Error Rate of the model. For each parameters combination, we averaged the results over ten repetitions. All simulations were conducted with stimuli that had 5% coherence.

5.3.2 Time course of decision: convergence to a local attractor

In Fig. 5.3 we illustrate the time course of a decision making. We can see the competition that leads to the convergence to a local attractor, alongside with the eye position over time. We see as well that the recurrent loops enable the model to keep in mind the decision even when the stimulus disappears. We can argue that we are implementing here a kind of working memory. In fact this decision is not expressed by the model unitll the difference of activity between the two populations has been consistent enough for the Eye to have accomplished its saccadic mouvement. WE see in Fig. 5.3 that the decision is kept in memory, because we have artificially reset the eye in the middle position when the stimulus stopped. However the system stays in the attractor and when the eye is released it expresses the delayed decision.

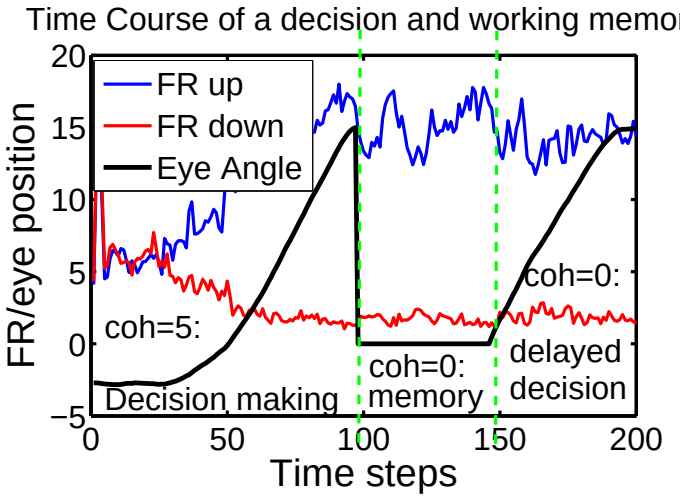

Fig. 5.3. Illustration of a decision making and working memory. The stimulus is presented during the first 100 timstep. then, the eye is reset to the middle position and the stimulus disappears (100 to 150). However, we see that the decision is maintained when we free the eye and the system expresses a delayed decision

5.3.3 Background activity controls decision making

Mean intensity of the background activity

Reaction Time

We clearly see in Fig. 5.4 that increasing the intensity of the background activity reduces the Reaction Time. We can still see the "switch" effect described by Salinas [13]: If the background activity tends to zero, than the reaction time tends to infinity. This switch effect is part of a more global control exerced by the external activity on the decision process.

Error Rate

The Error Rate increases with the intensity of the background activity following a sigmoid function. On Fig. 5.5, we can see a 4 parameters exponential approximation of this increase.

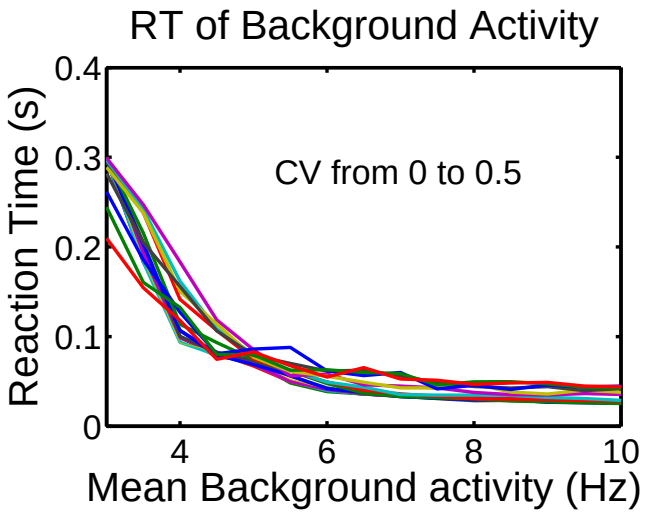

Fig. 5.4. Reaction Time as a function of the mean intensity of the background activity of the brain. The Decision processes were stopped after 0.3 seconds, in order to reduce computaional time. In fact, if no decision is taken, when the background activity is too weak, RT tends to infinity.

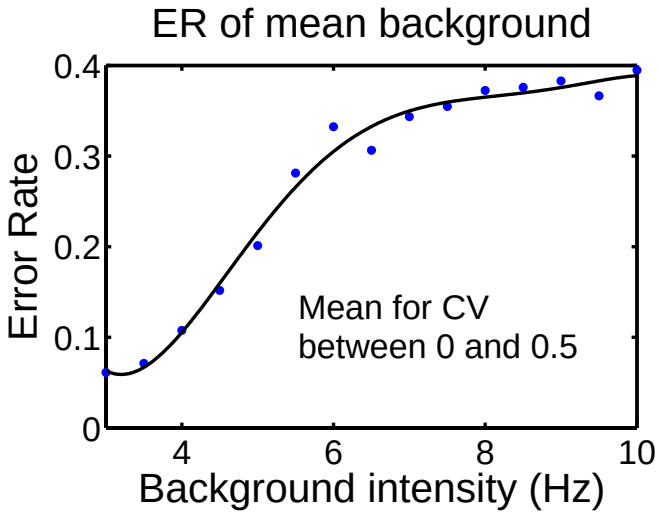

Fig. 5.5. Error Rate as a function of the mean intensity of the background activity of the brain. This an average over all the values of the Standart Deviation, between 0 and 5.

Error Rate=F(Reaction Time)

Fig. 5.6 shows the characteristic of ER as a function of RT, deducted from the previous results. This was possible because RT is a monotonically increasing function of background intensity. This result is important because it is a model prediction and gives a tool to evaluate our hypothesis that background activity controls the speed/accuracy trade off in decision making: If, during Psychological experiments, humans show a similar dependency between ER and RT, then our model for the underlying process is likely to be plausible.

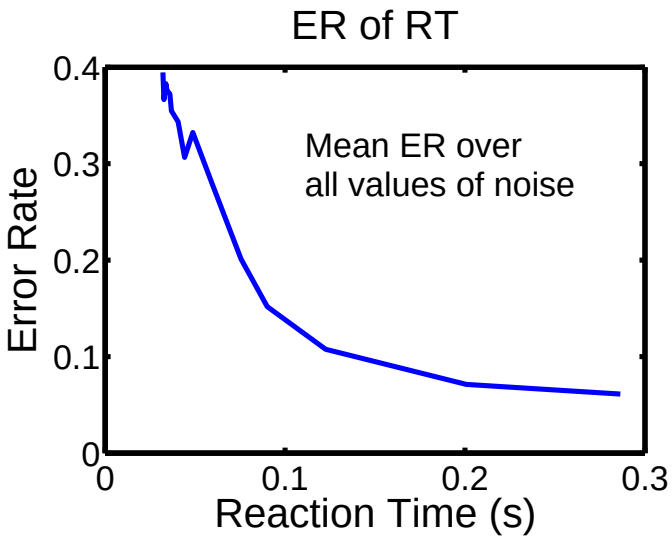

Fig. 5.6. ER as a function of the RT. Our method is basically a change of variables from the mean background activity to the Reaction Time. This works, because we have seen previously that the RT is a monotonic function of the background Intensity. Here, we have taken the mean over all the values of the Standart Deviation of the Background Activity.

Standart Deviation of the Background Activity

Reaction Time

Fig. 5.7 shows that the real noise also speeds up decision making. In this simulation, the mean of the low level background activity is constant. Its standart Deviation is the only parameter that varies. This is a new result, purely based on the second order momen of the the brain stochastic neural activity.

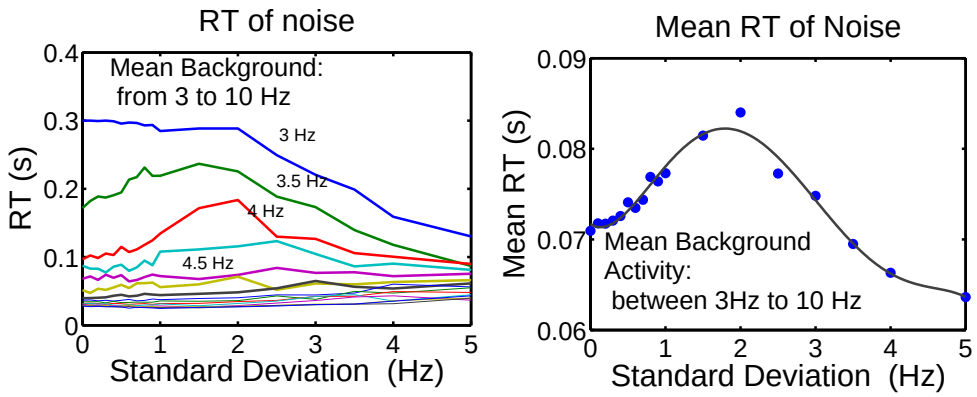

Fig. 5.7. Reaction Time as a function of the Standart Deviation of the Background Activity. On the first panel, the mean activity varies between 3Hz and 10Hz. The third panel is the mean function, averaged over the whole range of Background mean intensities (It is the average of the curves presented in the first panel).

Error Rate

Fig. 5.8 shows a significant influence of noise on the Error Rate. For each value of the Standart Deviation, we have measured the ER for the range of mean background intensities, and then taken the mean over all theses simulation.

5.4 Discussion

5.4.1 Summary of the Results

We have implemented a model that performs decision making and expresses it through a SEM. This is a step forward from the models in which the external observer has to take her-or-himself by watching a neural variable, because because we can use measures such as Reaction Time and Errror Rate of our model in order to compare it to living beings performance. We have shown that the low level noisy background activity of the brain can be beneficial to decision making, in the case of very ambiguous sensory evidence. We reproduce the results of Salinas that an increase in the mean of the low-level background activity can trigger a decision making. We went much further than this intuitive result (If you add more energy in a competitive system, the convergence to the outcome will be quicker). We explored quantitatively the influence of the background intensity on the Reaction Time and on the

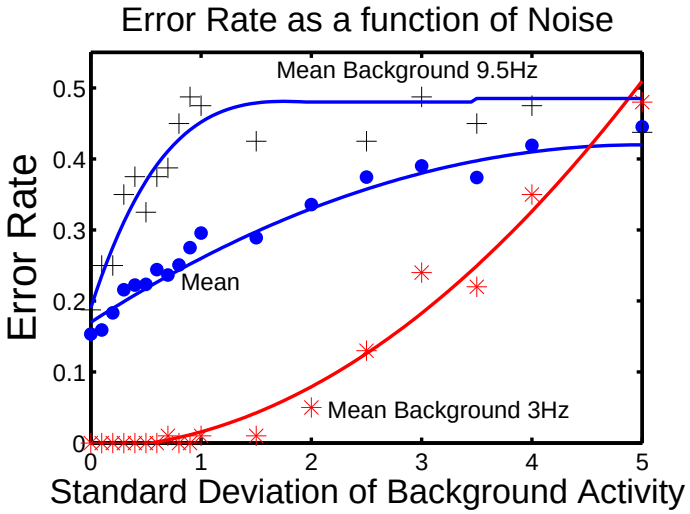

Fig. 5.8. Error Rate as a function of the Standart Deviation of the background activity of the brain. Three different behaviours for three different mean intensities of the background activity.

Error Rate, and deducted a relation between Error Rate and Reaction Time. Furthermore we showed that an increase in the actual noisy property of the background activity, without increase of its mean, also speeds up decision making at the cost of accuracy. This is a new result.

5.4.2 Limitations

The parameter space is huge, we only explored a small region. The results are dependent on the SEM model, which is currently oversimplistic and hasn't been compared to biological evidence. We only have simulations.

5.4.3 Developments

Moment Mapping

The second order statistics are fundamental to the results we present here. However, we assume that the spikes are emitted according to poisson processes: That means that the presynaptic noise is proportional to its mean, and enables us to write eq. 5.4, and gives us eq. 5.5 as an equation for the

propagation of the first moment of the Interspike Interval (ISI) distribution. However, this assumption does not hold in the general case, and furthermore there is little biological evidence for LIP neuronal activity to be Poissonian. So, we have a more general expression the eq.5.5. In the general case:

$$(\nu^1_{n+1}, \nu^2_{n+1}) = G(\nu^1_n, \nu^2_n) \tag{5.8}$$

where ν^1_{n+1} and ν^2_{n+1} are the first and second moment of the ISI distribution at time n+1 or at the next neuron layer, and ν^1_{n+1} and ν^2_{n+1} are the first and second moment of the ISI distribution at time n or at the current neuron layer. We currently have an analytical expression for G that has been derived from the IF equation, and we will apply it to our set up in subsequent work.

Formal Analysis

Our results are based on numerical simulations. We will try to develop an analytical understanding of a simplified version of this model. we will characterise the attractors of the system defined by eq. 5.8, their domain of attraction, their stability and and the speed of convergence to these attractors as a function of various system parameters.

Hypothesis

We deducted a relation between Error Rate and Reaction Time. This relation can be used to test the hypothesis that the background noisy activity of the brain controls the speed-accuracy trade off of decision making. Comparing our modell characteristic of ER(RT) to the one of living beings, measured via psychophysical experiments, could support or invalidate our hypothesis.

5.4.4 Conclusion

Our model is a step towards the construction of a bridge between detailed neural models and real living behaviour such as sensory-based decision making, between neurology and psychology. Computing with noise is also a new step towards less simplistic neural modelling, that takes into account the second order statistics of spike trains. This more refined approach should give us insights into domains unreachable by the classical mean FR approach.

References

1. N. Amit, D. J.and Brunel. Model of global spontaneous activity and local structured activity during delay periods in the cerebral cortex. *Cereb. cortex*, 7:237–252., 1997.
2. K. H. Britten, M. N. Shadlen, W. T. Newsome, and J. A. Movshon. The analysis of visual motion : A comparison of neuronal and psychophysical performance. *J. Neurosci.*, 12:2331–2355, 1992.
3. Y. Deng, P. Williams, F. Liu, and J. Feng. Discriminating between different input signals via single neuron activity. *Journal of Physics A: Mathematical and General*, 36(50):12379–12398, 2003.
4. J. Feng. Is the integrate-and-fire model good enough? - a review. *Neural Networks*, 14:955–975, 2001.
5. J. Feng and F. Liu. A modelling study on discrimination tasks. *Biosystems*, 67:67–73, 2002.
6. B. Gaillard and J. Feng. Modelling a visual discrimination task. *Neurocomputing*, 65-66:203–209, 2005.
7. B. Gaillard, J. Feng, and H. Buxton. Population approach to a neural discrimination task. *Biological cybernetics*, 2005. submitted.
8. W. Gerstner and W. Kistler. *Spiking Neuron Models, Single Neurons, Populations, Plasticity*. Cambridge University Press, 2002.
9. P. W. Glimcher. The neurobiology of visual-saccadic decision making. *Annu. Rev. Neurosci.*, 26:133–179, 2003.
10. D. H. Hubel and T. N. Wiesel. Receptive fields, binocular interaction and functional architecture in the cat's visual cortex. *J. Physiol. (Lond.)*, 148:574–591, 1962.
11. V. B. Mountcastle. Modality and topographic properties of single neurons of cat's somatosensory cortex. *J. Neurophysiol.*, 20, 1957.
12. M. L. Platt and P. W. Glimcher. Neural correlates of decision variables in parietal cortex. *Nature*, 400:233–238, 1999.
13. E. Salinas. Background synaptic activity as a switch between dynamical states in a network. *Neural Computation*, 15:1439–1475, 2003.
14. M. N. Shadlen and J. I. Gold. The neurophysiology of decision making as a window on cognition. In Gazzaniga, editor, *The Cognitive Neurosciences, 3rd edition*. MIT Press, 2004.
15. M. N. Shadlen and W. T. Newsome. Neural basis of a perceptual decision in the parietal cortex (area LIP) of the rhesus monkey. *J. Neurophysiol.*, 86:1916–1935, 2001.
16. M. N. Shadlen and W.T. Newsome. Motion perception : Seeing and deciding. *PNAS*, 93:628–633, 1996.
17. J. T. Townsend and F. G. A. Ashby. *The stochastic modelling of elementary psychological processes*. Cambridge University Press, Cambridge, 1983.
18. H. C. Tuckwell. *Introduction to Theoretical Neurobiology*, volume 2. Cambridge University Press, Cambridge, 1988.
19. R. VanRullen and C. Koch. Is perception discrete or continuous? *Trends in Cognitive Science*, 7(5):207–213, 2003.
20. X. J. Wang. Probabilistic decision making by slow reverberation in cortical circuits. *Neuron*, 36:955–968, 2002.

21. E. Zohary, M. N. Shadlen, and W. T. Newsome. Correlated neuronal discharge rate and its implications for psychophysical performance. *Nature*, 370:140–143, 1994.

6

Estimation of spike train statistics in spontaneously active biological neural networks

Henry C. Tuckwell and Jianfeng Feng

Summary. We consider the problem of theoretical determination of firing rates in some biological neural networks which consist of synaptically connected excitatory and inhibitory elements. A self-consistent argument is employed to write down equations satisfied by the firing times of the various cells in the network. We first present results for networks composed of leaky integrate and fire model neurons in the case of impulsive currents representing synaptic inputs and an imposed threshold for firing. Solving a differential-difference equation with specified boundary conditions yields an estimate of the mean interspike interval of neurons in the network. Calculations with a diffusion approximation yield the following results for excitatory networks: (i) for a given threshold for action potentials, there is a critical number of connections n_c such that for $n < n_c$ there is no nontrivial solution whereas for $n > n_c$ there are three solutions. Of these, one is at zero activity, one is unstable and the other is asymptotically stable; (ii) the critical frequency of firing of neurons in the network is independent of the ratio (α) of threshold voltage to excitatory postsynaptic potential amplitude and independent of the size of the network for $n > n_c$; (iii) the critical network size is proportional to α. We also consider a network of generalized Hodgkin-Huxley model neurons. Assuming a voltage threshold, which is a useful representation for slowly firing such nerve cells, a differential equation is obtained whose solution affords an estimate of the mean firing rate. Related differential equations enable one to estimate the second and higher order moments of the interspike interval.

6.1 Introduction

Investigations and theories of information processing in the nervous system have recently addressed the role of stochasticity in the activity of both single neurons [1-4] and neural networks [5-8]. One source of variability which occurs in cortical (and other) neurons is the "spontaneous" spiking activity in the absence of deliberate or known external input. The role of such spontaneous

activity in relation to the processing of afferent input is not yet fully understood. However, spontaneous activity is now not considered to be simply noisy background activity. According to [9], the spontaneous activity of many brain neuronal networks determines the nature of the response of the brain to external stimulation and may contribute to the quality of perception. In visual information processing, it has been found that spontaneous activity does indeed create extra variability in nervous system responses to visual stimuli [10]. Furthermore, some or all such spontaneous activity has been hypothesized to play an important role in visual information processing as it tends to provide a substrate for modulation by afferent input.

Spontaneous neural activity arises because the brain contains a large number of neurons with very dense patterns of connections between cells. Small trains or bursts of activity in one region, possibly due to spontaneous transmitter release at synaptic terminals, are propagated to other regions and may circulate in recurrent loops. The connections involved include both local and remote circuits, such as cortico-thalamic loops [9]. Some of the details of brain connection patterns have recently been described in detail for neurons of the mammalian neocortex [11]. However, in most studies, as for example in references [5-8], and the current article, the precise details of the connections are omitted in favor of randomly assigned connections.

In a sense, spontaneous neural activity represents the simplest electrophysiological state or ground state for populations of neurons in the living brain, even though the underlying circuits are possibly as complex as for networks with afferent inputs. It is clear that by virtue of the complexity of the spatial and temporal aspects of the dynamics of individual neurons as well as the enormous complexity of the underlying biochemical processes, that there are difficulties with analytical approaches to finding the quantitative features of spiking or nonspiking activity in neural networks with any degree of realism in the physiological properties of the composite single neurons. Analytical results concerning dynamical neuronal behavior are few even for single neurons [2,12-15] and very sparse for neural networks composed of nonlinear elements so that efficient simulation and other techniques have thus been developed for networks with stochastic dynamics [7,16].

In many network models the neurons are considered to be weakly connected so that they are treated as independent and a mean field approach is adopted. It is then possible to use solutions of a single-neuron Fokker-Planck (or Kolmogorov) equation for the neuronal depolarization [5, 12-15], with suitable boundary conditions, to provide an estimate of the fraction of cells in the network at various levels of excitation. Background noise has been found to play an important role in the propagation of signals through model networks [6] and in the understanding of behavior of cortical and subcortical neurons in-

volved in relation to cognitive information processes such as working memory [17-20].

It is of interest to attempt to determine as far as possible with analytical techniques the relationships between the microscopic physiological variables associated with single nerve cells, their patterns of connectivity and global spiking activity. Such relationships are expected to assist in casting light on computational aspects of neuronal information processing and cognitive activity. Here we describe a method for analytically estimating the firing rates of neurons in stochastic networks of an arbitrary number of elements using Markov process theory. We consider in Section 2 networks of generalized integrate and fire neurons and present some exact results for networks of excitatory neurons. In Section 3 we state corresponding results for networks composed of neurons with generalized Hodgkin-Huxley dynamics. In order that the theoretical estimates are as accurate as possible, our attention is focussed mainly on slowly firing networks whose spiking is in singlets. We explore the relation between single neuron dynamics, network size and the nature of sustainable spontaneous activity.

6.2 Networks of generalized leaky integrate and fire neurons

Let the electrical depolarization from rest for the k-th cell in a network of n neurons be $V_k(t)$ at time t. In general the dynamical equations for the network can be written

$$dV_k = f(V_k)dt + \sum_{j=1}^{n} a_{jk} dN_j(\lambda_j; t - d_{jk}), k = 1, 2, \ldots, n, \tag{1}$$

where a_{jk} (element of the matrix A) is the strength of the connection from neuron j to neuron k, which determines the magnitude of the postsynaptic potential elicited when this connection is activated (it is assumed that $a_{jj} = 0$ for all j). The threshold for action potential generation in the k-th cell is set at θ_k, here assumed to be constant. $N_j(\lambda_j; t)$ is the number of spikes emitted by neuron j in the time interval $(0, t]$; the parameter λ_j represents the mean rate of spiking so that as usual as an approximation $1/\lambda_j$ can be interpreted as the mean time between spikes from neuron j. The quantities d_{jk} are the time delays between emission of a spike by cell j and the appearance of a postsynaptic potential in cell k. According to (1), the input currents are delta-functions so that the detailed temporal structure of postsynaptic potentials is here ignored in a first approximation. This structure can easily be incorporated by adding subsidiary variables but this would make the theory much more complicated and so is omitted.

6.2.1 A network of excitatory and inhibitory neurons

Suppose there are n_E excitatory (type E) and n_I inhibitory (type I) cells, whose membrane potentials in the absence of synaptic activation satisfy $\dot{V_E} = f_E(V_E)$ and $\dot{V_I} = f_I(V_I)$, respectively. The postsynaptic potential amplitudes are the nonnegative quantities a_{EE}, a_{IE}, a_{EI} and a_{II}, where the first subscript refers to the presynaptic cell type and the second to the postsynaptic cell type. The corresponding numbers of connections for individual cells are n_{EE}, n_{IE}, n_{EI} and n_{II}, respectively. Thus each E-cell receives a total of $n_{EE}+n_{IE}$ synaptic inputs and each I-cell receives $n_{EI}+n_{II}$ such inputs. Since each E-cell has effectively the same input, its membrane potential satisfies

$$dV_E = f_E(V_E)dt + a_{EE}dN_{EE}(n_{EE}\lambda_E; t) - a_{IE}dN_IE(n_{IE}\lambda_I; t), \qquad (2)$$

whereas for each I-cell,

$$dV_I = f_I(V_I)dt + a_{EI}dN_{EI}(n_{EI}\lambda_E; t) - a_{II}dN_{II}(n_{II}\lambda_I; t). \qquad (3)$$

Here N_{EE}, N_{IE} are the pooled excitatory and inhibitory input point processes for E-cells and N_{EI}, N_{II} are the corresponding processes for the I-cells. Letting the thresholds of the two kinds of cell be θ_E and θ_I, we then have the following result, where now refractory periods are included. The proof of this follows by again considering the total input frequencies for the component neurons and their respective expected times taken for their membrane potentials to reach threshold.

If $\frac{1}{\lambda_E} + t_{R,E}$ is the mean time interval between spikes in an E-cell and $\frac{1}{\lambda_I} + t_{R,I}$ is the mean time interval between spikes in an I-cell of the network, then these quantities may be estimated implicitly by solving the simultaneous differential-difference equations

$$f_E(v)\frac{dF_E}{dv} + n_{EE}\Lambda_E F_E(v + a_{EE}) + n_{IE}\Lambda_I F_E(v - a_{IE})$$
$$-(n_{EE}\Lambda_E + n_{IE}\Lambda_I)F_E(v) = -1, \quad v < \theta_E, \qquad (4)$$
$$f_I(v)\frac{dF_I}{dv} + n_{EI}\Lambda_E F_I(v + a_{EI}) + n_{II}\Lambda_I F_E(v - a_{II})$$
$$-(n_{EI}\Lambda_E + n_{II}\Lambda_I)F_I(v) = -1, \quad xv\theta_I, \qquad (5)$$

with boundary conditions $F_E(v) = 0, v \geq \theta_E$, $F_I(v) = 0, v \geq \theta_I$ and $F_E(0) = \frac{1}{\lambda_E}$, $F_I(0) = \frac{1}{\lambda_I}$, provided such solutions exist.

Here we have put

$$\Lambda_E = \left(\frac{1}{\lambda_E} + t_{R,E}\right)^{-1} \qquad \Lambda_I = \left(\frac{1}{\lambda_I} + t_{R,I}\right)^{-1}$$

where $t_{R,E}$ and $t_{R,I}$ are the refractory periods of the excitatory and inhibitory cells respectively. In general in the search for such solutions, one may insist that f_E and f_I vanish for $v < v_E < 0$ and $v < v_I < 0$, respectively, and then let v_E and $v_I \to -\infty$ to ensure that the thresholds for action potentials are attained.

Equations (4) and (5) are difficult to solve exactly but may be solved numerically or approximately via simulation of the corresponding stochastic differential equations. In the simpler situation of a uniform network where each cell has the same membrane potential dynamics, including thresholds θ for action potentials, and the same numbers of excitatory, n_E, and inhibitory, n_I, inputs, with the same amplitudes a_E and a_I for the synaptic potentials, the same refractory periods t_R, and all cells fire at the same mean rate λ, (4) and (5) reduce to the single differential-difference equation

$$f(v)\frac{dF}{dv} + \Lambda[n_E F(v+a_E) + n_I F(v-a_I)] - (n_E+n_I)\Lambda F(v) = -1, \quad v < \theta, \tag{6}$$

where $\Lambda = \left(1/\lambda + t_R\right)^{-1}$. Equ (6) is solved with the constraints $F(v) = 0, v \geq \theta$ and $F(0) = \frac{1}{\lambda}$. Numerical solutions of (6) have been obtained in reference [28]. Again diffusion approximations may be employed to obtain approximate estimates.

6.2.2 A network of only excitatory cells

Suppose that all connections are only excitatory so $a_{jk} \geq 0$ and each cell *receives* the same number of inputs n_E. The network may or may not be fully connected - as long as each neuron receives synaptic input from n_E other cells. The number of inputs is thus $n_E \leq n-1$, with equality applying in the case of a fully connected network. It is feasible that there may neurons which are not presynaptic to any other cells, although this is unlikely in the mammalian cerebral cortex. To simplify, we ignore the transmission time intervals d_{jk} and assume further that all non-zero $a_{jk} = a_E$, which quantities may in fact be random but are assumed to be deterministic or at their mean values. We assume also that all cells have equal thresholds $\theta_j = \theta, j = 1 \ldots, n$ and the same subthreshold dynamics described by the function f. The network is described by the stochastic equations

$$dV_k = f(V_k)dt + a_E \sum_{j=1}^{n} dN_j(\lambda_j; t - d_{jk}), k = 1, 2, \ldots, n, \tag{7}$$

Now each cell receives EPSP's (excitatory postsynaptic potentials) according to n_E similar pooled point processes with the same mean rates, and their amplitudes are so the generic depolarization V of each neuron satisfies

$$dV = f(V)dt + a_E dN(n_E\lambda_E; t), V < \theta, V(0) = v < \theta. \tag{8}$$

In general we have the following result whose proof is immediate from the theory of mean exit times of Markov processes [27] and the requirement that the input frequency in a network of identical neurons each of which receives n_E inputs is n_E times the output frequency of each cell. Here $F(v)$ is the mean exit time of V from $(0, \theta)$ for an initial value $V(0) = v$.

If $\frac{1}{\lambda_E}$ is the mean time interval between spikes in a neuron of the network described by (7), then it may be estimated implicitly by solving the differential-difference equation

$$f(v)\frac{dF}{dv} + n_E\lambda_E[F(v + a_E) - F(x)] = -1, \quad v \in (0, \theta), \tag{9}$$

with boundary conditions $F(v) = 0, v \geq \theta$ and $F(0^+) = \frac{1}{\lambda_E}$, provided such a solution exists.

However, with the above kind of single neuron model, the time interval between spikes may have to take into account an additive refractory period, t_R, of order a few msec, which may be significant. In this case (9) becomes

$$f(v)\frac{dF}{dv} + n_E\left(\frac{1}{\lambda_E} + t_R\right)^{-1}[F(v + a_E) - F(v)] = -1, \quad v < \theta, \tag{10}$$

but the second boundary condition is still $F(0^+) = \frac{1}{\lambda_E}$.

Exact results for excitatory networks

We will demonstrate that a solution of Equ. (9) or (10) may fail to exist or there may be a three solutions, one of which may correspond to a stable connected network with nonzero firing rates. To do this we consider a network of cells with exponential decay, so that for subthreshold voltages

$$dV = -\frac{V}{\tau}dt + a_E dN(n_E\Lambda_E; t),$$

where $\Lambda_E = \left(1/\lambda_E + t_R\right)^{-1}$ and τ is the time constant, usually between 5 and 20 msec. One may simplify by scaling out the postsynaptic potential amplitude so that θ represents the ratio of threshold to the magnitude of each epsp. We also put $\sigma = 1/\tau$ giving $dV = -\sigma V dt + dN(n_E\Lambda_E; t)$. The exit of V from $[0, \theta)$, must be at θ and putting $\Lambda = n_E\Lambda_E$, the mean exit time satisfies

$$-\sigma v\frac{dF}{dv} + \Lambda[F(v + 1) - F(v)] = -1, v \in (0, \theta), \tag{11}$$

with constraints as for (9). For given values of n_E and θ the idea is to search for a λ_E which makes F satisfy (11) and the boundary conditions. In general an analytical solution is not known, but one may be found for $\theta \leq 3$, [21] and a numerical solution is possible for larger thresholds [22].

When $\theta \leq 1$ every synaptic input results in a spike and there is no solution to the network problem, the neuronal dynamics being irrelevant. We here consider in detail the nontrivial case $\theta = 2$. Solutions of (11) for $\Lambda = m\sigma$, where $m = 1, 2, 3, ...$ and $m = 1, 1/2, 1/3, ...$ are known and in particular so are their values at $v = 0$. With $\Lambda = \sigma/m$ we may put

$$F(0) = m\left[2 + \frac{1}{H(m)}\right]\tau, \tag{12}$$

where H is the infinite series

$$H(m) = 1 - \frac{1}{m}\sum_{j=0}^{\infty}\frac{2^{-(j+\frac{1}{m})}}{j+\frac{1}{m}}.$$

The expected interspike interval (ISI) is then

$$E[\text{ISI}] = \left(m\left[2 + \frac{1}{H(m)}\right] + t_R\right)\tau.$$

It is important to determine the behavior of the output frequency as a function of input frequency at very small firing rates. To this end, it is readily found that as $m \to \infty$, or as the input frequency goes to zero,

$$E[\text{ISI}] \to 2\tau m\left[1 + \frac{m^2(m+1)(2m+1)}{3m^2-1}\right]. \tag{13}$$

Even though the ISI is a random variable the reciprocal of whose mean is not exactly the expected frequency of spikes, we follow common practice and plot as the indicated curve in Figure 1 (called the frequency transfer curve) the inverse of $E[\text{ISI}] = f_{out}$ versus input frequency, assuming a refractory period of $t_R = 0.3$ time constants. The units of both f_{out} and f_{in} are inverse time constants. The curve for small input frequencies is shown in magnified form in Figure 2. Altogether 1020 points have been calculated which gave sufficient detail near the origin, where from (13) one may deduce that $f_{out} = kf_{in}^3$, with k a constant. For the conditions of the above result (10) to be met, the relation between input and output frequency must be $f_{out} = \frac{1}{n_E}f_{in}$ and such graphs are shown on Figure 1 for three values of n_E.

For the smallest one of these values, labelled case A, the line of slope $\frac{1}{n_E}$ does not intersect the frequency transfer function of the neuron so that theoretically no sustainably firing network of this size is possible with neurons

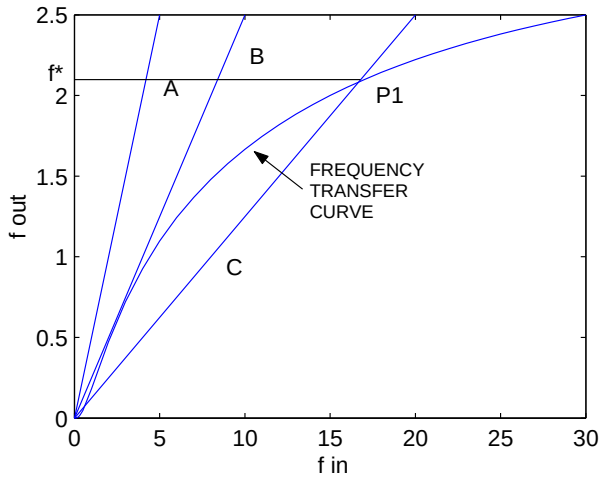

Fig. 6.1. Showing the output frequency of an exponential decay model (LIF) neuron with $\theta/a_E = 2$ within a network as a function of input frequency, where the units are spike counts per membrane time constant. The curves $f_{out} = \frac{1}{n_E} f_{in}$ for various n_E are shown, demonstrating that if the network is too small, no solution exists and that for networks greater than a critical size, there is a stable solution at P_1 and a unique firing frequency $f*$ which can be sustained in a network of that size or connectivity - see Figure 2 for details near the origin.

of the given properties. For the critical value $f_{out} = \frac{1}{n_c} f_{in}$, labelled B, the line is tangent to the frequency transfer curve. For $n_E > n_c$, where n_c is a critical number, as typified by the line, labelled C, there are three solutions, one being at zero input and zero output activity. Of the other two, P_2 is unstable whereas the asymptotically stable point P_1 at $f_{out} = f^*$ gives the firing frequency of neurons as shown in the expanded Figure 2. In the case shown it is seen that since $f_{out} = \frac{1}{8} f_{in}$ intersects the transfer curve at approximately $f^* = 2.1$ per spikes per time constant, a network of 9 fully connected neurons of the given dynamics would theoretically sustain spontaneous activity at a rate of about 85 spikes per second if a time constant of 15 msec and a refractory period of 0.3 time constants are assumed. Furthermore, if a network has an observed spontaneous firing rate f_s, the number of neurons in the network or the number of connections to each neuron could be estimated by ascertaining where $f_{out} = f_s$ intersects the transfer curve. The latter could be obtained empirically. The reciprocal of the slope of the line from the origin to the stable point of intersection gives an estimate of n_E. The approach outlined here is expected to provide a heuristic approach to estimating network activity from network anatomy and physiology or conversely - see the discussion.

For values of $\theta > 3$, exact analytical results are not available (for $2 < \theta \leq 3$ the expressions are already unwieldy) but numerical solutions are available

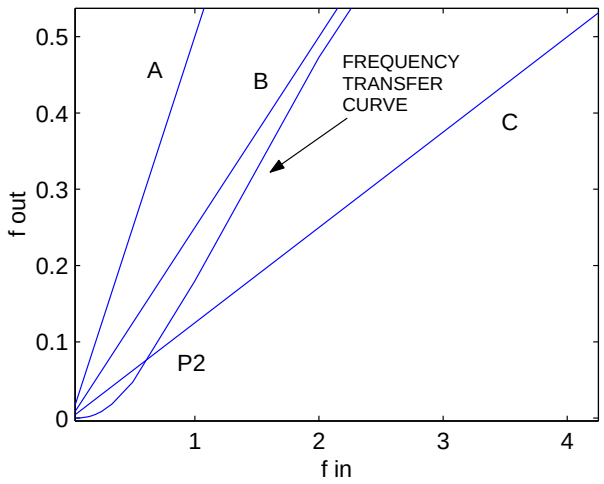

Fig. 6.2. Details of the curves in Figure 1 near the origin, showing for case C the unstable solution at P_2.

[22]. One could also use simulations to estimate the dependence of f_{out} on f_{in}. However, sampling and numerical errors make it difficult to ascertain accurately the behavior near the origin which is the region where the interspike intervals are the longest and the simulations the least accurate, hence rendering useful the above exact results. An alternative approach is to use smoothed versions of the network voltage processes called diffusion approximations. For such processes it is relatively easy to find the transfer characteristic not only for neurons of purely excitatory networks but also those including both excitation and inhibition. The validity of such an approximate approach depends on parameter values [23]. Further details of such approximations, which have computational advantages, are reported elsewhere. Using such diffusion approximations the following principles emerged for networks of identical excitatory LIF neurons:

(i) the critical frequency of firing needed to sustain activity is independent of the ratio of the threshold voltage to the excitatory post synaptic potential amplitude

(ii) the critical network size needed to sustain activity is proportional to the ratio of the threshold voltage to the excitatory post synaptic potential amplitude

6.3 A network of neurons with generalized Hodgkin-Huxley dynamics

As is well known, the original Hodgkin-Huxley model [24] was devised to describe subthreshold activity and action potential generation in squid axon and contained only sodium, potassium and leak channels. However, many types of ion channels with distinct roles and dynamics [25, 26] have been found in, for example, pyramidal cells so it is useful to generalize the Hodgkin-Huxley system.

Towards such a generalization we therefore consider $M+1$ neurons so that the neuronal dynamical system is, for $i = 1, ..., M + 1$,

$$C_i \frac{dU_i}{dt} = -\sum_{k=1}^{n} \overline{g}_{ki} \Big(U_i - V_{ki} \Big) \prod_{j=1}^{p_k} \gamma_{kji}^{m_{kj}} + I_i,$$

$$\frac{d\gamma_{kji}}{dt} = \alpha_{kj}(U_i)(1 - \gamma_{kji}) - \beta_{kj}(U_i)\gamma_{kji}$$

($n = 3$ for Hodgkin-Huxley) where V_{ki}=Nernst potential for k-th ion species of the i-th neuron, the maximal conductances are $\overline{g}_{ki}$, there are p_k gating variables asociated with the k-th ion species and I_i is the total input current for the i-th neuron.

In a network, of such neurons we have

$$C_i \frac{dU_i}{dt} = -\sum_{k=1}^{n} \overline{g}_{ki} \Big(U_i - V_{ki} \Big) \prod_{j=1}^{p_k} \gamma_{kji}^{m_{kj}} + I_i + \sum_{l} a_{li} dN_l(\lambda_l; t - \Delta_{li}),$$

where $i, l = 1, ..., M + 1$, N_l is the output process describing the spikes of the l-th neuron and where $\{a_{li}, i, l = 1, ..., M + 1\}$ is the connection matrix,where$\Delta_{li}$is the time delay.

Let now N be an (approximating) Poisson process representing the input train for each cell. Then for a generic cell, ignoring the time delays of transmission, with each cell firing at rate λ, and assuming a fully connected network,

$$C \frac{dU}{dt} = -\sum_{k=1}^{n} \overline{g}_{k} \Big(U_- V_k \Big) \prod_{j=1}^{p_k} \gamma_{kj}^{m_{kj}} + I + a dN(M\lambda; t),$$

where all nonzero elements of the connection matrix are set at a.

Let the Markov operator associated with the neuron's dynamics be L_{neuron} (that is, the operator for the non-driven neuron) and let $F(u, \mathbf{v})$ be the first

exit time of U to supra-threshold values with an initial value $(u, \mathbf{v})$ where u is the initial voltage and $\mathbf{v}$ contains the initial values of all gating variables (m,nand h for Hodgkin-Huxley). Then, assuming the spiking of each cell is not too rapid and occurs in distinct singlets, we have the following result.

Theorem

The network firing rate λ can be determined from the solution of the functional differential equation

$$L_{neuron}F(u, \mathbf{v}) + M\lambda[F(u + a, \mathbf{v}) - F(u, \mathbf{v})] = -1,$$

with the usual boundary conditions [27] and the additional constraint $F(0, \mathbf{v_0}) = \frac{1}{\lambda}$. Here $\mathbf{v_0}$are the initial values of the gating varibles.The theorem follows immediately from standard first exit-time theory for discontinuous Markov processes [27] assuming that each neuron fires at rate λ and receives excitation at rate $M\lambda$.

6.4 Discussion

We have outlined an approach for determining whether a network of neurons satisfying general physiological models (subthreshold dynamics, threshold and refractory period) can sustain spontaneous activity and if it can, additionally how to determine approximately the output frequency for each neuron. We have concentrated on networks whose neuronal spike trains are roughly Poisson and given exact results for an excitatory network of neurons whose EPSP amplitudes are large relative to the threshold for action potentials. We were able to demonstrate that there may be three solutions where $f_{out} = f_{in}/n_E$ intersects the frequency transfer curve of each neuronal element and that one of these was stable and gave the frequency of spontaneous activity. With realistic parameter values it is thus possible to estimate the average number of connections to each cell. This approach may provide insight into the factors controlling spontaneous activity of neurons in the mammalian and other nervous systems. Networks with small EPSP amplitudes and those with excitatory and inhibitory connections can be similarly analyzed, but more easily with diffusion approximations. However, the theory is likely to be accurate only for networks in which synchronization is unlikely as this tends to destroy the possibility of continued randomness in individual neuronal spike trains. This was amply demonstrated in simulations of networks containing up to a hundred neurons. Additional sources of randomness, especially those which can be considered to be of a perturbative nature and tend to remove the

possibility of synchronization can easily be included in the analytical framework presented here. Such perturbative noise has been included, and found to play an essential role in maintaining network activity in studies of both a theoretical [6] and more applied nature [17,18].

References

1. M. Badoual, M. Rudolph, Z. Piwkowska, A. Destexhe, T. Bal, Neurocomputing 65-66 (2005) 493.
2. J-F. Feng, H.C. Tuckwell, Phys. Rev. Lett. 91 (2003) 018101.
3. N.Iannella, H.C.Tuckwell, S. Tanaka, Math. Biosci. 188 (2004) 117.
4. P. Heil, Curr. Opinion Neurobiol. 14 (2004) 461.
5. M. Mattia, P. Del Giudice, Scientiae Mathematicae Japonicae 18 (2003) 335.
6. M.C.W. van Rossum, G.G. Turrigiano, S.B. Nelson, The Journal of Neuroscience 22 (2002) 1956.
7. H. Hasegawa, Phys. Rev. E 67 (2003) , 041903.
8. M. Shiino, M. Yamana, Phys. Rev. E 69 (2004) 011904.
9. M. Steriade, Neuroscience 101 (2000) 243.
10. J. Fiser, C. Chiu, M. Weliky, Nature 431 (2004) 573.
11. Douglas,R.J., Martin, K.A.C., Ann. Rev. Neurosci. 27 (2004) 419.
12. H.C. Tuckwell, F.Y.M. Wan, J-P. Rospars, Biol. Cybernetics 86 (2002) 137.
13. H.C. Tuckwell, *Introduction to Theoretical Neurobiology, Vol 2.* (Cambridge University Press, New York, NY, 1988).
14. Holden, A.V., *Models of the Stochastic Activity of Neurones.* (Springer-Verlag, Berlin, 1976).
15. Gerstner,W., Kistler,W.M. *Spiking Neuron Models.* (Cambridge University Press, New York, NY, 2002).
16. R. Rodriguez, H.C. Tuckwell, Phys. Rev. E 54 (1996) 5585.
17. D. Durstewitz, J.K. Seamans, T.J. Sejnowski, Nature Neuroscience 3 (2000) 1184.
18. D. Durstewitz, J.K. Seamans, T.J. Sejnowski, J. Neurophysiol. 83 (2000) 1733.
19. G.S. Berns, T.J. Sejnowski, J. Cognitive Neuroscience 10 (1998)108.
20. D. Durstewitz, J.K. Seamans, Neural Networks 15 (2002) 561.
21. H.C. Tuckwell, Biol. Cybernetics. 24 (1976) 147.
22. H.C. Tuckwell, W.Richter, J.Theor. Biol 71 (1978) 167.
23. H.C. Tuckwell, D.K. Cope, J. Theor. Biol. 83 (1980) 377.
24. A.L. Hodgkin, A.F. Huxley, J. Physiol. 117 (1952) 500.
25. Z.F.Mainen, J. Joerges, J.R. Huguenard, T.J. Sejnowski, Neuron 15 (1995) 1427.
26. M.Migliore, D.A. Hoffman, J.C. Magee, D. Johnston, J. Comp. Neuroscience 7 (1999) 5.
27. H.C. Tuckwell, J. Appl. Prob. 13 (1976) 39.
28. D.K.Cope, H.C. Tuckwell, J. Theor. Biol. 80 (1979) 1.

7

Physiology and Related Models of Associative Visual Processing

R. Eckhorn, A. Gail, B. Al-Shaikhli, A. Bruns, A. Gabriel, and M. Saam

Summary. This is a review of our work on multiple microelectrode recordings from the visual cortex of monkeys and subdural recordings from humans – related to the potential underlying neural mechanisms. The former hypothesis of object representation by synchronization in visual cortex (or more generally: of flexible associative processing) has been supported by our recent experiments in monkeys. They demonstrated local synchrony among rhythmic or stochastic γ-activities (30–90 Hz) and perceptual modulation, according to the rules of figure-ground segregation. However, γ-synchrony in primary visual cortex is restricted to few millimeters, challenging the synchronization hypothesis for larger cortical object representations. We found that the spatial restriction is due to γ-waves, traveling in random directions across the object representations. It will be argued that phase continuity of these waves can support the coding of object continuity. Based on models with spiking neurons, potentially underlying neural mechanisms are proposed: (i) Fast inhibitory feedback loops can generate locally synchronized γ-activities. (ii) Hebbian learning of lateral and feed forward connections with distance-dependent delays can explain the stabilization of cortical retinotopy, the limited size of synchronization, the occurrence of γ-waves, and the larger receptive fields at successive levels. (iii) Slow inhibitory feedback can support figure-ground segregation. In conclusion, it is proposed that the hypothesis of flexible associative processing by γ-synchronization, including coherent representations of visual objects, has to be extended to more general forms of signal coupling.

7.1 Dynamic Associative Processing by Different Types of Signal Coupling in the Visual Cortex

In the proposed view of the visual system, temporal coding is intimately linked to the neural mechanisms of dynamic cortical cooperativity and flexible associative processing, including the largely unknown mechanisms of perceptual feature binding. How are local features flexibly grouped into actually perceived

objects and events, and how do their current representations interact with visual memory and other higher-order processes? It has been proposed that binding of spatially distributed features and inter-areal cooperation are supported by the temporal code of fast synchronization among neurons involved in a common task, for example, the coding of a visual object [1, 2]. This hypothesis attracted attention when synchronized γ-oscillations (30–90 Hz) were found in the primary visual cortex (V1) of anesthetized cats [3, 4, 5] and awake monkeys [6, 7]. Many subsequent experiments were supportive, some challenging with respect to binding of local features by γ-synchronization (reviews, e.g., [8, 9]). For example, synchronization of signals in the γ-range was found to be restricted to few millimeters in primary visual cortex, even with large coherent stimuli [5, 10]. According to a strict interpretation of the original synchronization hypothesis, this should result in locally restricted perceptual feature binding. But this is in contradiction to the capability of perceiving local features of large objects as coherently bound. However, the capability of long-range feature binding across the surface of a large visual object is probably due to a continuous binding among overlapping regions of locally restricted feature binding (as demonstrated by the perceptual laws of Gestalt psychology; e.g., [11]). This view is supported by our observation of γ-waves that propagate across the surface of the representation of visual objects in the primary visual cortex of awake monkeys. Accordingly, we suggest that the phase continuity of such γ-waves (by which we mean a continuum of overlapping near-synchronized patches as opposed to strict long-range synchrony), may be a basis of spatial feature binding across entire objects. Such (locally synchronous) long-range phase coupling has been found to cover larger cortical areas than γ-synchrony as it is measured with spectral coherence [12], and we will argue why it can fill the entire surface representation of visual objects in primary visual cortex.

Such continuity may not be available between separate topographical maps (different visual cortical areas). However, γ-synchronization has been found between neural groups with overlapping receptive fields in adjacent visual cortical areas V1 and V2 in cats [3, 5] and monkeys [7]. It is probable that such synchrony is also present among other visual areas when feed-forward-backward delays are short (e.g., as between V1 and MT [13]). In contrast, when cortical areas are far apart, long conduction delays may cause cooperativity to be reflected in other forms of signal coupling which are less sensitive to any spatio-temporal restriction of synchronization. Taking into account the time-varying amplitude (amplitude envelope) of γ-signals seems to be a particularly promising approach [14].

For our present work different types of neural signals have been recorded, and different forms of temporal coding have been investigated by means of various coupling measures. We will demonstrate dynamic coupling of cortical signals in the form of local intra-areal phase synchrony, and medium-range

phase continuity of γ-waves. Our examples show that neural-signal measures correlate with sensory events, and with perceptual and behavioral outputs in monkeys. In essence, we argue that the temporal coding hypothesis of binding-by-synchronization, initially restricted to γ-synchrony of oscillatory signals, has to be extended to more general forms of temporal coding, including non-linear signal coupling across the entire frequency range of cortical activity with phase- and amplitude-coupling among transient and stochastic (non-rhythmic) signals. On the basis of neural models with locally coupled spiking neurons we will discuss most of the physiological results and suggest potential neural mechanisms underlying the presented types of flexible temporal coding.

7.2 Experimental Evidence

7.2.1 γ-Activity in Monkey Primary Visual Cortex is Phase-Coupled within Representations of Scene Segments and Decoupled Across their Contours

The binding-by-synchronization hypothesis suggests coupling among γ-activities representing the same object, or more generally, the same scene segment. Accordingly, neural groups representing different scene segments should decouple their γ-activities. Both predictions have been tested by investigating the effect of a static figure-ground stimulus on local field potentials (LFPs) in primary visual cortex (V1) of awake monkeys, recorded simultaneously from inside and outside a figure's representational area (Fig. 15.1A) [15]. Time-resolved analysis of phase coupling by means of spectral coherence revealed: (i) γ-coherence between neurons representing the same scene segment (figure or ground) is higher than for a homogeneous gray background of the same average luminance (Fig. 15.1B,D); (ii) stimulus-specific γ-coherence is strongly reduced across the representation of the figure-ground contour compared to a spatially continuous stimulus (Fig. 15.1B,D); (iii) decoupling across the contour emerges with a latency of about 100 ms, and is absent in the earliest neuronal response transients (Fig. 15.1D); (iv) coherence of low-frequency components does not show a difference between the figure-ground and the continuous condition (not shown). We propose that the increased γ-coherence between neurons representing the same scene segment and the decoupling of γ-activity at a contour representation are crucial for figure-ground segregation, in agreement with the initial binding-by-synchronization hypothesis.

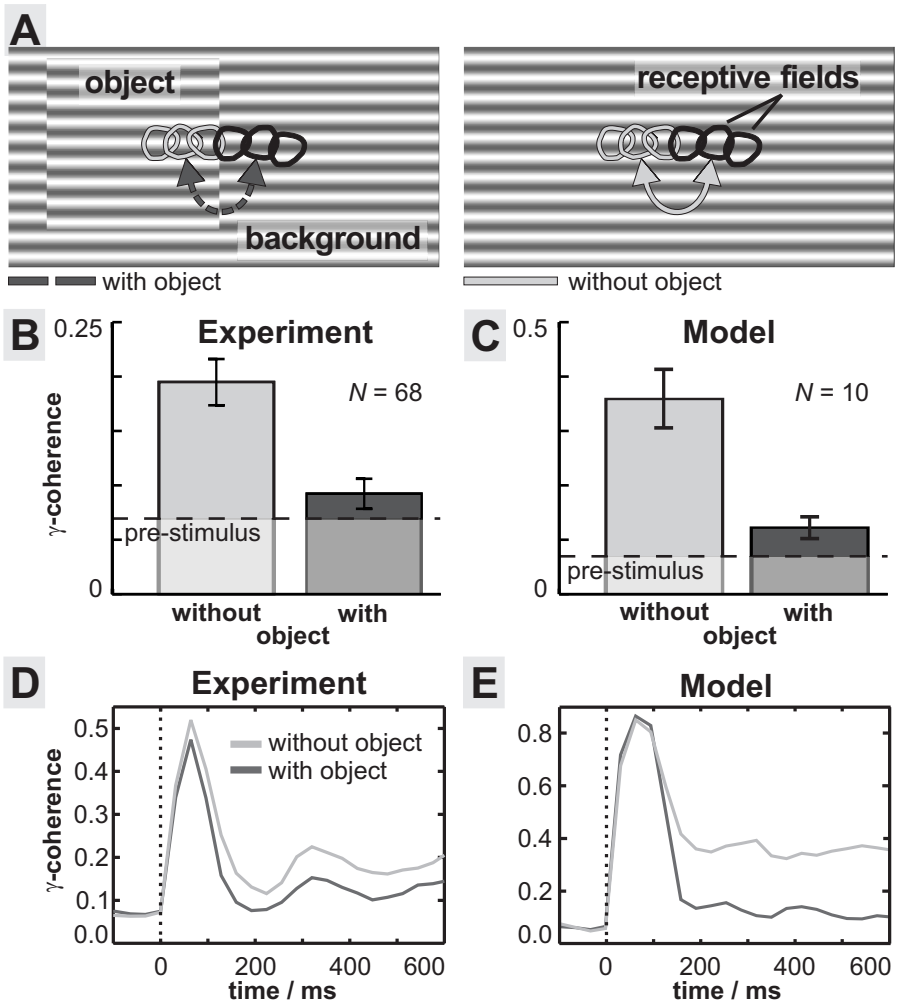

Fig. 7.1. Coherence of γ-activity is reduced across the representation of an object's contour. (**A**) Figure-ground stimulus and schematic positions of receptive fields. Stimuli were arranged in such a way that some of the receptive fields from the simultaneously recorded sites were located on the "object" (only present in the left condition), the others on the "background". (**B**) A grating without object (right condition in A) induced a substantial increase in γ-coherence among local field potentials (LFPs) (light gray) compared to a blank screen condition (pre-stimulus: dashed line). Introduction of the object (left condition in A) reduced LFP γ-coherence between object and background representations almost to pre-stimulus level (dark gray) [15]. Coherence within each segment (object or background) remained high (data not shown). (**C**) A network model (Fig. 7.10) shows equivalent results. (**D,E**) Time courses of coherence in the no-object condition (light gray) and across the object-background contour (dark) in the experiment and the model. Note that decoupling across the contour emerges about 100 ms after stimulus-onset. Data in B is taken from the time intervals with maximal decoupling for each monkey. (Modified from [15, 16])

7.2.2 γ-Phase Coupling in Monkey Extra-Striate Cortex Correlates with Perceptual Grouping

Are such synchronization effects correlated with perceptual feature grouping and figure-ground segregation? This was tested in a difficult figure-ground task in which a monkey indicated whether he perceived a figure composed of blobs among identical distractor blobs serving as background [17] (Fig. 15.2). This task was sufficiently difficult such that about 25% of responses were incorrect (failed figure detection). Pairs of local populations of figure-activated neurons in visual area V2 showed increased synchronization within the γ-range in correct compared to incorrect responses during a short period before the monkey's behavioral response (Fig. 15.2). Other signal measures were unrelated to perception. These were the first indications that γ-synchronization in V2 may not only represent physical stimulus properties but also supports perceptual grouping.

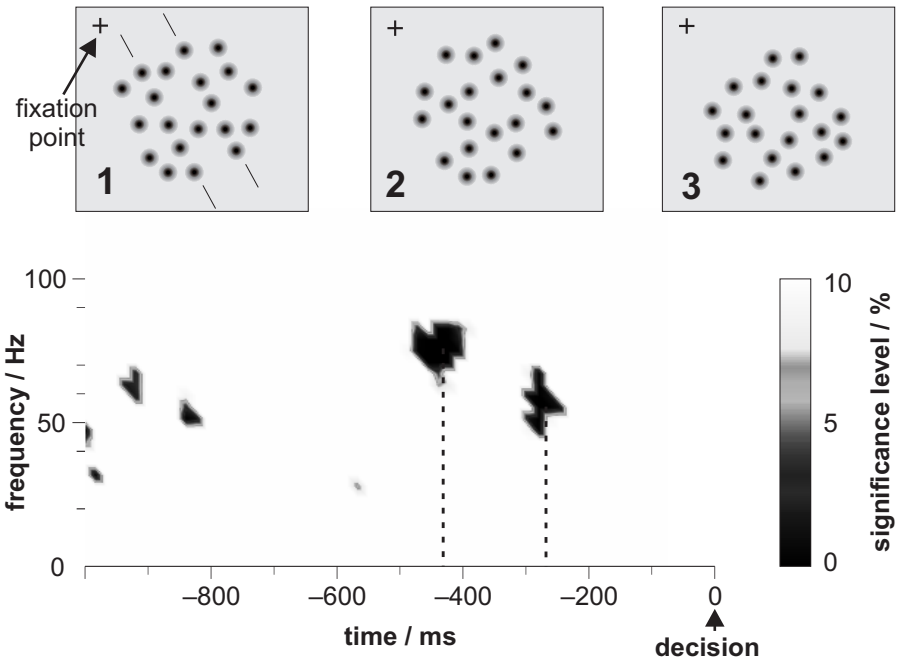

Fig. 7.2. A monkey's correct perception of the orientation of a dual-inline row of dots within a set of distractors (stimuli 1 and 2) caused a short increase in coherence at about 80 Hz and 60 Hz in visual area V2, shortly before the monkey reported his perception (time t=0 ms). The time-frequency map indicates the significance of increase in LFP coherence in trials with correct vs. failed detection of the figure. Three figure-ground stimuli are shown above, with dot rows being left-tilted (left), right-tilted (middle) or absent (right). (Modified from [17])

7.2.3 Phase Continuity but not Synchrony of γ-Waves is Present Across Medium Cortical Distances in Monkey Primary Visual Cortex

Previous work demonstrated that the synchronization range of γ-activity in primary visual cortex is limited to about 5 mm (e.g., [10, 18] and Fig. 15.4A). Hence, objects with larger cortical representations can not solely be coded by γ-synchrony within their representational area. One explanation for the limited synchronization range lies in the spatio-temporal characteristics of γ-activity. In fact, wave-like phenomena defined by spatially continuous phase-fronts (γ-waves) do extend farther than 5mm, but phase differences between any two sites change randomly already within 100 ms and also increase with cortical distance (Fig. 15.2A) [15]. Conventional pairwise coupling measures (cross-correlation, coherence) do not capture such non-trivial phase relationships across medium-range cortical distances, which explains the findings of restricted synchronization ranges. To quantify those waves a new method has been developed in our group [12]. It revealed that γ-waves travel at variable velocities and directions. Fig. 15.2C shows the velocity distribution measured with a 4×4 microelectrode array in monkey primary visual cortex during retinally static visual stimulation. Note that this distribution is rather similar to the distribution of spike velocities of horizontal connections in this area (V1) [13]. We suggest that continuity of γ-waves supports the coding of object continuity, in which case their extent over object representations in visual area V1 and the related visual fields should be much larger than that covered by γ-synchronization. We have indeed found that the cortical span of γ-wave fronts is much larger than the span of γ-synchronization (Fig. 15.4A,B) and that y-waves are cut-off (damped down) at the cortical representation of object contours.

7.3 Potential Neural Mechanisms of Flexible Signal Coupling

At present it is not possible to identify directly from experimental measurements the neural mechanisms underlying the above mentioned experimental observations of spatio-temporal processing in cortical sensory structures. We therefore use largely reduced model networks with spike-coding neurons to discuss potential mechanisms.

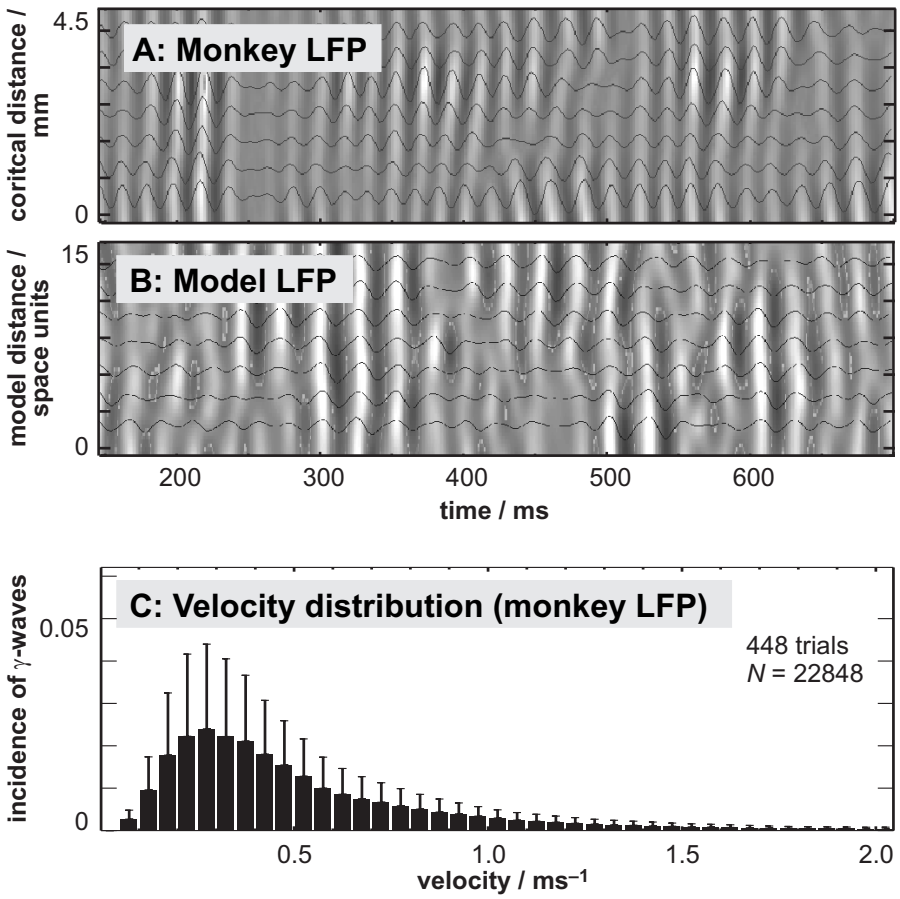

Fig. 7.3. γ-waves occur with fast and random changes of spatial phase relations in monkey primary visual cortex. (**A**) Time-space maps of simultaneously recorded single-trial time courses of local field potentials (LFPs) from a linear array of 7 recording positions during sustained static visual stimulation. Gray scales give the instantaneous electrical potentials at the electrodes (in arbitrary units). (**B**) Model-LFPs during presentation of an equivalent stimulus. (Modified from [16]) (**C**) Velocity distribution of traveling waves of γ-activity measured with 4×4 microelectrode arrays in monkey primary visual cortex

7.3.1 γ-Oscillations and Synchrony of Spike Densities in Local Populations, Generated by Feedback Inhibition and Local Lateral Coupling

How can the cortex generate γ-oscillations in local neural groups, as observed in LFP- and MUA-recordings? We argue (see Fig. 8.5) that membrane potentials of local populations of excitatory neurons are simultaneously modulated

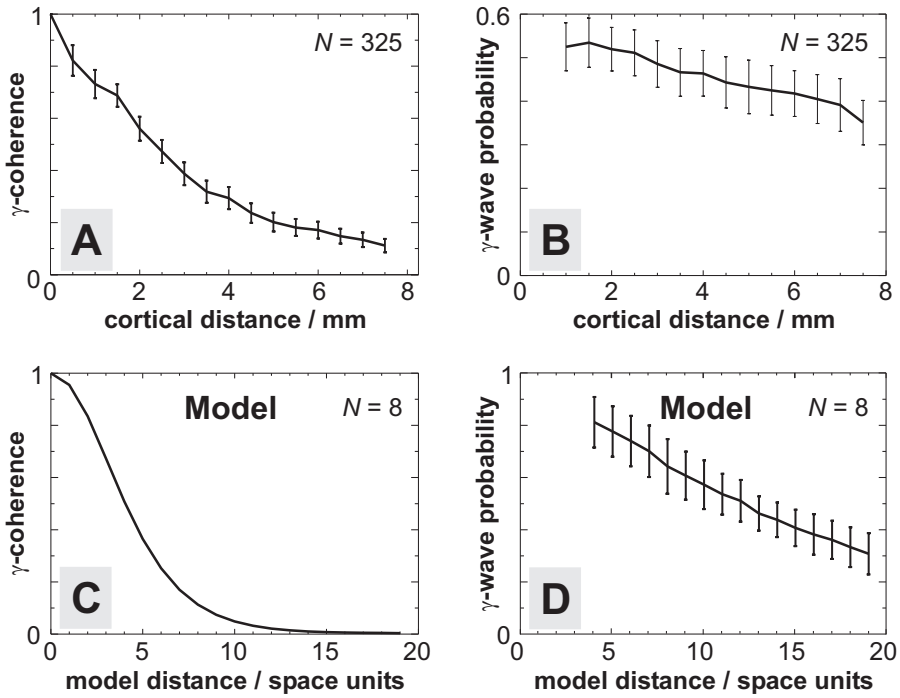

Fig. 7.4. The spatial range of γ-waves is larger than that of γ-coherence. (**A**) Coherence of local field potentials in monkey primary visual cortex is restricted to few millimeters (half-height decline 2.2mm). (**B**) The probability of occurrence of continuous γ-waves remains high across larger distances (estimated half-height decline: 9.5mm). (**C,D**) The model shows equivalent dependencies (4.1 vs. 12.8 space units). (Modified from [16])

by inhibition exerted via a common feedback loop (physiology: [19, 20, 21]; models: [22, 23, 24, 25, 26]; discussion in [27]). This loop can quickly reduce transient activations, whereas sustained input will lead to repetitive inhibition of the population in the γ-frequency range (Fig. 8.5). In both modes – transient and rhythmic chopping – the common modulation of the neurons' membrane potentials causes their spike trains to become partially synchronized, even if they fire at very different rates. The stronger a neuron is activated and depolarized, the earlier it will discharge its first spike during the common repolarization phase, whereby such a population burst will be dominated by the most strongly activated neurons. As local cortical populations generally project to common targets [28], synchronized spike densities (population spike packages) will have stronger impact there than uncorrelated spike densities of equal average amplitudes, because they (i) appear quasi-simultaneously, and (ii) mainly comprise spikes of strongly activated neurons, which represent the stimulus at a better signal-to-noise ratio than the neurons that were less ac-

tivated by the same stimulus. In addition to partial local synchronization by inhibitory feedback, the most relevant mechanism for explaining synchronization in our models are lateral, activity-dependent, facilitatory connections. Local (instead of global) lateral connections are critically important for models of visual feature-binding by synchronization when pattern segmentation (desynchronization) is an important task (e.g. [29, 30, 31]). While Wang used lateral excitatory connections that were modulated in their efficacy by scene properties (in some respect similar to the facilitatory connections in our models [29]), others used lateral connections from excitatory to inhibitory neurons for synchronization [25, 31]. It is likely that a mixture of these local mechanisms is operative in the generation of rhythmic spiking activities and their partial synchronization. Future experiments have to answer this question.

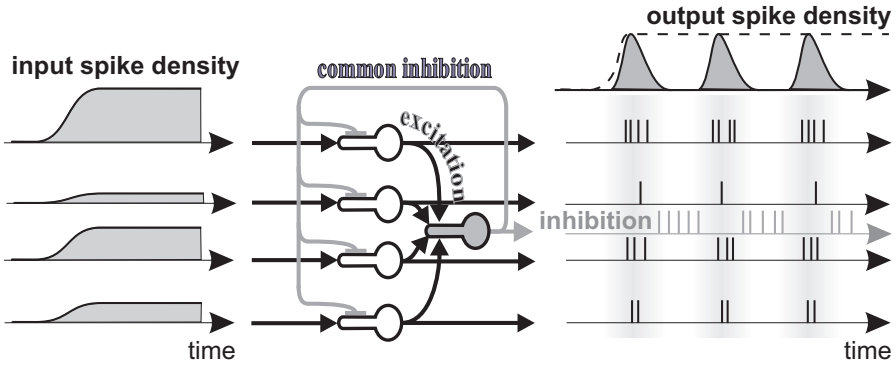

Fig. 7.5. Basic model of common spike density modulation in a local population of excitatory neurons by a common inhibitory feedback neuron. Note that first-spike latencies in each modulation cycle at the outputs (right) are roughly inversely proportional to the input spike densities (profiles at left), whereas the output spike rates are proportional to it (details in text)

We can apply the discussed schemes to the primary visual cortex, where local neural clusters represent similar feature values (e.g., receptive field position, contour orientation, etc.). According to the synchronization hypothesis, partial synchronization of spike densities by a common inhibitory feedback means that currently present local combinations of visual feature values are systematically selected by their strength of activation and tagged as belonging together, which is reflected in single or repetitive population discharges.

Other models of visual feature binding use local oscillators, consisting of excitatory and inhibitory units with mutual feedback that generate local oscillations depending on a driving input (e.g. [32, 30, 31]). In these models, the oscillatory signal of a local element stands for the spike density of a local group of partially synchronized spike-coding neurons. Thus, local inhibition in

these models implicitly represents the synchrony of local populations of spike-coding neurons with similar receptive field properties, as has been explicitly modeled in our and other simulations (e.g., [23, 25]).

7.3.2 Lateral Conduction Delays can Limit γ-Synchrony to Few Millimeters in Cortex, Produce Wave-Like Phenomena, Stabilize Cortical Topography, and Lead to Larger Receptive Fields at Successive Levels of Processing

The synchronization effect of fast orientation-specific inhibitory neurons is probably restricted to an area smaller than a single hypercolumn in primary visual cortex [28]. The most relevant mechanism for explaining flexible synchronization across several millimeters in the cortex in our [29] and Wang's [30] model are the activity-dependent facilitatory connections. They are also highly useful for enabling fast desynchronization as is required for scene segmentation. Their putative physiological substrate in the primary visual cortex are the dense horizontal connections: they cannot directly excite their target neurons, but modulate their activities evoked from their classical receptive fields. The lateral connections project monosynaptically over a range of several hypercolumns [19, 33, 20, 34], and models have shown that this type of connectivity is capable of synchronizing neural populations across larger distances [29, 30]. Another type of local lateral connectivity enabling transient synchronization over larger distances was proposed in the model of König and Schillen [31]. They connected their oscillators by coupling the excitatory units via delay lines to the neighboring inhibitory units. However, it is difficult to show experimentally which mechanisms are operative in the visual cortex for synchronization across several hypercolumns.

In visual processing for example, one could suppose that neural populations representing the entire surface of a visual object might synchronize their spike packages via horizontal connections. However, γ-synchrony is restricted to about 5 mm of cortical distance in area V1 of awake monkeys (corresponding to 5 hypercolumns), even if the cortical representation of a visual object is much larger [5, 10]. Hence, feature binding based on γ-synchrony would also be restricted to visual objects being not larger in their cortical representations. In the following we will develop a concept of how distance-dependent spike conduction delays can explain this restricted range of γ-synchrony and the occurrence of wave-like phenomena in a network of spiking neurons. In addition, we will show that Hebbian learning combined with distance-dependent spike conduction delays leads to spatially restricted lateral connectivity within the same layer and restricted feed-forward divergence between different layers. Therefore, such a mechanism is also suitable to explain the emergence of larger receptive fields at successive levels of processing while preserving

a topographical mapping. Note that these conditions are also present in topographically organized cortical areas of other sensory modalities, including auditory and somatosensory.

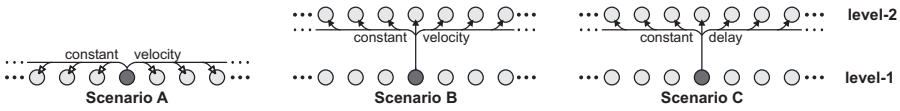

Fig. 7.6. One-dimensional sketch of the initial connectivity in the Hebbian learning model with distance-dependent lateral conduction delays. For a given level-1 neuron (dark), the scheme shows lateral modulatory (facilitatory) connections (scenario A), and feed-forward connections with either distance-dependent (scenario B) or constant (scenario C) conduction delays. (Modified from [35])

Hebbian-Learning Model with Finite Conduction Velocities

The local generation of γ-oscillations and their spatial synchronization are two separate mechanisms. For the sake of simplicity, the following model solely investigates synchronization effects, thereby neglecting any inhibition and the generation of oscillations. The model [35] consists of spike-coding neurons (as in Fig. 7.10B) at two successive, 2-dimensional retinotopic visual processing stages named level-1 (representing visual cortical area V1) and level-2 (V2) (Fig. 7.6). Learning of lateral weights and level-1-to-level-2 weights is implemented using a Hebbian spike correlation rule [36]. Feed-forward connections are additive excitatory and determine the properties of the classical receptive fields. Lateral connections are multiplicatory (with a positive offset of one), which means they cannot directly evoke spikes in a target neuron (as exitatory synapses can do), but require quasi-simultaneous feed-forward input to that neuron (model: [29]; physiology: [37]). Spikes evoked by quasi-simultaneous feeding input to neighboring neurons can synchronize via their mutual lateral facilitatory connections because these spikes will often occur within the so-called capture range of the spike encoder's dynamic threshold [29, 38, 39]. The lateral connections have constant conduction velocities, i.e., conduction delays become proportionally larger with distance. This reduces the probability of neurons becoming quasi-synchronized because constructive superposition of locally evoked and laterally conducted activities gets less probable for increasing delay. Hence, synchrony is laterally restricted to a spatial range which is proportional to the conduction velocity of the lateral connections.

Spatio-Temporal Structuring of Lateral Connectivity with Hebbian Learning

The relation between conduction velocity and synchronization range suggests an influence of temporal neighborhood (defined by the distance-dependent delays) on the ontogenetic, possibly prenatal formation of functionally relevant structures from an initially unstructured system [40, 41, 42]). This effect can be simulated with our model. In the beginning, neurons are fully interconnected within level-1 (Fig. 7.6, scenario A). Feed-forward input spike trains have spatially homogeneous random patterns and are given a temporally confined, weak co-modulation, mimicking activity before visual experience. This type of spike pattern appears, slightly modified by the connections, at the output of the level-1 neurons (Fig. 7.7) and hence, is used for Hebbian learning. The only topography in the network is given by the distance-dependent time delays of the lateral connections. During a first learning period, the homogeneous coupling within layer-1 shrinks to a spatially limited coupling profile for each neuron, with a steep decline of coupling strength with increasing distance (Fig. 7.8). The diameter of the resulting coupling profile for each neuron is near the lateral synchronization range, and hence directly proportional to the lateral conduction velocity (Fig. 7.9A).

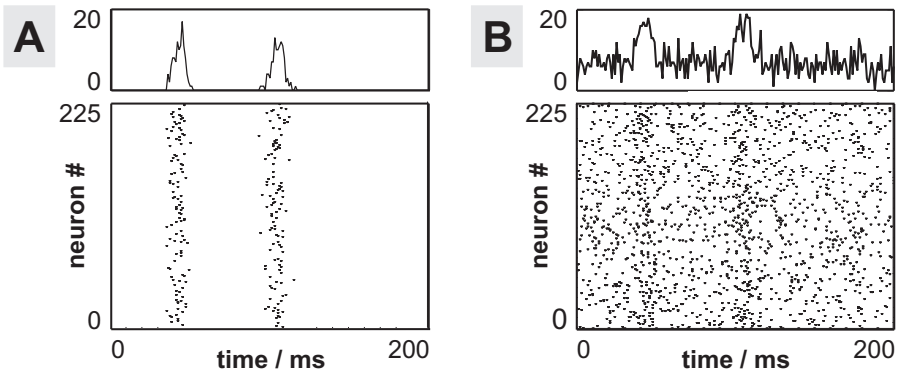

Fig. 7.7. Spatio-temporal properties of level-1 output activity in the Hebbian learning model. (**A**) Two events of spatially homogeneous, transient spike-rate enhancement (upper panel: total population spike density; lower panel: single spike traces). (**B**) As in A, but with additional independent Gaussian white noise at the inputs. Note that the activity is spatially homogeneous in the sense that any two spike trains have the same weakly correlated temporal statistics. (Modified from [35])

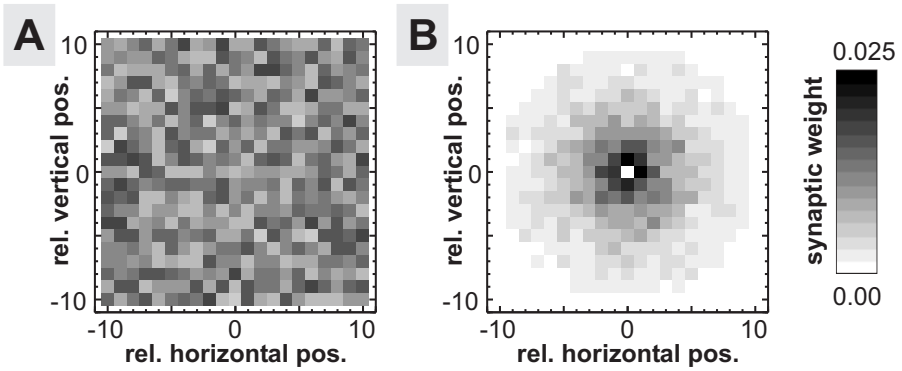

Fig. 7.8. Spatial coupling profile between a single level-1 neuron (center position) and its neighbors. (**A**) Before learning weights are randomly initialized. (**B**) After learning synaptic strength decays with increasing distance. (Modified from [35])

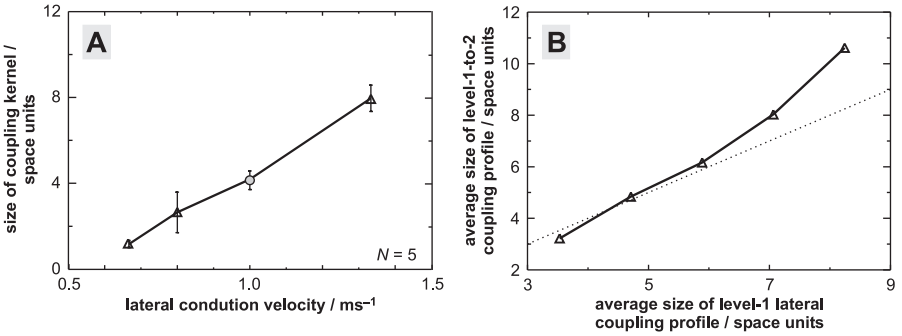

Fig. 7.9. (**A**) As a result of Hebbian learning, the size of the synaptic weight profile (coupling kernel) of lateral linking connections within level-1 becomes directly proportional to the lateral conduction velocity. (**B**) The size of level-1 synchronization fields determines the size of receptive fields of level-2 neurons. Synaptic weight profiles of level-1-to-2 feeding connections evolve correspondingly to synaptic weight profiles of level-1 lateral linking connections. (Modified from [35])

Spatio-Temporal Structuring of Inter-Level Connectivity

In a second learning period following the learning period within level-1, the excitatory level-1-to-level-2 connections are adapted, also starting from full connectivity (Fig. 7.6, scenario B). Again, as a result of Hebbian correlation learning [36], the feed-forward divergence retracts to a limited spatial range which is given by the size of the level-1 synchronization fields, i.e., excitatory forward connections from neurons within a level-1 synchronization field (sending near-synchronized spike packages) converge onto one level-2 neuron (Fig. 7.9B). This convergent projection pattern even emerges if the

feed-forward connections and the level-2 lateral connections are modeled with distance-independent constant delays (Fig. 7.6, scenario C). The physiological interpretation of this result is that the size of level-1 synchronization fields (in visual area V1) can determine the size of level-2 receptive fields (in area V2). Indeed, synchronization fields in V1 and classical receptive fields in V2 of the monkey do have similar sizes. Since equivalent considerations should hold for projections from the retina to V1, the model accounts for the emergence not only of a spatially regular, but also of a retinotopically organized connectivity.

Traveling γ-Waves with Altering Phase Relations

After the learning period, we wanted to investigate the network dynamics. To compare the results with experimental data, we added local inhibitory feedback neurons and provided a sustained spatially homogeneous input to level-1 neurons. This inhibition did not invalidate the previous results, because its dynamics rarely overlap with the learning process. This model reproduces the phenomenon of waves with jittering phase relations, traveling in random directions, just as it was observed in the primary visual cortex (Fig. 15.2) [12, 16]. Traveling waves of γ-activity, though concentrically expanding, have already been described in different cortical areas of different animal species (e.g., [43]). The varying phase relations in our model as well as the more rapid spatial decline of γ-coherence (compared to γ-wave probability) are consistent with the experimental data (Figs. 15.4AB,8.5). Formation of γ-waves in the model results from the locally restricted inhibition, the lateral conduction velocity, and the steep spatial decline of coupling strength [35]. It seems probable that cortical γ-waves are also strongly depending on the lateral conduction velocities, because the distribution of γ-wave velocities (Fig. 15.2C) is similar to the distribution of spike conduction velocities of lateral connections in primary visual cortex. These velocities have been estimated in different preparations, including rat slices and in vivo recordings from cats and monkeys, to range between 0.1 and $1.0\,\mathrm{m\,s^{-1}}$ (review: [13]).

In conclusion, the lateral conduction velocities in primary visual cortex, combined with Hebbian correlation learning, can explain the restricted spatial range of γ-synchrony and the occurrence of traveling γ-waves with random phase relations. They can also account for the larger receptive fields at higher processing levels and for the emergence and stability of topographic visual (and other sensory) representations without the need for visual (sensory) experience. During visual experience, of course, similar influences on synchronization-field and receptive-field size and on topographic stability are probably operative at successive levels of processing, including other parts of the visual system. As the traveling waves can cover the entire representation of an object's surface in the primary visual area, we propose that phase con-

tinuity of γ-waves may constitute a mechanism that supports the coding of object continuity in visual cortex [12].

7.3.3 Model Explaining Figure-Ground Segregation and Induced Modulations at Lower Frequencies by Slower and More Globally Acting Feedback Circuit

In a further approach the above model of the visual cortex has been expanded by using orientation-selective excitatory neurons and two types of inhibitory neurons with different spatio-temporal properties. However, the lateral connections among the excitatory neurons were modeled without delay and learning has been excluded in order to keep the complexity of the network within limits in order to understand its processing. Fig. 7.10A shows a simplified wiring diagram of this model. The spiking neurons (Fig. 7.10B) have linearly and nonlinearly acting synapses and are retinotopically arranged in two primary layers with receptive fields at perpendicular orientation preferences. Additionally to the fast inhibitory feedback loop, serving neurons with similar orientation preference and generating local γ-rhythms (see above and Fig. 8.5), a slow shunting inhibition is added in this model that forms a feedback circuit among neurons with overlapping receptive fields and receive input from, as well as feed output to, excitatory neurons of all orientation preferences.

Decoupling of γ-Signals Across Figure-Ground Contour

In the figure-ground experiment, representations of different scene segments in primary visual cortex (area V1) were decoupled in their γ-activities (Fig. 15.1B,D), while the same sites showed substantial γ-coupling when representing one coherent scene segment. Analogous results are obtained with the model (Fig. 15.1C,E). It explains the reduced γ-coherence as a blockade of lateral coupling at the position of the contour representation due to several effects: First, neurons responding preferentially to the horizontal grating are only weakly activated by the vertical contour. Second, their activity is even more reduced by the orientation-independent slow shunting inhibition that is evoked by the strongly activated vertically tuned neurons at the contour. As a consequence, neurons activated by the horizontal grating near both sides of the contour can not mutually interact, because the orientation-selective lateral coupling is interrupted by the inhibited horizontally tuned neurons at the contour representation. The resulting decoupling of inside and outside representations is not present during the first neural response transient after stimulus onset (Fig. 15.1D,E) since the sharp, simultaneous response onset common to both orientation layers denotes a highly coherent broad-band signal which dominates internal dynamics. Note that orientation-selectivity was

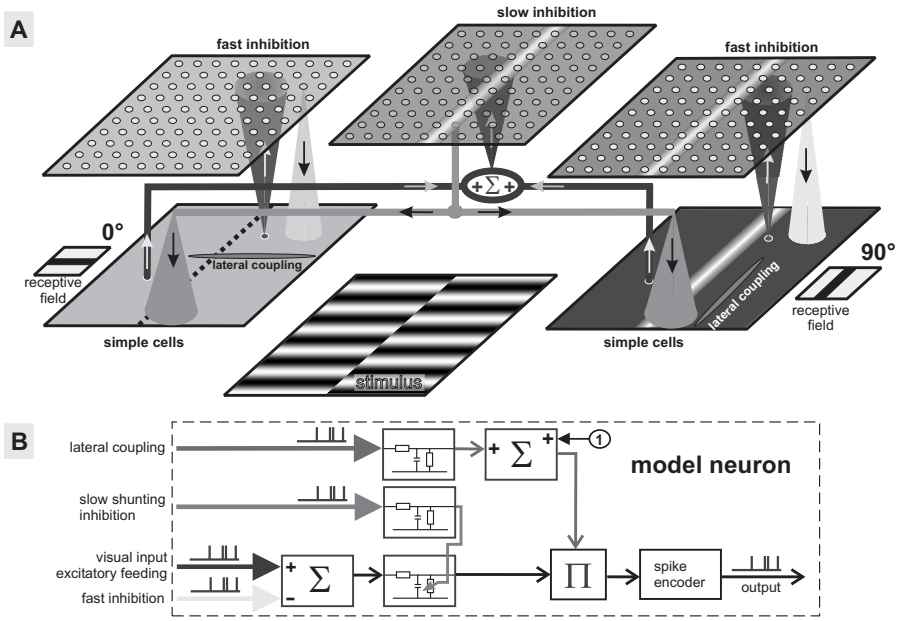

Fig. 7.10. (**A**) Simplified model of primary visual cortex with two retinotopic layers (left and right) of orthogonal orientation detectors. Each layer consists of an excitatory (simple cells at 0 and 90) and an inhibitory sublayer forming fast, local feedback loops preferring the γ-frequency range (Fig. 7.7). The cones between layers indicate direction and width of divergent projections of each single neuron. Modulatory (facilitatory) lateral coupling is confined to excitatory neurons of the same orientation preference with coaxially aligned receptive fields. Both orientation maps share an additional sublayer (middle) mediating slow, local shunting inhibition. To account for stochastic input from brain regions excluded from the model, all neurons receive independent broad-band noise. (**B**) The spike-coding model neuron with dynamic threshold [27] is extended by inputs exerting shunting inhibition on the feeding pathway. Synapses are modeled by leaky RC-filters, lateral modulatory input is offset by a value of +1 and then coupled to the feeding pathway by multiplication

implemented for the sake of comparability with the experimental data. This does not limit the general validity of this model, since any object border constitutes a discontinuity in at least one visual feature dimension, and therefore an analogous argumentation always holds for other local visual features.

7.3.4 Spatial and Temporal Aspects of Object Representations

We have seen that within an object's representation in primary visual cortex (V1), locally synchronized γ-activations emerge that overlap in space and time and thereby support the formation of γ-waves traveling across the object's

surface representation with random phase relations. When waves of γ-activity travel across V1, this is paralleled by quasi-synchronous activity of those neurons in area V2 having corresponding receptive field positions [3, 5, 7], i.e., those receiving input from, and sending γ-feedback to, corresponding V1 neurons. Thus, adjacent V2 neurons, driven simultaneously by adjacent parts of a traveling wave, will also form a traveling wave of γ-activity (with similar extent, velocity and direction if projected to visual space). We expect such an argumention to hold for subsequent stages of processing, provided that they are retinotopically arranged, are activated by bottom-up input, and have fast inter-areal feedback (compared to a half-cycle of a γ-wave). Accordingly, quasi-synchrony should generally be present among neurons with overlapping receptive field positions across cortical levels connected via fast feed-forward-backward loops (e.g., as among V1-V2 and V1-MT [13, 44])). As the traveling waves are γ-activities and we observed γ-decoupling across the cortical representation of a figure-ground contour (explained in our model by the slow inhibition of neurons at the contour), we assume that the waves do not pass object contour representations with any figure-ground feature contrast. *Object continuity* across the entire surface may thus be coded by *phase continuity* of traveling γ-waves.

7.4 Summary

We investigated neural mechanisms of associative processing by considering a variety of flexible forms of signal coupling. In particular, we were interested in associations of local visual features into perceptually coherent visual objects by transient synchronization. In our recent experiments in monkeys, we have shown that local synchrony among γ-activities correlates with perceptual modulation, which supports the hypothesis of object representation by synchronization in the visual cortex. The synchronization hypothesis for larger cortical object representations, however, has been challenged by our experimental finding that γ-synchrony in primary visual cortex (V1) already drops to noise levels across few (4–6) millimeters of cortex. We can explain this restriction by the randomly changing phase relations among locally synchronized patches, which, however, form continuous waves of γ-activity, traveling across object representations. Extending the initial synchronization hypothesis, we propose that phase continuity of these waves may support the coding of object continuity across intermediate and longer ranges within V1.

We have discussed the different types and ranges of experimentally observed signal coupling on the basis of visual cortex models with locally coupled, spike-coding neurons. In these models, the lateral, activity-dependent facilitatory connections with distance-dependent delays are the most important feature for explaining synchronous activity. They can account for lo-

cal and medium-range γ-synchronization, the occurrence of γ-waves and the limited extent of γ-synchrony. Hebbian learning of these connections can explain the stabilization of cortical retinotopy and the larger receptive fields at successive levels of visual cortical processing. Fast local feedback inhibition in our models can generate local γ-oscillations and support local synchrony, while slow shunting-inhibitory feedback supports figure-ground segregation by decoupling activities within neighboring cortical representations of figure and background. In conclusion, we propose that the hypothesis of associative processing by γ-synchronization be extended to more general forms of signal coupling.

References

1. Reitboeck HJ. A multi-electrode matrix for studies of temporal signal correlations within neural assemblies. In: Basar E et al., editors. Synergetics of the Brain. Berlin: Springer, 1983;174–182.
2. von der Malsburg C, Schneider W. A neural cocktail-party processor. Biol Cybern 1986;54:29–40.
3. Eckhorn R, Bauer R, Jordan W, Brosch M, Kruse W, Munk M, et al. Coherent oscillations: a mechanism of feature linking in the visual cortex? Multiple electrode and correlation analyses in the cat. Biol Cybern 1988;60:121–130.
4. Gray CM, König P, Engel AK, Singer W. Oscillatory responses in cat visual cortex exhibit inter-columnar synchronization which reflects global stimulus properties. Nature 1989;338:334–337.
5. Eckhorn R. Oscillatory and non-oscillatory synchronizations in the visual cortex of cat and monkey. In: Pantev C, Elbert T, and Lütkenhöner B, editors. Oscillatory event-related brain dynamics. New York: Plenum Press, 1994;115–134.
6. Kreiter A, Singer W. Oscillatory neuronal responses in the visual cortex of the awake macaque monkey. Eur J Neurosci 1992;4:369–375.
7. Frien A, Eckhorn R, Bauer R, Woelbern T, Kehr H. Stimulus-specific fast oscillations at zero phase between visual areas V1 and V2 of awake monkey. Neuroreport 1994;5:2273–2277.
8. Gray CM. The temporal correlation hypothesis of visual feature integration: still alive and well. Neuron 1999;24:31–47.
9. Eckhorn R. Neural mechanisms of visual feature binding investigated with microelectrodes and models. Vis cogn 1999;6:231–265.
10. Frien A, Eckhorn R. Functional coupling shows stronger stimulus dependency for fast oscillations than for low-frequency components in striate cortex of awake monkey. Eur J Neurosci 2000;12:1466–1478.
11. Wertheimer M. Untersuchungen zur Lehre von der Gestalt: II. Psychologische Forschung. 1923;4:301–350.
12. Gabriel A, Eckhorn R. Multi-channel correlation method detects traveling gamma-waves in monkey visual cortex. J Neurosci Methods 2003;131:171–184.

13. Nowak LG, Bullier J. The timing of information transfer in the visual system in extrastriate cortex in primates. In: Rockland et al., editors. Cerebral Cortex. New York: Plenum Press, 1997;205–240.
14. Bruns A, Eckhorn R. Task-related coupling from high- to low-frequency signals among visual cortical areas in human subdural recordings. Int J Psychophysiol 2004;51:97–116.
15. Gail A, Brinksmeyer HJ, Eckhorn R. Contour decouples gamma activity across texture representation in monkey striate cortex. Cereb Cortex 2000;10:840–850.
16. Eckhorn R, Bruns A, Saam M, Gail A, Gabriel A, Brinksmeyer HJ. Flexible cortical gamma-band correlations suggest neural principles of visual processing. Vis cogn 2001;8:519–530.
17. Woelbern T, Eckhorn R, Frien A, Bauer R. Perceptual grouping correlates with short synchronization in monkey prestriate cortex. Neuroreport 2002;13:1881–1886.
18. Steriade M, Amzica F, Contreras D. Synchronization of fast (30–40 Hz) spontaneous cortical rhythms during brain activation. J Neurosci 1996;16:392–417.
19. McGuire BA, Gilbert CD, Rivlin PK, Wiesel TN. Targets of horizontal connections in macaque primary visual cortex. J Comp Neurol 1991;305:370–392.
20. Bosking WH, Crowley JC, Fitzpatrick D. Spatial coding of position and orientation in primary visual cortex. Nature Neurosci 2002;5:874–882.
21. Jefferys JGR, Traub RD, Whittington MA. Neuronal networks for induced 40 Hz rhythms. Trends Neuosci 1996;19:202–208.
22. Chang HJ, Freeman WJ. Parameter optimization in models of the olfactory neural system. Neural Networks 1996;9:1–14.
23. van Vreeswijk C, Abbott LF, Ermentrout GB. When inhibition not excitation synchronizes neural firing. J Comput Neurosci 1994;1:313–321.
24. Freeman WJ. Feedback models of gamma rhythms. Trends Neurosci 1996;19:468–470.
25. Bush P, Sejnowski T. Inhibition synchronizes sparsely connected cortical neurons within and between columns in realistic network models. J Comput Neurosci 1996;3:91–110.
26. Wennekers T, Palm G. Cell assemblies, associative memory and temporal structure in brain signals. In: Miller R, editor. Time and the Brain. Conceptual Advances in Brain Research, vol. 3. Harwood Academic Publishers, 2000;251–273.
27. Eckhorn R. Cortical processing by fast synchronization: high frequency rhythmic and non-rhythmic signals in the visual cortex point to general principles of spatiotemporal coding. In: Miller R, editor. Time and the Brain. Lausanne: Gordon&Breach, 2000;169–201.
28. Braitenberg V, Schüz A. Anatomy of the cortex. Berlin: Springer, 1991.
29. Eckhorn R, Reiboeck HJ, Arndt M, Dicke P. Feature linking via synchronization among distributed assemblies: simulations of results from cat visual cortex. Neural Comput 1990;2:293–307.
30. Wang DL. Emergent synchrony in locally coupled neural oscillators. IEEE Trans Neural Netw 1995;6:941–948.
31. König P, Schillen TB. Stimulus-dependent assembly formation of oscillatory responses: I. Synchronization. Neural Comput 1991;3:155–166.
32. Li Z. A neural model of contour integration in the primary visual cortex. Neural Comput 1998;10:903–940.

33. Bosking WH, Zhang Y, Schofield B, Fitzpatrick D. Orientation selectivity and the arrangement of horizontal connections in tree shrew striate cortex. J Neurosci 1997;17:2112–2127.
34. Gilbert C. Circuitry, architecture, and functional dynamics of visual cortex. Cereb Cortex 1993;3:373–386.
35. Saam M, Eckhorn R. Lateral spike conduction velocity in visual cortex affects spatial range of synchronization and receptive field size without visual experience: a learning model with spiking neurons. Biol Cybern 2000;83:L1–L9.
36. Kempter R, Gerstner W, van Hemmen JL. Hebbian learning and spiking neurons. Phys Rev E 1999;59:4498–4514.
37. Fox K, Daw N. A model of the action of NMDA conductances in the visual cortex. Neural Comput 1992;4:59–83.
38. Johnson JL. Waves in pulse-coupled neural networks. In: Proc of the World Congress on Neural Networks, vol. 4, 1993;299–302.
39. Johnson JL. Pulse-coupled neural networks. In: Proc of the SPIE Critical Rev, 1994;55:47–76.
40. Trachtenberg JT, Stryker MP. Rapid anatomical plasticity of horizontal connections in the developing visual cortex. J Neurosci 2001;21:3476–3482.
41. Ruthazer ES, Stryker MP. The role of activity in the development of long-range horizontal connections in area 17 of the ferret. J Neurosci 1996;16:7253–7269.
42. Crair MC, Gillespie DC, Stryker MP. The role of visual experience in the development of columns in cat visual cortex. Science 1998;279:566–570.
43. Freeman WJ, Barrie JM. Analysis of spatial patterns of phase in neocortical gamma EEGs in rabbit. J Neurophysiol 2000;84:1266–1278.
44. Girard P, Hupé JM, Bullier J. Feedforward and feedback connections between areas V1 and V2 of the monkey have similar rapid conduction velocities. J Neurophysiol 2001;85:1328–1331.

8

Gestalt Formation in a Competitive Layered Neural Architecture

Helge Ritter, Sebastian Weng, Jrg Ontrup, Jochen Steil

8.1 Introduction

Visual input is extremely high-dimensional: the brightness of each pixel in an image represents one degree of freedom (actually, three degrees of freedom, when we allow for color), and a typical picture offers on the order of several millions of them. Remarkably, our visual system has found highly efficient ways to extract from this extremely high-dimensional input rapidly and reliably a much smaller number of constituents that appear to us as conspicuous "patterns" or "gestalts". This amazing capability has already puzzled the psychologists of the early 20-th century, and the "Gestaltists" have attempted to characterize good "gestalts" by a number of rules to explain general features to which our perception is tuned when organizing its inputs into "meaningful" constitutents [10].

Some of these "classical" gestalt rules are shown schematically in Fig. 8.1, where each row illustrates the gestalt rules of proximity, similarity, topological features such as closure or good continuation, or symmetry properties. As another major grouping principle the Gestaltists observed the visual system's tendency to organize many inputs into figure and ground (bottom row). Also dynamical features, such as shared movement direction ("common fate") can induce the perception of a gestalt, e.g., when we watch fireworks or perceive a directed movement in a chain of merely alternatingly flashing light bulbs.

These "laws" show that our perception is strongly biased: we prefer particular organizations of the visual input over other ones, which on purely logical grounds would be defendable as well. However, the particular gestalt biases of the visual system are well in line with the computational task of decomposing the visual input into constituents that have a high chance of "good correspondence" with physical counterparts in our surroundings [12]

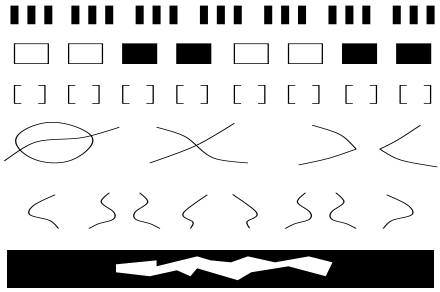

Fig. 8.1. Gestalt laws: proximity, similarity, closure, good continuation, symmetry and figure-ground.

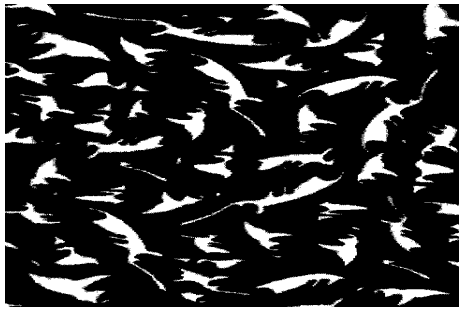

Fig. 8.2. An example where prior knowledge is required.

However, not all of these biases are "hardwired" into our visual system. There are many patterns whose recognition relies on higher-level world knowledge which we only can have acquired by learning. Obvious examples are highly trained patterns such as digits or letters. Another example is depicted in Fig. 8.2 Here, we first discern only irregular white patches on a black "background". Only when looking longer, we discern a pattern[1], which, once we see it, forcefully masks the perception of the former patches as individual units (turning the page by 180^o restores the perception of the patches, illustrating that higher level grouping processes need not be rotationally invariant).

8.2 Gestalt Grouping and Feature Binding

Forming a group or gestalt seems inevitably to require some operation of binding to implement the property that the gestalt is more than the "sum of its parts" (for instance, a suitable subset of the patches in Fig. 8.2 has to be

[1] A hidden face in the middle of the picture

"bound" into the unity of the face, separating it from the background of the remaining patches).

The need for such binding operations arises also in numerous other contexts that require the formation of units from simpler constituents, e.g. elementary features. Fig. 8.3 illustrates the issue for the simple example of representing for two objects the conjunction of their shape and their color: to represent the simultaneous presence of a red round ball and a green triangle require a binding within the four-element feature set { red, green, round, triangular } such that "red" goes with "round" and "green" with "triangular" and not vice versa.

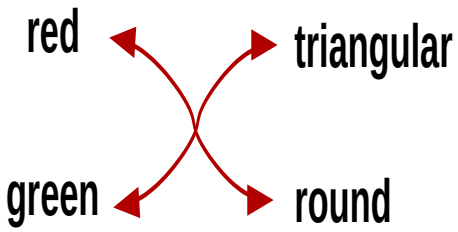

Fig. 8.3. Binding between color and shape attributes.

The problem that such a binding cannot be represented by just the co-presence of neural activity for the individual constituents was first emphasized by Christoph von der Malsburg almost three decades ago [13], together with an elegant proposal for a solution: to use neural synchrony as a means to represent togetherness.

Subsequent research attempting to corroborate or refute this hypothesis has a long and controversial history (for a recent discussion, see [20] and the accompanying special issue of Neuron, as well as the paper by Rainer Eckhorn, this volume). While there exist numerous experimental results that have been interpreted in favor of the brain's use of neural synchrony to represent togetherness of visual stimuli [4, 23], opponents of this hypothesis have pointed out that these results are largely indirect and not necessarily conclusive [22].

In computer science, the binding problem usually is solved by the use of *pointers*. In fact, pointers are a major means to construct the complex data structures required in almost all computer vision or graphics programs[2].

[2] Since the use of pointers has proven to be very error-prone for human programmers, the development of modern programming languages, such as Java, has invested great efforts to "hide" pointers from the programmer. Still, pointers are "working under the hood" even in these languages.

Therefore, considering neural computation as a serious alternative to conventional programming, faces us with the question of how to implement the functionality of pointers within these systems [7]. However, from a computational perspective, we can explore different possibilities more freely than in the context of careful biological modeling. This has motivated us to explore a computational approach that is complementary in that it uses *space* instead of *time* (such as, e.g. [25, 21, 24]) to express binding between features. This is achieved by using a stack of competitively interacting neural layers, each layer competing for a group (and, thereby, roughly playing the role of a "time slice" in synchrony models [25, 21, 24] of binding). We have dubbed this model "Competitive Layer Model" (CLM) [19, 29] and will describe its functionality in the next section.

8.3 The Competitive Layer Model (CLM)

An intuitive explanation of the idea underlying the CLM is most easily given in the context of the simple grouping situation of Fig. 8.3. For each potential group we have to introduce one layer, which has to implement a "feature map" of all features that might be present in a group. So, for the present example, two layers, each consisting of four feature units implementing a "feature map" for the set { red, green, round, triangular }, would be sufficient (Fig. 8.4).

The structuring of a collection of active features into groups (such as (red,round),(green,triangular)) is then expressed by a corresponding sharing of layers by the associated feature cell activities (i.e., a "red" and "round" feature cell active in one layer, and a "green" and "triangular" feature cell active in a second layer).

Of course, we wish this representation to emerge as the result of a suitable interaction dynamics among the units in the layers. To this end we split the required interactions into a lateral (within-layer) and a "vertical" (inter-layer) component. The within-layer component should be excitatory for features that are compatible with a group (e.g., shape-color) and inhibitory between incompatible features (e.g., shape-shape or color-color).

The inter-layer component only connects corresponding locations in all layers (e.g., runs "perpendicularly" through the layer stack). It is pairwise inhibitory in order to enforce for each feature a unique assignment to one layer (i.e., one group). An additional, excitatory interaction to an additional input layer (not shown in Fig. 8.4) imposes the constraint that the superposition of all groups matches a prescribed, to-be-decomposed, input pattern, which is represented by the joint activity of all feature cells of all groups.

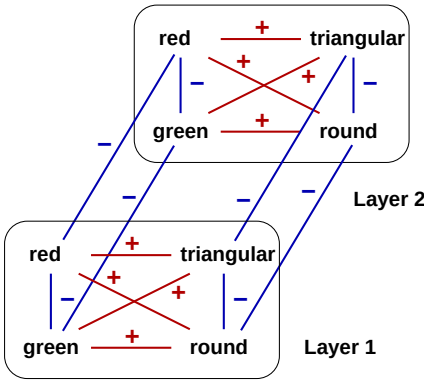

Fig. 8.4. CLM scheme for the simple toy problem of Fig.

More formally, this model can be described as follows.

The neurons are organized in layers $\alpha = 1, \ldots, L$ and columns $r = 1, \ldots, N^3$ where each layer contains all neurons belonging to the same label α and each column contains the neurons belonging to the same image location r. The neurons of each column have access to a local feature vector $\mathbf{m}_r$ (which may augment the spatial position r by additional local image properties, such as color $\mathbf{c}_r$, texture features $\mathbf{t}_r$, or orientation vectors $\mathbf{o}_r$ of a local edge: $\mathbf{m}_r = (r, \mathbf{c}_r, \mathbf{t}_r, \mathbf{o}_r, \ldots)^T$).

The lateral interactions between neurons at locations r, r' of a layer are assumed to be symmetric functions $f(\mathbf{m}_r, \mathbf{m}_{r'})$ of the feature vectors of the associated columns (we will use the shorthand notation $f_{rr'}$ in many places below). To achieve the intended assignment of input features to layers, weights f_{rr} will be excitatory (> 0), if features $\mathbf{m_r}$,$\mathbf{m_{r'}}$ are compatible in the same group, inhibitory (< 0) otherwise. For instance, choosing $f_{rr'}$ as the simple "on-center-off-surround" function

$$f_{rr'} = \begin{cases} 1 & : \quad \| r - r' \| < R \\ -1 & : \quad \| r - r' \| \geq R \end{cases}, \tag{8.1}$$

leads to a grouping according to spatial proximity, where R sets the spatial scale. For more complex tasks, like texture or color segmentation, the lateral connections have to be specified by more complex functions as the later application examples will demonstrate.

The unique assignment of each feature to a single layer is realized by a columnar 'winner-takes-all" (WTA) circuit, which uses mutually symmetric

[3] to simplify notation, we "overload" symbol r by the (discrete) index $\in \{1 \ldots N\}$ identifying a column and the 2-dimensional coordinate vector indicating the associated location in the image.

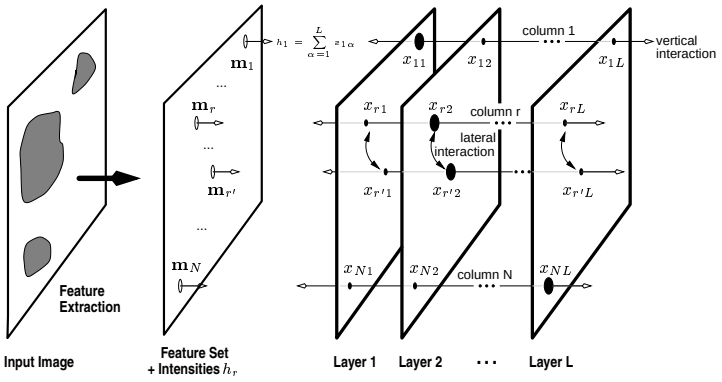

Fig. 8.5. CLM Architecture: Feature extraction from an input image (left) gives rise to a set of local feature vectors $\mathbf{m}_r$ with activities h_r represented in an input layer (second left). Subsequent layers arranged in a stack decompose each h_r into a sum of layer-wise responses $x_{r,\alpha}$ as a result of lateral (within-layer) and vertical (across-layer) interactions. After convergence, each location r elicits a non-zero activity $x_{r,\alpha} > 0$ in maximally one layer α, defining a grouping of the features $\mathbf{m}_r$ into layers $\alpha(r) = \arg\max_\alpha x_{r,\alpha}$.

inhibitory connections with absolute strength $J > 0$ between the neural activities $x_{r\alpha}$ and $x_{r\beta}$ that share a common column r. Due to the WTA coupling, for a stable state of the CLM only a single neuron from one layer can be active within each column [28].

$$\forall r: \quad \forall \beta \neq \hat{\alpha}(r): \quad x_{r\hat{\alpha}(r)} > 0, \quad x_{r\beta} = 0, \tag{8.2}$$

where $\hat{\alpha}(r)$ is the index of the maximally supporting layer characterized by

$$\forall r: \quad \forall \beta \neq \hat{\alpha}(r): \quad \sum_{r'} f_{rr'} x_{r'\hat{\alpha}(r)} > \sum_{r'} f_{rr'} x_{r'\beta}. \tag{8.3}$$

A binding between two feature, associated with the columns r and r', is expressed by simultaneous activities $x_{\hat{\alpha}(r)}$ and $x_{\hat{\alpha}(r')}$, $\hat{\alpha}(r) = \hat{\alpha}(r') = \hat{\alpha}$ that share a common layer $\hat{\alpha}$. Each neuron receives a constant input Jh_r, where h_r specifies the basic amount of activity that is available in each column r. The activity of the single active neuron per column is given by

$$\forall r: \quad x_{r\hat{\alpha}(r)} = h_r + \frac{1}{J} \sum_{r'} f_{rr'} x_{r'\hat{\alpha}(r)}. \tag{8.4}$$

Thus, it suffices to consider only the subset of columns for which $h_r > 0$, i.e., where input is present.

The combination of afferent inputs and lateral and competitive interactions can be formulated into the standard additive activity dynamics

$$\dot{x}_{r\alpha} = -x_{r\alpha} + \sigma\Big(J(h_r - \sum_{\beta} x_{r\beta}) + \sum_{r'} f_{rr'} x_{r'\alpha} + x_{r\alpha}\Big). \tag{8.5}$$

An essential role for the functionality of the CLM plays the threshold function $\sigma(\cdot)$ which is defined by a unsaturated linear threshold function $\sigma(x) = \max(0, x)$ that cuts off negative interactions. As a result, the CLM dynamics corresponds to gradient descent in the energy function

$$E = -J \sum_{r\alpha} h_r x_{r\alpha} + \frac{1}{2} J \sum_{r} \sum_{\alpha\beta} x_{r\alpha} x_{r\beta} - \frac{1}{2} \sum_{\alpha} \sum_{rr'} f_{rr'} x_{r\alpha} x_{r'\alpha}, \tag{8.6}$$

under the constraint $x_{r\alpha} > 0$, since E is non-increasing under the dynamics (8.5) [28]. Dynamical systems of this type have recently attracted interest as candidates for "cortex-inspired" analog silicon circuits [6].

8.4 Some Properties of the Binding Process

The special form of the linear threshold function makes it possible to formulate concrete statements about the behavior of the CLM dynamics. The main statements can be summarized in two theorems about the convergence and assignment properties of the CLM [29].

Convergence Theorem: If $J > \lambda_{\max}\{f_{rr'}\}$, where $\lambda_{\max}\{f_{rr'}\}$ is the largest eigenvalue of the lateral interaction matrix, or $J > \max_r (\sum_{r'} \max(0, f_{rr'}))$, then the CLM dynamics is bounded and convergent.

Assignment Theorem: If the lateral interaction is self-excitatory, $f_{rr} > 0$ for all r, then an attractor of the CLM has in each column r either
(i) at most one positive activity $x_{r\hat{\alpha}(r)}$ with

$$x_{r\hat{\alpha}(r)} = h_r + \frac{1}{J} \sum_{r'} f_{rr'} x_{r'\hat{\alpha}(r)}, \quad x_{r\beta} = 0 \quad \text{for all } \beta \neq \hat{\alpha}(r), \tag{8.7}$$

where $\hat{\alpha}(r)$ is the index of the maximally supporting layer characterized by

$$\sum_{r'} f_{rr'} x_{r'\hat{\alpha}(r)} > \sum_{r'} f_{rr'} x_{r'\beta}, \quad \text{for all } r, \beta \neq \hat{\alpha}(r) \tag{8.8}$$

or,
(ii) all activities $x_{r\alpha}$, $\alpha = 1, \ldots, L$ in a column r vanish and $\sum_{r'} f_{rr'} x_{r'\alpha} \leq -J_r h_r$ for all $\alpha = 1, \ldots, L$.

The dynamics (8.5) has an energy function of the form

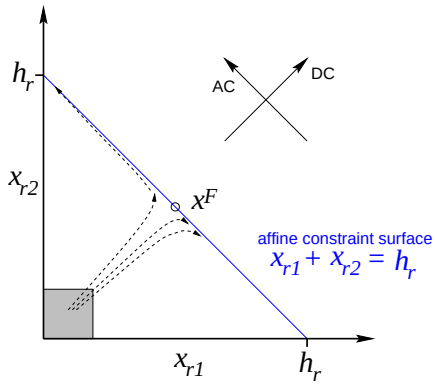

Fig. 8.6. Sketch of the AC and DC eigenmodes of the CLM dynamics for two neuron activities in the same column. The AC modes occur in the hyperplane $\sum_\alpha x_{r,\alpha} = h_r = \text{const}$, the DC mode is responsible for enforcing this constraint.

$$E = -J \sum_{r\alpha} h_r x_{r\alpha} + \frac{1}{2} J \sum_r \sum_{\alpha\beta} x_{r\alpha} x_{r\beta} - \frac{1}{2} \sum_\alpha \sum_{rr'} f_{rr'} x_{r\alpha} x_{r'\alpha}. \tag{8.9}$$

The energy is non-increasing under the dynamics (8.5) [28] :

$$d/dt\ E = -\sum_{r\alpha} E_{r\alpha} \dot{x}_{r\alpha} = -\sum_{r\alpha} E_{r\alpha}(-x_{r\alpha} + \sigma(E_{r\alpha} + x_{r\alpha})) \leq 0, \tag{8.10}$$

where

$$E_{r\alpha} = -\partial E / \partial x_{r\alpha} = J h_r - J \sum_\beta x_{r\beta} + \sum_{r'} f_{rr'} x_{r'\alpha}. \tag{8.11}$$

Thus the attractors of the dynamics (8.5) are the local minima of (8.9) under constraints $x_{r\alpha} \geq 0$. Additionally a kind of annealing process can be included in the dynamics, by extending the energy function with:

$$E' = E + T \sum_{r\alpha} x_{r\alpha}^2, \tag{8.12}$$

which adds a convex term that biases the local minima towards graded assignments and thus "softens" the WTA dynamics. Within the dynamics this introduces a new self-inhibitory term

$$\dot{x}_{r\alpha} = -x_{r\alpha} + \sigma\Big(J(h_r - \sum_\beta x_{r\beta}) + \sum_{r'} f_{rr'} x_{r'\alpha} + (1 - T) x_{r\alpha}\Big). \tag{8.13}$$

Through gradually lowering the self-inhibition T, (8.12) becomes (8.9) and (8.13) becomes (8.5).

A detailed analysis of the annealing process can be found in [28]. The result of this linear analysis is that the CLM-dynamics is driven by two kind of eigenmodes called the AC- and DC-eigenmodes (sketched in Fig. 8.6), whose eigenvalues and eigenvectors mainly depend on the matrix F of lateral weights $f_{rr'}$. The DC-eigenmodes are driving the equilibration of the layer activities, while the AC-eigenmodes are responsible for the winner-takes-all behavior. The stability of both sets of modes can be controlled with the "temperature" parameter T.

8.5 Implementation Issues

The CLM dynamics can be simulated efficiently with a Gauß-Seidel approach of solving iteratively the fixed point equations of (8.5) for a randomly chosen activity $x_{r\alpha}$ while all other activities are held constant [28, 5]. The algorithm can be implemented in the following way:

1. Initialize all $x_{r\alpha}$ with small random values around
   $x_{r\alpha}(t=0) \in [h_r/L - \epsilon, h_r/L + \epsilon]$.
   Initialize T with greatest eigenvalue of matrix $\{f_{rr'}\}$.
2. Do $N \cdot L$ times: Choose (r, α) randomly and update $x_{r\alpha} = \max(0, \xi)$, where
   $\xi := \frac{J(h_r - \sum_{\beta \neq \alpha} x_{r\beta}) + \sum_{r' \neq r} f_{rr'} x_{r'\alpha}}{J - f_{rr} + T}$
3. Decrease T by $T := \eta T$, with $0 < \eta < 1$. Go to step 2 until convergence.

8.6 Image Preprocessing

Before we can apply the CLM to images we require some preprocessing in order to achieve a dimension reduction from the extremely high-dimensional pixel input to a more manageable dimensionality. In our visual system, such dimensionality reduction starts already in the retina, where the activity values of the about 10^8 rods and cones are "compressed" into an activity pattern of the about 1.5 million fibres of the optical nerve connecting each eye (via the geniculate bodies, where further recoding occurs) to the visual cortex.

The response properties of many cells in the visual cortex have been found to coarsely resemble local Gabor-filters [8]. A Gabor filter can be represented

by a basis function parametrized by a position vector $r \in \mathrm{R}^2$, a wave vector $k \in \mathrm{R}^2$ and a range σ:

$$g_{r,k,\sigma}(x) = \cos(k \cdot (x - r)) \exp(-(x - r)^2/2\sigma^2) \tag{8.14}$$

The "overlap" or scalar product

$$c_{r,k,\sigma} = \sum_x g_{r,k,\sigma}(x) I(x) \tag{8.15}$$

of a Gabor filter with an image intensity function $I(x)$ can be interpreted as a measure of the contribution of a spatial frequency k to the local image structure within a radius σ around location r. A neuron implementing a response described by $c_{r,k,\sigma}$ thus represents spatial and frequency information for a local image patch simultaneously (and it can be shown that the choice of Gabor profiles leads to a compromise for representing the two conflicting observables location and spatial frequency that in a certain sense is optimal [2]).

From the set of Gabor filter responses $c_{r,k,\sigma}$ one can reconstruct an approximation $\hat{I}(x)$ of the original image as

$$\hat{I}(x) = \sum_{r,k,\sigma} c_{r,k,\sigma} \tilde{g}_{r,k,\sigma}(x) \tag{8.16}$$

where $\tilde{g}_{r,k,\sigma}(x)$ denote the dual basis functions for the $g_{r,k\sigma}$.

Data from psychophysical measurements have led to sampling grids (r, k, σ) in position-frequency-scale space that permit rather accurate modeling of the measured position-frequency-scale variation of our ability to discriminate local contrast patterns [26].

For the following experiments, we have used a simplified filter arrangement, consisting of an "artificial fovea" comprising three octaves of spatial frequency, with five directions uniformly separated by 72^o. The range σ is chosen proportional to the wave length of the associated wave number k (Fig. 8.7).

In addition to the sampling of r, k, σ the visual cortex also performs some sort of pooling process where input stimuli from neighboring points are pooled together. Following a proposal by [15], we compute the following pair of local feature coefficients

$$M_k(r) = c_k(r) * G_k(r) \tag{8.17}$$

$$S_k(r) = \sqrt{(c_k(r) - M_k(r))^2 + G_k(r)} \tag{8.18}$$

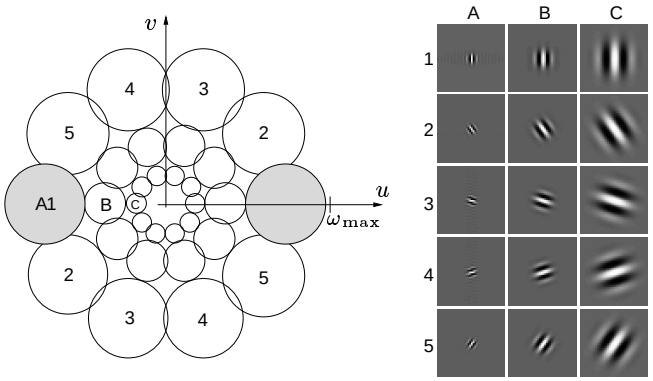

Fig. 8.7. Artificial "fovea" for image preprocessing.

where $*$ denotes the convolution operation, $c_k(r)$ is the response in channel k after a nonlinear scaling with a contrast transfer function, and $G_k(r)$ is the corresponding Gaussian filter kernel given by

$$G_k(r) = e^{-\frac{k^2}{2\rho_k^2}},$$

where the parameter ρ_k is a critical choice reflecting the size of the pooling area. A reliable description of the local feature statistics around r calls for large sizes. On the other hand, an accurate localization of feature positions demands smaller sizes. In our experiments we found a heuristical value of three times the size of the Gabor range σ as a good compromise. As a result, for each position r in the input image, we get a 30-dimensional feature vector $\mathbf{m}(r)$ describing the local texture at that point:

$$\mathbf{m}_r = (M_1(r), \ldots, M_{15}(r), S_1(r), \ldots, S_{15}(r))^T \tag{8.19}$$

This leads to a 30-dimensional feature vector at each image pixel $r = (x, y)$. To further reduce processing burden, we use subsampling on 8×8 pixel blocks and project at each (subsampled) location the 30-dimensional feature distribution on the 4 principal components of maximal variance. For more details, see [18].

8.7 Interaction Function

As already indicated before, it is the interaction function $f_{rr'}$ that determines which features are "compatible" (such as "color" and "shape" in the introductory toy example) to be bound together as a group, and which features cannot be bound for lack of compatibility. For the perceptual grouping experiments reported below, a suitable interaction was chosen as

$$f_{rr'} = \exp\left[-\frac{d^2_{text}(r,r')}{R_1^2}\right] + \gamma \cdot \exp\left[-\frac{d^2_{pos}(r,r')}{R_2^2}\right] - I \tag{8.20}$$

Here, $d_{pos}(r,r')$ is the position distance of locations r and r', and $d_{text}(r,r')$ is a measure of the difference of the local textures around r and r'. Interpreted in Gestalt psychology terms, the first part can be identified with the Gestalt law of similarity, which states that similar features are bound together; the second part corresponds to the Gestalt law of spatial proximity, with the constant γ controlling the weighting between these two principles. The parameter $I > 0$ causes inhibition of features that are both dissimilar and far apart.

While d_{pos} is straightforward, our choice for d_{text} was motivated by a proposal of Manjunath and Ma [14] and chosen as the L_1-norm of the difference $\hat{p}_r - \hat{p}_{r'}$ between the (normalized[4]) vectors $\hat{p}_r$, where the unnormalized p_r is the feature vector $\mathbf{m}(r)$ of Eq. (8.19), projected into the eigenspace spanned by the 4 leading principal components (for details, cf. [18]). Parameters were chosen as $\gamma = 0.6$, $I = 0.5$, $R_1 = 6.6$, $R_2 = 0.63$ and all held constant for the examples shown in the next section.

8.8 "Perceptual Experiments"

With the described preprocessing, we can perform "artificial perceptual experiments" to compare the grouping behavior of the CLM for various images with that of human subjects. Fig. 8.8 shows examples for arrangements of dot patterns (upper row) which exemplify the laws of proximity and similarity.

The lower row shows the superimposed responses of the CLM layers. Since in the converged state each location r can at most have a single layer $\alpha(r)$ with non-vanishing activity $x_{r,\alpha(r)} > 0$, it suffices to directly display the "layer indicator function" $\alpha(r)$ (using colors to distinguish different layers and black for the absence of activity in *all* layers).

As can be seen, in the case of equidistant dots (left), the system just performs (except for edge effects) figure-ground separation. Closer proximity, e.g. along the horizontal direction (middle) causes in addition the activation of horizontal bars, indicating a grouping by proximity, without loosing the identity of the dots themselves. Returning to an equidistant arrangement, but instead introducing different types of dots again creates a corresponding grouping - this time according to similarity (right).

[4] normalization consisted of dividing each component of p_r by the standard deviation of all its values over the input grid

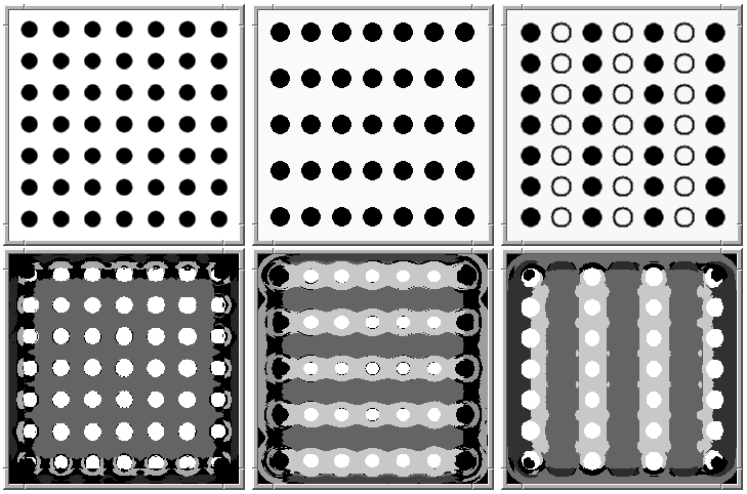

Fig. 8.8. Grouping of dot patterns. Top: input patterns. Bottom: CLM layer activities.

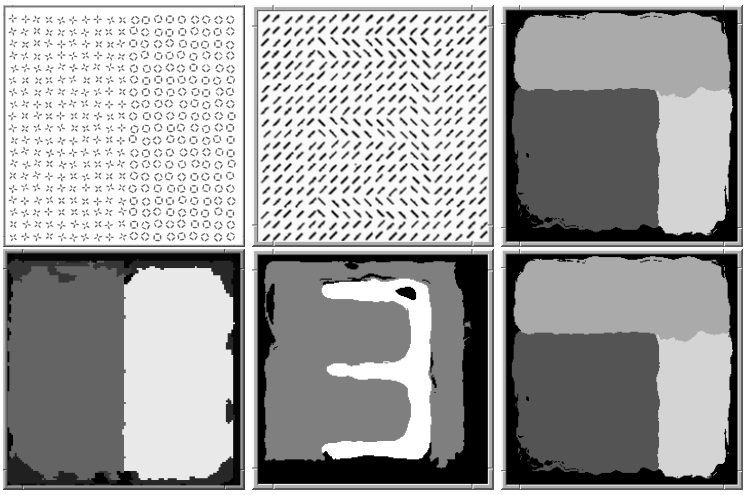

Fig. 8.9. Top row: types of testimages used for the benchmark. The rightmost image is an example where preattentive human perception misses the segregation of the lower left square area, in line with the CLM result.

Fig.8.9 shows a different set of examples, this time with regions demarkated by similarity in local texture features. Remarkably, in the rightmost column the CLM only "sees" three areas. However, if we take a closer (serial) look, we can distinguish one further border, which is not perceived preattentively. Thus, the model can mimic some effects that have been explained in terms of interactions of elementary texture elements ("textons") [9].

Finally, Fig. 8.11 depicts a last set of examples, demonstrating the grouping of line terminations into an apparent contour (left) and its disappearance when the lines are getting too sparse (middle). The right column finally presents an example for natural textures from the Brodatz album [1].

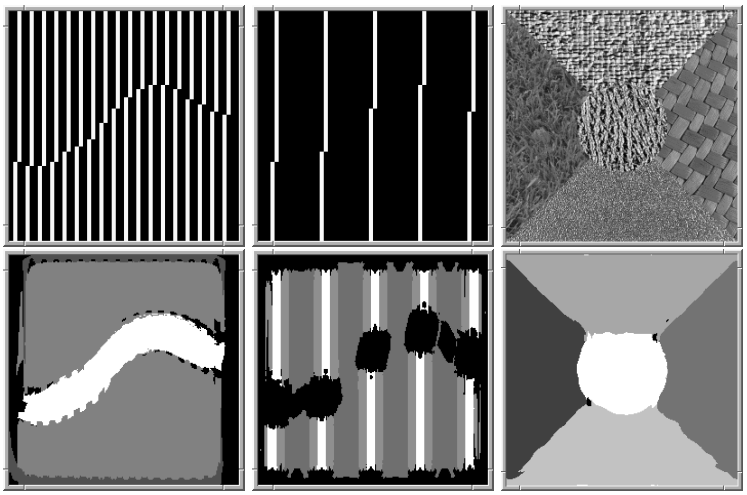

Fig. 8.10. In the top left a pattern of broken lines is shown. Because the points marked by the discontinuities lie on a smooth line, we perceive a wavelike illusory contour. The grouping result obtained with the CLM also shows this wavelike contour in the bottom row.

In order to give a quantitative comparison of our model's performance with human data, we have constructed a set of seven texture pairs according to [11] (one example was already depicted in Fig.8.9 on the left). For each pair, we created 10 texture images of 512x512 pixels with random orientation of the elements plus an additional positional random jitter of 4 pixels. Table 8.8 shows that the rank order of human discriminability of these patterns according to [11] is almost identical to the rank order of the classification rates of the CLM, indicating a significant similarity of the CLM grouping to human texture perception (for details, see [18]).

Texture Pair	Psychophysical Data (Discriminability)	CLM Model (Classification rate)
(a)	100	89.1
(b)	88.1	89.3
(c)	68.6	82.1
(d)	52.3	79.7
(e)	37.6	74.7
(f)	30.6	69.7
(g)	30.3	69.0

Table 1: Comparison of psychophysical data from [11] with CLM Model's performance. The *rank order* of the classification rate of the CLM matches the rank order of the psychophysical data remarkably well.

8.9 Learning the Interaction Function

While we have shown that the heuristic specification of the interaction functions $f_{rr'}$ given in Sec. 8.7 can also be adapted to other exacting applications, such as the identification of cell contours in microscope images ([16],[17]), the required hand tuning can be cumbersome and certainly is undesireable for a broader use of the CLM in practical computer vision tasks.

This has motivated the search for learning approaches that permit the data driven construction of a good interaction function from a set of example images with specified groupings in form of target labels $\hat{\alpha}(r)$. These groupings are transferred into target states of the CLM $\mathbf{y} = (y_{11}, \ldots, y_{N1}, \ldots, y_{NL})^T$.

Some useful guidance is given by the stability conditions that must be met for any activity pattern in the converged state:

$$\forall r: \quad : \forall \beta \neq \hat{\alpha}(r): \quad \sum_{r'} f_{rr'} y_{r'\hat{\alpha}(r)} > \sum_{r'} f_{rr'} y_{r'\beta}. \tag{8.21}$$

If we only require the stability of a single pattern, we can write down the following analytic solution from "group contrasts" [27]:

$$\hat{f}_{rr'} = \sum_{\mu\nu} (\mathbf{y}_\mu - \mathbf{y}_\nu)(\mathbf{y}_\nu - \mathbf{y}_\mu)^T, \tag{8.22}$$

where $\mathbf{y}_\nu$ are the layer-wise subvectors $\mathbf{y}_\nu = (y_{1\nu}, \ldots, y_{N\nu})$ of the target state $\mathbf{y}$ and

$$y_{\nu,r} = \begin{cases} 1 & : \quad \hat{\alpha}(r) = \nu \text{i.e., } m_r \text{ belongs to group } \nu \\ 0 & : \quad \hat{\alpha}(r) \neq \nu \text{else} \end{cases}. \tag{8.23}$$

However, this is only an expression in (r, r')-space and does not include any spatial variation of the features $\mathbf{m}_r$. A straightforward way to generalize this to arbitrary $(\mathbf{m}_r, \mathbf{m}_{r'})$-pairs can be implemented by the following steps:

1. sample $(\mathbf{m}_r, \mathbf{m}_{r'})$-pairs from training inputs
2. use associated $f_{r,r'}$ values from the above 1-pattern-solution as target values
3. apply a standard machine learning algorithm (e.g. SVM classifier or multilayer perceptron (MLP)) to create a mapping $\phi : (\mathbf{m}_r, \mathbf{m}_{r'}) \rightarrow f_{r,r'}$ that yields the desired interpolation in $(\mathbf{m}_r, \mathbf{m}_{r'})$-space.

A major drawback of this approach is the need for one evaluation of the trained network *for each* interaction pair in the CLM: this makes the method very time-consuming and practically rules out the application of the SVM. The MLP is considerably faster, but we found it rather difficult to achieve good training results for the required interaction function: the MLP strongly suffers from the danger of overfitting to the feature positions r if only one pattern is presented for learning.

Therefore, in [27] we developed an alternative approach based on an expansion of $f_{rr'}(m_r, m_{r'})$

$$f_{rr'}(m_r, m_{r'}) = \sum_k c_k \cdot b^k_{rr'}(m_r, m_{r'}) \tag{8.24}$$

into a suitable set of basis functions b_k, thereby reducing the learning task to the determination of the required expansion coefficients c_k. Since in most grouping tasks the important information mainly lies in the similarity or dissimilarity of the features $(\mathbf{m}_r, \mathbf{m}_{r'})$ it has proven beneficial to first transform the $(\mathbf{m}_r, \mathbf{m}_{r'})$-space into a dissimilarity space so that "relevant" dissimilarities can be made more explicit. A rather flexible way to achieve this is to choose a number of (application specific) dissimilarity functions $d_1(\cdot,\cdot), \ldots, d_P(\cdot,\cdot)$ for mapping each pair $(\mathbf{m}_r, \mathbf{m}_{r'})$ into a P-dimensional vector $\mathbf{D}(\mathbf{m}_r, \mathbf{m}_{r'})$:

$$\mathbf{D}(\mathbf{m}_r, \mathbf{m}_{r'}) = (a_1 d_1(\mathbf{m}_r, \mathbf{m}_{r'}), \ldots, a_P d_P(\mathbf{m}_r, \mathbf{m}_{r'}))^T. \tag{8.25}$$

Examples of dissimilarity functions are the local distance $\| \mathbf{r} - \mathbf{r}' \|$ or distances in color $\| \mathbf{c}_r - \mathbf{c}_{r'} \|$ of texture space $\| \mathbf{t}_r - \mathbf{t}_{r'} \|$ as also component-wise distances in these feature vectors. The dissimilarity functions do not necessarily need to fulfill properties of a distance metric, and choices such as e.g. the scalar product $\mathbf{o}_r \cdot \mathbf{o}^T_{r'}$ of two orientation vectors $\mathbf{o}_r$ and $\mathbf{o}_{r'}$ are admissible as well. The only necessary condition is that the distance functions are symmetric under feature exchange $d_p(\mathbf{m}_r, \mathbf{m}_{r'}) = d_p(\mathbf{m}_{r'}, \mathbf{m}_r)$ to guarantee

the symmetry of the lateral interaction weights. The scaling factors a_p permit to implement a normalization of the different distance functions $d_p(\cdot,\cdot)$ to the same range of values.

Finally, we have to make a choice of a set of basis functions in the transformed space. A computationally very attractive scheme results if we use as basis functions the characteristic functions of a Voronoi tesselation generated from a number of prototype vectors adjusted by means of a training data set: this allows to reduce the computation of the expansion coefficients c_k to a simple counting of hits in Voronoi cells. The necessary computations can be compactly summarized in the following two steps:

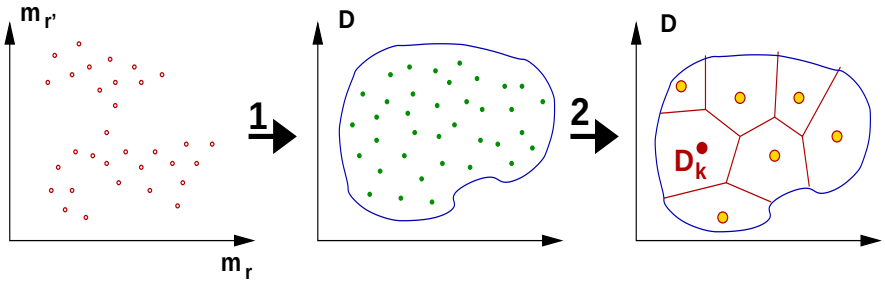

Fig. 8.11. Interaction quantization for learning: A transformation of feature pairs from a training set (left) into a "dissimilarity space" (center) and a subsequent Voronoi tesselation (generated by prototype vectors $\mathbf{D}_k$) provides the basis to approximate the desired interaction function as a step-wise constant function on the Voronoi cells (right).

1. **Adaptive tesselation in the transformed space:** using a suitable vector quantization algorithm, position a number of prototype vectors $\mathbf{D}_1 \ldots \mathbf{D}_K$ to define a Voronoi tesselation of the training data in the transformed space. The main parameter to be chosen here is the number K of prototype vectors to use.

2. **Computing the interaction function:** Using the characteristic functions on the Voronoi cells V_k as basis functions, the interaction function can be cast into form

$$\hat{f}_{rr'}(\mathbf{m}_r, \mathbf{m}_{r'}) = c_k^+ - \Lambda c_k^-, \tag{8.26}$$

with

$$k = arg\min_k \parallel \mathbf{D}(\mathbf{m}_r, \mathbf{m}_{r'}) - \mathbf{D}_k \parallel, \tag{8.27}$$

where Λ is a weighting parameter and the expansion coefficients c_k can be obtained by simple counting:

$$\begin{array}{l} c_k^+ = \#\text{of within-group } \mathbf{D}(\mathbf{m}_r, \mathbf{m}_{r'})\text{-samples in } V_k \\ c_k^- = \#\text{of across-group } \mathbf{D}(\mathbf{m}_r, \mathbf{m}_{r'})\text{-samples in } V_k \end{array} \tag{8.28}$$

The choice of Λ allows to control the degree of segmentation: small values of Λ favor few and large groups, while large values of Λ favor many small groups. For more details, the reader is referred to [27].

8.10 Experiments with Artificial Data

In this section, we illustrate how the above learning algorithm can generate interaction fields for the grouping of line segments into contours. Here, the line segments $\mathbf{m}_r = (\mathbf{r}, \mathbf{o}_r)$ are represented by 2D position $\mathbf{r}$ and an undirected orientation vector $\mathbf{o}_r$ of the lines, while the distance space between features is given by the local distance and the inner angle between two lines segments.

Training data consisted always of a single image, containing several hundred line segments forming the contours of five randomly positioned contours of circles (Fig. 8.12 top left), squares (Fig. 8.12 top center) and triangles (Fig. 8.12 top right), respectively (since already a single image usually contains a very large number of line segment pairs a single image can usually offer enough training data to estimate a good interaction function). The learnt interaction function is depicted in the corresponding diagrams below: each figure depicts for a horizontally oriented "reference" line segment (positioned at the center of the figure) the distribution of excitatorily connected line orientations within a 11x11 neighborhood around the reference line segment. Longer line segments indicate stronger excitation, whereas only weakly excitory connections are indicated with correspondingly shorter lines. From this visualization it becomes apparent that the loci of excitatory connectivity are distributed such as to favor the continuation of the reference line segment in a way that follows the geometrical shape that was used during training.

The second set of pictures (Fig. 8.13) shows some grouping results obtained with a CLM using the trained interaction functions. The first two pictures show grouping results for almost "perfect" input shapes, while the last two pictures illustrate the effect of the grouping in the presence of strong positional or orientational jitter in the input arrangements.

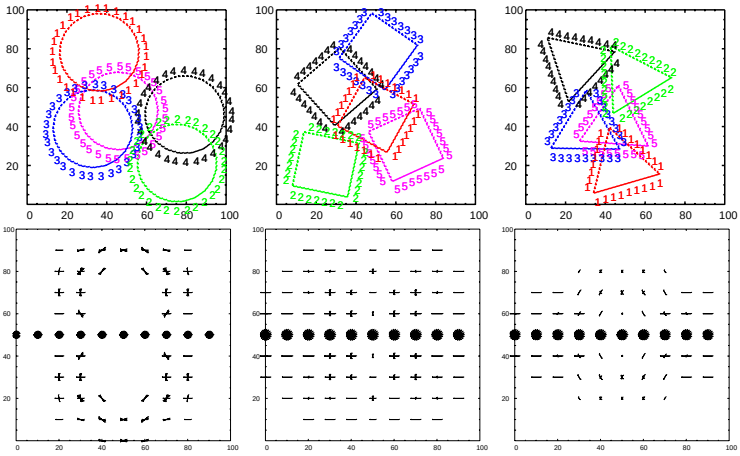

Fig. 8.12. Learning interaction functions for grouping of line segments. Top row: groupings used for training. Bottom row: resulting interaction functions (for explanation, see text).

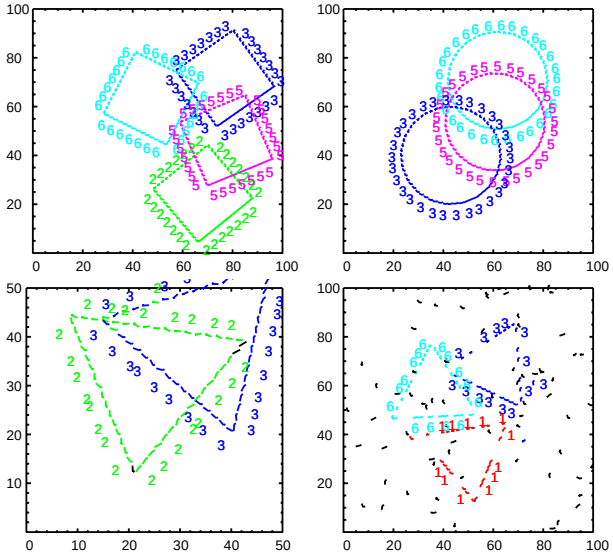

Fig. 8.13. Grouping examples from learnt interaction functions for noiseless arrangements of line segments (left) and for noise in line segment parameters or in background (right).

8.11 Application Example: Cell Image Segmentation

In this section we illustrate the learning approach for a more complex domain from medical image processing. The goal is to determine in microscope images the number, positions and shape of lymphocyte cells that have been stained with a fluorescent dye. An automated system for this has been presented in [17]. In the context of that work, we have found the CLM as a very suitable method for an accurate determination of cell boundaries, however, good results required a careful "hand tuning" of the underlying interaction function.

To apply the present learning method for an automated generation of the interaction function, we use as features directed edge vectors $\mathbf{m}_r = (\mathbf{r}, \mathbf{o}_r)$ whose orientation is estimated from the responses of a pair of 3x3 Sobel filter masks $\mathbf{o}_r = (S_r^x, S_r^y)^T$. The interaction function $f_{rr'}(\mathbf{m}_r, \mathbf{m}_{r'})$ can then be parameterized by the local distance $\parallel \mathbf{r} - \mathbf{r}' \parallel$ and the two relative angles between the connection vector $(\mathbf{r} - \mathbf{r}')$ and the orientation vectors of the two edges $\mathbf{o}_r$ and $\mathbf{o}_{r'}$ (for details, see [27]). Images consist of 45x45 pixel squares, leading to a total number of 2025 input features. For the grouping, we use a 10-layered CLM.

For the interaction vector quantization, we use 100 prototype vectors (leading to the same number of basis functions in the expansion (8.24)). We then use Eq. (8.26) to define interactions for three different values of Λ. With these interactions, we obtain the segmentation results depicted in Fig. 8.14. While the value of $\Lambda = 1$ yields the best segmentation, we also see that the system is rather robust to the setting of this single main parameter and there is a rather good segmentation also for the other values of Λ. For comparison, the last line depicts the (much worse) segmentation results obtained with direct k-means vector quantization when applied directly to the feature vectors $\mathbf{m}_r$ (using 7 prototype vectors, expecting 7 cells or less).

8.12 Discussion

Pattern recognition is frequently equated with the process of classification and often mathematically idealized as a mapping from some feature space into a (usually discrete) set of output values ("categories"). While this view has been very useful and led to the development of powerful classifiers, such as feedforward neural networks or support vector machines, it tends to deemphasize an aspect already brought to our attention by the early work of the Gestaltists: in many cases, the desired result of a pattern recognition system is not just an "opaque" category, but a richer structure that represents

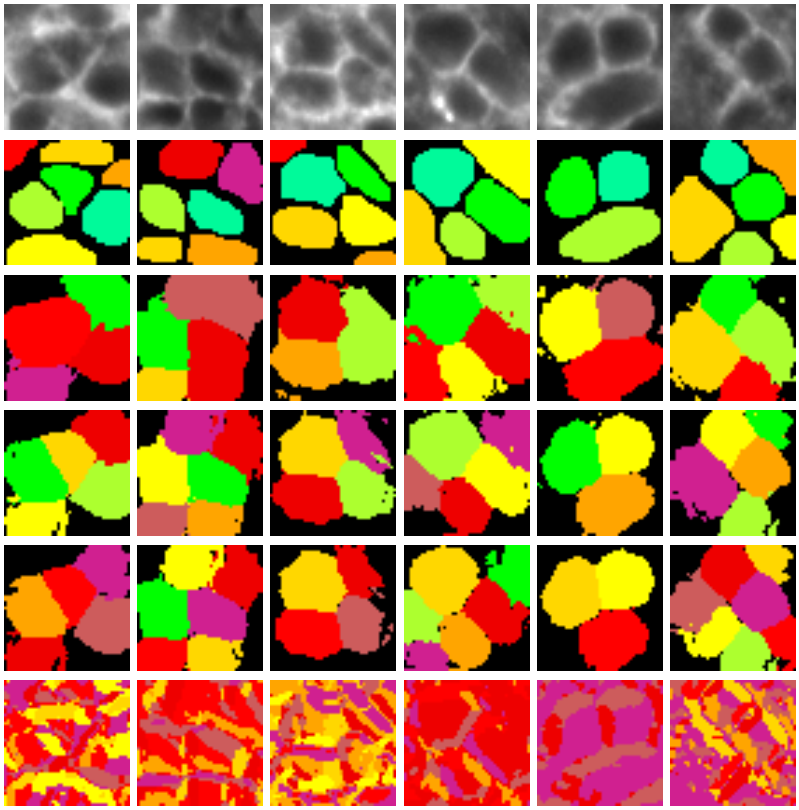

Fig. 8.14. CLM cell image segmentation (from top row to bottom row): input images, target regions, CLM segmentation results after learning for $\Lambda = 1$, $\Lambda = 2$ and $\Lambda = 3$, "naive" k-NN-segmentation results (adapted from [27]).

the "pattern" in a more explicit and invariant way than the original data (e.g., the image pixels). Perceptual grouping appears to be one of the fundamental operations that produce such representations by establishing "bindings" between suitable, simpler constituents, such as predefined features.

Mappings that can create such richer representations are much harder to construct, motivating an approach that generates the required structures as the response of a suitable dynamical system to constraints representing the input. For the task of feature grouping or binding, we have presented the Competitive Layer Model (CLM), consisting of a "stack" of layers of feature-selective units ("neurons") coupled in such a way that an input pattern "projected" onto the stack as an activity constraint for the activity sums of its vertical columns can become partitioned into groups of constituents by dividing the activity among the different layers.

A critical element of this system is the choice of interactions between cells sharing a layer: together with the chosen basis features, they determine the grouping characteristics of the resulting dynamics. We have shown that we can choose the interactions in such a way that the resulting grouping dynamics resembles human perceptual grouping for quite a wide range of input patterns. In addition, we have described a learning procedure that can construct suitable interactions from a small set of training patterns specifying examples of desired target groupings.

The emphasis of this work is towards the development of computational systems that implement non-trivial computations in the form of distributed dynamical systems that can be constructed efficiently from data examples. While there is a large number of approaches focusing on the learning of temporal trajectories, e.g., for sensori-motor-control, we think that dynamical systems *for performing binding operations* are another very important class of building blocks for the following reason: real environments do not provide "carefully formatted" input and output spaces with stable and obvious sets of low-dimensional input and output variables that we then could correlate by mappings constructable from a training data sets of realistic size. Currently, it is largely the work of the engineer to prestructure the "binding" of its devices to the relevant degrees of freedom in their environment, sacrificing in this way a large part of their flexibility. Only when we succeed to treat the selection of relevant degrees of freedom on the input (and output) side as an integral part of the task that a perceptual (and actor) system has to solve, we can approach the flexibility that we admire in living animals. We think that perceptual grouping can provide us with an interesting starting point to tackle this task, and that the next step will be an extension of perceptual grouping to situations, where "good gestalts" have to be formed *at the level of coordination patterns between an agent and its environment.* We are confident that the CLM can offer guidance for the design of systems with such capabilities, which are closely related with the important issues of attention and dynamic dimension reduction.

References

1. P. Brodatz (1966) *Texture: A Photographic Album for Artists and Designers.* Dover, NewYork
2. John G. Daugman (1985) Uncertainty relation for resolution in space, spatial frequency, and orientation optimized by two-dimensional visual cortical filters. *Journal of the Optical Society of America A*, 2(7):1160–1169
3. Dennis Dunn, William E. Higgins, and Joseph Wakeley (1994) Texture segmentation using 2D Gabor elementary functions. *IEEE Transactions on Pattern Analysis and Machine Intelligence*, 16(2):130–149

4. R. Eckhorn (1999) Neural Mechanisms of visual feature binding investigated with microelectrodes and models. *Visual Cognition*, 6:231-265.
5. Jianfeng Feng (1997) Lyapunov functions for neural nets with nondifferentiable input-output characteristics. *Neural Computation*, 9:43–49
6. Richard H.R. Hahnloser, Rahul Sarpeshkar, Misha A. Mahowald, Rodney J. Douglas, and H. Sebastian Seung (2000) Digital selection and analogue amplification coexist in a cortex-inspired silicon circuit. *Nature*, 405:947–951
7. G. E. Hinton (1990) *Mapping part-whole hierarchies into connectionst networks.* Artificial Intelligence 46 47-75.
8. J. Jones and L. Palmer (1987) An evaluation of the two-dimensional Gabor filter model of simple receptive fields in cat striate cortex. *Journal of Neurophysiology*, 58:1233–1258
9. Bela Julesz (1981) Textons, the elements of texture perception and their interaction. *Nature*, 290:91–97
10. W. Khler (1929) Gestalt Psychology. Liveright, New York (NY) 1929.
11. B.J. Kröse (1987) Local structure analyzers as determinants of preattentive pattern discrimination. *Biological Cybernetics*, 55:289–298
12. David G. Lowe (1985) *Perceptual Organization and Visual Recognition,* Kluwer Academic Publishers, Boston, Mass., 1985.
13. Von der Malsburg, C. (1981). *The Correlation Theory of Brain Function.* Internal Report 81-2, Max Planck Institute for Biophysical Chemistry, Göttingen, Germany.
14. W.Y. Ma and B.S. Manjunath (1996) Texture features and learning similarity. In *Proceedings of IEEE Int. Conference on Computer Vision and Pattern Recognition*
15. B.S. Manjunath and W.Y. Ma (1996) Texture features for browsing and retrieval of image data. *IEEE Transactions on Pattern Analysis and Machine Intelligence*, 18(8):837–842
16. Tim W. Nattkemper, Heiko Wersing, W. Schubert, and Helge Ritter (2000) Flourescence micrograph segmentation by gestalt-based feature binding. In *Proceedings of the International Joint Conference on Neural Networks (IJCNN)*, 248–254
17. T. W. Nattkemper, H. Ritter, W. Schubert (2001) A Neural Classificator Enabling High-Throughput Topological Analysis of Lymphocytes in Tissue Sections. *IEEE Trans. on Inf. Techn. in Biomed.* vol. 5 , no. 2, pp. 138-149.
18. J. Ontrup, H. Wersing, H. Ritter (2004) A Computational Feature Binding Model of Human Texture Perception. *Cognitive Processing,* 5, (1), pp. 32-44.
19. H. Ritter (1990) A spatial approach to feature linking. In *Proc. of the International Neural Network Conference*, Vol. 2, 898–901, Paris.
20. A. L. Roskies (1999) *The Binding Problem.* Neuron 24, 7-9.
21. T.B. Schillen and P. Knig (1994) Bindig by temporal structure in multiple feature domains of an oscillatory network. *Biological Cybernetics*, 70:397–405
22. M.N. Shadlen and J.A. Movshon (1999) *Synchrony Unbound: A Critical Evaluation of the Temporal Binding Hypothesis* Neuron 24 67-77.
23. W. Singer (1999) Neuronal synchrony: A versatile code for the definition of relations? *Neuron*, 24:49–65
24. D. Terman and D.L. Wang (1995) Global competition and local cooperation in a network of neural oscillators. *Physica D*, 81:148–176
25. C. von der Malsburg and J. Buhmann (1992) Sensory segmentation with coupled oscillators. *Biological Cybernetics*, 54:29–40

26. Andrew B. Watson (1987) Efficiency of a model human image code. *Journal of the Optical Society of America A*, 4(12):2401–2417
27. S. Weng, H. Wersing, J.J. Steil and H. Ritter (2006) Lateral Interactions for Feature Binding and Sensory Segmentation from Prototypic Basis Interactions. *IEEE Transactions on Neural Networks 17 (3)* (to appear).
28. H. Wersing (2000) *Spatial Feature Binding and Learning in Competitive Neural Layer Architectures.* Cuvillier, Goettingen
29. Heiko Wersing, Jochen J. Steil, and Helge Ritter (2001) A competitive layer model for feature binding and sensory segmentation. *Neural Computation*, 13 (2):357–387

Part III

Applications in Bioinformatics

9

Regulatory Signals in Genomic Sequences

Sonja J. Prohaska, Axel Mosig, Peter F. Stadler

Summary. Gene expression is a complex multiple-step process involving multiple levels of regulation, from transcription, nuclear processing, export, post-transcriptional modifications, translation, to degradation. Over evolutionary timescales, many of the interactions determining the fate of a gene have left traces in the genomic DNA. Comparative genomics therefore promises a rich source of data on the functional interplay of cellular mechanisms. In this contribution we review a few aspects of such a research agenda.

9.1 Introduction

Gene expression is the process by which a gene's information is converted into a structural and/or functional gene product. This product is typically a protein, but might also be an RNA molecule or a complex of RNA and protein. A specific spatial and temporal distribution of these units within a cell is crucial for their function. The process of gene expression involves multiple steps, starting with the DNA in a state that makes the information accessible, transcription (DNA $\rightarrow$ RNA) and perhaps translation (RNA $\rightarrow$ protein), which is then followed by protein folding, post-translational modification, and targeting. Once started, gene expression does not run through unaffected. Every step in the process is under tight control and actively regulates, or at least modulates, the flow through each checkpoint. Trapping intermediates at any step of the process may halt or even abort gene expression. Together, all regulatory effects from the gene to the functional gene product determine, whether a gene product exceeds its threshold of expression to be effective. Therefore, the state of expression is not simply on or off.

In the last years it has become apparent that gene expression is a complex network comprising different layers of often inter-twined regulatory layers. A

few of these mechanisms, such as the binding of transcription factors to the DNA, leave direct traces in the genomic sequences that can be detected and deciphered by comparative approaches. In other cases, gene regulation is afforded by *trans*-acting RNAs, first and foremost microRNAs. In this situation, one first has to identify the transacting regulator before it becomes possible to search for the target that it regulates.

From a comparative genomics perspective, on the other hand, we can identify a plethora of evolutionary conserved DNA sequences that apparently do not code for proteins. Among these signals are also sizable regions with very high levels of sequence conservation and no reported function [128, 127, 82, 29]. The question that we at least begin to address in this contribution is how we can identify evolutionary conserved DNA, and how we can determine the mechanisms that they are involved in. While it is clear that comparative genomics cannot by itself elucidate the complete complexity of cellular regulation, it has also become clear in recent year that over evolutionary timescales, this regulatory network has left trace evidence at the DNA level. This requires, however, an understanding of the many distinct mechanism.

Nucleic acid sequence motifs are (with a few examples such as self-splicing introns and some non-coding RNAs) not catalytically active. Additional proteins or (sometimes) ncRNAs are therefore involved that exert their regulatory function by binding either to the DNA or to the transcribed RNA at "regulatory elements". Regulatory mechanisms that alter the components binding directly or indirectly to the sequence motifs are beyond the scope of this contribution. The generic mechanisms involving the motifs and their accessibility are listed in table 9.1.

Changes at the nucleotide sequence level occur either by recombination/repair processes or covalent modification of single bases. Direct DNA modifications yield stable or even irreversible gene expression patterns in descending cells. Genomic imprinting reduces gene expression to one parental allele through DNA methylation. Once established, the methylation pattern is rather constant and hardly reversible.

Eukaryotic DNA is packed into a compact structure, the chromatin. Every 150 bp the linear DNA molecule is wrapped around a protein core in 1.65 turns, forming the nucleosome. Regulation at the epigenetic level concerns modifications of the histone protein core. The pattern of acetylation, (mono-, di- and tri-)methylation, phosphorylation and other covalent modifications at about 40 different amino acids of the 5 different histone proteins (H4, H3, H2A, H2B, and H1) is also referred to as "histone code". Histone modification patterns are able to recruit specific protein complexes just like binding sites on the DNA and/or set the chromatin state. Heterochromatin or condensed

Table 9.1. Overview of major regulatory modes in Eukaryotic cells

regulatory mechanism	effect on gene expession	example (organism)	reference
DNA rearrangements	selective/irreversible	V(D)J-joining (human)	[105]
site-specific recombination	selective/reversible	mating-type switching (yeast)	[26]
DNA amplification	enhancing	chorion genes (*Drosophila*)	[22]
DNA methylation of CpG dinucleotides	silencing/imprinting	parent-of-origin-specific silencing (human)	[120]
DNA demethylation by DNA repair	enhancing	glycosylase at polycomb genes (*Arabidopsis*)	[96]
histone code	silencing/enhancing	everywhere	[81]
heterochromatin barrier (fixed/flexible)	insulator/silencing/enhancing	USF binding at HS4 (chicken)	[146]
enhancer blocker	insulator/silencing	su(Hw) (*Drosophila*), CTCF (human)	[146]
enhancer promoter contact	insulator/silencing/enhancing	trithorax at Ubx promoter (*Drosophila*)	[146]
nuclear matrix attachment region (MAR)	insulator/silencing/enhancing	lysozyme locus (chicken), tyrosinase locus (mouse)	[146]
subnuclear compartment	silencing/enhancing	LCR at β-globin gene (human)	[145]
gene competition for enhancers	silencing/enhancing	β-globin gene (human)	[131]
chromatin remodeling	silencing/enhancing	SWI/SNF at PHO5 or PHO8 genes (yeast)	[15]
RNA-directed transcriptional gene silencing	silencing	X chromosome inactivation (human)	[7]
promoters (TF binding sites)	basal	everywhere	[14]
enhancer (TF binding sites)	enhancing	everywhere	[148]
silencer/repressor (TF binding sites)	silencing	Ume6 at URS1-containing promoters (yeast)	[148]
alternative transcription start sites	silencing/enhancing	IGF-1 (human)	[77]
antisense transcripts	silencing/enhancing	frq gene (*Neurospora*)	[18]
regulation of elongation phase	silencing/enhancing	Fkh at CLB2 locus (yeast)	[98]
pre-mRNA processing (nucleus)	silencing/enhancing	everywhere	[68]
alternative splicing (nucleus)	selective/silencing/enhancing	sex lethal (*Drosophila*)	[73]
trans-splicing (nucleus)	selective/alteration	SL RNA at all genes (*Trypanosoma*	[78]
mRNA editing (nucleus)	alteration	ADAR at GluR mRNA (human)	[6]
sequestration of mRNA (nucleus)	silencing	Rrp6 at exosomes (yeast)	[117]
nonsense-mediated mRNA decay (nucleus)	silencing	pseudogenes	[144]
mRNA export	silencing/enhancing	EJC at spliced mRNAs (*Drosophila*)	[117]
RNA-directed mRNA degradation	silencing	DCL1 mRNA (*Arabidopsis*)	[80]
degradation and stability of RNAs (cytoplasm)	silencing/enhancing	HuR at ARE-containing RNAs (human)	[147]
mRNA localization (cytoplasm)	silencing/enhancing	ASH1 (yeast)	[41]
alternative translation start sites	silencing/enhancing	IRES	[69]
scanning for translation start sites	silencing/enhancing	uORF at GCN4 (yeast)	[38]
translation initiation regulators	silencing/enhancing	CPEB at CPE-containing mRNA (human)	[38]
RNA-directed translational gene silencing	silencing	lin-4 miRNA at lin-14 mRNA (*C. elegans*)	[38]

USF = upstream stimulatory factor, HS4 = hypersensitive site at the LCR of the β-globin gene, su(Hw) = suppressor of hairy wing protein, CTCF = CCCTC-binding factor, MAR = nuclear matrix attachment region, LCR = locus control region, SWI/SNF = remodeling complex, PH05 = repressible acid phosphatase precursor, PHO8 = repressible alkaline phosphatase precursor, TF = transcription factor, Ume6 = transcriptional regulator, URS1 = Ume6-binding site, frq = frequenin, Fkh = fork head protein, CLB2 = G2/mitotic-specific cyclin 2, ADAR = double-stranded RNA-specific adenosine deaminase, GluR = glutamate receptor, mRNA = messenger RNA, Rrp6 = exosome complex exonuclease, EJC = exon-junction complex, DCL1 = Dicer-like 1, HuR = Human-antigen R (stability factor), ARE = AU-rich element, ASH1 = daughter cells HO repressor protein, IRES = internal ribosomal entry site, uORF = upstream open reading frame, GCN4 = general control protein, CPEB = cytoplasmic polyadenylation element binding protein, CPE = cytoplasmic polyadenylation element, miRNA = micro RNA

chromatin is in the "silent" state, while euchromatin or open chromatin is "transcribable" mainly due to histone acetylation.

Insulators describe a phenotype rather than a single kind of element with a fixed mechanism of action. They have the ability to protect genes they surround from the influence either of outside enhancers or inactivating chromatin structures. An important part of the underlying mechanism might be the formation of insulator bodies. Insulator binding proteins form complexes which divide the chromatin into looped domains that are functionally isolated from one another. This could be a step towards regulation by discrete subnuclear compartment. For example, actively expressed genes migrate to nuclear compartments enriched in RNAPol II, so called transcription factories, while inactive genes loop out. Such agglomerations may serve to raise the local concentration of associated components, favoring interactions that might not otherwise occur.

The promoter is the assembly site for the basal transcription machinery right next to the transcription start site. Transcription factors (TFs) binding to enhancers facilitate recruitment of RNA polymerase to the promoter if a physical contact can be established by cofactors. Silencers, on the other hand, circumvent such an interaction and therefore initiation of transcription. In general, binding sites for TFs are short (4-12 bp) and occur clustered upstream of the promoter sequence. While there are numerous examples where the context (i.e., order, orientation, distance, presence of certain TFs) of TF binding sites is functionally relevant, there is an equally large number of examples wehere the context is not relevant.

The following elongation of transcription and all regulatory steps at the RNA level that take place in the nucleus are coupled to a large extent. For example, nuclear export of RNAs is linked to the subnuclear compartment of transcription, transcription elongation, mRNA processing (splicing) and mRNA stability. Once the mRNA is exported to the cytoplasm, it is either degraded or translated, but it might also be stored for later use.

Translation of mRNA is the final step in gene expression, that involves nucleic acid sequence elements in control. Not only upstream regulatory elements like secondary structures or upstream ORF may effect scanning of the small ribosomal subunit for the initiation codon. Close proximity of the 5' and 3' end of the mRNA allows protein binding sites located in the 3'-UTR to control tranlation initiation. In fact, most known regulatory sequences, and miRNA binding sites are found within the 3' UTR.

The regulatory mechanisms and phenomena described above leave more or less visible traces in their genome sequences. For some regulatory elements, the corresponding traces on DNA level are very well understood and have been

studied in much detail. Throughout the rest of this chapter, we will review known sequence characteristics of regulatory elements. Whenever available, we will give an overview over the corresponding computational methods for unveiling those traces in genomic sequences.

9.2 Gene Finding

The most conspicuous traces found in a genome sequence arise from protein coding regions. Since proteins are key players in the gene regulatory network, identifying the positions of the protein coding genes in whole genome sequences is an elementary step. Beside identifying the protein coding sequences, genome annotations serve a second purpose, namely to obtain those regions in the vicinity of the annotated genes that contain *cis*-regulatory elements, such as transcription factor binding sites. Furthermore, gene annotations give an estimate of the number of players involved in regulatory networks.

Once a complete genome sequence is available, a first step typically is to identify protein coding genes in the sequence by computational means, a task commonly referred to as *gene prediction* or *gene finding*. Due to statistically noticeable features such as being grouped in coding triplets or protruding traits such as start or stop codons, protein coding genes typically show comparatively strong signals in genome sequences. Consequently, a number of well-established methods have contributed to detecting protein coding genes in genomes. The first type of gene prediction methods, so-called *ab initio* methods, are based on considering a single genome sequence in combination with a probabilistic model involving multiple characteristic traits of transcriptional, translational or splicing sites that are typically visible on sequence level. Approaches such as `GENSCAN` [13] or `Genie` [72] incorporate this information into a hidden Markov model for unveiling genomic regions that have a striking probability of being protein coding.

While the accuracy of *ab-initio* gene prediction methods turned out to be principally limited [43, 118], more reliable results can be obtained by *comparative gene prediction* approaches, which incorporate pairwise alignments of the underlying genomes produced by programs such as `Blastx`. Due to a very specific selectional pressure on the coding triplets of protein coding regions, predictions produced by programs such as `Twinscan` [67] or `Procrustes` [40] yield much more reliable results than *ab-initio* methods.

As has been demonstrated by several studies, incorporating issues such as protein similarity or expressed sequence tags may enhance the reliability of gene prediction methods [113, 54, 150]. For surveys on gene prediction methods, we refer to [12, 39, 34, 71]. Gene prediction methods yield estimates

Table 9.2. Estimated number of protein coding genes.

Species	**Estimated # of Genes**	Ref.
Homo Sapiens	20,000-25,000	[132]
Drosophila melanogaster	12,000	[133]
Caenorhabditis elegans	19,000	[135]

of the number of (protein coding) genes, some of which are shown in Table 9.2.

While detecting protein coding genes appears to be a largely resolved problem, finding non-coding RNA genes is much more involved. For details on RNA gene prediction, see Section 9.4.

9.3 Identifying *Cis*-Regulatory Elements

Once the protein coding genes and non-coding RNAs (see Section 9.4) as the key players in the regulatory network and their coding regions are known, one is naturally interested in their *cis*-regulatory elements, i.e., sequence elements associated with the gene to be regulated that serve as sequence-based "addresses" for their regulators. On the level of transcription regulation, the most striking sequence signals of a gene are given by the basal promoter and the proximal promoter. In Mammals, 60% of all promoters colocalize with regions of high C+G content, known as CpG islands. A feature that can also be used to find unknown genes. In the immediate upstream region of the basal an proximal promoter, auxiliary binding sites can be located for further transcription factors, which are often observed to be organized in regulatory modules.

9.3.1 Polymerases and Associated Promoters

Transcription of DNA into RNA is performed by the three different types of RNA polymerases. For the modes of transcription associated with the different RNA polymerases, we refer to Table 9.3. Each of the polymerases requires certain *cis*-acting elements in order to initiate transcription; due to its crucial relevance in transcribing mRNA necessary for protein coding genes, much effort has been spent on studying the polymerase II core promoter as the minimal stretch of contiguous DNA sufficient for initiating transcription. In most (yet not all) polymerase II transcribed genes, the core promoter contains the *TATA box*, which is located 25 bases upstream of the transcription start site. The TATA box is a usually 6 nucleotide long sequence motif characterizing

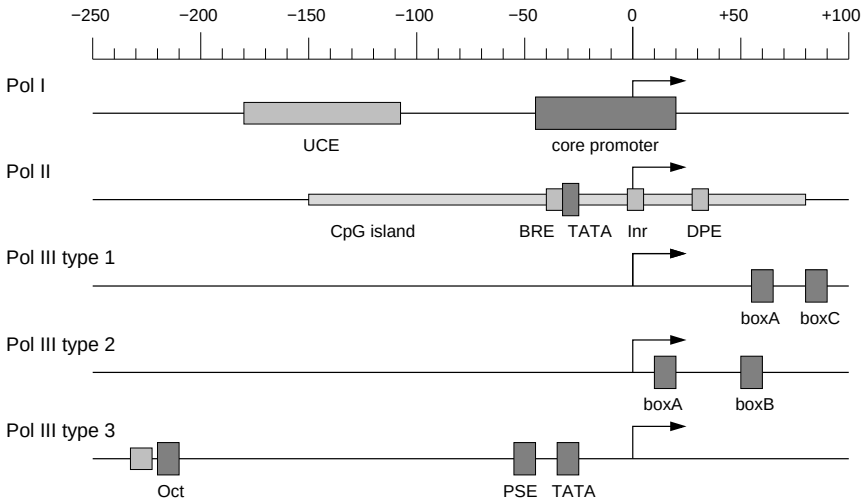

Fig. 9.1. Core motifs of the different promoter types. Motifs in dark gray are less dispensable than motifs in light gray. Any specific promoter may contain just a subset or, in the worst case, none of these motifs. UCE = upstream control element, BRE = TFIIB recognition element, Inr = initiator element, DPE = downstream core promoter element, Oct = octamer binding site, PSE = proximal sequence element. The arrow indicates the transcription start site at +1.

the binding site for the tata-binding-protein TBP. TBP usually interacts with other transcription factors, whose binding sites are typically found within 40 nt upstream to the transcription start site. For details on the RNA polymerase II core promoter, we refer to the survey by Butler and Kadonaga [14]. The action of the polymerase II promoter is often enhanced by several distal promoters organized in *cis*-regulatory modules, see Section 9.3.3.

Polymerase I transcripts are also regulated by a a core promoter, which is separated by about 70 base pairs from a second elementary promoter element, the so-called *the upstream control element* (UCE). In place of the TBF for polymerase II, pol I requires two core transcription factors, namely UBF1 (*upstream binding factor*) binding to a GC-rich region and SL1 (*selectivity factor*).

Promoters for RNA polymerase III occur in several variants. First, they may consist of bipartite sequences downstream of the start point, with promoter element *boxA* separated from either of the promoter elements *boxC* or *boxB*. Secondly, some U snRNA genes are regulated by upstream type promoters involving an octamer binding site, a so-called *proximal sequence element* and a TATA box.

Table 9.3. Major modes of transcription.

RNA polymerase	Promoter	Location relative to start site	Transcript	Function
Pol I	core element UCE (upstream control element)	-45 to +20 -180 to -107	pre-rRNA (28S, 18S, 5.8S)	components of the ribosome; translation
Pol II	TATA-Box Initiator CpG islands	-25 to -35 -100	mRNA snRNA (U1-4)	protein coding genes components of the spliceosome; mRNA splicing
	no		LINEs	Retrotransposon
Pol III	type 1: A-box, C-box type 2: A-box, B-box type 3: TATA-Box	+50 to +80 +10 to +60 -30 to -70	5S rRNA tRNA snRNA (U6)	component of large ribosomal subunit translation components of the spliceosome; mRNA splicing
			7SL RNA	component of the SRP (signal recognition particle); protein transport to ER (endoplasmatic reticulum)
	internal		SINEs	Retrotransposon

9.3.2 Identification of Transcription Factor Binding Sites

Transcription factors are known to bind to short, specific sequences of DNA. Experimental evidence obtained by techniques such as DNase footprinting [36] and gel-shift assays [37] suggests that protein-DNA binding of transcription factors involves a relatively short, contiguous DNA segment, whose length usually ranges between 8 and 15 nucleotides. Repositories of known transcription factors and their experimentally derived binding site motifs can be found in databases such as TRANSFAC [45] or JASPAR [123]. However, experimental determination of binding sites and their relevance *in vivo* takes a significant effort, so that numerous computational approaches have been proposed for determining candidates for TFBSs *in silico*.

While the length of the binding sites corresponding to one specific TF is observed to be essentially constant, the individual positions of the binding site sequences may vary up to a certain degree. Hence, in order to derive a suitable model of the sequences that a TF binds to, different notions of

describing TFBS sequence variability have been proposed. Such models are also important in the context of computationally determining TFBSs based on comparative genomics approaches.

Different observed binding sites corresponding to a given transcription typically show a high degree of sequence similarity; moreover, the observed binding site motifs have the same length ℓ. In order to capture the observed binding sites in one unique structure, we define a *binding site model of length* ℓ as a mapping $M\colon \Sigma^\ell \to \mathbb{R}\geq 0$ assigning a weight to each sequence of length ℓ over the DNA alphabet Σ. While $M(s)$ ideally should be related to the physical binding affinity of sequence s binding to the transcription factor modeled by M, $M(s)$ usually is obtained on the basis of the frequency of observed or putative binding sites in a given set of genomic sequences.

The concept of binding site models introduced above is too general in many situations: first of all, there are usually not enough data to derive reasonable weights for each DNA sequence of length ℓ and secondly, storing and retrieving the complete mapping M would be too expensive. Hence, several simplified models of TFBSs have been established. The most simple model of a binding site model is to derive a *consensus sequence*. In this model, each of the ℓ positions is associated with a subset of the DNA nucleotide alphabet. A given sequence fragment s of length ℓ is assigned score $M(s) = 1$ if at each position, the nucleotide of the fragment is contained in the corresponding nucleotide set of the model; otherwise, we have $M(s) = 0$. Alternatively, one can define $M(s)$ as the number of positions in s where the nucleotide in s is contained in the corresponding set in M.

Consensus sequences disregard a major information contained in the sequences used for deriving the consensus model, namely they do not take into account frequencies of occurrence. This is overcome in the most established way of TFBS modeling, namely *position weight matrices* (PWMs). In the PWM model (sometimes also referred to as a *position specific weight matrix*), each of the ℓ positions of the binding site is assumed to be distributed independently: for each position i, we are given a probability density function $pi\colon \Sigma \to [0, 1]$ over the four nucleotides. Given $s := s1 \dots s\ell \in \Sigma^\ell$, this allows us to define

$$M(s) := p1(s1) + \cdots + p\ell(s\ell).$$

PWMs can be derived canonically from a collection of sequences $S1, \dots, SM \in \Sigma^\ell$: for $x \in \Sigma$ and $i \in \{1, \dots, \ell\}$, let $\nu(x, i)$ denote the number of sequences in which letter x occurs at position i. By setting $pi(x) := \nu(x, i)/M$, we indeed obtain a PWM model. In practice, the sequences $S1, \dots, SM$ are typically obtained either from a set of experimentally determined binding sites or from motif discovery methods, as discussed in Section 9.3.2.

PWMs, however, disregard any information about the correlation between sites that may be contained in the sequences that a matrix was derived from. As a remedy, Pudimat *et al.* [112] have developed a more sophisticated way of modeling TFBSs based on parameter estimation in a Bayesian Belief network. As opposed to most other approaches of TFBS modeling, their approach allows to model correlations between the individual sequence positions. Another approach for modeling dependencies between positions in PWMs based on χ^2 statistics has been investigated in [33].

While obtaining models for TFBSs from experimental data is relatively easy, deriving them computationally from genomic sequences is a complex problem. Essentially all approaches are based on comparative genomics in the sense that they seek for motifs contained in each, or at least most, of K promoter regions belonging to K co-regulated (or orthologous) genes. The returned motifs usually result from optimizing a scoring function which measures how well a candidate motif statistically differs from global properties of the promoter sequences.

Among the earliest non-trivial approaches to extracting over-represented short motifs as potential TFBSs, Hertz and Stormo [48] proposed a greedy algorithm. Their `CONSENSUS` approach starts with a position weight matrix derived from a single sequence of a fixed length, which is extended to a pairwise alignment of same width by considering a best-matching subsequence of the second sequence. The algorithm proceeds by successively adding one subsequence of each remaining input sequence to obtain the final PWM, along with a P-value that allows to assess the statistical significance of the result.

A different approach based on the expectation maximization (EM) algorithm is investigated in `MEME` [4], improving a previous approach by Lawrence and Reilly [75]. The EM-based approach starts with an a priori guess for a position weight matrix representing a binding site of fixed length ℓ, which is then improved according to the input sequences in each of the subsequent iteration steps. A single iteration step works as follows: for each subsequence ℓ of the input sequences, the score of the current matrix is computed. After normalization, the matrix entries are updated by summing up the individual position contributions of each of the length ℓ subsequences, weighted by its corresponding normalized probability computed before. The resulting new matrix is then used as input for the next iteration step, until convergence of the process is observed.

`AlignACE` developed by Roth, Hughes *et al.* [119, 56] is yet another approach to obtain PWMs from genomic regulatory sequences. `AlignACE` based on Gibbs sampling, enhancing approaches previously used for locally aligning motifs in protein sequences such as [74] in a way such that both strands of the input sequences are considered. Furthermore, single motifs that were found

are masked iteratively to allow for the extraction of more than one binding site motif.

9.3.3 Discovering Regulatory Modules

As numerous studies demonstrate, transcription factors exhibit their function synergistically through complexes of several transcription factors activating or deactivating gene expression by binding to their corresponding binding sites [27, 152]. which thus form the building blocks of regulatory modules. On the genome level, regulatory modules are characterized by binding sites being located close to each other, usually within a segment whose length does not exceed a few hundred nucleotides.

In recent years, a number of approaches have been developed in the context of discovering *cis*-regulatory modules. Kel-Margoulis *et al.* [65] propose a method based on identifying clusters with the property that pairwise distances between occurrences of TFBSs range within certain bounds; sets of binding sites that maximize a certain cluster score are searched by the means of a genetic algorithm. Other methods are based on probabilistic methods [109] or require (only sparsely available) knowledge about interactions between transcription factors such as the algorithm presented in [130].

Among the most established methods, Sharan *et al.* proposed an approach implemented in the program `CREME` [129], which is conceptually somewhat related to our approach. Given a set of candidate binding sites, `CREME` seeks to identify motif clusters of limited length that occur more than once in a set of regulatory sequences. However, the capabilities of the `CREME` approach is limited to discovering repetitive occurrences of modules that contain *precisely* the same set of binding sites. While biological data indeed indicate that functionally related modules share a significant number of binding sites, modules observed in a given regulatory region might as well contain occurrences of known binding site motifs, which are not functional in the given context. If this number of additional, non-shared binding sites is non-zero, the method underlying `CREME` does not allow to discover such functional modules reliably.

In order to overcome this shortcoming, the hypothesis underlying the `bbq` approach [99] is that CRMs are characterized by sharing a significant number of common binding sites, but do not necessarily contain precisely the same set of binding sites. More formally, we are given a set of candidate binding sites $s1, \ldots, sm$ together with a set of genomic sequences $T1, \ldots, TK$. The role of the genomic sequences Tj is taken by the regulatory regions of genes that are suspected to share a regulatory module (due to being orthologous or having a similar expression scheme), while the binding site motifs can be derived from databases such as `TRANSFAC` or `JASPAR`. Alternatively, these motifs can be

derived from $T1, \ldots, TK$ using the motif discovery approaches discussed in Section 9.3.2. Finally, an upper bound for the length L (specified as a number of nucleotides) of the regulatory module is given as an input parameter.

The `bbq` approach starts with determining the occurrences of each motif si in each Tj and associating a color i with binding site si. For each occurrence of si, an interval of length $L - |si|$ ending at the position of the occurrence is introduced, so that one finally obtains K arrangements of colored intervals. By "stabbing" into this arrangement, one obtains a cell in this arrangement. Such a cell is associated with a set of colors, which corresponds to a set of binding sites occurring within a genomic subsequence whose length is at most L nucleotides. Finally, attempting to stab a maximum number of common colors in each of the K arrangements leads to the so-called *best-barbecue problem*. This problem leads to a natural combinatorial and geometric optimization problem which is NP-complete in general.

9.3.4 Phylogenetic Footprinting

Just as genomic regions that code for proteins or functional RNAs, regulatory elements are also subject to stabilizing selection. They evolve much more slowly than adjacent non-functional DNA, so that one can observe conserved islands of regulatory regions within intergenic or intronic regions. These conserved islands are commonly referred to as *phylogenetic footprints*, which can be detected by comparison of the sequences surrounding orthologous genes in different species. The loss of phylogenetic footprints as well as the acquisition of conserved non-coding sequences in some lineages, but not others, can provide evidence for the evolutionary modification of *cis*-regulatory elements.

While the motifs detected by the discovery methods discussed in Section 9.3.2 can be seen as one particular type of footprints, one can often observe conserved islands that are much longer, up to several hundred nucleotides, than individual binding sites. Therefore, phylogenetic footprinting tools are usually based on pairwise or multiple local alignment algorithms such as `blastz` [125] or `Dialign` [97]. The tools `PipMaker` and `MultiPipMaker` [125] (among others) process these alignments in order to provide information on significantly conserved regions. The `Tracker` tool [111] assembles individual pairwise `blastz` alignments into cliques of overlapping alignments. This results in the possiblity to list alternative multiple local alignments if the pairwise matches are not consistent with one multiple alignment.

As demonstrated in [111], the analysis of sequence conservation of non-protein-coding DNA can be used to unveil the evolutionary origin of phenomena such as the duplication of Hox clusters in shark, human, and the duplicated zebrafish and Takifugu (Figure 9.2). In this context, information

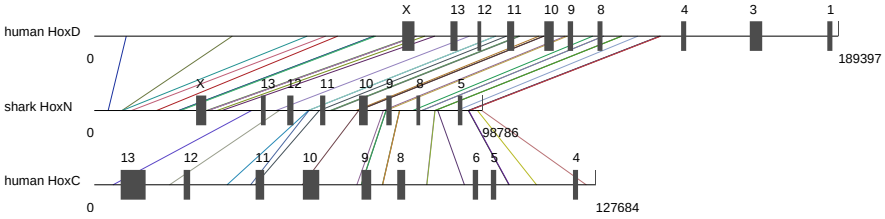

Fig. 9.2. Distribution of phylogenetic footprints in regulatory regions between the horn shark HoxN sequence and the human HoxC and HoxD sequences obtained by the `tracker` tool. Using this information for phylogenetic inference, this supports the hypothesis that the shark HoxN sequence is orthologous to the mammalian HoxD sequence [110]. Boxes indicate the location of the coding regions for the paralog groups 1 to 13, X denotes the evx gene. Lines conecting sequences represent phylogenetic footprints shared with the shark HoxN sequence.

contained in the regulatory regions yields insights that are not visible on the level of the corresponding protein coding regions.

9.4 Regulatory ncRNAs and RNA Motifs

9.4.1 Diversity of the RNA Inventory

Non-coding RNAs form a diverse group of transcripts with often poorly understood function. In contrast to protein-coding mRNAs there is little that they all have in common. One group, which itself is composed of a heterogeneous set of RNA families including tRNAs, the U6 snoRNA, the RNA component of the signal recognition particle, and a small number of less well-known ncRNAs including 7SK RNA and Y RNAs are transcribed by RNA polymerase-III. Ribosomal RNAs, transcribed by pol-I, form a group by themselves. Almost all of these ncRNAs are evolutionarily very well conserved, and most of are evolutionarily ancient.

In contrast, the majority of the known ncRNAs are transcribed by pol-II. These can be subdivided into messenger-RNA-like transcripts, such as *Xist*, which are typically spliced and polyadenylated, "structural ncRNAs" (such as spliceosomal RNAs (snRNAs) and many microRNAs) which are neither spliced nor polyadenylated, and a class of functional RNAs that is processed from introns (in particular snoRNAs). Informally, it is useful to distinguish a restricted group of *"classical"* ncRNAs containing the rRNAs, the pol-III transcripts listed above, spliceosomal RNAs, box-C/D and hox-H/ACA small nucleolar RNAs (snoRNAs), microRNAs, as well as telomerase RNA. As far

as we know, these RNAs are evolutionarily old, they have distinctive RNA secondary secondary structure, and most of them are reasonably well conserved at sequence level.

Recently, a number of small, non-mRNA-like ncRNAs have been found e.g. in the nematode *C. elegans* which do not appear to belong to one of the classical families, although at least some of them share the distinctive promoter features of tRNAs or pol-II transcribed snRNAs [28]. Bacterial genomes also contain a large and diverse set of small RNAs (sRNAs) in addition to the classical ncRNAs. A recent survey discusses 55 known *E. coli* sRNAs [47] and their conservation patterns within Enterobacteria. For a review of functional aspects of various bacterial sRNAs see [42]. An additional class of small antisense transcripts derived from UTRs is discussed in [64]. For a recent survey focussing on the regulatory effects of ncRNAs in eucaryotes, we refer to [25].

The function of almost all mRNA-like ncRNAs remains unknown. The few well-studied examples, such as *Xist* or *H19*, have functions in imprinting [103].

Regulation by means of RNA can follow at least three distinct principles: `RNA switches` sense changes in temperature or chemical environment and react by conformational changes. *Cis*-acting RNA signals, often located in untranslated regions of mRNAs, are bound by proteins. *Trans*-acting RNAs, such as microRNAs, preform their function by binding to complementary nucleic acid sequence motifs.

9.4.2 RNA Secondary Structure Prediction and Comparison

From a theoretical perspective, computational RNomics draws much of its appeal from the fact that most quantities of interest can be computed exactly within the secondary structure model. In contrast to proteins, nucleic structures are dominated by a single, very specific type of interaction: the formation of Watson-Crick and wobble (G-U) base pairs. The resulting contact structures, which are predominantly stabilized by the stacking interactions of adjacent base pairs, are not only a convenient and routinely used representation [70, 104, 124, 106], they also quantitatively describe the energetics of RNA structure formation, and they form intermediate steps in the folding process itself.

Formally, a *secondary structure* is a set Ω of base pairs such that (1) each nucleotide position i is paired with at most one other nucleotide (i.e., Ω is a matching), and (2) base pairs do not cross, i.e., $(i,j),(k,l) \in \Omega$ with $i < j, k < l$ implies $j < k$ or $l < j$. The second condition ensures that two base pairs are either separated along the sequence or nested within each other. A secondary structure can therefore be seen as a circular matching. Drawing the

bases along a circle, the base pairs form chords that do not cross. It follows that RNA secondary structures can be dealt with by means of exact dynamic programming algorithms, Fig. 9.3.

A plethora of careful thermodynamic measurement confirmed that the energetics of RNA structures can be understood in terms of additive contributions of "loops", Fig. 9.3, see [84, 83] and the references therein. Exact dynamic programming algorithms can be used to compute e.g. the minimum energy structure given any RNA sequence s [136, 155, 153]. The most frequently used implementations of these algorithms are `mfold` [153, 155] and the `Vienna RNA Package` [53, 50].

An RNA molecule, however, does not only form a single (ground state) structure; rather, there is an ensemble $\Sigma(s)$ of different structures Ψ that depend on the sequence s, which are populated in proportion to their Boltzmann factors $F(\Psi)/RT$. The partition function

$$Z = \sum \Psi \in \Sigma(s) \exp\left(-\frac{F(\Psi)}{RT}\right) , \tag{9.1}$$

from which all thermodynamics quantities of interest can be readily derived, can be computed by the same type of dynamic programming approach [87].

9.4.3 Suboptimal Structures and RNA Switches

Some RNA molecules exhibit two competing conformations, whose equilibrium can be shifted easily by molecular events such as the binding of another molecule. This can be used to regulate of gene expression, when the two mutually exclusive alternatives correspond to an active and in-active conformation of the transcript [90, 46]. While most riboswitches were found in bacteria, where they regulate several key metabolic pathways [11, 101], metabolite-binding RNA domains are also present in some eukaryotic genes [134]. An early computational study concluded that RNA switches are readily accessible in evolution and are therefore probably not exceptional instances of unusual RNA behavior [35]. These findings, and the fact that riboswitches bind their effectors directly without the need of additional factors, suggest that riboswitches represent one of the oldest regulatory systems [139].

9.4.4 Detection of functional RNAs in genomic DNA

Large-scale efforts to uncover the human and mouse transcriptomes, using very different experimental techniques including tiling arrays [8, 63, 61, 21],

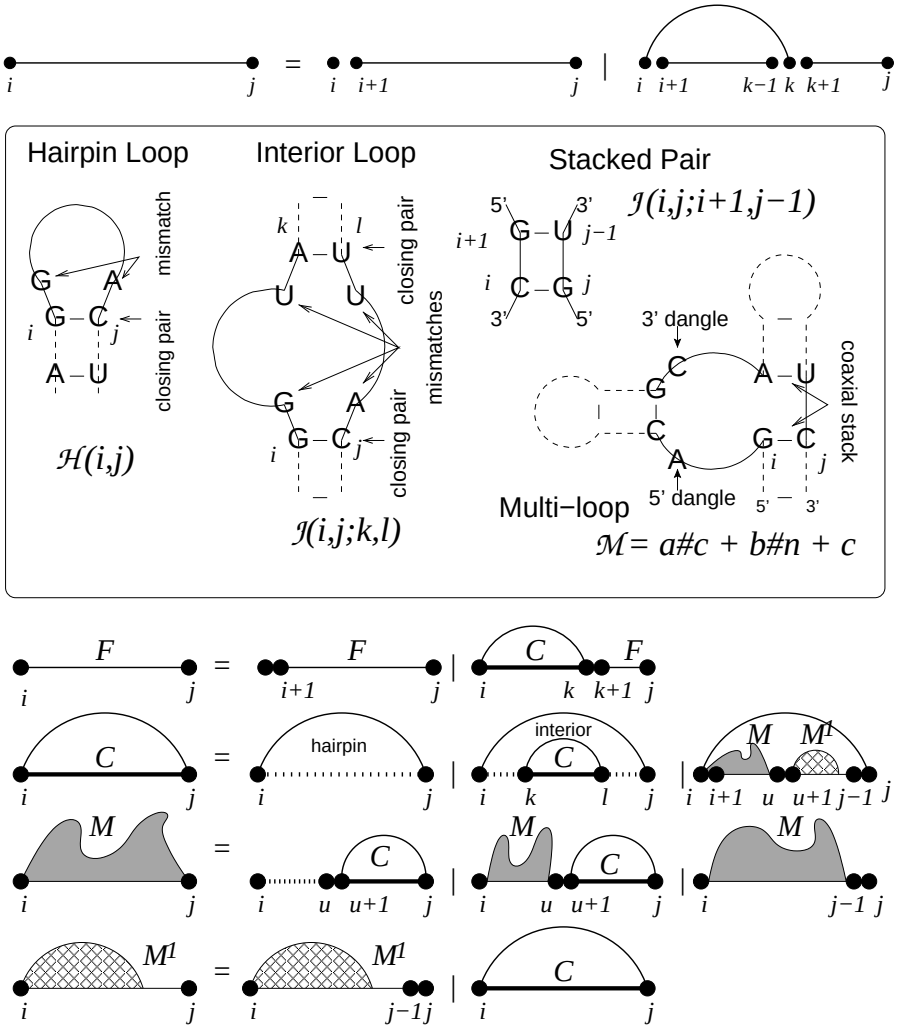

$$
\begin{aligned}
Fij &= \min\{Fi+1,j,\ \min i<k\le j Cik + Fk+1,j\}\\
Cij &= \min\left\{\mathcal{H}(i,j),\ \min i<k<l<j Ckl + \mathcal{I}(i,j;k,l),\ \min i<u<j Mi+1,u+M^1u+1,j-1+a\right\}\\
Mij &= \min\{\min i<u<j (u-i+1)c + Cu+1,j+b,\ \min i<u<j Mi,u+Cu+1,j+b,\ Mi,j-1+c\}\\
M^1ij &= \min\left\{M^1i,j-1+c,\ Cij+b\right\},
\end{aligned}
$$

Fig. 9.3. RNA folding in a nutshell. *Caption continued overleaf...*

Fig. 9.3, continued.
Top: The basic recursion for RNA folding is based on the observation that each structure either terminates in an unpaired base or in base pair that then separates the the structure into two *independent* parts: the one enclosed by the base pair, and the one out-side.
Box: The standard energy model distinguishes three types of loops: hairpin loops with a single closing pair, interior loops (including bulges and the stabilizing stacking pairs) which are delimited by two base pairs, and multi-loops at which the structure branches. For the latter the energy model assume additive contributions depending on the number of branches $\#c$ and the number of unpaired bases $\#n$ in the loop.
Middle: Using the loop-based energy model complicated the recursion since one now has to distinguish the different types of loops because of their distinct energy contributions. Instead of a single array storing the optimal energies Fij for substructure on the subsequence $x[i..j]$, one now need a few auxiliary arrays that correspond to restricted classes of structures. For instance Cij is the optimal energy subject to the constraint that i and j form a base pair.
Below we give the complete recursion for energy minimization in the loop-based energy model. Replacing minima by sums, and sums by products leads leads to the recursions for the partition function Z.

cDNA sequencing [102, 58], and unbiased mapping of transcription factor binding sites [17], agree that a substantial fraction of these genomes is transcribed and that the majority of these transcripts do not code for proteins. It is still unclear at present, however, which fraction are functional non-coding RNAs (ncRNAs), and which constitutes "transcriptional noise" [57].

Genome-wide computational surveys of ncRNAs, on the other hand, have been impossible until recently, because ncRNAs do not share common signals that could be detected at the sequence level. An exception are bacterial genomes, where are purely sequence-based machine learning approach was fairly successful [122].

Most of the "classical" ncRNAs mentioned above, however, have characteristic (secondary) structures that are functional and hence are well conserved over evolutionary timescales. The stabilizing selection acting on the secondary structure causes characteristic substitution patterns in the underlying sequences: Consistent and compensatory mutations replace one type of base-pair by another one in the paired regions (helices) of the molecule. In addition, loop regions are more variable than helices. These patterns not only have a significant impact on phylogenetic inference based on ribosomal RNA sequences (see, e.g., [62] and the references therein), but it also can be exploited for ncRNA detection in comparative computational approaches. Examples are the `alidot` [51] and `qrna` [116] programs. Related approaches predict consensus secondary structures for a set of aligned sequences [107, 52].

A second effect of stabilizing selection for RNA secondary structure is even easier to measure. It was first suggested by Maizel and co-workers that functional RNA elements should have a more stable secondary structure than comparable random sequences [76, 19].

As demonstrated in [137], selection for structure implies that in the long run sequences evolve that are more robust against mutations, i.e., for which a larger fraction of mutations does not lead to a change in the ground state structure. This effect can be detected e.g. in viral RNA structures [140]. Mutational robustness, however, is in turn strongly correlated with the thermodynamic stability of the ground state structure [149, 2]. Thus we expect that the ground states of functional RNA structures should be thermodynamically more stable than expected by chance, independently of whether there is a direct selection pressure for thermodynamic stability or not. While this effect can indeed be demonstrated [23], it is not statistically significant enough for reliable ncRNA detection [115]. It can be quite large for specific classes of ncRNAs, in particular microRNAs, however [10, 141].

Combinations of thermodynamic stability and information on gene structure such as positions of rho-independent terminators were quite successful for ncRNA prediction in intergenic regions of prokaryotic genomes, see e.g. [16, 79]. Such methods cannot be employed in eukaryots because of their much larger genome size and the much more complex gene structures.

Sufficient statistical power for ncRNA detection in eukaryotic genomes can be obtained, however, by combining measures for both thermodynamics stability and structural conservation. An implementation of such a combined approach is the `RNAz` program [143]: A structure conservation index (SCI) is computed by comparing the predicted minimum free energies of the sequences in an alignment with a consensus energy, which is computed by incorporating covariation terms into a free energy minimization computation [52]. Thermodynamic stability is quantified by means of a z-score that measures the folding energy relative to shuffled sequences (a regression approach replaces time-consuming shuffling methods). A support vector machine then classifies an alignment as "structured RNA" or "other" based on z-score and SCI. The significance of the classification is quantified as "RNA-class probability" p.

Various computational screens [1, 116, 20, 16, 122, 79] predict several hundred ncRNA candidates, these predictions however show relatively little mutual overlap in general. Indeed, the majority of bacterial sRNAs was discovered based on computational predictions and subsequent experimental verification.

A `RNAz` survey based on the most conserved parts of the vertebrate genomes estimates that the ncRNA content of mammalian genomes is comparable to their protein coding genes [142], and hence at least an order magnitude

larger than in nematodes. In contrast, only a few thousand structured RNAs in the urochordate *Ciona intestinalis* [93] and in the nematode *Caenorhabditis elegans* [94, 28]. Only a few hundred ncRNAs appear to be present in the yeast *Saccharomyzes cerevisiae* [88]. This indicates that higher vertebrates have dramatically expanded their ncRNA inventory relative to their complement of protein coding genes. This is consistent with the assumption that the function of the ncRNAs is primarily regulatory [85, 86].

9.4.5 RNA-RNA Interaction

Algorithmically, the "co-folding" of two RNAs can be dealt with in the same way as folding a single molecule by concatenating the two sequences and using different energy parameters for the loop that contains the cut-point between the two sequences. A corresponding `RNAcofold` program is described in [53], the `pairfold` program [3] also computes suboptimal structures in the spirit of `RNAsubopt` [149]. A restricted variant of this approach is implemented in the program `RNAhybrid` [114] as well as `RNAduplex` from the Vienna RNA package, see also [154, 30]: here secondary structures within both monomers are neglected so that only intermolecular base pairs are taken into account. The program `bindigo` uses a variation of the Smith-Waterman sequence alignment algorithm for the same purpose [49].

The most prominent application of RNA co-folding algorithms is the prediction of microRNA target genes [95, 70, 9, 151, 104, 124]. The biological activity of siRNAs and miRNAs is influenced by local structural characteristics of the target mRNA. In particular, the binding site at the target sequence must be accessible for hybridization in order to achieve efficient translational repression. Recent contributions [106, 124] suggest two significant parameters: The stability difference between 5' and 3' end of the siRNA, that determines which strand is included into the RISC complex [66, 126] and the local secondary structure of the target site [124, 104, 95, 70, 9, 151].

The energetics of RNA-RNA interactions can be understood in terms of two contributions: the free energy of binding consists of the contribution ΔGu that is necessary to expose the binding site in the appropriate conformation, and contribution ΔGh that describes the energy gain due to hybridization at the binding site. The first term can be computed from a partition function computation as described above, the second term is obtain through a version of the co-folding algorithm. Comparison with the partition function of the isolated systems and standard statistical thermodynamics can be used to explicitly compute the concentration dependence of RNA-RNA binding, see e.g. [30].

9.4.6 RNA-Protein Interaction

In recent years an increasing number of functional features has been reported in the untranslated regions of eukaryotic mRNA [60, 92, 108]. Well-known motifs include internal ribosomal entry sites (IRES) in viral as well as cellular mRNAs, see e.g. [121, 55, 108], and the AU-rich elements (ARE) [5, 89]. In many cases, secondary structure motifs are recognized by regulatory proteins with only highly degenerate, or no sequence constraints at all [138, 91]. In such cases, the thermodynamics of RNA folding can influence binding specificities.

Consider a (protein) ligand that can bind to certain set RNA$*$ of structural conformations a given RNA molecules:

$$\text{Ligand} + \text{RNA}* \rightleftharpoons \text{Ligand} \cdot \text{RNA}$$

The law of mass action implies that the concentrations [RNA$*$], [Ligand], and [Ligand $\cdot$ RNA] of free accessible RNA, free protein, and complex are related through the dissociation constant

$$Kd = \frac{[\text{RNA}*]\ [\text{Ligand}]}{[\text{Ligand} \cdot \text{RNA}]} \tag{9.2}$$

Writing $A(s) \subseteq \Sigma(s)$ for the accessible structures of our RNA molecule s we obtain

$$[\text{RNA}*] = p* [\text{RNA}] \tag{9.3}$$

where $p*$ is the fraction of accessible secondary structures, which can be computed as a ratio of two partition functions

$$p* = \sum \Psi \in A(s) p(\Psi) = \frac{1}{Z} \sum \Psi \in A(s) \exp\left(-\frac{F(\Psi)}{RT}\right) = \frac{Z*}{Z}\,. \tag{9.4}$$

$Z*$, the partition function of all RNAs with suitable structure can be computed by dynamic programming [87, 100] or by means of stochastic backtracking an sampling [32, 31].

Using conventional methods to measure RNA protein interactions, only the total concentration of unbound RNA, [RNA], can be measured. Hence, only the apparent dissociation constant $Kd^{\text{app}} = Kd/p*$ can be determined experimentally. The theory therefore predicts structure dependence of the measured values of Kd^{app}. Under the assumption that the true value of Kd depends only on the ligand and the sequence-structure motif that binds the ligand, we can predict sequence-dependent variations in RNA-ligand binding affinity by means of a computational analysis of the ensemble of RNA structures. In [89, 44] it has been shown that the interaction of the HuR protein with ARE-carrying mRNAs indeed follows this scheme.

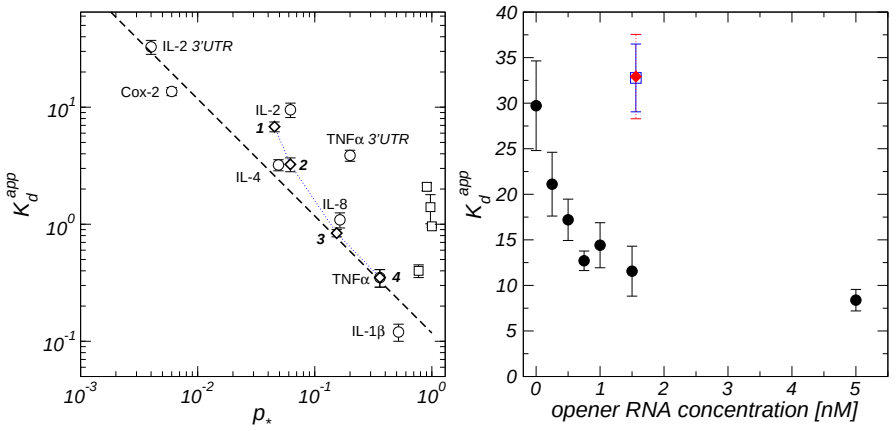

Fig. 9.4. Left: Apparent dissociation constants for *HuR*-mRNA complexes at $23.5°C$ for natural ARE and UTR sequences (○), artificial molecules (□), and designed mutants of the TNFα 3'UTR (◊), [44]. Right: Effect of a complementary opener of length $N0 = 20$ on *in vitro* *HuR*/RNA affinities. The apparent affinity of recombinant HuR to IL-2 3'UTR was determined in presence and absence of the opener Op3 (black circles) and of the negative controls with 1D-FIDA detection. Data redrawn from [89].

An immediate consequence of this mechanism is possibility to use small RNA "modifiers" to modulate the binding affinities of RNAs and ligands by binding to their target RNA in such a way that it alters the local structure at the ligand binding site. The *HuR*-mRNA interaction again serves as a well-studied *in vitro* example for such a technique [89, 44], Fig. 9.4. The regulation of *HuR*-ARE-mediated export and RNA stability *in vivo*, however, remains enigmatic. There is only the single ubiquitously expressed protein *HuR* (and a handful of tissue specific relatives such as the neuronal specific homologue *HuD*) that up-regulates the export and stability of potentially thousands of ARE-carrying mRNAs. It is tempting to speculate that modifying RNA "openers" could be involved in target gene specific regulation of *HuR* activity.

9.5 Concluding Remarks

In this contribution we have discussed at least some of the regulatory mechanism that leave traces at the DNA level. A significant fraction of the non-repetitive DNA of higher eukaryotes is subject to stabilizing selection. It has been estimated, for example, that about 5% of the human genome is under

stabilizing selective pressure [59, 24], while less than 2% are protein-coding genes. It is a major challenge for bioinformatics to elucidate the meaning of the remaining conserved DNA.

The information about at least a large part of the regulatory circuitry of a is accessible by means of comparative genomics. Without a large body of independent experiments, however, we have little chance to decode this information. The first, and maybe crucial step, beyond identifying the DNA footprints themselves is to discriminate between regulatory elements that exert their function at the DNA level, *cis*-acting elements that function at the mRNA level, and non-coding RNAs.

We have reviewed here some of the currently available computational approaches that can be used to detect and analyze such elements. Few general tools are available. A subclass of non-coding RNAs and *cis*-acting mRNA elements, for example, can be recognized because of its conserved secondary structure. On the other hand, at present there is not even a way to distinguish protein binding sites on the genomic DNA from those on the mRNA, unless specific knowledge about a particular sequence motifs is available from experiments.

References

1. L. Agarman, R. Hershberg, J. Vogel, G. Bejerano, E. G. Wagner, H. Margalit, and S. Altuvia. Novel small RNA-encoding genes in the intergenic regions of *Escherichia coli*. *Curr. Biol.*, 11:941–950, 2001.
2. L. Ancel Meyers, J. F. Lee, M. Cowperthwaite, and A. D. Ellington. The robustness of naturally and artificially selected nucleic acid secondary structures. *J. Mol. Evol.*, 58:681–691, 2004.
3. M. Andronescu, Z. Zhang, and A. Condon. Secondary structure prediction of interacting RNA molecules. *J. Mol. Biol.*, 345:987–1001, 2005.
4. T. Bailey and C. Elkan. The value of prior knowledge in discovering motifs with MEME. *Proc Int Conf Intell Syst Mol Biol*, 3:21–29, 1995.
5. T. Bakheet, M. Frevel, B. R. Williams, W. Greer, and K. S. Khabar. ARED: human AU-rich element-containing mRNA database reveals an unexpectedly diverse functional repertoire of encoded proteins. *Nucl. Acids Res.*, 29:246–254, 2001.
6. S. Barlati and A. Barbon. RNA editing: a molecular mechanism for the fine modulation of neuronal transmission. *Acta Neurochir Suppl*, 93:53–57, 2005.
7. E. Bayne and R. Allshire. RNA-directed transcriptional gene silencing in mammals. *Trends Genet*, 21:370–373, 2005.
8. P. Bertone, V. Stoc, T. E. Royce, J. S. Rozowsky, A. E. Urban, X. Zhu, J. L. Rinn, W. Tongprasit, M. Samanta, S. Weissman, M. Gerstein, and M. Snyder. Global identification of human transcribed sequences with genome tiling arrays. *Science*, 306:2242–2246, 2004.

9. E. A. Bohula, A. J. Salisbury, M. Sohail, M. P. Playford, J. Riedemann, E. M. Southern, and V. M. Macaulay. The efficacy of small interfering RNAs targeted to the type 1 insulin-like growth factor receptor (IGF1R) is influenced by secondary structure in the IGF1R transcript. *J. Biol. Chem.*, 278:15991–15997, 2003.
10. E. Bonnet, J. Wuyts, P. Rouzé, and Y. Van de Peer. Evidence that microRNA precursors, unlike other non-coding RNAs, have lower folding free energies than random sequences. *Bioinformatics*, 20:2911–2917, 2004.
11. S. Brantl. Bacterial gene regulation: from transcription attenuation to riboswitches and ribozymes. *Trends Microbiol.*, 12:473–475, 2004.
12. M. Brent and R. Guigó. Recent advances in gene structure prediction. *Curr Opin Struct Biol*, 14:264–272, 2004.
13. C. Burge and S. Karlin. Prediction of complete gene structures in human genomic DNA. *J Mol Biol*, 268:78–94, 1997.
14. J. Butler and J. Kadonaga. The RNA polymerase II core promoter: a key component in the regulation of gene expression. *Genes Dev*, 16:2583–2592, 2002.
15. B. Cairns. Chromatin remodeling complexes: strength in diversity, precision through specialization. *Curr Opin Genet Dev*, 15:185–190, 2005.
16. R. J. Carter, I. Dubchak, and S. R. Holbrook. A computational approach to identify genes for functional RNAs in genomic sequences. *Nucl. Acids Res.*, 29:3928–3938, 2001.
17. S. Cawley, S. Bekiranov, H. H. Ng, P. Kapranov, E. A. Sekinger, D. Kampa, A. Piccolboni, V. Sementchenko, J. Cheng, A. J. Williams, R. Wheeler, B. Wong, J. Drenkow, M. Yamanaka, S. Patel, S. Brubaker, H. Tammana, G. Helt, K. Struhl, and T. R. Gingeras. Unbiased mapping of transcription factor binding sites along human chromosomes 21 and 22 points to widespread regulation of noncoding RNAs. *Cell*, 116:499–509, 2004.
18. J. Chen, M. Sun, L. Hurst, G. Carmichael, and J. Rowley. Genome-wide analysis of coordinate expression and evolution of human cis-encoded sense-antisense transcripts. *Trends Genet*, 21:326–329, 2005.
19. J. H. Chen, S. Y. Le, B. Shapiro, K. M. Currey, and J. V. Maizel Jr. A computational procedure for assessing the significance of RNA secondary structure. *Comput. Appl. Biosci.*, 6:7–18, 1990.
20. S. Chen, E. A. Lesnik, T. A. Hall, R. Sampath, R. H. Griffey, D. Eker, and L. Blyn. A bioinformatics based approach to discover small RNA genes in the *Escherichia coli* genome. *Biosystems*, 65:157–177, 2002.
21. J. Cheng, P. Kapranov, J. Drenkow, S. Dike, S. Brubaker, S. Patel, J. Long, D. Stern, H. Tammana, G. Helt, V. Sementchenko, A. Piccolboni, S. Bekiranov, D. K. Bailey, M. Ganesh, S. Ghosh, I. Bell, D. S. Gerhard, and T. R. Gingeras. Transcriptional maps of 10 human chromosomes at 5-nucleotide resolution. *Science*, 308:1149–1154, 2005.
22. J. Claycomb and T. Orr-Weaver. Developmental gene amplification: insights into DNA replication and gene expression. *Trends Genet*, 21:149–162, 2005.
23. P. Clote, F. Ferré, E. Kranakis, and D. Krizanc. Structural RNA has lower folding energy than random RNA of the same dinucleotide frequency. *RNA*, 11:578–591, 2005.
24. G. M. Cooper, M. Brudno, E. A. Stone, I. Dubchak, S. Batzoglou, and A. Sidow. Characterization of evolutionary rates and constraints in three mammalian genomes. *Genome Res*, 14:539–48, 2004.

25. F. F. Costa. Non-coding RNAs: New players in eucaryotic biology. *Gene*, 357:83–94, 2005.
26. J. Dalgaard and S. Vengrova. Selective gene expression in multigene families from yeast to mammals. *Sci STKE*, 2004(256), 2004.
27. E. Davidson. *Genomic Regulatory Systems*. Academic Press, San Diego, 2001.
28. W. Deng, X. Zhu, G. Skogerb , Y. Zhao, Z. Fu, Y. Wang, L. He, Housheng Cai, H. Sun, C. Liu, B. L. Li, B. Bai, J. Wang, Y. Cui, D. Jai, Y. Wang, D. Du, and R. Chen. Organisation of the *Caenorhabditis elegans* small noncoding transcriptome: genomic features, biogenesis and expression. *Genome Res.*, 16:20–29 2006.
29. E. T. Dermitzakis, A. Reymond, N. Scamuffa, C. Ucla, E. Kirkness, C. Rossier, and S. E. Antonarakis. Evolutionary discrimination of mammalian conserved non-genic sequences (CNGs). *Science*, 302:1033–1035, 2003.
30. R. A. Dimitrov and M. Zuker. Prediction of hybridization and melting for double-stranded nucleic acids. *Biophys. J.*, 87:215–226, 2004.
31. Y. Ding, C. Y. Chan, and C. E. Lawrence. Sfold web server for statistical folding and rational design of nucleic acids. *Nucl. Acids Res.*, 32(Web Server issue):W135–141, 2004.
32. Y. Ding and C. E. Lawrence. A statistical sampling algorithm for RNA secondary structure prediction. *Nucl. Acids Res.*, 31:7280–7301, 2003.
33. X. Feng, W. Lin, D. Minghua, S. Fengzhu, and Q. Minping. An efficient algorithm for deciphering regulatory motifs. In These Proceedings, 2005.
34. J. Fickett. Finding genes by computer: the state of the art. *Trends Genet*, 12: 316–320, 1996.
35. C. Flamm, I. L. Hofacker, S. Maurer-Stroh, P. F. Stadler, and M. Zehl. Design of multi-stable RNA molecules. *RNA*, 7:254–265, 2000.
36. D. Galas and A. Schmitz. DNAse footprinting: a simple method for the detection of protein-DNA binding specificity. *Nucl. Acids Res.*, 5:3157–3170, 1978.
37. M. Garner and A. Revzin. A gel electrophoresis method for quantifying the binding of proteins to specific DNA regions: application to components of the Escherichia coli lactose operon regulatory system. *Nucl. Acids Res.*, 9:3047–3060, 1981.
38. F. Gebauer and M. Hentze. Molecular mechanisms of translational control. *Nat Rev Mol Cell Biol*, 5:827–835, 2004.
39. M. Gelfand. Prediction of function in DNA sequence analysis. *J Comput Biol*, 2:87–115, 1995.
40. M. Gelfand, A. Mironov, and P. Pevzner. Gene recognition via spliced sequence alignment. *Proc Natl Acad Sci U S A*, 93:9061–9066, 1996.
41. G. Gonsalvez, C. Urbinati, and R. Long. RNA localization in yeast: moving towards a mechanism. *Biol Cell*, 97:75–86, 2005.
42. S. Gottesman. The small RNA regulators of *Escherichia coli*: roles and mechanisms. *Annu. Rev. Microbiol.*, 58:303–328, 2004.
43. R. Guigó, E. Dermitzakis, P. Agarwal, C. Ponting, G. Parra, A. Reymond, J. Abril, E. Keibler, R. Lyle, C. Ucla, S. Antonarakis, and M. Brent. Comparison of mouse and human genomes followed by experimental verification yields an estimated 1,019 additional genes. *Proc Natl Acad Sci U S A*, 100:1140–1145, 2003.
44. J. Hackermüller, N.-C. Meisner, M. Auer, M. Jaritz, and P. F. Stadler. The effect of RNA secondary structures on RNA-ligand binding and the modifier RNA mechanism: A quantitative model. *Gene*, 345:3–12, 2005.

45. T. Heinemeyer, E. Wingender, I. Reuter, H. Hermjakob, A. E. Kel, O. V. Kel, E. V. Ignatieva, E. A. Ananko, O. A. Podkolodnaya, F. A. Kolpakov, N. L. Podkolodny, and N. A. Kolchanov. Databases on transcriptional regulation: TRANSFAC, TRRD, and COMPEL. *Nucl. Acids Res.*, 26:364–370, 1998.
46. T. M. Henkin and C. Yanofsky. Regulation by transcription attenuation in bacteria: how RNA provides instructions for transcribtion termination/antitermination decision. *BioEssays*, 24:700–707, 2002.
47. R. Hershberg, S. Altuvia, and H. Margalit. A survey of small RNA-encoding genes in *Escherichia coli*. *Nucl. Acids Res.*, 31:1813–1820, 2003.
48. G. Hertz and G. Stormo. Identifying DNA and protein patterns with statistically significant alignments of multiple sequences. *Bioinformatics*, 15:563–577, 1999.
49. N. Hodas and D. Aalberts. Efficient computation of optimal oligo-RNA binding. *Nucl. Acids Res.*, 32:6636–6642, 2004.
50. I. L. Hofacker. Vienna RNA secondary structure server. *Nucl. Acids Res.*, 31:3429–3431, 2003.
51. I. L. Hofacker, M. Fekete, C. Flamm, M. A. Huynen, S. Rauscher, P. E. Stolorz, and P. F. Stadler. Automatic detection of conserved RNA structure elements in complete RNA virus genomes. *Nucl. Acids Res.*, 26:3825–3836, 1998.
52. I. L. Hofacker, M. Fekete, and P. F. Stadler. Secondary structure prediction for aligned RNA sequences. *J. Mol. Biol.*, 319:1059–1066, 2002.
53. I. L. Hofacker, W. Fontana, P. F. Stadler, S. Bonhoeffer, M. Tacker, and P. Schuster. Fast folding and comparison of RNA secondary structures. *Monatsh. Chem.*, 125:167–188, 1994.
54. P. Hooper, H. Zhang, and D. Wishart. Prediction of genetic structure in eukaryotic DNA using reference point logistic regression and sequence alignment. *Bioinformatics*, 16:425–438, 2000.
55. I. Huez, L. Créancier, S. Audigier, M. Gensac, A. Prats, and H. Prats. Two independent internal ribosome entry sites are involved in translation initiation of vascular endothelial growth factor mRNA. *Mol. Cell. Biol.*, 18:6178–6190, 1998.
56. J. Hughes, P. Estep, S. Tavazoie, and G. Church. Computational identification of cis-regulatory elements associated with groups of functionally related genes in Saccharomyces cerevisiae. *J Mol Biol*, 296:1205–1214, 2000.
57. A. Hüttenhofer, P. Schattner, and N. Polacek. Non-coding RNAs: hope or hype? *Trends Genet.*, 21:289-97 2005.
58. T. Imanishi and *et al.* Integrative annotation of 21,037 human genes validated by full-length cDNA clones. *PLoS Biology*, 2:0856–0875, 2004.
59. International Mouse Genome Sequencing Consortium. Initial sequencing and comparative analysis of the mouse genome. *Nature*, 420:520–562, 2002.
60. G. H. Jacobs, O. Rackham, P. A. Stockwell, W. Tate, and C. M. Brown. Transterm: a database of mRNAs and translational control elements. *Nucl. Acids Res.*, 30:310–311, 2002.
61. J. M. Johnson, S. Edwards, D. Shoemaker, and E. E. Schadt. Dark matter in the genome: evidence of widespread transcription detected by microarray tiling experiments. *Trends Genet.*, 21:93–102, 2005.
62. H. Jow, C. Hudelot, M. Rattray, and P. G. Higgs. Bayesian phylogenetics using an RNA substitution model applied to early mammalian evolution. *Mol. Biol. Evol.*, 19:1591–1601, 2002.

63. D. Kampa, J. Cheng, P. Kapranov, M. Yamanaka, S. Brubaker, S. Cawley, J. Drenkow, A. Piccolboni, S. Bekiranov, G. Helt, H. Tammana, and T. R. Gingeras. Novel RNAs identified from an in-depth analysis of the transcriptome of human chromosomes 21 and 22. *Genome Res.*, 14:331–342, 2004.
64. M. Kawano, A. A. Reynolds, J. Miranda-Rios, and G. Storz. Detection of 5'- and 3'-UTR-derived small RNAs and *cis*-encoded antisense RNAs in *Escherichia coli*. *Nucl. Acids Res.*, 33:1040–1050, 2005.
65. O. Kel-Margoulis, T. Ivanova, E. Wingender, and A. Kel. Automatic annotation of genomic regulatory sequences by searching for composite clusters. In *Proc. Pac. Symp. Biocomput.*, pages 187–198, 2002.
66. A. Khvorova, A. Reynolds, and S. D. Jayasena. Functional siRNAs and miRNAs exhibit strand bias. *Cell*, 115:209–16, 2003.
67. I. Korf, P. Flicek, D. Duan, and M. Brent. Integrating genomic homology into gene structure prediction. *Bioinformatics*, 17 Suppl 1:140–148, 2001.
68. A. Kornblihtt, M. de la Mata, J. Fededa, M. Munoz, and G. Nogues. Multiple links between transcription and splicing. *RNA*, 10:1489–1498, 2004.
69. M. Kozak. Alternative ways to think about mRNA sequences and proteins that appear to promote internal initiation of translation. *Gene*, 318:1–23, 2003.
70. R. Kretschmer-Kazemi Far and G. Sczakiel. The activity of siRNA in mammalian cells is related to structural target accessibility: a comparison with antisense oligonucleotides. *Nucl. Acids Res.*, 31:4417–4424, 2003.
71. A. Krogh. Gene finding: putting the parts together. In M. Bishop, editor, *Guide to human genome computing*, pages 261–274. Academic Press, 2nd edition, 1998.
72. D. Kulp, D. Haussler, M. Reese, and F. Eeckman. A generalized hidden Markov model for the recognition of human genes in DNA. *Proc Int Conf Intell Syst Mol Biol*, 4:134–142, 1996.
73. L. Lareau, R. Green, R. Bhatnagar, and S. Brenner. The evolving roles of alternative splicing. *Curr Opin Struct Biol*, 14:273–282, 2004.
74. C. Lawrence, S. Altschul, M. Boguski, J. Liu, A. Neuwald, and J. Wootton. Detecting subtle sequence signals: a Gibbs sampling strategy for multiple alignment. *Science*, 262:208–214, 1993.
75. C. Lawrence and A. Reilly. An expectation maximization (EM) algorithm for the identification and characterization of common sites in unaligned biopolymer sequences. *Proteins*, 7:41–51, 1990.
76. S. V. Le, J. H. Chen, K. M. Currey, and J. V. Maizel Jr. A program for predicting significant RNA secondary structures. *Comput. Appl. Biosci.*, 4:153–159, 1988.
77. D. LeRoith and C. Roberts. The insulin-like growth factor system and cancer. *Cancer Lett*, 195:127–137, 2003.
78. X. Liang, A. Haritan, S. Uliel, and S. Michaeli. *trans* and *cis* splicing in trypanosomatids: mechanism, factors, and regulation. *Eukaryot Cell*, 2:830–840, 2003.
79. J. Livny, M. A. Fogel, B. M. Davis, and M. K. Waldor. `sRNAPredict`: an integrative computational approach to identify sRNAs in bacterial genomes. *Nucl. Acids Res.*, 33:4096–4105, 2005.
80. A. Mallory and H. Vaucheret. MicroRNAs: something important between the genes. *Curr Opin Plant Biol*, 7:120–125, 2004.
81. R. Margueron, P. Trojer, and D. Reinberg. The key to development: interpreting the histone code? *Curr Opin Genet Dev*, 15:163–176, 2005.

82. E. H. Margulies, M. Blanchette, D. Haussler, and E. D. Green. Identification and characterization of multi-species conserved sequences. *Genome Res.*, 13:2507–2518, 2003.
83. D. H. Mathews. Using an RNA secondary structure partition function to determine confidence in base pairs predicted by free energy minimization. *RNA*, 10:1178–1190, 2004.
84. D. H. Mathews, J. Sabina, M. Zuker, and D. H. Turner. Expanded sequence dependence of thermodynamic parameters improves prediction of RNA secondary structure. *J. Mol. Biol.*, 288:911–940, 1999.
85. J. S. Mattick. Challenging the dogma: the hidden layer of non-protein-coding RNAs in complex organisms. *Bioessays*, 25:930–939, 2003.
86. J. S. Mattick. RNA regulation: a new genetics? *Nature Genetics*, 5:316–323, 2004.
87. J. S. McCaskill. The equilibrium partition function and base pair binding probabilities for RNA secondary structure. *Biopolymers*, 29:1105–1119, 1990.
88. J. P. McCutcheon and S. R. Eddy. Computational identification of non-coding RNAs in *Saccharomyces cerevisiae* by comparative genomics. *Nucl. Acids Res.*, 31:4119–4128, 2003.
89. N.-C. Meisner, J. Hackermüller, V. Uhl, A. Aszódi, M. Jaritz, and M. Auer. mRNA openers and closers: A methodology to modulate AU-rich element controlled mRNA stability by a molecular switch in mRNA conformation. *Chembiochem.*, 5:1432–1447, 2004.
90. E. Merino and C. Yanofsky. Regulation by termination-antitermination: a genomic approach. In A. L. Sonenshein, J. A. Hoch, and R. Losick, editors, Bacillus subtilis *and its closest relatives: From Genes to Cells*, pages 323–336. ASM Press, Washington D.C., 2002.
91. A. C. Messias and M. Sattler. Structural basis of single-stranded RNA recognition. *Acc. Chem. Res.*, 37:279–287, 2004.
92. F. Mignone, C. Gissi, S. Liuni, and G. Pesole. Untranslated regions of mRNAs. *Genome Biology*, 3, 2002. reviews0004.1-0004.10.
93. K. Missal, D. Rose, and P. F. Stadler. Non-coding RNAs in *Ciona intestinalis*. *Bioinformatics*, 21(S2):i77-i78, 2005.
94. K. Missal, X. Zhu, D. Rose, W. Deng, G. Skogerb , R. Chen, and P. F.Stadler. Prediction of structured non-coding RNAs in the genome of the nematode *Caenorhabitis elegans*. *J. Exp. Zool.B: Mol. Dev. Evol.*, 2006. DOI: 10.1002/jez.b.21086
95. V. Mittal. Improving the efficiency of RNA interference in mammals. *Nat. Rev. Genet.*, 5:355–365, 2004.
96. H. Morgan, F. Santos, K. Green, W. Dean, and W. Reik. Epigenetic reprogramming in mammals. *Hum Mol Genet*, 14(Spec No 1):47–58, 2005.
97. B. Morgenstern. `DIALIGN 2`: improvement of the segment-to-segment approach to multiple sequence alignment. *Bioinformatics*, 15:211–218, 1999.
98. A. Morillon, J. O'Sullivan, A. Azad, N. Proudfoot, and J. Mellor. Regulation of elongating RNA polymerase II by forkhead transcription factors in yeast. *Science*, 300(5618):492–495, 2003.
99. A. Mosig, T. Bıyıkoğlu, S. J. Prohaska, and P. F. Stadler. Discovering cis regulatory modules by optimizing barbeques. *Theor. Comput. Sci.*, 2005. submitted.
100. U. Mückstein, H. Tafer, J. Hackermüller, S. B. Bernhard, P. F. Stadler, and I. L. Hofacker. Thermodynamics of RNA-RNA binding. In *German Conference*

on Bioinformatics 2005, A. Torda, S. Kurtz, M. Rarey (eds.), Lecture Notes in Informatics P-71, Gesellschaft f. Informatik, Bonn, pp.3–13, 2005.
101. E. Nudler and A. S. Mironov. The riboswitch control of bacterial metabolism. *Trends Biochem. Sci.*, 29:11–17, 2004.
102. Y. Okazaki, M. Furuno, T. Kasukawa, J. Adachi, H. Bono, S. Kondo, I. Nikaido, N. Osato, R. Saito, H. Suzuki, and *et al.* Analysis of the mouse transcriptome based on functional annotation of 60,770 full-length cDNAs. *Nature*, 420:563–573, 2002.
103. M. J. O'Neill. The influence of non-coding RNAs on allele-specific gene expression in mammals. *Hum Mol Genet.*, 14:R113–120, 2005.
104. M. Overhoff, M. Alken, R. K. Far, M. Lemaitre, B. Lebleu, G. Sczakiel, and I. Robbins. Local RNA target structure influences siRNA efficacy: A systematic global analysis. *J. Mol. Biol.*, 348:871–881, 2005.
105. P. Pan, M. Lieber, and J. Teale. The role of recombination signal sequences in the preferential joining by deletion in DH-JH recombination and in the ordered rearrangement of the IgH locus. *Int Immunol*, 9:515–522, 1997.
106. J. S. Parker, S. M. Roe, and D. Barford. Structural insights into mRNA recognition from a PIWI domain-siRNA guide complex. *Nature*, 434:663–666, 2005.
107. J. Parsch, J. M. Braverman, and W. Stephan. Comparative sequence analysis and patterns of covariation in RNA secondary structures. *Genetics*, 154:909–921, 2000.
108. G. Pesole, F. Mignone, C. Gissi, G. Grillo, F. Licciulli, and S. Liuni. Structural and functional features of eukaryotic mRNA untranslated regions. *Gene*, 276:73–81, 2001.
109. A. Philippakis, F. He, and M. Bulyk. Modulefinder: a tool for computational discovery of cis regulatory modules. In *Proc. Pac. Symp. Biocomput.*, pages 519–30, 2005.
110. S. J. Prohaska, C. Fried, C. T. Amemiya, F. H. Ruddle, G. P. Wagner, and P. F. Stadler. The shark HoxN cluster is homologous to the human HoxD cluster. *J. Mol. Evol.*, 58:212–217, 2004.
111. S. J. Prohaska, C. Fried, C. Flamm, G. Wagner, and P. F. Stadler. Surveying phylogenetic footprints in large gene clusters: Applications to Hox cluster duplications. *Mol. Phyl. Evol.*, 31:581–604, 2004.
112. R. Pudimat, E. Schukat-Talamazzini, and R. Backofen. A multiple-feature framework for modelling and predicting transcription factor binding sites. *Bioinformatics*, 21: 3082–3088, 2005.
113. M. Reese, G. Hartzell, N. Harris, U. Ohler, J. Abril, and S. Lewis. Genome annotation assessment in Drosophila melanogaster. *Genome Res*, 10:483–501, 2000.
114. M. Rehmsmeier, P. Steffen, M. Hochsmann, and R. Giegerich. Fast and effective prediction of microRNA/target duplexes. *RNA*, 10:1507–17, 2004.
115. E. Rivas and S. R. Eddy. Secondary structure alone is generally not statistically significant for the detection of noncoding RNAs. *Bioinformatics*, 16:583–605, 2000.
116. E. Rivas, R. J. Klein, T. A. Jones, and S. R. Eddy. Computational identification of noncoding RNAs in *E. coli* by comparative genomics. *Curr. Biol.*, 11:1369–1373, 2001.
117. M. Rodriguez, C. Dargemont, and F. Stutz. Nuclear export of RNA. *Biol Cell*, 96:639–655, 2004.

118. S. Rogic, A. Mackworth, and F. Ouellette. Evaluation of gene-finding programs on mammalian sequences. *Genome Res*, 11:817–832, 2001.
119. F. Roth, J. Hughes, P. Estep, and G. Church. Finding DNA regulatory motifs within unaligned noncoding sequences clustered by whole-genome mRNA quantitation. *Nat Biotechnol*, 16:939–945, 1998.
120. S. Rousseaux, C. Caron, J. Govin, C. Lestrat, A. Faure, and S. Khochbin. Establishment of male-specific epigenetic information. *Gene*, 345:139–153, 2005.
121. R. R. Rueckert. Picornaviridae: The viruses and their replication. In N. Fields, D. Knipe, and P. Howley, editors, *Virology*, volume 1, pages 609–654. Lippincott-Raven Publishers, Philadelphia, New York, third edition, 1996.
122. P. Sætrom, R. Sneve, K. I. Kristiansen, O. Sn ve jr., T. Grünfeld, T. Rognes, and E. Seeberg. Predicting non-coding RNA genes in *Escherichia coli* with boosted genetic programming. *Nucl. Acids Res.*, 33:3263–3270, 2005.
123. A. Sandelin, W. A. Pär Engström, W. Wasserman, and B. Lenhard. Jaspar: an open access database for eukaryotic transcription factor binding profiles. *Nucl. Acids Res.*, 32:D91–D94, 2004.
124. S. Schubert, A. Grunweller, V. Erdmann, and J. Kurreck. Local RNA target structure influences siRNA efficacy: Systematic analysis of intentionally designed binding regions. *J. Mol. Biol.*, 348(4):883–93, 2005.
125. S. Schwartz, Z. Zhang, K. A. Frazer, A. Smit, C. Riemer, J. Bouck, R. Gibbs, R. Hardison, , and W. Miller. `PipMaker` — a web server for aligning two genomic DNA sequences. *Genome Research*, 4:577–586, 2000.
126. D. Schwarz, G. Hutvagner, T. Du, Z. Xu, N. Aronin, and P. Zamore. Asymmetry in the assembly of the RNAi enzyme complex. *Cell.*, 115:99–208, 2003.
127. S. Shabalina, A. Ogurtsov, V. Kondrashov, and A. Kondrashov. Selective constraint in intergenic regions of human and mouse genomes. *Trends Genet*, 17:373–376, 2001.
128. S. A. Shabalina and A. S. Kondrashov. Pattern of selective constraint in *C. elegans* and *C. briggsae* genomes. *Genet Res*, 74:23–30, 1999.
129. R. Sharan, I. Ovcharenko, A. Ben-Hur, and R. M. Karp. CREME: a framework for identifying cis-regulatory modules in human-mouse conserved segments. In *ISMB (Supplement of Bioinformatics)*, pages 283–291, 2003.
130. S. Sinha, E. van Nimwegen, and E. Siggia. A probabilistic method to detect regulatory modules. *Bioinformatics*, 19, 2003.
131. G. Stamatoyannopoulos. Control of globin gene expression during development and erythroid differentiation. *Exp Hematol*, 33:259–271, 2005.
132. L. Stein. Human genome: end of the beginning. *Nature*, 431:915–916, 2004.
133. F. Sterky and J. Lundeberg. Sequence analysis of genes and genomes. *J Biotechnol*, 76:1–31, 2000.
134. N. Sudarsan, J. E. Barrick, and R. R. Breaker. Metabolite-binding RNA domains are present in the genes of eukaryotes. *RNA*, 9:644–647, 2003.
135. The *C. elegans* Sequencing Consortium. Genome sequence of the nematode *C. elegans*: A platform for investigating biology. *Science*, 282:2012–2018, 1998.
136. D. Turner, N. Sugimoto, and S. Freier. RNA structure prediction. *Annu. Rev. Biophys. Biophys. Chem.*, 17:167–92, 1988.
137. E. van Nimwegen, J. P. Crutchfield, and M. A. Huynen. Neutral evolution of mutational robustness. *Proc. Natl. Acad. Sci. USA*, 96:9716–9720, 1999.
138. G. Varani. RNA-protein intermolecular recognition. *Acc. Chem. Res.*, 30:189–195, 1997.

139. A. G. Vitreschak, D. A. Rodionov, A. A. Mironov, and M. S. Gelfand. Riboswitches: the oldest mechanism for the regulation of gene expression? *Trends Gen.*, 20:44–50, 2004.
140. A. Wagner and P. F. Stadler. Viral RNA and evolved mutational robustness. *J. Exp. Zool. (Mol. Dev. Evol.)*, 285:119–127, 1999.
141. S. Washietl and I. L. Hofacker. Consensus folding of aligned sequences as a new measure for the detection of functional RNAs by comparative genomics. *J. Mol. Biol.*, 342:19–30, 2004.
142. S. Washietl, I. L. Hofacker, M. Lukasser, A. Hüttenhofer, and P. F. Stadler. Genome-wide mapping of conserved RNA secondary structures predicts thousands of functional non-coding RNAs in human. *Nature Biotech.*, 23:1383-1390, 2005.
143. S. Washietl, I. L. Hofacker, and P. F. Stadler. Fast and reliable prediction of noncoding RNAs. *Proc. Natl. Acad. Sci. USA*, 102:2454–2459, 2005.
144. J. Weischenfeldt, J. Lykke-Andersen, and B. Porse. Messenger RNA surveillance: neutralizing natural nonsense. *Curr Biol*, 15:559–562, 2005.
145. A. West and P. Fraser. Remote control of gene transcription. *Hum Mol Genet*, 14 Spec No 1:101–111, 2005.
146. A. West, M. Gaszner, and G. Felsenfeld. Insulators: many functions, many mechanisms. *Genes Dev*, 16:271–288, 2002.
147. C. Wilusz and J. Wilusz. Bringing the role of mRNA decay in the control of gene expression into focus. *Trends Genet*, 20:491–497, 2004.
148. G. Wray, M. Hahn, E. Abouheif, J. Balhoff, M. Pizer, M. Rockman, and L. Romano. The evolution of transcriptional regulation in eukaryotes. *Mol Biol Evol*, 20:1377–1419, 2003.
149. S. Wuchty, W. Fontana, I. L. Hofacker, and P. Schuster. Complete suboptimal folding of RNA and the stability of secondary structures. *Biopolymers*, 49:145–165, 1999.
150. R. Yeh, L. Lim, and C. Burge. Computational inference of homologous gene structures in the human genome. *Genome Res*, 11:803–816, 2001.
151. K. Yoshinari, M. Miyagishi, and T. K. Effects on RNAi of the tight structure, sequence and position of the targeted region. *Nucl. Acids Res.*, 32:691–9, 2004.
152. C. H. Yuh, H. Bolouri, and E. H. Davidson. Genomic cis-regulatory logic: Experimental and computational analysis of a sea urchin gene. *Science*, 279:1896–1902, 1998.
153. M. Zuker. Calculating nucleic acid secondary structure. *Curr. Opin. Struct. Biol.*, 10:303–310, 2000.
154. M. Zuker. Mfold web server for nucleic acid folding and hybridization prediction. *Nucl. Acids Res.*, 31:3406–15, 2003.
155. M. Zuker and P. Stiegler. Optimal computer folding of large RNA sequences using thermodynamics and auxiliary information. *Nucl. Acids Res.*, 9:133–148, 1981.

10

Dynamic properties of cell-cycle and life-cycle networks in budding yeast

Fangting Li, Ying Lu, Tao Long, Qi Ouyang and Chao Tang

Summary. Dynamic behaviors of protein-protein and protein-DNA interactions in living cells are investigated using the cell-cycle network and life-cycle network in budding yeast as model systems. Our analysis reveals important dynamic properties of the biological networks. In phase space, the resting states of the networks are global attractors, almost all initial protein states evolve to these stationary states; the biological pathways toward the stationary state are globally attracting trajectories, all initial states are through these well-defined sequences. The distributions of attractor size and pathway thickness of biological network are distinct from that of random networks. Perturbation analysis shows that these networks are dynamically stable. These results suggest that protein networks are robustly designed for their functions and that the global dynamic properties of protein networks are intimately coupled to their functions.

10.1 Introduction

Protein-protein and protein-DNA interactions in living cells constitute molecular dynamic networks that govern various cellular functions. Recently, much attention has been paid to the global or "system" properties of protein networks rather than isolated functions of proteins. Researches in this field have achieved significant results. For example, Jeong et al. showed that biological networks have the same topological power-law scaling properties, and the highly connected proteins with a central role in the networks' architecture are essential in the systems [1, 2]. Albert et al. demonstrated that networks with power-law connection distributions are topologically stable; they are highly tolerant against random failures [3]. Milo et al. discussed the basic building blocks of most networks. They suggest that different network motifs are used to build different biological networks that perform different functions [4]. However, despite of these achievements, we are still in an early stage of understanding the global properties of the networks. Previous studies are focused

on the topological properties of the biological networks while few studies address their dynamic behavior [5, 6]. Here we report our dynamic analysis of the cell-cycle network and the life cycle network of the budding yeast. Our study reveals important properties of the networks. In the cell-cycle network, almost all (about 96%) initial protein states evolve to the stationary state G1, making it a global attractor; the dynamic paths to G1 for these initial states are through the cell-cycle sequence, making it a globally attracting trajectory. Similar findings are obtained for the life-cycle network, where the cell-cycle network is one of components. We also found that the distributions of the sizes of attractors and trajectories in phase space are very different from that of random networks, and both networks are dynamically stable against random perturbations.

10.2 The cell-cycle and life-cycle networks in budding yeast

Budding yeast Saccharomyces cerevisiae is chosen as a model system in our dynamic study of biological networks because a comprehensive protein-protein interaction network of this single-cell eukaryotic model organism is emerging [7-13]. Budding yeast has a relatively simple life cycle. Yeast cells can exist in either diploid or haploid genetic state. Cells in both forms can proliferate by an ordinary cell-division process under rich nutrition conditions; the process is named as cell cycle. Triggered by starvation, cells in diploid form undergo meiosis to give rise to spores-haploid cells in a dormant state that are resistant to harsh environmental conditions. Under appropriate conditions, pheromone stimulates cells in haploid form to fuse to create a new diploid cell. The whole processes are named as life cycle. Figure 1 shows the protein interaction network governing the cell cycle and the life cycle processes in budding yeast. The network is based on extensive literature studies, the Chen's model [14] and the database of http://mips.gsf.de/ and http://www.proteome.com. Careful document checking and cross verifying are conducted in order to correct errors in the published draft. The network shown in Fig. 1 can be divided into three interacting functional modules: the sporulation and meiosis sub-network (left), the pheromone and mating cascade (upper-right), and the cell-cycle sub-network (lower-right). Depending on the nutrient condition and the genotype, different modules may be activated in response to different 'signals'. We first focus on the dynamic properties of the most comprehensive sub-network: the module governing the cell cycle process.

The simplified cell-cycle network is shown as the inset of Fig. 2. We simplify the network by removing and reconnecting nodes in a way that do not affect the network dynamics, e.g., intermediate nodes on a linear path are replaced

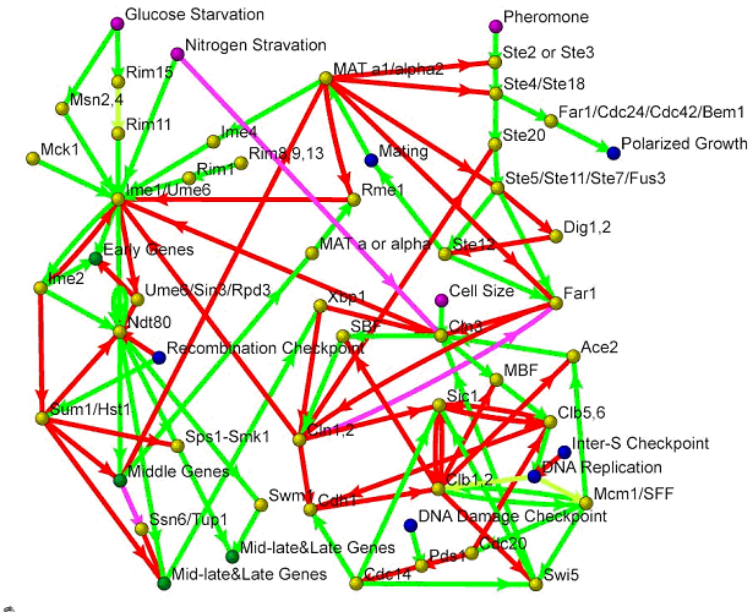

Fig. 10.1. The protein network governing the processes of mating, sporulation and cell cycle. Yellow nodes represent single protein, complex of proteins or several related proteins. Green nodes represent group of proteins that expressed in a special time section. Blue nodes represent physiological process or checkpoint. Purple nodes represent signal or corresponding condition. Green and red lines represent positive and negative actions respectively. Light green and purple lines represent undetermined or indirect actions. All self-degradation actions, yellow lines pointing to nodes selves, are omitted for clarity. Some of them are displayed in simplified cell-cycle and life-cycle networks inserted in Fig.2 and Fig.3 respectively. The whole net can be divided into three modules: mating (upper right), sporulation (left) and cell cycle (lower right).

by an arrow connecting the beginning and the ending nodes. In the simplified network, there are 11 key nodes governing the cell cycle process: Cln3/Cdc28 complex, MBF, SBF, Cln1 or Cln2/Cdc28 complex, Clb5 or Clb6/Cdc28 complex, Sic1, Mcm1/SFF, Clb1 or Clb2/Cdc28 complex, Cdh1, Cdc20&Cdc14, and Swi5. Under rich nutrition conditions, when a yeast cell in either diploid or haploid form grows large enough, the protein Cln3/Cdc28 complex is 'activated', driving the cell into the 'excited' G1 state. The cell then goes through a sequence of phases of the cell cycle. Activated Cln3/Cdc28 complex activates MBF and SBF, which in turn activate the Cln1 or Cln2 and Clb5 or Clb6 which control the late G1 genes. During the synthesis, or S phase, the cell's DNA is duplicated. After a G2 transition period, Clb1 or Clb2 is activated; the cell enters mitotic, or M phase. Mitosis partitions the genome equally to the opposite ends of the cell, and the cell divides into two by bud-

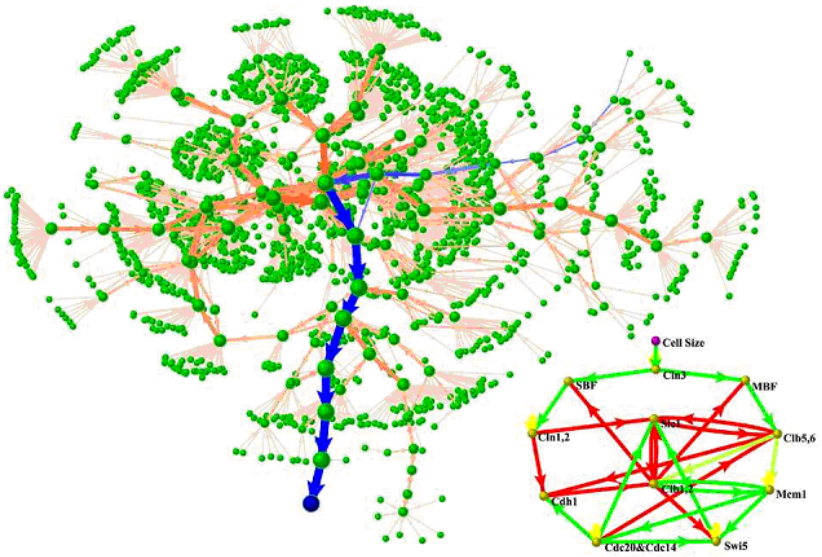

Fig. 10.2. The Dynamic Pathways of the simplified Cell-cycle network in phase space. There are 2048 nodes, representing all $2^{11} = 2048$ possible initial states of the system (signal node "Cell Size" is not included in calculation). An evolution from one state to a next is represented by an arrow. One pathway is defined as an initial state and a series of states that the evolution passes, as well as arrows between them. The real biological pathway and the 'ground' G1 state are colored blue. Thickness of each arrow is in proportion to logarithm of the number of pathways passing through it, and so is the diameter of each node. The insert of the figure in lower right is the simplified cell-cycle network.

ding out a daughter cell. Eventually the cell undergoes cell cycle arrest period, the 'ground' G1 state, and waits for another dividing signal. Thus, the cell cycle process starts with the excitation by the protein complex Cln3/Cdc28 from the 'ground' G1 state to the 'excited' G1 state, and evolves back to the 'ground' G1 state through a series of well-defined phases.

10.3 Boolean models and simulation results

We now study the dynamic behavior of the cell-cycle network. Because we only concern the overall global dynamic properties of the network consisting of key nodes, we choose to use a simple discrete dynamic model. In the model, each node i has only two states, $S_i = 0$ and $S_i = 1$, representing, respectively, the active and inactive state of the protein. The protein states in the next

time step are determined solely by the protein states in the present time step via the following rule:

$$S_i(t+1) = \begin{cases} 1, & \sum_j a_{ij} S_j(t) > 0 \\ 0, & \sum_j a_{ij} S_j(t) < 0 \\ S_i(t), & \sum_j a_{ij} S_j(t) = 0 \end{cases} \tag{10.1}$$

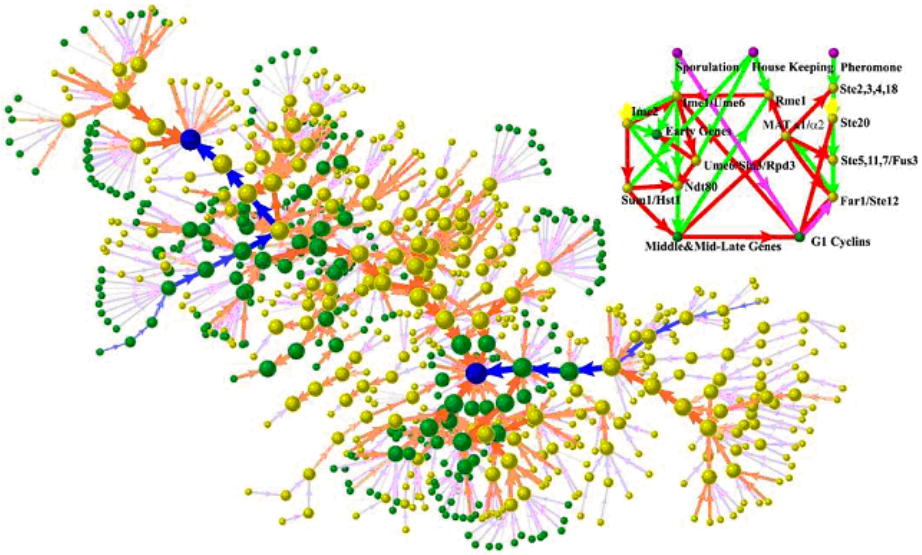

Fig. 10.3. The dynamic pathways of simplified life-cycle network in phase space. Green and red nodes represent diploid states and haploid states respectively. Two Biological pathways and Biological Attractors are colored blue. Thick arrows are highlighted by red color. The thickness of arrows and diameter of nodes are applied with the same demonstrating rules with Fig 2. (In principle, there should be $2^{14} = 16384$ nodes (Two purple sporulation and pheromone signals are not included in the simulation, while the state of "House Keeping" is always 1), arrows with value less than 3 are omitted and corresponding nodes to make the graph clear.) The insert of the figure in upper-right is the simplified life-cycle network.

where is the interaction coefficient from protein j to protein i, which depends on the color of the arrow from j to i (See inset of fig. 2). Note that the time steps here are logic steps that represent causality more than actual times. The network dynamics defined by Eq. (1) is a Boolean network. Boolean networks have been used to model a variety of biological networks and cell states [6, 15, 16]. Refer to general gene expression rules, we take to be 1 and (the minus infinity) for the positive interactions (green arrows) and the negative

Table 10.1. Temporal evolution of protein-states from the excited G1 state. The right row indicates the cell cycle phase. Note that the number of time steps in each phase does not reflect its actual duration. Also note that while the on/off of certain nodes sets the start or end of certain cell-cycle phases, for other nodes the precise duration at which they are turned on or off do not have an absolute meaning in this simple model.

Step	Cln3	SBF	MBF	Cln1,2	Cdh1	Swi5	Cdc20	Clb5,6	Sic1	Clb1,2	Mcm1	Phase
1	1	0	0	0	1	0	0	0	1	0	0	Excited G1
2	1	1	1	0	1	0	0	0	1	0	0	G1
3	1	1	1	1	1	0	0	0	1	0	0	G1
4	1	1	1	1	0	0	0	0	0	0	0	G1
5	0	1	1	1	0	0	0	1	0	0	0	S
6	0	1	1	1	0	0	0	1	0	1	1	G2
7	0	0	0	1	0	0	1	1	0	1	1	M
8	0	0	0	1	0	0	1	0	0	1	1	M
9	0	0	0	0	0	0	1	0	0	1	1	M
10	0	0	0	0	1	0	1	0	0	1	1	M
11	0	0	0	0	1	0	1	0	0	0	1	M
12	0	0	0	0	1	1	1	0	1	0	1	M
13	0	0	0	0	1	1	1	0	1	0	0	M
14	0	0	0	0	1	1	0	0	1	0	0	M
15	0	0	0	0	1	0	0	0	1	0	0	Ground G1

interactions (red arrows), respectively. The self degradation (yellow arrows) are modelled as a time-delayed interaction: if a protein with a self yellow arrow is activated at time t ($S_i(t) = 1$) and it receives no further positive or negative inputs from $t+1$ to $t = t+t_d$, it will be degraded at $t = t+t_d$ ($S_i(t+t_d) = 0$). We use $t_d = 4$ in our model [17]. The presence of time-delayed interactions in Boolean networks changes their global dynamic properties significantly. The advantage of using such a discrete and simple dynamic model is that it enables us to analyze a much larger phase space and hence to study the global dynamic properties of the network.

Using the dynamic rules described above on the protein interaction network, we study the evolution of the cell-cycle network as a function of time. First, we set the initial state to the 'excited' G1 state, and observe the system evolve to the 'ground' G1 state. The temporal evolution of protein-states is

presented in Table 1, which follows the cell-cycle sequence-the protein states in each cell-cycle phase are consistent with experimental observations [18-21]. Next, we study the attractors of the network dynamics in phase space. Starting from all possible $2^{11} = 2048$ initial states in the 11-protein network, the system evolves into 7 stationary states. No limit cycle is present in the system. We find that 1973 of 2048 initial states (about 96%) evolve to the 'ground' G1 state-the biological stationary state of the cell, making it a super and the only global attractor. The rest of stationary states attract only less than 4% of initial state, so that the cell cycle network has no attractors of medium size; only an unusually large global attractor exists. This design of the network ensures the stability of the cell against external and internal noise and perturbations.

Another interesting result of our investigation comes out when we ask the following question: how do the initial protein-states evolve to their final attractors? Figure 2 shows in phase space the temporal evolution from all 2048 initial protein-states. The biological path-the cell cycle sequence (Table 1)-is labelled in blue. Thickness of each arrow between two nodes is in proportion to logarithm of the number of pathways passing through it, and so is the diameter of each node. We see that the most probable trajectory from any initial state is the biological path: the system is first attracted to the biological path and then follows the path to the final stationary state. This means not only that the 'ground' G1 state is a globally stable fixed point, but also that the cell cycle sequence is a globally stable dynamic trajectory. This striking dynamic property of the yeast cell cycle network, which is dictated by the network topology that in turn has been shaped up by many years of evolution, makes the cell cycle sequence an extremely robust process. We find similar results in cell cycle networks of fission yeast and frog egg, indicating a rather generic behavior.

We next analyze the dynamics of the entire network given by Fig. 1, which consists of the cell cycle and the life cycle processes. Again we simplify the network by removing and reconnecting nodes in a way that do not affect the network dynamics. The simplified network is shown as the inset of Fig. 3. Note that according the rules of simplification, single node (G1 cyclins) can represent the cell-cycle network. To keep certain nodes on in the normal cell state, we have introduced a housekeeping node in the simplified network; the state of this housekeeping node is always 1. The dynamic rules are the same as described above, except that the node Ime1 can only be activated with both an active Mat a1/alpha2 (diploid form) and an active sporulation signal (only a diploid cell receiving a sporulation signal can start sporulation). The other green arrows of "AND" logic have already been deleted, so there is no need to interpret it, the simplification rule in supplement explains this. Starting from all 2^{14} initial states, we trace their evolution trajectories and calculate the number of attractors. There are 7 stationary states and no limit cycle.

The 'ground' G1 states of haploid and diploid form are the only two global attractors, attracting, respectively, 34.7% and 58.7% of all initial states in this bi-stable bio-system; the rest 5 stationary states only attract about 6.6% of initial states in phase space. The two biological pathways-sporulation and mating-are both attracting trajectories. We calculate all the 2^{14} states and delete the arrows whose weight is less than 3 and the corresponding nodes, the evolution trajectories are shown in Fig. 3, the two biological paths are very pronounced.

The dynamics of bio-networks (cell-cycle & life-cycle) own two special features distinct from random networks: they possess super and global attractors and thick biological pathways. Both of the attractors and the pathways have well-defined biological meanings and functions. These features stand out when we compare the dynamic behavior of the bio-networks with that of random networks. Here, we defined random networks to have the same number of nodes and red green, yellow lines with the cell-cycle network. As shown in Fig. 4(A), the attractor size distribution of random network follows a power-law, so that they have attractors of all sizes. In comparison, in the cell-cycle network only a single global attractor exists, no medium size attractors are observed. Less than 0.1 of random networks possess this special property. To quantify the thick pathway property, a W value is defined for each pathway to measure the average thickness of the path. Explicitly, for the nth pathway, $W_n = \sum_{i=1}^{L_n-1} Weight_{i,i+1}/L_n$, with $Weight_{i,j}$ to be the number of pathways crossing the arrow from node i to node j, and L_n is the steps of the pathway. A large average W and narrow distribution is the characteristic of bio-networks as shown in Fig. 4(B), while the W distribution for random networks is quite different, since they lack a main thick pathway corresponding to a narrow W-distribution.

10.4 Perturbations of cell-cycle network

Finally, we study the dynamic stability of the cell-cycle network against perturbations. In the simplified cell-cycle network (see the insert of Fig. 2), there are 31 interactions, including 12 negative interactions, 14 positive interactions, and 5 self-degradations. We give the system a perturbation by deleting one interaction in the network, adding one positive (or negative) interaction, or switching a negative interaction to positive or vice versa, then calculate $\triangle S/S_0$ and $\triangle\overline{W}/\overline{W}_0$. Where $\triangle S/S_0$ and $\triangle\overline{W}/\overline{W}_0$. are, respectively, the change of the biggest attractor size and the change of the average W value after the perturbation; S_0 and $\overline{W}_0$. are, respectively, the size of biggest attractor and the average W value of original network. We also study the dynamic stability of 11-node randomly generated networks for comparison. Fig. 4(C) and Fig. 4(D) summarize the results of the perturbation study. We observe that most

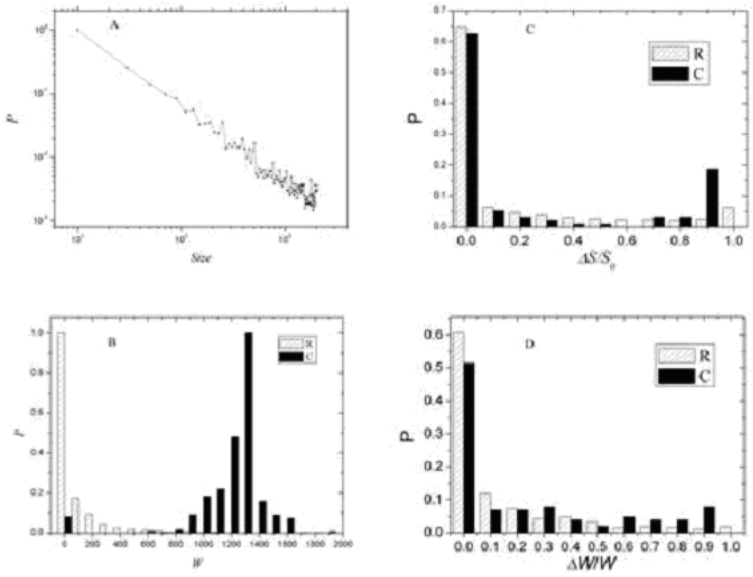

Fig. 10.4. Cell-cycle dynamics in comparison with random networks. (A). Attractor Size Distribution. The Size of an Attractor is defined as the number of states that can evolve into it. According to the simulation, cell-cycle is characterized by one "Ultra-big" attractor and several small ones, in contrast with random nets whose attractor size distribution demonstrate to be power-law. (B). W Value Distribution. (R: random networks; C: cell-cycle network) W Value is defined for each pathway to characterize the average thickness of it. The Thick-Pathway property of cell-cycle corresponds to a relatively narrow W distribution with a big average, while random nets has a much smaller average W value and a quite different distribution. (C)$\triangle S/S_0$ distribution. $\triangle S/S_0$is the relative change of the attractive basin of the original biggest fixed state. (D)$\triangle \overline{W}/\overline{W}_0$ distribution. $\triangle \overline{W}/\overline{W}_0$ is the relative change of the average W value. The stability of a network is studied with $\triangle S/S_0$ and $\triangle \overline{W}/\overline{W}_0$. The perturbations consist of deleting, adding or reversing one interaction line in the network. (10000 random nets have been tested).

perturbations have little effect on the size of biggest attractor and attractive trajectory, so that the cell-cycle network is dynamically stable. The stability of the cell-cycle network is similar to that of random networks, except that the change of a few connections in the cell-cycle network causes large change of S_0 and $\overline{W}_0$, which hints that these connections play the key roles in the biological functions in the network.

10.5 Conclusions

Our results suggest that besides their topological properties [1-4] biological networks have distinct and robust dynamic properties that are very different from random networks. These properties are intimately related to the underlying biological functions [22]. The study shows that simple and discrete dynamic models can play a complimentary role to differential equations in network modelling [23] and can be very useful in analyzing large-scale global properties of the network.

References

1. H. Jeong, B. Tombor, R. Albert, Z. N. Oltval, A.-L. Barabasi (2000) Nature, 407: 651
2. H. Jeong, Sp. P. Mason, A.-L. Barabasi, Z. N. Oltvai (2001) Nature, 411: 41
3. R. Albert, Jeong, A.-L. Barabasi (2000) Nature, 406: 378
4. R. Milo, et al.(2002) Science, 298: 824
5. J. J. Tyson, K. Chen, B. Novak (2001) Nature Review Molecular Biology,2: 908
6. S. Huang, D. E. Ingber (2000) Exp. Cell Res. 261: 91
7. P. Uetz, et al. (2000) Nature 403: 623-627
8. B. Schwikowski, et al. (2000) Nat. Biotechnol. 18: 1257
9. T. Ito et al. (2001) Proc. Natl. Acad. Sci. USA 98:4569
10. A. H. Tong, et al. (2001) Science 294: 2364
11. A. C. Gavin, et al. (2002) Nature 415: 141
12. Y. Ho, et al. (2002) Nature 415: 180
13. C. Mering et al. (2002) Nature 417: 399
14. K. Chen, et al. (2000) Mol. Biol. Cell 11: 369
15. S. A. Kauffman, "The origins of order" (Oxford University Press 1993) p191.
16. I. Shmulevich, E.R. Dougherty, W. Zhang (2002) Proc. IEEE 90: 1778
17. For simplicity, we use the same lifetime td for all proteins with a self-loop. The results are essentially the same for $t_d > 2$
18. T. I. Lee, et al. (2002) Science 298: 799
19. P. T. Spellman, et al. (1998) Mol. Biol. Cell 9: 3273
20. F. R. Cross, et al. (2002) Mol. Biol. Cell 13: 52
21. I. Simon, et al. (2001) Cell 106: 697
22. U. Alon, M.G. Surette, N. Barkai, S. Leibler (1999) Nature 397: 168
23. D. Endy, R. Brent (2001) Nature 409: 391
24. This work was partly supported by the National Key Basic Research Project of China (No. 2003CB715900). We thank T. Hua, H. Li, C. M. Zhang and L.H. Tang and for helpful discussions. The networks and dynamic trajectories are drawn with Pajek (http://vlado.fmf.uni-lj.si/pub/networks/pajek/).

11

Understanding Protein-Protein Interactions: From Domain Level to Motif Level

Huan Yu,Minping Qian, Minghua Deng

Summary. Understanding protein functional interactions is an important research focus in the post-genomic era. The identification of interacting motif pairs is essential for exploring the mechanism of protein interactions. We describe a word-counting approach for discovering motif pairs from known interactions and pairs of proteins that are putatively not to interact. Our interacting motif pairs are validated by multiple-chain PDB structures and motif pairs extracted from PDB structures. The predicted motif pairs are used to predict interactions between proteins by three different methods. For all the methods used, our predicted protein-protein interactions significantly overlap with the experimental physical interactions. Furthermore, the mean correlation coefficients of the gene expression profiles for our predicted protein pairs are significantly higher than that for random pairs.

Supplementary materials are available online at `http://ctb.pku.edu.cn/~yuhuan`.

11.1 Introduction

With the finishing of genome sequencing projects, functional annotation of the entire genomes has been a major goal in the post-genomic era. Moreover, the relationships between proteins play more important role than the function of individual proteins since proteins interact and regulate each other in most biological process. Many experimental and computational methods are developed to identify protein-protein interactions (PPIs).

Traditional Methods

Traditionally, protein-protein interactions have been studied by genetic, biochemical or biophysical techniques such as protein protein affinity chromatography, immunoprecipitation, sedimentation and gel-filtration[42]. However,

these methods are not suitable for genome-wide interaction detection. High-throughput methods have being developed to identify protein-protein interactions in parallel.

The Yeast Two-hybrid System

The most widely used large-scale approach for detecting protein interactions is the yeast two-hybrid system introduced by Fields and Song [12]. An eukaryotic transcription factor is split into two distinct functional domains called Binding Domain (BD) and Activating Domain (AD). If the bait protein fused to the BD interacts with the prey protein fused to the AD, the transcription machinery will be reconstructed and activate the transcription of the reporter gene. If the two proteins do not interact, the transcription of the reporter gene will not be activated.

Recently, the yeast two-hybrid system is used for high-throughput protein-protein interaction detection from several organisms including *Saccharomyces cerevisiae (yeast)*[49, 26], *Caenorhabditis elegans*[50, 4, 29], *Helicobacter pylori*[43], vaccinia virus[35], *Mouse*[48] and *Fly*[16, 47, 13].

Uetz *et al.*[49] used two different approaches in their experiments. In the first approach, 192 yeast bait proteins fused to Gal4-DNA-binding domain were screened against nearly 6000 yeast proteins fused to Gal4-activation domain as prey. 281 interactions were found among 87 proteins. In the second experiment, an interaction sequence tag (IST) approach, 5,341 yeast bait proteins were screened against the yeast proteome (nearly 6000 preys) and identified 692 interactions among 817 proteins. Ito *et al.*[26] used IST approach and 4549 interactions among 3278 proteins were reported.

Although the yeast two-hybrid system is suitable for automated large-scale protein-protein interaction screening, the false positive and false negative errors are huge. Possible mutations during PCR-amplification and stochastic activation of reporter gene may lead to the false positives and the inability to detect interactions of membrane proteins, post-translational modification proteins, and weak interactions may lead to the false negatives[26, 38, 8].

Affinity Purification of Protein Complexes

An alternative way to study protein-protein interactions in large-scale is affinity purification of protein complexes. Tagged bait proteins and associated proteins assemble as protein complexes. The complexes are purified and then separated by gel electrophoresis. The components of complexes are identified by mass spectrometry (MS). MS-based approaches provide protein components

in a complex but do not give the direct physical interaction. It is different from the yeast hybrid system, although a relationship does exist since proteins in the same complex are more likely to physically interact with one another. Over 700 different complexes in yeast are identified in two studies[14, 24]. So far the MS-based methods provide the largest protein complex data.

The disadvantage of MS-based approaches is that the interactions may not be detected due to low affinity, low expression level or detection limits of the MS facilities. Most interactions from MS-based methods are indirect interaction.

Protein Chips

Another direct approach to identify genome-wide protein-protein interactions in parallel is the protein chip method. The purified proteins are printed onto glass slides and then analyzed for binding or enzymatic activities.

MacBeath and Schreiber [32] used protein chips to detect antibody-antigen interactions, protein kinase activities and protein interactions with small molecules. Zhu *et al.* [55] developed protein chips to identify protein-protein interactions. They identified 39 calmodulin-interactors by adding biotinylated calmodulin to the yeast protein chips. Some of the identified interactions are well known interaction between calmodulin and calmodulin kinase, but were missed in large-scale yeast two-hybrid and the MS-based approach.

Protein chips can be used to identify not only protein-protein interaction but also protein-lipid, protein-nucleic acid or protein-drug interactions. The major limitation is the preparation of proteins to analyze, not all proteins can be purified easily and efficiently.

Protein-protein Interaction Databases

Since most of the protein interactions were reported in the literature where the information is difficult to manage and compute upon, various protein-protein interaction databases were built to gather the information for further data mining such as MIPS[36] (`http://mips.gsf.de`), BIND[2] (`http://www.bind.ca`), DIP[44] (`http://dip.doe-mbi.ucla.edu/`), GRID[5] (`http://biodata.mshri.on.ca/grid/servlet/Index`), MINT[54] (`http://cbm.bio.uniroma2.it/mint/`), IntAct[23] (`http://www.ebi.ac.uk/intact/index.jsp`) and STRING[37] (`http://string.embl.de/`). Among these databases, we consider MIPS as golden standard data since it is a collection of manually curated high-quality PPI data collected from the scientific literature by expert curators.

Furthermore, the PDB database[9] (`http://www.rcsb.org/pdb/`) contains some protein complex structures, which are direct evidences for protein-protein interactions. The protein complex structures allows us to find out the protein contact interface by simply calculate the Euclidean distance of atoms. The only problem is that the data size of PDB is too small.

Computational Method for Predicting Protein-protein Interactions

Although many experimental methods have been developed to identify genome-wide interactions, the overlaps among different data sets are small suggesting that they contain only a very small fraction of the potential protein-protein interactions[26]. Analysis by computational (*in silico*) methods are required to complete the protein interaction map.

With the completion of genome-sequencing projects, sequence homology search tools such as BLAST (`http://www.ncbi.nlm.nih.gov/blast`)[1] have been widely used to extend knowledge of protein functions. However, sequence similarity analysis is applicable only when the function of matched protein is known and the sequence homology is significant. Several computational methods for predicting genome-wide functional linkages between proteins are developed. These methods can be classified into three categories:

1. phylogenetic profiles[25, 41], analysis of co-presence or co-absence of genes within entire genomes indicates the interactions between those gene products;

2. gene fusion[10, 33], the facts of two separate proteins in one organism is often found as a fusion into a single protein in some other species indicates physical interactions;

3. gene neighborhood[6, 40], two proteins are neighbors on the chromosome in several genomes tend to be functionally linked.

To understand protein function, elements of protein that are self-stabilizing and often fold independently of the rest of the protein chain are defined as protein domains. Protein domains have distinct evolutionary origin and function. As a unit of structures, each domain is responsible for a specific interaction with another domain, so it serves as a unit for protein-protein interactions. Several machine learning approaches have been developed to predict protein interactions on the basis of domainCdomain interactions. Including Support vector machine (SVM)[3], association method[46, 28, 39], interacting domain profile[52], Bayesian method[17, 18, 19], EM based MLE method[7, 53] and linear programming method[22].

Protein-protein interactions are also studied in the motif level. Motif is short amino acid sequence with a certain functional meaning. Motifs are very important for drug and protein design, often referred as protein contact interfaces or binding sites. Wang *et al.*[51] identified active motif pairs from interacting protein pairs by an approximate EM algorithm with the motifs from the Prosite database[11]. Li *et al.*[30, 31] discovered the significant motif pairs based on the PDB structures[9] and known protein-protein interactions.

We use a word-counting method to study the protein-protein interactions in the motif level. Starting from protein sequences and protein complexes only, the statistical significant motif pairs are identified as the signature of the protein-protein interactions. By comparing them with PDB structure, we validate our identifications. Furthermore, we predict genome-wide protein-protein interactions from the identified motif pairs, and validate our prediction based on the analysis of overlapping with the MIPS physical interaction and gene expression profiles.

11.2 Data

In our study, yeast sequence data and protein complex data are used to find the signature motif pairs. We use ORF names to identify yeast proteins resulting 6294 proteins involved in our experiment. 265 MIPS complexes are downloaded from MIPS to build the protein-protein interaction training data.

To estimate the reliability of our results, protein structures obtained from PDB, MIPS physical interactions, and gene expression data from Spellman *et al.*[45] are used. The protein structures used in this study are a non-redundant subset from PDB where the maximum pairwise sequence identify is 30%, consisting of at least two chains in one entry with resolution 2.0 $\mathring{A}$ or better. The PDB data contains the 3-dimension coordinates of amino acid atoms. The data was obtained on April 8, 2004 containing 544 entries. For MIPS physical interaction data, we exclude those interactions supported only by high throughput experiment, resulting in 2579 interactions used in this study. The expression data are obtained from the Yeast cell cycle analysis project, containing 6178 genes at 77 time points.

11.3 Methods

11.3.1 Overview of our method

We transform the MIPS complexes into pairwise interactions as the positive protein-protein interaction training data. We also generate a negative interacting data set described in the following paragraph. We count all 4-tuple amino acid (AA) pairs occuring in positive and negative data and select statistical significant positive and negative 4-tuple pairs as the word dictionary for further prediction. The identified 4-tuple positive pairs are verified by the tuple pairs on protein complex structures, and are compared with motif pairs discovered by Li *et al.*[30, 31]. Finally we use an iterative dependent Naive Bayesian classifier to predict protein-protein interactions based on the identified 4-tuple pairs. The reliability is estimated by comparing the predicted interactions with MIPS physical interactions and gene expression profile correlation coefficients.

11.3.2 Protein-protein interaction training data

We need both positive and negative protein-protein interaction training data to learn the significant 4-tuple pairs. The positive interactions are extracted from MIPS complexes. We transform the MIPS complexes into pairwise interactions by connecting all possible protein pairs within the complex resulting in $NP = 10198$ protein pairs.

Several methods have been proposed to construct negative interaction data set. The two most popular approaches are described as follows. In the first approach, proteins in separate subcellular compartments are considered as negatives[34]. The shortcoming of this approach is that there is no information showing whether proteins can bind with each other if they are being put together. Different subcellular locations only indicates that the proteins have no chance to bind. The second approach assumes that two proteins do not interact if there is no positive evidence of interaction[19]. The incomplete and low quality positive interaction data bring in more false negatives. We use a different approach to generate negative data from positive data. To overcome the shortcoming of the above two approaches. We define a negative PPI pair to be a pair of proteins that have chance to interact with each other but fail to be observed in the interaction map. To be precise, we first build a protein interaction graph with proteins as nodes and positive interactions as edges. Then all pairs among nodes in connected graph with shortest path length greater than a cutoff are treated as putative negative protein-protein interactions. For example, when cutoff=6, we obtain $NN = 26605$ negative protein-protein interactions.

11.3.3 Significant 4-tuple pairs

There are 20^8 possible 4-tuple pairs in the protein pairs. We count all the 4-tuple pairs in the positive and negative protein-protein interaction data. If a 4-tuple pair occurs multiple times in a protein pair, we just count it once. For each 4-tuple pair TP, we denote N_{TP+} and N_{TP-} as the number of protein pairs containing the 4-tuple pair TP in positive and negative protein pairs, respectively.

We select the significant 4-tuple pairs as following. For a 4-tuple pair TP and the counts N_{TP+} and N_{TP-}, we test whether the 4-tuple pair is over-represented in the positive interacting protein pairs. The negative count N_{TP-} is used to estimate the background distribution. The approximate background distribution is a Poisson distribution with parameter $\lambda_p = N_{TP-} \times \frac{NP}{NN}$. The p-value for the hypothesis can be calculated as:

$$P_{raw}(X >= N_{TP+}) = \sum_{k=N_{TP+}}^{\infty} \frac{\lambda_p^k}{k!} e^{-\lambda_p}.$$

For all $N = 20^8$ 4-tuple pairs, a large number of statistical tests are performed. To avoid the multiple testing problem, the p-value p_{raw} is adjusted to $max(1, p_{raw} \times N)$ by Bonferroni correction. The 4-tuple pairs with adjusted p-value lower than 0.001 are selected as the significant positive 4-tuple pairs set S_p resulting in 968,882 4-tuple pairs. Let S_p be the set of these significant positive 4-tuple pairs.

Similarly, the p-value for the hypothesis that the 4-tuple pair is under-represented in the putative negative interacting pairs can be calculated as:

$$P_{raw}(X >= N_{TP-}) = \sum_{k=N_{TP-}}^{\infty} \frac{\lambda_n^k}{k!} e^{-\lambda_n},$$

in which $\lambda_n = N_{p+} \times \frac{NN}{NP}$. Similarly, we select 2,529,775 4-tuple pairs as the significant negative 4-tuple pairs and denote the set of them as S_n.

We call $W = S_p \bigcup S_n$ as the significant 4-tuple pairs set.

11.3.4 Protein-protein interaction prediction

In the following, we will predict protein-protein interactions from the identified significant 4-tuple pairs set W. We propose three different prediction models step by step.

Independent model

We will start the prediction from a simple independent classification system. Given a pair of proteins (P_a, P_b), we denote all significant 4-tuple pairs occur in (P_a, P_b) as $S = \{(LT_i, RT_i, Lpos_i, Rpos_i), i = 1, 2, \cdots, M\}$, where LT_i is the 4-tuple occurs in P_a and RT_i occurs in P_b, and $(Lpos_i, Rpos_i)$ is the occurrence position of (LT_i, RT_i), respectively, and M is total number of significant 4-tuples occur in (P_a, P_b). If we denote I_{ab} the event that (P_a, P_b) interact. For 4-tuple pairs TP_A and TP_B in S, we make the following conditional independence assumption:

$$P(TP_A, TP_B|I_{ab}) = P(TP_A|I_{ab}) \times P(TP_B|I_{ab}) \tag{11.1}$$

Following the Bayesian rule, we have:

$$\begin{aligned} P(I_{ab}|S) &= \frac{P(I_{ab}, S)}{P(S)} \\ &= \frac{P(S|I_{ab}) \times P(I_{ab})}{P(S|I_{ab}) \times P(I_{ab}) + P(S|\overline{I_{ab}}) \times P(\overline{I_{ab}})} \\ &= \frac{1}{1 + \frac{P(\overline{I_{ab}})}{P(I_{ab})} \times \frac{P(S|\overline{I_{ab}})}{P(S|I_{ab})}} \\ &= \frac{1}{1 + \frac{P(\overline{I_{ab}})}{P(I_{ab})} \times \prod_{TP \in S} \frac{P(TP|\overline{I_{ab}})}{P(TP|I_{ab})}} \\ &= \frac{1}{1 + \frac{1 - P(I_{ab})}{P(I_{ab})} \times factor(S)} \end{aligned} \tag{11.2}$$

where $factor(S) = \prod_{TP \in S} \frac{P(TP|\overline{I_{ab}})}{P(TP|I_{ab})}$.

We estimate $factor(S)$ as:

$$\widehat{factor}(S) = \prod_{TP \in S} \frac{N_{TP-}/NN}{N_{TP+}/NP} \tag{11.3}$$

We use an iterative algorithm to estimate the prior probability $P(I_{ab})$. It was estimated in Hazbun and Fields [21] that each protein interacts with about 5 to 50 proteins. For 6294 yeast proteins and 5 interactions for each protein, it gives a total of $6294 \times 5/2 = 15,735$ real interaction pairs. Given the initial prior probability

$$\widehat{P}_k(I_{ab}) = \frac{2 * 15735}{6293 \times 6294}$$

For step $k = 0$, we estimate $P(I_{ab}|S)$ as:

$$\widehat{P}(I_{ab}|S) = \frac{1}{1 + \frac{1 - \widehat{P}_k(I_{ab})}{\widehat{P}_k(I_{ab})} \times \prod_{TP \in S} \frac{N_{TP-}/NN}{N_{TP+}/NP}}$$

We give a positive interaction prediction of (P_a, P_b) if $P(I_{ab}|S) > 0.999$. We predict all yeast protein pairs and denote the number of positive predictions as K_k. In the next step prior probability is updated by:

$$\widehat{P}_{k+1}(I_{ab}) = \frac{2 * K_k}{6293 \times 6294}$$

The algorithm is iterated until $K_{k+1} = K_k$.

Since we obtain the 4-tuple pairs set S using sliding windows, the assumption of independence (11.1) is not true if TP_A and TP_B overlap. The converged prior probability in the independent algorithm described above is significantly higher than the upper bound of empirical probability 50/6294.

To overcome the shortcoming of independent model, we present two dependent models to estimate $factor(S)$ in the equation (11.2).

Dominating model

In contrast to the independent model, the dominating model assumes that only the most significant 4-tuple pairs in S contribute to $factor(S)$. The most significant 4-tuple pairs dominate the interaction. We denote the most significant positive and negative 4-tuple pair in S as $PTP(S)$ and $NTP(S)$. In the dominating model, we modify $factor(S)$ to:

$$factor_{dom}(S) = \begin{cases} \frac{P(NTP(S)|\overline{I_{ab}})}{P(NTP(S)|I_{ab})}, & \text{no positive 4-tuple pairs belong to } S \\ \frac{P(PTP(S)|\overline{I_{ab}})}{P(PTP(S)|I_{ab})}, & \text{no negative 4-tuple pairs belong to } S \\ \frac{P(PTP(S)|\overline{I_{ab}})}{P(PTP(S)|I_{ab})} \times \frac{P(NTP(S)|\overline{I_{ab}})}{P(NTP(S)|I_{ab})} & \end{cases} \tag{11.4}$$

$factor_{dom}$ is estimated by:

$$\widehat{factor}_{dom}(S) = \begin{cases} \frac{N_{NTP(S)-}/NN}{N_{NTP(S)+}/NP}, & \text{no positive 4-tuple pairs belong to } S \\ \frac{N_{PTP(S)-}/NN}{N_{PTP(S)+}/NP}, & \text{no negative 4-tuple pairs belong to } S \\ \frac{N_{NTP(S)-}/NN}{N_{NTP(S)+}/NP} \times \frac{N_{PTP(S)-}/NN}{N_{PTP(S)+}/NP} & \end{cases} \tag{11.5}$$

The dominating model runs from one extreme to the other. A majority of information in S is ignored. The prediction is unstable because of the inaccuracy of the selected significant 4-tuple pairs.

Combined model

The final model is a combination of the independent and the dominating model. The 4-tuple pairs set S is partitioned into disjoint independent sets $S_1, S_2, ..., S_m$ as following: S is used as nodes to construct a graph, and two 4-tuple pairs $(LT_i, RT_i, Lpos_i, Rpos_i)$ and $(LT_j, RT_j, Lpos_j, Rpos_j)$ are assigned an edge if $|Lpos_i - Lpos_j| \leq 4 \times M$ or $|Rpos_i - Rpos_j| \leq 4 \times M$ ($M = 3$ in this study). Figure 11.1 shows a simple example of the partition. In figure11.1, each connected component is clustered as a subset S_i.

The $factor$ in the combined model is calculated as:

$$factor_{com}(S) = \prod_{i=1}^{m} factor_{dom}(S_i)$$

where $factor_{dom}(S_i)$ is calculated by equation (11.4) for each individual set S_i. $factor_{com}(S)$ is estimated similarly as equation (11.5):

$$\widehat{factor}_{com}(S) = \prod_{i=1}^{m} \widehat{factor}_{dom}(S_i)$$

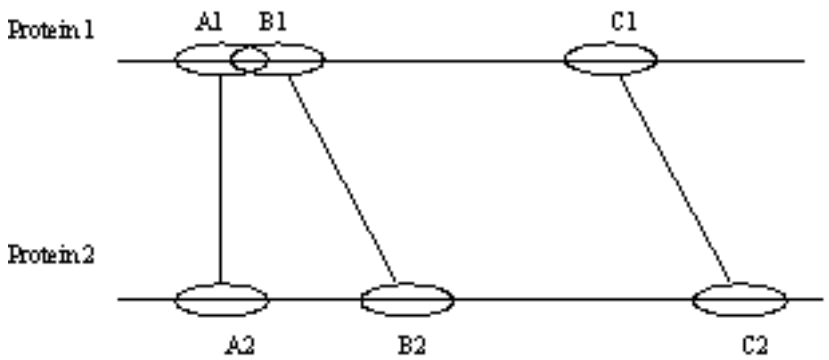

Fig. 11.1. Partition example: motif pairs (A1, A2), (B1, B2) on Protein 1 and protein 2 are grouped since A1 and B1 are neighborhood, the isolated motif pair (C1, C2) builds up a group by itself.

11.4 Results

First we verify the over-represented 4-tuple pair set S_p by comparing it with PDB structure data. The significance of matching is evaluated by random re-sampling. We then compare S_p with the significant motif pairs discovered by Li *et al.*[30]. Finally, we measure the significance of our predicted protein-protein interactions by MIPS physical interactions and gene expression profiles.

Comparing with PDB structure

First we give some definitions related to protein structures.

Definition 1. *Atoms contact: Given two protein chains with 3-D structural coordinates, $Atom_A$ from one protein chain and $Atom_B$ from the other contact if $dist(Atom_A, Atom_B) < \varepsilon$, where $dist(\cdot,\cdot)$ is the Euclidean distance, and ε is an empirical threshold 5Å.*

Definition 2. *Tuple pairs contact: Given two protein chains with 3-D structural coordinates and a tuple pair $(Tuple_A, Tuple_B)$, $Tuple_A$ occurs in one protein chain and $Tuple_B$ occurs in the other. $(Tuple_A, Tuple_B)$ contact if one atom from $Tuple_A$ and one atom from $Tuple_B$ contact.*

Definition 3. *Chains verifiable by a set of tuple pairs S: Given two protein chains with 3-D structural coordinates, if there exist a tuple pair in S that contact each other.*

Definition 4. *PDB structure verifiable by a set of tuple pairs S: Given a PDB protein complex with 3-D structural coordinates, if at least one pair of chains is verifiable by S.*

For the identified over-represented positive 4-tuple pairs in S_p, 169 of 544 PDB structures are verifiable. Figure 11.2 is an example of verifiable 4-tuple pair. However, when we repeatly draw the same number (968,882) of 4-tuple pairs randomly as set $R_1, R_2, \cdots, R_1000$, and compare each set with PDB structures, the average number of verifiable PDB structures is only 20.9. We use binomial distribution $B(544, p_{binom})$ to approximate the background distribution, in which $p_{binom} = 20.5/544$. The p-value of the verifiable performance of set S_p is,

$$P(X \geq 169) = \sum_{k=169}^{544} \binom{544}{k} \times p_{binom} \times (1 - p_{binom}) = 1.47e - 144$$

Which means a very significant match.

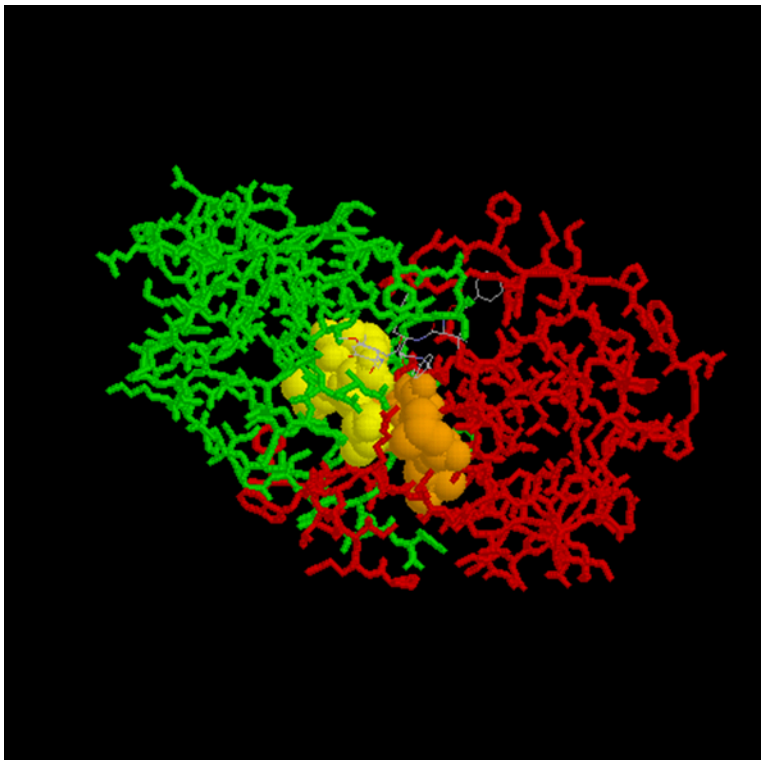

Fig. 11.2. PDB verifying example: PDB1a8g (Two molecular: HIV-1 PROTEASE) is verified by 4-tuple pair (LLDT LLDT)

Comparing with motif pairs extracted from PDB

Li *et al.*[30, 31] discovered 930 motif pairs from PDB structures. Our significant tuple pairs is derived from sequence data without any knowledge of protein structures or protein domains. Comparing our identification with their discovery, 496 of 930 motif pairs are confirmed by 4-tuple pairs in S_p and the average match number of random resampling set is only 22.8. Using the similar background binomial distribution approximation $B(930, p_{binom*})$, where $p_{binom*} = 22.8/930$, the p-value of match performance of set S_p is:

$$P(X \geq 496) = \sum_{k=496}^{930} \binom{930}{k} \times p_{binom*} \times (1 - p_{binom*}) < 1.00e - 460$$

Which is also a very significant match.

Comparing with MIPS physical data

We use MIPS physical interactions to test our protein-protein interaction predictions. There are 2579 MIPS physical interactions. Excluding those interactions in the training set, a test data set of 1964 interactions is obtained. To measure the statistical significance, we use the standard Z-score

$$Z = \frac{k_0 - n \times p}{\sqrt{n \times p \times (1-p)}}$$

where $p = K/L$, and L is the total number of protein pairs, $K = 1964$, n is the number of predictions, and k_0 is the number of matching protein pairs between the 1964 interactions in the test data set and the n predicted interactions. Z has an approximate standard normal distribution under the null hypothesis.

Another measure of the significance is $Fold$[7], the ratio of the fraction of the predicted protein pairs in the test data set with those in all protein pairs as following:

$$Fold = \frac{k_0/K}{n/L}$$

Table 11.1 shows the overlapping numbers between the test set and our predictions and the corresponding statistics. We can see that, although the overlap is not quiet large, it's statistically significant.

Table 11.1. Number of Matched Protein Pairs Between the Predictions

Model	Prediction	Train	MIPS	MIPS1	$Fold$	Z score	P value
Independent Model	4496949	10186	1328	718	1.61	14.72	2.3e-49
Dominating Model	38302	10194	618	7	2.51	2.53	5.7e-3
Combined Model	68927	10194	630	19	3.26	5.47	2.3e-8

Number of predicted PPIs(Prediction), number of matching PPIs with the training set (Train), number of matching PPIs with the MIPS data (MIPS), and number of matching PPIs with the MIPS excluding the training data (MIPS1), respectively. The corresponding statistics (Fold, Z score, and P value) are also given.

Comparing with gene expression profiles

It has been shown that genes with similar expression profiles are likely to encode interacting proteins[15, 20, 27]. We study the distribution of correlation coefficients for protein pairs with predicted interaction probability. We use the

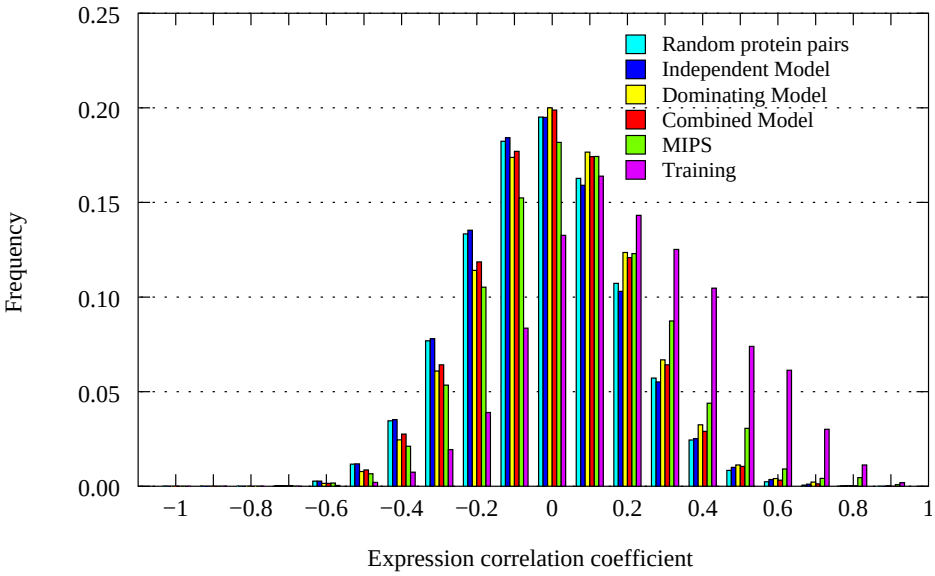

Fig. 11.3. Distributions of the pairwise correlation coefficients for all gene pairs, MIPS interaction data, training data and our predicted protein pairs excluding the training data.

genome-wide cell cycle gene expression data. Figure 11.3 gives the distributions of the pairwise correlation coefficients for all gene pairs, our predicted protein pairs by three models, and the MIPS interaction data.

The statistical significance for the difference between the mean expression correlation coefficient of a putative interaction set and that of random pairs is measured by the T-score and the P-value for the null hypothesis of no difference between the sample mean and the mean of random gene pairs. The T-scores are calculated as the two sample T-test statistic with unequal variances.

$$T_f = \frac{\mu_1 - \mu_2}{\sqrt{\frac{S_1^2}{n_1} + \frac{S_2^2}{n_2}}}$$

with the approximate freedom:

$$f = \frac{\left(\frac{S_1^2}{n_1} + \frac{S_2^2}{n_2}\right)^2}{\frac{\left(\frac{S_1^2}{n_1}\right)^2}{n_1} + \frac{\left(\frac{S_2^2}{n_2}\right)^2}{n_2}}$$

where μ is the mean of samples, and

$$S^2 = \frac{1}{n-1}\sum_{i=1}^{n}(x_i - \mu)^2$$

is the variance of the samples [7].

Table 11.2. Distribution of the pairwise correlation coefficients

Pairs	Pairs	Sample mean	Sample variance	T-score	P-value
All ORFs	18474081	0.031	0.041	0	0.5
Independent Model	4271174	0.030	0.042	-7.37	1
Dominating Model	25067	0.062	0.041	23.93	2.1e-125
Combined Model	52079	0.053	0.040	25.33	1.5e-149
MIPS	2415	0.100	0.051	14.92	1.4e-48
Training data	8723	0.253	0.063	82.70	0

Summary statistics of distribution of the correlation coefficient between the gene expression profiles of protein pairs(with gene expression profiles from MIPS, random(all ORFs), training data and our predictions of three models excluding the training data).

Figure 11.3 and Table 11.2 show that the mean correlation coefficient for predicted protein pairs is significantly higher than that for random pairs. Except for the independent model, the mean correlation coefficients for protein pairs are significantly higher than that for random pairs. It should be noted that transforming from the MIPS complexes into pairwise interactions enlarged the mean correlation coefficient of training data. For our predictions, the overlap between training data and our predictions are not used in the calculation of correlation coefficient.

11.5 Discussion

This work describes a general method for predicting protein-protein interactions from sequences. Putative negative protein-protein interactions generated by positive interactions enable us to choose the significant signature pairs by word-counting. The signature pairs are compared with multiple-chain PDB structures and motif pairs extracted from PDB structures. By resampling, it shows that the quality of chosen pairs are significantly better than that of the random 4-tuple pairs, thus validating the theory that protein folding is a consequence of the primary structure and the functional motifs are highly conserved in the evolution.

In the protein level, protein-protein interactions are separated into attractive and repulsive forces associated with the signatures. We introduce three ways to combine the signatures probabilities into a single protein-protein interaction probability. The significance of our PPI prediction is measured in two ways: (1) comparing the prediction with MIPS physical interactions derived by methods other than the yeast two-hybrid system and (2) comparing the distribution of gene expression correlation coefficient for the predicted interacting protein pairs with that for random protein pairs. The results show our predictions are statistical significant.

The results also show that using the dependent models to predict protein-protein interactions from the over-represented and under-represented 4-tuple pairs indeed improves performance. Generally, the independent assumption is introduced to simplify the computing, it may work if the dependence among features are not too strong. However, as the existence of long-range correlation between the amino acids after protein folding, the independent model does not fit the current case. In our combined model, the long-range correlation has been taken into account somehow by considering the overlapping between the signatures on the protein pair. So that the predictions by the combined model have the best performance among those by other two models.

Although our predictions is statistical significant, the overlaps between our predictions and MIPS physical interactions are very small. A possible reason is that the size of the protein interactions network is huge. It is known that every experimental method is biased to certain kinds of proteins and interactions. It is possible that some of our predictions are not suitable to verified by MIPS physical interactions identifying methods. Another explanation for the small overlaps is that the way to transform the MIPS complexes into pairwise interaction may amplify the data source noise. Moreover, The time and space constraints among protein-protein interactions is ignored in our study. Two proteins may not interact with each other at different expression time or different subcellular location. Also, depending on the environmental conditions such as temperature et al., proteins may have different interaction behavior with others.

11.6 Acknowledgements

This research is supported by the grants from National Natural Science Foundation of China (No. 90208022, No. 10271008, No. 10329102), the National High Technology Research and Development of China (No. 2002AA234011) and the National Key Basic Research Project of China (No. 2003CB715903).

References

1. Altschul SF, Madden TL, Schaffer AA, Zhang J, Zhang Z, Miller W *et al.* (1997) Nucleic Acids Res 25(17):3389–3402
2. Alfarano C, Andrade CE, Anthony K, Bahroos N, Bajec M, Bantoft K *et al.* (2005) Nucleic Acids Res 33(Database Issue):D418–D424
3. Bock JR, Gough DA (2001) Bioinformatics 17(5):455–460
4. Boulton SJ, Gartner A, Reboul J, Vaglio P, Dyson N, Hill DE *et al.* (2002) Science 295(5552):127–131
5. Breitkreutz BJ, Stark C, Tyers M (2003) Genome Biol 4(3):R23
6. Dandekar T, Snel B, Huynen M, Bork P (1998) Trends Biochem Sci 23(9):324–328
7. Deng M, Mehta S, Sun F, Chen T (2002) Genome Res 12(10):1540–1548
8. Deng M, Sun F, Chen T (2003) Pac Symp Biocomput 2003:140–151
9. Deshpande N, Addess KJ, Bluhm WF, Merino-Ott JC, Townsend-Merino W, Zhang Q *et al* (2005) Nucleic Acids Res 33(Database issue):D233–D237
10. Enright AJ, Iliopoulos I, Kyrpides NC, Ouzounis CA (1999) Nature 402(6757):86–90
11. Falquet L, Pagni M, Bucher P, Hulo N, Sigrist CJ, Hofmann K *et al* (2002) Nucleic Acids Res 30(1):235–238
12. Fields S, Song O (1989) Nature 340(6230):245–246
13. Formstecher E, Aresta S, Collura V, Hamburger A, Meil A, Trehin A *et al.* (2005) Genome Res 15(3):376–384
14. Gavin AC, Bösche M, Krause R, Grandi P, Marzioch M, Bauer A *et al.* (2002) Nature 415(6868):141–147
15. Ge H, Liu Z, Church GM, Vidal M (2001) Nat Genet 29(4): 482–486
16. Giot L, Bader JS, Brouwer C, Chaudhuri A, Kuang B, Li Y *et al.* (2003) Science 302(5651):1727–1736
17. Gomez SM, Lo SH, Rzhetsky A (2001) Genetics 159(3):1291–1298
18. Gomez SM, Rzhetsky A (2002) Pac Symp Biocomput 2002:413–424
19. Gomez SM, Noble WS, Rzhetsky A (2003) Bioinformatics 19(15):1875–1881
20. Grigoriev A (2001) Nucleic Acid Res 29(17):3513–3519
21. Hazbun TR, Fields S (2001) Proc Natl Acad Sci USA 98(8):4277–4278
22. Hayashida M, Ueda N, Akutsu T (2003) Bioinformatics 2003 19 Suppl 2:ii58–ii65.
23. Hermjakob H, Montecchi-Palazzi L, Lewington C, Mudali S, Kerrien S, Orchard S *et al.* (2004) Nucleic Acids Res 32(Database issue):D452–D455
24. Ho Y, Gruhler A, Heilbut A, Bader GD, Moore L,Adams SL *et al.* (2002) Nature 415(6868):180–183
25. Huynen MA, Bork P (1998) Proc Natl Acad Sci USA 95(11):5849–5856
26. Ito T, Chiba T, Ozawa R, Yoshida M, Hattori M, Sakaki Y (2001) Proc Natl Acad Sci USA 98(8):4569–4574
27. Jansen R, Greenbaum D, Gerstein M (2002) Genome Res 12(1):37–46
28. Kim WK, Park J, Suh JK (2002) Genome Inform Ser Workshop Genome Inform 13:42–50
29. Li S, Armstrong CM, Bertin N, Ge H, Milstein S, Boxem M*et al.* (2004) Science 303(5657):540–543
30. Li H, Li J, Tan SH, Ng SK (2004) Pac Symp Biocomput 2004:312–323

31. Li H, Li J (2005) Bioinformatics 21(3):314–324
32. MacBeath G, Schreiber SL (2000) Science 289(5485):1760–1763
33. Marcotte EM, Pellegrini M, Ng HL, Rice DW, Yeates TO, Eisenberg D (1999) Science 285(5428):751–753
34. Martin S, Roe D, Faulon JL (2005) Bioinformatics 21(2):218–226
35. McCraith S, Holtzman T, Moss B, Fields S (2000) Proc Natl Acad Sci USA 97(9):4879–4884
36. Mewes HW, Frishman D, Güldener U, Mannhaupt G, Mayer K, Mokrejs M*et al.* (2002) Nucleic Acids Res 30(1):31–34
37. von Mering C, Jensen LJ, Snel B, Hooper SD, Krupp M, Foglierini M *et al*(2005) Nucleic Acids Res 33(Database issue):D433–D437
38. Mrowka R, Patzak A, Herzel H (2001) Genome Res 11(12):1971–1973
39. Ng SK, Zhang Z, Tan SH (2003) Bioinformatics 19(8):923–929
40. Overbeek R, Fonstein M, D'Souza M, Pusch GD, Maltsev N (1999) Proc Natl Acad Sci USA 96(6):2896–2901
41. Pellegrini M, Marcotte EM, Thompson MJ, Eisenberg D, Yeates TO (1999) Proc Natl Acad Sci USA 96(8):4285–4288
42. Phizicky EM, Fields S (1995) Microbiol Rev 59(1):94–123
43. Rain JC, Selig L, Reuse HD, Battaglia V, Reverdy C, Simon S*et al.* (2001) Nature 409(6820):211–215
44. Salwinski L, Miller CS, Smith AJ, Pettit FK, Bowie JU, Eisenberg D (2004) Nucleic Acids Res 32(Database issue):D449–D451
45. Spellman PT, Sherlock G, Zhang MQ, Iyer VR, Anders K, Eisen MB *et al.* (1998) Mol Bio Cell 9(12):3273–3297
46. Sprinzak E, Margalit H. (2001) J Mol Biol 311(4):681–692
47. Stanyon CA,Liu G, Mangiola BA, Patel N, Giot L, Kuang B *et al.* (2004) Genome Biol 5(12):R96
48. Suzuki H, Fukunishi Y, Kagawa I, Saito R, Oda H, Endo T*et al.* (2001) Genome Res. 11(10):1758–1765
49. Uetz P, Giot L, Cagney G, Mansfield TA, Judson RS, Knight JR *et al.* (2000) Nature 403(6770):623–627
50. Walhout AJ, Sordella R, Lu X, Hartley JL, Temple GF, Brasch MA, Thierry-Mieg N, Vidal M (2000) Science 287(5450):116–122
51. Wang H, Segal E, Ben-Hur A, Koller D, Brutlag DL (2004) Identifying Protein-Protein Interaction Sites on a Genome-Wide Scale. In: Saul LK, Weiss Y, Bottou L (eds) Advances in Neural Information Processing Systems 17. MIT Press, Cambridge, MA
52. Wojcik J, Schachter V (2001) Bioinformatics 17 Suppl 1:S296–S305
53. Liu Y, Liu N, Zhao H (2005) Bioinformatics 21(15):3279–3285
54. Zanzoni A, Montecchi-Palazzi L, Quondam M, Ausiello G, Helmer-Citterich M, Cesareni G (2002) FEBS Lett 513(1):135–140
55. Zhu H, Bilgin M, Bangham R, Hall D, Casamayor A, Bertone P *et al.* (2001) Science 293(5537):2101–2105

12

An Efficient Algorithm for Deciphering Regulatory Motifs

Xiucheng Feng, Lin Wan, Minghua Deng, Fengzhu Sun, and Minping Qian

Summary. The identification of transcription factor binding sites (TFBS) by computational methods is very important in understanding the gene regulatory network. Although many methods have been developed to identifying TFBSs, they generally have relatively low accuracy especially when the positions of the TFBS are dependent. Motivated by this challenge, an efficient algorithm, IBSS, is developed for the identification of TFBSs. Our results indicate that IBSS outperforms other approaches with a relatively high accuracy.

12.1 Introduction

To understand the gene regulatory networks on the genomic scale is one of the great challenges in the post-genome era. Deciphering the regulatory binding sites (regulatory motifs) of a transcription factor (TF) on DNA sequences is especially fundamental and important for understanding gene regulatory networks. Experimental identification of TF binding sites (TFBS) is slow and laborious, while computational methods for the identification of TFBSs in genomic scale are difficult because binding sites are typically short and degenerate, and the binding mechanisms are not very clear. The availability of high throughput data, such as gene expressions, complete genome sequences of many species and ChIP-chip (Chromatin Immunoprecipitation) data, has facilitated bioinformatians to develop new computational methods to identify TFBSs.

There are two basic paradigms of computational identification of TFBSs. One is weight matrix model (WMM). The basic assumption of WMM is that it is position specific in the TFBS and mutations at different positions of the TFBS are independent. However this is not true in many cases. Short random sequences may be inserted in the TFBS such that the position specificity may be destroyed. There are often significant dependencies between positions within a TFBS [28]. Thus, real TFBSs sometimes do not fit the WMM model well, and the results from this model may not be satisfactory. First order and higher order Markov models have also been

developed to consider the position dependence, but they usually require large data to estimate the exponentially increasing number of parameters in such models [28].

Another paradigm for the identification of TFBSs is based on consensus pattern enumeration (word counting) methods. The main idea of word counting methods is to find out the over-represented words from a set of given samples. The word counting methods do not need any assumptions of position specific and independence between positions in the TFBS. Because no statistical models for TFBSs are assumed, word counting methods lack the ability to give description on the properties of TFs and discrimination on any given sequence to find out whether and where they contain TFs. Furthermore, word counting methods sometimes fail to find out the TFBS if the TFBS has large variation and the number of training sequences is small. In addition, word counting methods require to search a large candidate consensus pattern space, which can be time consuming.

We have developed an efficient algorithm, IBSS (Intelligent Binding Sites System), for the identification of TFBSs. The procedures and ideas of IBSS can be described as follows. (Fig. 12.1 gives the schematic view of IBSS.)

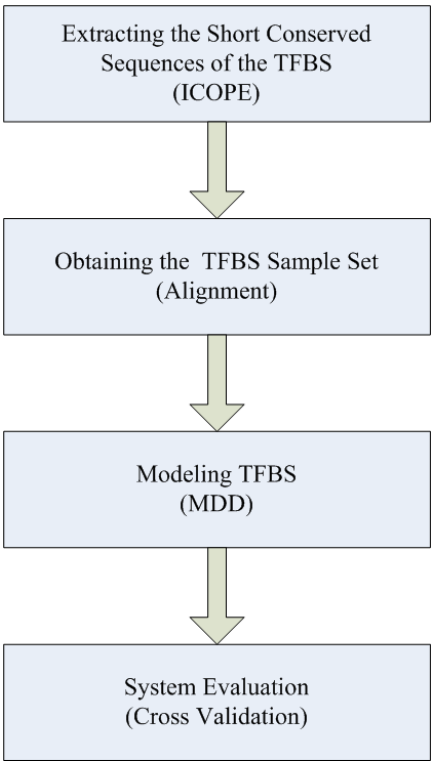

Fig. 12.1. Scheme of IBSS

A. Extracting the Short Conserved Sequences of the TFBS. Suppose that we have a set of sample sequences, which a TF may bind to. Because TFBSs can be degenerate, real TFBSs may not be found to be over-represented through word counting methods. On the other hand, short sub-sequences of the TFBS may be more conserved and be found to be over-represented through word counting methods. The main purpose of this step is to extract all these short conserved sub-sequences. A program, ICOPE (Intelligent Consensus Pattern Enumeration), based on this idea is developed.

B. Obtaining the TFBS Sample Set. From step A, a collection of typical short conserved sub-sequences of the TFBS can be gotten to obtain the TFBS sample sequences for further statistical analysis. We then develop a technique.

C. Modeling the TFBS. In step A, no statistical models are assumed. Therefore, a proper statistical model is needed for the description and discrimination of TFBSs. Our result indicate that the dependencies between positions in the TFBS sometimes can be very important. Therefore, a model based on the Maximal Dependence Decomposition (MDD) [3] with insertions is developed for the TFBS to model the dependencies between different positions in the TFBS. We derive statistical inference procedure for the discrimination of TFBSs based on the MDD model.

D. System Evaluation. Cross validation is used to evaluate the performance of our algorithm and the model.

In Section 12.2.2, we show that ICOPE, which is based on the first step of IBSS, achieves higher accuracy than six well known motif-finding programs based on large scale ChIP-chip data of transcription factors with known DNA-binding specificities documented in databases.

In Section 12.4, we show that the nucleotide bases for the TFBS of TF—YAP7 are highly dependent. We then use the MDD to model the TFBS. The cross validation results indicate that the MDD model significant outperform the weight matrix model (WMM).

12.2 ICOPE

To obtain the set of sample sequences for finding the motifs of the TFBS, usually gene expressions under different conditions or TF mutants are needed. For gene expressions under different conditions, co-expressed genes are clustered. Over-represented motifs can then be discovered in the promoter regions of these co-expressed genes using motif-finding algorithms. The basic assumption is that the binding sites of the same TF are similar and co-expressed genes are likely to be regulated by the same TFs [7]. In the TF mutant microarray, a TF is deleted or over-expressed, and then up-regulate or down-regulate genes are selected out for motif finding. The basic assumption is that these genes are more likely to be regulated by this TF. However it

is difficult to distinguish the effects of direct or indirect regulation by the TF among these up-regulate and down-regulate genes. Recently a functional clustering method is developed to use mutant expression data for motif finding of TFBSs [6].

Motif-finding algorithms can also be used to identify the transcription factors' DNA-binding specificities from ChIP-chip data [18], which provides a way to reveal the genome-wide location of DNA-binding proteins and can be used to construct a genome-wide map of in vivo protein-DNA interactions for any given protein. ChIP-chip has produced large amount of data [11, 14]. However, the resolution of typical yeast ChIP-chip experiments is only about 1 kb. As a result, computational methods are required to identify the transcription factors' exact DNA binding specificities.

Many computational methods have been developed in the past two decades for discovering motif patterns and TF binding sites in a set of promoter sequences. Most of the motif finding programs can be classified into two groups.

The first group of methods for motif finding use WMM as the motif model, and usually combine with Expectation Maximization (EM) or Gibbs Sampling to iteratively refine the WMM. Stormo and Hartzell [21] used a heuristic progressive alignment procedure to find motifs. Early WMM based methods using EM or Gibbs Sampling include Lawrence and Reilly [12], Lawrence et al. [13], Bailey and Elkan [1] etc. By iteratively masking out aligned sites, AlignACE [19] is more effective in finding multiple distinct motifs. BioProspector [16] uses third order Markov chain to model the background sequences to improve the motif specificity.

The other group of programs for motif finding use enumeration method to find the best consensus pattern, we refer to these methods as word counting methods. Galas [10] developed the earliest motif-finding program using consensus enumeration. Brazma et al. [2] analyzed over representation of regular expression-type patterns. Recent word-counting methods are reported by Wolfertstetter et al. [26], van Helden et al. [25] and Sinha and Tompa [22]. DWE [23] is a word-counting-based tool to discover tissue-specific transcription factor binding sites.

Recently, MDScan [17] combines the two widely adopted motif search strategies, word counting and WMM updating, and incorporates the ChIP-chip ranking information to accelerate searches to enhance its success rates.

The program, ICOPE, is developed based on the first step of IBSS. We search the ensemble of all short sequences combined with a limited number of degenerate letters and a range of spacer inserted in the set of sample sequences, and select out all the over-represented short sequences. These short sequences can not be too short so that it can contain sufficient information of the TFBS and be over-represented in the sample sequences than in the background sequences, while they can not be too long so that their occurrence probabilities will be big enough such that their occurrences can be approximated by their occurrence frequencies. Usually $6 \sim 7$ base pair (bp) informative positions for DNA sequences could serve practical use.

It has been show by several investigators that some TFs when in low concentration show a significant preference for multiple occurrences of motifs; while in high

concentration, they don't have such a preference [4, 11]. ICOPE take this fact into account. ICOPE uses two different word-counting methods to deal with these two groups of TFs. Obviously, we don't know which group a TF belongs to in advance. So a simple mixture model to combine the two methods is used. Both methods are examined and the method that gives a lower p-value will be accepted.

Another character of ICOPE over existing methods lies in the background model. It has been shown that different background models can greatly influence the performance of motif-finding programs [16]. Most other programs use high order Markov model as background model, which is relatively inaccurate. Background model of ICOPE is based on directly resampling from the background sequences.

12.2.1 Systems and Methods

A consensus pattern that occurs significantly more often than chance expectation is said to be over-represented. Like other consensus enumeration method, consensus patterns are evaluated based on their over-representation in the input sequences. A statistical significance (p-value) is given to objectively measure the degree of over-representation.

Most conserved patterns of the TFBS are usually in the range 6-10 bp long [22]. ICOPE searches against a very large consensus pattern space. All strings of length 6 over the alphabet {A, C, G, T} and strings of length 7 over the alphabet {A, C, G, T, R, Y, S, W} with a limited number of degenerate letters {R, Y, S, W} are considered. In addition, all the above strings with a spacer inserted are also incorporated. The spacer inserted is a string of 1-12 consecutive N's. The spacer can be inserted at any position in the original string. For the search space, our method is found similar to the motif method used in YMF [22] except that in YMF the spacer can only be inserted in the center of the motif, while we allow the spacer to occur at any position.

For each consensus pattern S in the search space, we calculate p-value p_S^M assuming that the factor has a preference for multiple occurrences of motifs, referred as factor class I, and calculate p-value p_S^S assuming the factor has no such a preference, referred as factor class II. Then we find the best consensus pattern S_M that minimizes p_S^M and S_S that minimizes p_S^S. If both $p_{S_M}^M$ and $p_{S_S}^S$ are greater than 0.05, we think the result is not statistically significant and ICOPE outputs nothing. If $p_{S_M}^M < p_{S_S}^S$ and $p_{S_M}^M < 0.05$, ICOPE assumes the corresponding factor is of factor class I. If $p_{S_S}^S < p_{S_M}^M$ and $p_{S_S}^S < 0.05$, ICOPE assumes the corresponding factor is of factor class II.

First, we discuss how p_S^S is calculated. This p-value is calculated by assuming the factor has a preference of single motif occurrence. For counting word, only one occurrence of the motif in the promoter region is considered even if a motif occurs several times in a sequence. We count the number of sequences with the motif in the input sequence set. Let N_S^S be the number of sequences in the input sequence set in which pattern S occurs. A good measure of over-representation of the consensus pat-

tern must take into account both N_S^S and the background genomic distribution. We merge all the yeast intergenic sequences into one large sequence as the background. Then random sequence sets with the same size as the input sequence set are drawn from the background. The sequences in the resampled random sequence sets have the same sequence length with the input sequence set. For the resampled sequence sets, let n_S^S be the average number of sequences on which the consensus pattern S occurs. Let M be the size of the input sequence set. Then p-value is approximately calculated by using binominal distribution $B(M, n_S^S/M)$.

The p_S^M can be similarly calculated. This p-value calculated is by assuming that the factor has a preference for multiple motif occurrences in the promoter regions. For word counting, every occurrence of motif should be considered. We count N_S^M the number of occurrences of consensus pattern S in the input sequence set. We set an upper limit for the number of occurrences in a single sequence to avoid the interference of repetitive sequence. Currently we set this upper limit to 5. Resampled random sequence sets with the same sequence number and same sequence length as the input sequence set are generated by similar method from background sequences and scanned to count the number of occurrences of pattern S. For the resampled random sequence sets, let n_S^M be the average number of occurrences of pattern S. Then p-value is approximately calculated by using the Poisson distribution $P(n_S^M)$.

For every consensus pattern in the search space, we test the hypothesis that the pattern is a binding motif based on p_S^S for factor class I and p_S^M for factor class II. So millions of hypothesis are being tested simultaneously. The p-value calculated above by using binominal distribution or Poisson distribution of each class must be corrected for multiple tests. We use formula the $p_c = 1 - (1 - p)^N$ to adjust for multiple testing, where p is the p-value before correction and p_c is the corrected p-value. N is the number of tests conducted, i.e. the size of the searched consensus space. Both p_S^S and p_S^M are corrected using this formula. For more advanced and technical discussion of p-value choice in large-scale simultaneous hypothesis testing, see [9].

In practice, the most time consuming part is in the resampling process. This process is done in advance and the result is stored in disk. For every possible length l, let η_{Sl}^S be the probability that a sequence with length l has motif S if the sequence is drawn randomly from background. Let η_{Sl}^M be the average number of occurrences of motif S if the sequence is drawn randomly from background. n_S^S is calculated by summing over η_{Sl}^S for every sequence in the input sequence set. n_S^M is calculated by summing over η_{Sl}^M for every sequence in the input sequence set. In fact we do not need and can't afford to do resampling for every possible length. Because most of promoter regions in yeast are less than 1500 bp, we only do this process for length $l \in L$, $L = \{50, 100, 150 \cdots 1450, 1500\}$. If l is not in L, we round it to the nearest length in L.

12.2.2 Results

In Harbison et al. [11], a large set of transcription factor's genome-wide location analysis was conducted under several different conditions. Among those factors, 81 factors have known DNA binding specificities documented in databases (TRANSFAC, YPD, SCPD). Harbison et al. [11] conducted 175 ChIP-chip experiments for these 81 factors. We tested ICOPE on this set of 175 experiments. For 76 of the 175 experiments and for 49 of the 81 factors, the most significant consensus pattern reported by ICOPE match the corresponding database record. Harbison et al. [11] tested six other programs on their data. For these factors with known binding specificities, the best program, MDScan, successfully predicted 37 factors' binding specificity in 59 of 175 experiments. In addition ICOPE made 135 predictions for those 175 experiments while MDScan made 156 predictions. It is obvious that ICOPE has a higher accuracy. The five other programs used by Harbison et al. [11] can successfully predicted only 20 $\sim$ 33 of the factors' binding pattern. Detailed information is given in Supplementary Table 1. A comprehensive result of ICOPE's prediction on these 175 experiments and comparison with database record is given in Supplementary Table 2.

We did a similar evaluation on a subset of the 81 transcription factors, which contains 52 factors for which at least one program's prediction matches the known specificity. We dropped those that have only database record but have no program's prediction matching the record for three reasons. First, the database might have errors, although the chance is small. Second, the ChIP-Chip experiment is rather noisy. Third and the most important, transcription factors may take effect only in certain specific condition. The condition under which ChIP-Chip experiment is conducted might not be that exact condition. So if none of the programs can predict the binding specificity, the condition under which ChIP-Chip experiment is conducted might be incorrect. The result for this set of factors is given in Table 1 and summarized in Table 15.2.

Table 12.1: **Comparison of ICOPE with Six Other Programs** Comparison of ICOPE with six other programs on a set of 52 factors with database documented binding specificity. FA=factor name, KN=known specificity, I=icope, A = AlignACE, C = CONVERGE, D = MDscan, K = Kellis et al., M = MEME, N = MEME_c.

FA	KN	I	A	C	D	K	M	N
Abf1	rTCAyTnnnnACGw	+	+	+	+	+	+	+
Ace2	GCTGGT					+		
Aft2	AAAGTGCACCCATT	+	+	+	+		+	+
Azf1	TTTTTCTT							+
Bas1	TGACTC	+	+			+	+	+
Cad1	TTACTAA	+	+	+	+		+	+
Cbf1	rTCACrTGA	+	+	+	+	+	+	+
Cin5	TTACrTAA	+	+	+	+			
Fkh1	GGTAAACAA	+	+	+	+	+	+	+
Fkh2	GGTAAACAA	+	+	+	+	+	+	+

continued on next page

Table 12.1: *continued*

FA	KN	I	A	C	D	K	M	N
Gal4	CGGnnnnnnnnnnCCG	+	+			+		
Gat1	GATAA	+				+		
Gcn4	ArTGACTCw	+	+	+	+	+	+	+
Gcr1	GGCTTCCwC	+			+			
Gln3	GATAAGATAAG	+		+	+	+		
Hap1	CGGnnnTAnCGG	+		+			+	
Hap3	CCAAT	+						
Hap4	YCNNCCAATNANM	+	+	+	+		+	+
Hsf1	TTCTAGAAnnTTCT	+	+	+	+	+	+	+
Ino2	ATTTCACATC	+		+	+		+	+
Ino4	CATGTGAAAT	+	+	+	+	+	+	+
Leu3	yGCCGGTACCGGyk	+	+		+	+	+	+
Mac1	GAGCAAA	+			+			
Mbp1	ACGCGT	+	+	+	+	+	+	+
Mcm1	wTTCCyAAwnnGGTAA	+	+	+	+		+	+
Mot3	yAGGyA	+						
Msn2	mAGGGG	+					+	
Nrg1	GGaCCCT	+	+	+	+		+	+
Pdr1	CCGCGG						+	
Pho4	cacgtkng	+			+	+		+
Put3	CGGnnnnnnnnnnCCG	+						
Rap1	wrmACCCATACAyy	+	+	+	+		+	+
Rcs1	AAmTGGGTGCAkT	+		+	+		+	+
Reb1	TTACCCGG	+	+	+	+	+	+	+
Rph1	CCCCTTAAGG	+						
Rpn4	GGTGGCAAA	+	+	+	+	+	+	+
Sip4	yCGGAyrrAwGG	+			+			
Skn7	ATTTGGCyGGsCC	+	+	+	+		+	+
Sko1	ACGTCA	+						
Stb5	CGGnstTAta	+			+			+
Ste12	ATGAAAC	+	+	+	+	+	+	+
Sum1	AGyGwCACAAAAk	+	+	+	+		+	+
Sut1	CGCG	+	+		+		+	
Swi4	CnCGAAA	+	+	+	+	+	+	+
Swi6	CnCGAAA / ACGCGT	+	+	+	+		+	+
Tec1	CATTCy	+		+				
Tye7	CAnnTG	+	+	+	+		+	
Ume6	wGCCGCCGw	+	+	+	+	+	+	+
Xbp1	CTTCGAG	+						
Yap1	TTAsTmA	+	+	+	+		+	
Yap7	TTACTAA	+	+	+	+		+	+
Zap1	ACCCTAAAGGT	+			+			+

Table 12.2: **Summary of Supplementary Table 1 and Table 15.1**
MA : the number of factors for which each program's prediction match the database record. Percent_1=MA/81, 81 is total number of factors with database documented DNA binding specificity. Percent_2=MA/52, 52 is number of factors with database documented DNA binding specificity and with at least one program's prediction match the database record.

	I	A	C	D	K	M	N
MA	49	30	31	37	20	33	31
Percent_1	60.5%	37.0%	38.3%	45.7%	24.7%	40.7%	38.3%
Percent_2	94.2%	57.7%	59.6%	71.2%	38.4%	63.5%	59.6%

As mentioned in Section 12.2.1, ICOPE uses a very simple strategy to combine the two p-values. We find that such a strategy to combine those two p-values is much better than using one of the two p-values alone. Using one p-value alone will miss some of the factors belonging to the other group. Fig. 15.1 compares the results of considering different p-values. As illustrated in Fig. 15.1, ICOPE_M is the program that uses p-value p_S^M, and ICOPE_S is the program that uses p-value p_S^S. Both program can correctly predict 36 factors' DNA binding specificity. Seven factors (CAD1,GCR1,PUT3,RPH1,STB5,XBP1,ZAP1) can be correctly predicted by ICOPE_M and can not be correctly predicted by ICOPE_S. Seven other factors (GAT1,HAP2,HAP3,MSN2,SUM1,SUT1,TEC1) can be correctly predicted by ICOPE_S and can not be correctly predicted by ICOPE_M. ICOPE can correctly predict DNA binding specificity for 49 factors whose DNA binding specificity can be correctly predicted by either ICOPE_M or ICOPE_S. There is only one exception, HAP2. For this factor, both ICOPE_M and ICOPE_S make predictions. ICOPE_M gives lower p-value, but it's prediction is incorrect. While prediction of ICOPE_S is correct. So ICOPE take the result of ICOPE_M and makes a mistake.

We sorted the ICOPE's predictions on the 175 experiments based on the p-values given by ICOPE. The sorted results are given in Supplementary Table 3 and summarized in Table 15.3. We can see that the p-value is a pretty indicator to whether the prediction is reliable. ICOPE makes 39 predictions with $\log 10$ p-values less than -14 among which 37 (95%) predictions are correct. ICOPE makes 23 predictions with $\log 10$ p-values between -14 and -7, among which 18 (78%) predictions are correct. ICOPE makes 73 predictions with $\log 10$ p-values between -7 and -1.3, among which 21 (29%) predictions are correct. If the p-value is very low, as low as 10^{-14}, the prediction is highly reliable. As the p-value goes higher, the prediction becomes less reliable.

Table 12.3: **The p-value given by ICOPE indicates the reliability of it's prediction**
N=number of predictions, N_C=number of correct predictions, P(%)=percentage of correct predictions

p-value range	N	N_C	P(%)
$\log_{10} p \leq -14$	39	37	95%

$$\begin{array}{l|lll} -14 \leq \log_{10} p \leq -7 & 23 & 18 & 78\% \\ -7 \leq \log_{10} p \leq -1.3 & 73 & 21 & 29\% \end{array}$$

We run ICOPE on the 135 ChIP-chip experiment for 101 factors without known DNA binding specificity. The predictions is given in Supplementary Table 4. The result sorted by p-value is given in Supplementary Table 5. The program made 87 predictions for these 135 experiment. Six of the predictions have very low p-value (less then 10^{-14}). Based on the prediction accuracy on factors with known DNA binding specificity, we estimate that these predictions may be highly reliable (95% accurate). Sixteen of predictions have very low p-value (between 10^{-14} and 10^{-7}). Based on the prediction accuracy on factors with known DNA binding specificity, we estimate that these predictions might have an accuracy of 78%. The predictions with p-value less than 10^{-7} are given in Table 15.4.

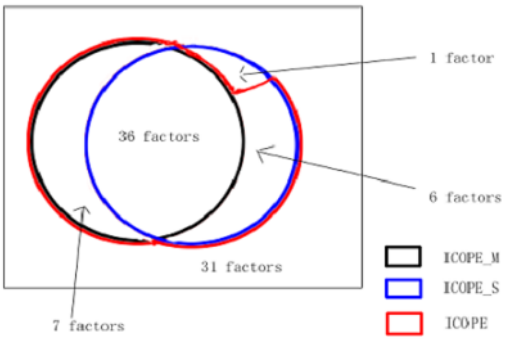

Fig. 12.2. ICOPE has a significantly higher accuracy than both ICOPE_M and ICOPE_S. In the rectangle are the 81 factors with known DNA binding specificity. The black circle stands for the factors whose DNA binding specificity can be correctly predicted by ICOPE_M. The blue circle stands for the factors whose DNA binding specificity can be correctly predicted by ICOPE_S. The red curve stands for the factors whose DNA binding specificity can be correctly predicted by ICOPE.

Table 12.4: **The predictions made by ICOPE on factors with unknown DNA binding specificity.**
(Only predictions with a p-value lower than 10^{-7} are shown.)

Experiment	Prediction	p-value
FHL1_YPD	TGTNNGGRT	-54.0149
FHL1_RAPA	TGTNNGGRT	-53.7184
FHL1_SM	TGTNNGGRT	-49.6275
RDS1_H2O2Hi	CGGCCG	-15.7688
SFP1_SM	AYCNNTACA	-15.6778
GAT3_YPD	GCTNAGCS	-14.4517
DIG1_Alpha	YGTTTCA	-13.1135
YFL044C_YPD	TANNNATWTA	-12.0532
PHD1_YPD	AGGCAC	-11.735
SNT2_YPD	GGSGCTA	-11.4775
STB1_YPD	CGCSAAA	-11.2591
HOG1_YPD	ACNNNNNCRCAC	-10.9645
DAT1_YPD	GCTNAGCS	-9.77751
RDS1_YPD	CGGCCG	-9.60608
MET4_YPD	CACGTG	-9.46732
SPT23_YPD	TTAWTAA	-9.42808
DIG1_BUT90	YGTTTCA	-8.70506
MET4_SM	CACGTG	-8.61795
YDR026c_YPD	TASCCGG	-8.54541
MGA1_H2O2Hi	CGGCCG	-8.50797
RGM1_YPD	GCTNAGCS	-7.38143

continued on next page

Table 12.4: *continued*

Experiment	Prediction	p-value
YDR520C_YPD	CCGSCGG	-7.17487

Because we did the resampling process in advance for almost every possible length of input sequence and stored the result in disk, ICOPE runs pretty fast. For an input sequence set with 10 sequences and average length of 500, about 1.5 minutes being required. For an input sequence set with 100 sequences and average length of 500, about 9 minutes being required.

ICOPE is implemented using C++ programming language and a web interface is implemented using PHP. The URL for the web interface is at `http://ctb.pku.edu.cn/~xcfeng/icope/`.

Supplementary information, including data and omitted results are available at `http://ctb.pku.edu.cn/~xcfeng/icope/supp/`.

12.3 Obtaining the TFBS Sample Set

Although ICOPE's prediction on transcription factors' DNA binding specificity has a high accuracy, the sequences generated by ICOPE are typical sequences of the TFBS. Real TFBS sample sequences should be obtained for further statistical analysis by MDD. The technique to obtain the TFBS sample set is described as follows.

Let C be the collection of over-represented short sequences generated from ICOPE. Align each short sequence in C, to all the sample sequences mentioned in step A of IBSS, with a limited number of mismatches and highlight the aligned part. Then get all connected segments that are highlighted, and denote the set of all segments by D_O. After multiple alignment on all segments in D_O, we choose the aligned consensus sequences as the TFBS sample set, denote by D. Gaps are usually contained in sequences of D since insertions are kept from multiple alignment.

12.4 Modeling the TFBS

Because no statistical models for TFBSs are assumed in ICOPE, it is not possible to test whether there are some binding sites and where they are for a given sequence.

Weight matrix model (WMM) introduced by Staden [20] is a more accurate representation, but weight matrix assumes independence between different positions in the motif. For some transcription factors, it has been shown that there are strong dependencies between different positions of their binding motif [28]. So weight matrix

is not a good choice to represent such transcription factors' DNA binding specificity, although they are good enough for other transcription factors. Weight array model (WAM) [27] which applied by Zhang and Mar could detect dependencies between adjacent positions by using first-order (non-stationary) Markov models. Higher order WAMs can be used to model higher order dependencies in the TFBS sequences, but there are often insufficient data available to estimate the exponentially increasing number of parameters in such models [28].

Recently, some new methods have been developed to model such long distant dependence. A Maximal Dependence Decomposition (MDD) [3] based model, with the insertion, denoted by O added in as a symbol, is developed for the TFBS. The MDD model has advantage to capture and model the dependencies between different positions in the TFBS. The main idea of MDD is that it splits up the training data to fit different WMM to suitably defined subsets of the data based on most dependent positions which are measured by χ^2 test.

12.4.1 Using χ^2 Test to Measure Dependence Between Positions

For a given TFBS sample set D obtained from Section 12.3, we use the χ^2 test to measure dependencies between positions of the sequences in D. Suppose D contains N aligned sequences of length k. For any given position i and j ($1 \le i, j \le k$, $i \ne j$), and for a given nucleotide b ($b \in$ {A,C,T,G,O})[1], we use $\chi^2(C_{ib}, X_j)$ test, to measure the dependency between the consensus indicator variable, C_{ib} (1 if the nucleotide b at position i matches the consensus at i, 0 otherwise) and nucleotide indicator X_j identifying the nucleotide at position j.

For given position i, nucleotide b and position j, we have

	$C_{ib}=0$	$C_{ib}=1$	
$X_j = A$	n_{A0}	n_{A1}	$n_{A\cdot}$
$X_j = C$	n_{C0}	n_{C1}	$n_{C\cdot}$
$X_j = G$	n_{G0}	n_{G1}	$n_{G\cdot}$
$X_j = T$	n_{T0}	n_{T1}	$n_{T\cdot}$
$X_j = O$	n_{O0}	n_{O1}	$n_{O\cdot}$
	$n_{\cdot 0}$	$n_{\cdot 1}$	

where

$$n_{c\cdot} = \sum_{t=0,1} n_{ct}, \qquad c \in \{A, C, G, T, O\}.$$

$$n_{\cdot t} = \sum_{c \in \{A,C,G,T,O\}} n_{ct}, \qquad t = 0, 1.$$

$$\sum_{\substack{c \in \{A,C,G,T,O\} \\ t=0,1}} n_{ct} = N$$

Define

[1] O stands for one gap.

$$\hat{p_c} = \frac{n_{c\cdot}}{N}, \qquad c \in \{A, C, G, T, O\}.$$
$$\hat{q_t} = \frac{n_{\cdot t}}{N}, \qquad t = 0, 1.$$

We use the statistic

$$\chi^2(C_{ib}, X_j) = \sum_{\substack{c\in\{A,C,G,T,O\} \\ t=0,1}} \frac{(n_{ct} - N\hat{p_c}\hat{q_t})^2}{N\hat{p_c}\hat{q_t}}$$

$\chi^2(C_{ib}, X_j)$ obey the $(2-1)\times(5-1) = 4$ d.f. χ^2-distribution [5], and significant χ^2 value should be great than 13.3 at the relatively level of $p < 0.01$ indicating a significant dependent position in the TFBS.

Based on the χ^2 test, we find that some cases of the transcription factors' binding motif show strong dependencies between different positions.

12.4.2 Maximal Dependence Decomposition (MDD)

For a given TFBS sample sequence set D, the MDD model is to build conditional probability model, based on the significant dependence between positions (both non-adjacent and adjacent dependencies are considered), instead of the unconditional WMM probabilities model [3].

The algorithm of the MDD model is described as follows: For a given sequence set D, assume that it contains N aligned sequences of length k.

1. Check whether there exist i, j, b such that satisfy $\chi^2(C_{ib}, X_j) \geq 13.3$, that is whether there exist significant dependent positions. If yes, continue to the next step; otherwise, stop.
2. For each position i and nucleotide b, calculate $S_{ib} = \sum_{j\neq i} \chi^2(C_{ib}, X_j)$, which measures the amount of dependencies between the variable C_{ib} and the nucleotides at the remaining positions. Choose i_1 and b_1 that maximize S_{ib},
$$S_{i_1 b_1} = \max_{i,b} S_{ib}$$
3. Divide D into two subsets based on whether or not position i_1 has nucleotide b_1. Check whether each of the two subsets contains enough sequences to estimate WMM frequencies for further subdivision. If each of the two subsets contains enough sequences to estimate WMM frequencies, we divide set D into $D_{i_1 b_1}$ and $\overline{D}_{i_1 b_1}$. $D_{i_1 b_1}$ contains all the sequences that has nucleotide b_1 at position i_1 and $\overline{D}_{i_1 b_1}$ contains no nucleotide b_1 at position i_1.
4. Repeat steps 1 , 2 and 3 on the subsets $D_{i_1 b_1}$ and $\overline{D}_{i_1 b_1}$, and from the time on, position i_1 will be not considered.

The MDD model splits the set D into subsets, constructs a binary tree structure based on the above algorithm, and we use WMM model to describe for each leaf of subsets. Fig. 12.3 shows the procedures for splitting data set D of TF—YAP7.

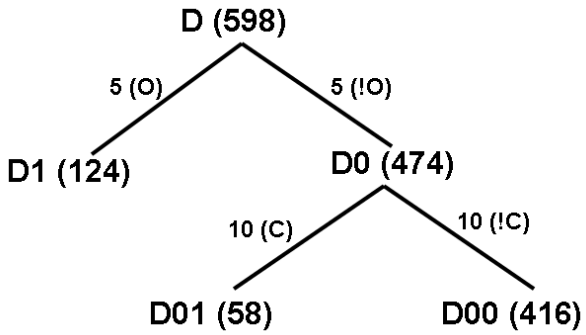

Fig. 12.3. Tree result of YAP7. D, $D1$, $D0$, $D01$, $D00$ stand for the node names of tree. The number in the parentheses behind the node name stands for the number of sequences. The annotation on the edge represents how to split the set of the parent node into two subset. For example, D splits into $D1$ and $D0$ based on position 5 has or has no O. O stands for gap, ! stands for NOT.

To make the algorithm more clear, we give an example of YAP7. We use ChIP-chip data from [11] of YAP7 under the condition H2O2Lo. ICOPE is used to predict the binding sites of YAP7. ICOPE predicts 100 words with $p \leq 10^{-5}$. We highlight the 123 ChIP-chip selected sequences that can be aligned, with no mismatch, by the 100 words. 117 (about 95.12%) of the 123 ChIP-chip selected sequences could be highlighted. We then obtain all the 598 sequence segments that have been highlighted. The 598 sequence segments are aligned by ClustalW [24] with its default parameters, and the most consensus aligned sequences of 10 bp length from 598 sequence segments are picked out as the TFBS sample set D.

Using χ^2 test, we find significant dependencies between the positions of the sequences in D. The TFBS sample set D is used to train the MDD model, and the results are summarized in Fig. 12.3 and Fig. 12.4. Fig. 12.3 shows the binary tree constructed by the MDD model. From it we learn that other positions have significant dependencies on whether position 5 has a gap. Condition on position 5 having no gap, the other positions have significant dependencies on whether position 10 has C. Fig. 12.4 shows the sequence logo [7] plots of the data set in each node of the binary tree in Fig. 12.3. From the sequence logo, it can be seen strong dependencies between the positions of YAP7.

12.4.3 Statistical Model and Discrimination

The MDD model splits training data set into subsets and constructs a binary tree based on most significant dependent positions. Any sequences could find a corresponding unique leaf on the binary tree. For each leaf l, the MDD model assigns a probability $P_{mdd}(L = l)$ for reaching this leaf from the root. Separate WMM models are estimated for each subset on the leaf of the binary tree. For a given leaf l, it has

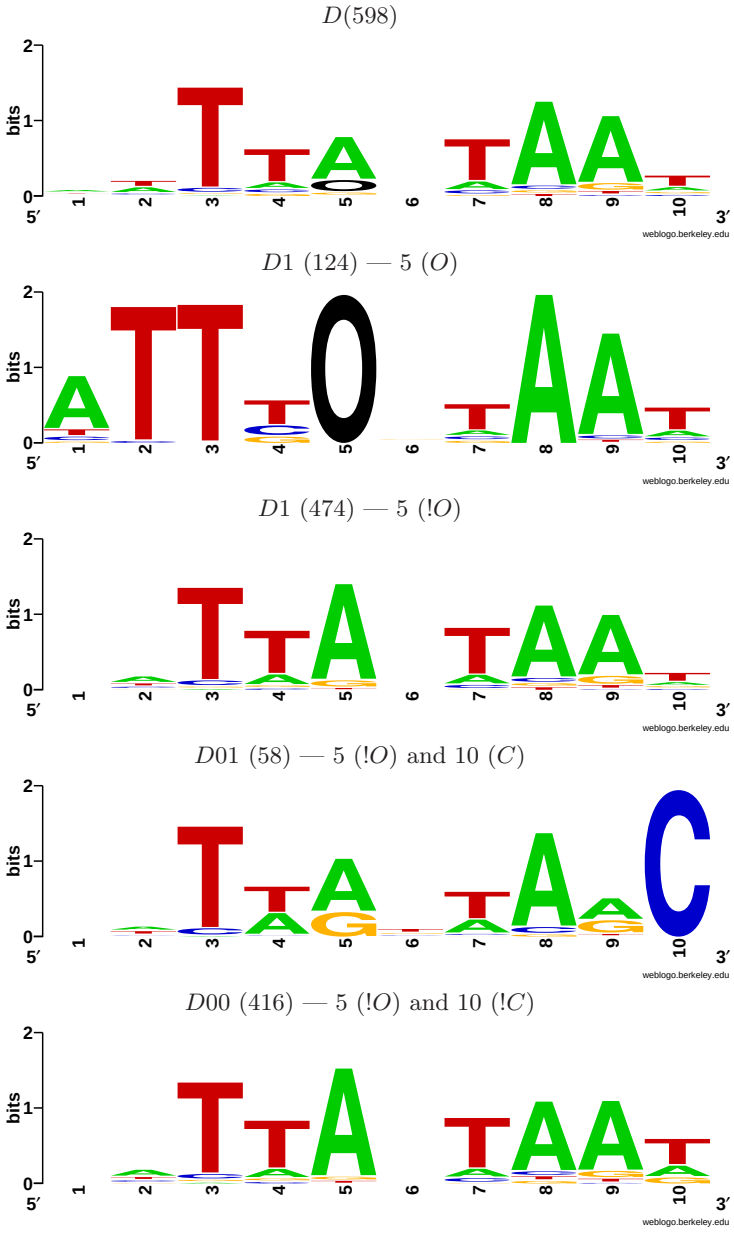

Fig. 12.4. Sequence logo plots for TFBS of YAP7. Each of the plot corresponds to the node of the binary tree in Fig. 12.3. The positions dependencies can been seen from sequence logo plots.

weight matrix $\mathbf{W}^l$, and W^l_{ib} stands for the frequency of nucleotide b in position i on leaf l.

Suppose that we have a sequence $S = s_1 s_2 \dots s_k$, and it is on leaf l from the MDD model. Condition on leaf l, sequence S has the probability

$$P(S = s_1 s_2 \dots s_k | L = l) = \prod_{i=1,2,\dots,k} W^l_{is_i}$$

From the MDD model, the probability of obtaining such a sequence S is

$$P_{mdd}(S = s_1 s_2 \dots s_k) = P_{mdd}(L = l) \cdot P(S = s_1 s_2 \dots s_k | L = l)$$

Next we give a discriminant method to identify whether or not a sequence, $S = s_1 s_2 \dots s_k$, is a transcription factor's binding sides. Let $\Omega = 1$ indicates for a given sequence that is a TFBS, and $\Omega = 0$ otherwise. Suppose that for any sequence S with length k,

$$P_{mdd}(S|\Omega = 1) \sim N(\mu_1, \sigma_1)$$
$$P_{mdd}(S|\Omega = 0) \sim N(\mu_2, \sigma_2)$$

From [8], the threshold μ^* is derived as

$$\mu^* = \frac{\mu_1 \sigma_2 + \mu_2 \sigma_1}{\sigma_1 + \sigma_2}$$

The discriminant rule for S is

$$\begin{cases} \text{S is TFBS}, & \text{when } P_{mdd}(S) > \mu^* \\ \text{S is not TFBS}, & \text{when } P_{mdd}(S) \le \mu^* \end{cases}$$

We use the sequence set D generated from the procedures described in Section 12.3 as the positive sample, and randomly select the same number of sequences with the same length from background sequences as our negative sample, denote as B. We use the positive sequences to train the MDD model, and use both the positive and negative sequences to estimate the threshold μ^* for further discrimination.

To test the efficiency of the MDD model, we use the 598 TFBS sample sequences of YAP7 described in Section 12.4.2 as our positive sample, and obtain the negative sample B from the background sequences. We use 10-fold cross validation to evaluate the MDD model. To compare with the WMM model, we also use the same positive and negative sample to do the 10-fold cross-validation on the WMM model. Fig. 12.5 gives the receiver operating characteristic (ROC) curve of the results, which shows their performances in terms of TPr and FPr, where TPr is the sensitivity of a classifier measuring the fraction of positive cases that are classified as positive, and FPr is the false alarm measuring the fraction of incorrectly classified negative cases: $TPr = \frac{TP}{TP+FN} = \frac{TB}{Pos}$, $FPr = \frac{FP}{TN+FP} = \frac{FP}{Neg}$.

From Fig. 12.5, we learn that the MDD model outperforms the WMM model. It is because that the MDD model can capture and model the dependencies between positions while the WMM model cannot.

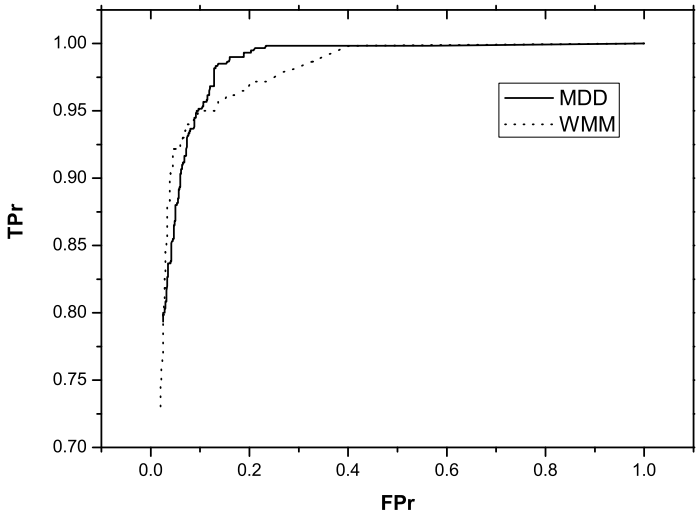

Fig. 12.5. ROC Curve of the MDD model and the WMM model of YAP7. The X-axis is FPr (false positive rate), Y-axis is TPr (true positive rate).

12.5 Discussion

The identification of transcription factor binding sites by computational methods is an essential step to understand the gene regulatory network. Although many methods have been developed to identifying TFBSs, they generally have relatively low accuracy especially when the positions of the TFBS are dependent. Motivated by this challenge, an efficient algorithm, IBSS, is developed for the identification of TFBSs. Our results indicate that IBSS outperforms other approaches with a relatively high accuracy.

In this study, the background model of ICOPE is only based on resampling. The binominal and Poisson distributions are only an approximation. More further study on the background model may help to improve the accuracy of ICOPE.

Combinatorial regulation is an essential feature of transcriptional regulation. Identification of TFBSs provides the materials for further understanding the combinational regulation. TFs usually form a protein complex to regulate the gene, so the distance between the TFBSs of the cooperative TFs should be limited, sometime the TFBSs of the cooperate TFs may even overlap. This biological knowledge gives us a clue to find out the cooperative TFs by the distances of TFBS pairs.

An inverse problem of TFBS finding is to detect the protein motif sequences which bind to the DNA sequences. A natural question is to ask whether or not the protein motif sequences which bind to the common binding sites on DNA sequences are conserved. With known the TFBSs of many TFs, the protein sequences of the TFs which share common binding sites on the DNA sequences may be used for further statistical analysis.

On the statistical model of TFBSs, the MDD based model is used instead of traditional WMM based model. The advantage of MDD model is that it considers the positions dependencies of the TFBS. In the future, a more accurate model of TFBSs should be developed.

Acknowledgement

The work benefits greatly from the research environment and the super computer at the Center for Theoretical Biology of Peking University. This work is supported in part by grants from the National Natural Sciences Foundation of China (90208002, 10271008), State 863 High Technology R&D Project of China (2002AA234011) and the Special Funds for Major State Basic Research of China (2003CB715903).

References

1. Bailey TL, Elkan C (1994) Fitting a mixture model by expectation maximization to discover motifs in biopolymers. In: Altman R, Brutlag, D., Karp P, Lathrop R, Searls D (eds) Proceedings of the Second International Conference on Intelligent Systems for Molecular Biology. AAAI Press, Menlo Park, California.
2. Brazma A, Jonassen I, Vilo J, Ukkonen E (1998) Predicting gene regulatory elements in silico on a genomic scale. Genome Res 8:1202–1215.
3. Burge C, Karlin S (1997) Prediciton of complete gene structures in human genomic DNA. Journal of Molecular Biology 268:78–94.
4. Bussemaker HJ, Li H, Siggia ED (2001) Regulatory element detection using correlation with expression. Nature Genetics 27:167–171.
5. Casella G, Berger RL (2001) Statistical Inference (2nd edition).Duxbury Press.
6. Chen GX, Hata N, Zhang MQ (2004) Transcription factor binding element detection using fucntional clustering of mutant expression dat. Nucl Acids Res 32:2362–2371.
7. Crooks GE, Hon G, Chandonia JM, Brenner SE WebLogo (2004) A sequence logo generator. Genome Research 14:1188–1190.
8. Duda RO, Hart PE, Stork DG (2000) Pattern Classification (2nd Edition). Wiley-Interscience.
9. Efron B (2004) Large-Scale Simultaneous Hypothesis Testing: The Choice of a Null Hypothesis. Journal of the American Statistical Association 99:97–104.

10. Galas DJ, Eggert M, Waterman MS (1985) Rigorous pattern-recognition methods for DNA sequence: analysis of promoter sequences from Escherichia coli. J Mol Biol 186:117–128.
11. Harbison CT et al (2004) Transcriptional regulatory code of a eukaryotic genome. Nature 431:99–104.
12. Lawrence CE, Reilly AA (1990) An expectation maximization (EM) algorithm for the identification and characterization of common sites in unaligned biopolymer sequences. Proteins 7:41–51.
13. Lawrence CE, Altschul SF, Boguski MS, Liu JS, Neuwald AN, Wootton J (1993) Detecting subtle sequence signals: a Gibbs sampling strategy for multiple alignment. Science 262:208–214.
14. Lee TI et al (2002) Transcriptional regulatory networks in Saccharomyces cerevisiae. Science 298:799–804.
15. Li H, Wang W (2003) Dissecting the transcription networks of a cell using computational genomics. Current Opinion in Genetics & Development 13:611–616.
16. Liu XS, Brutlag DL, Liu JS (2001) BioProspector: discovering conserved DNA motifs in upstream regulatory regions of co-expressed genes. Pac Symp Biocomput 6:127–138.
17. Liu XS, Brutlag DL, Liu JS (2002) An algorithm for finding protein-DNA binding sites with applications to chromatin-immunoprecipitation microarray experiments. Nature Bioteh 20:835–839.
18. Ren B, Robert F, Wyrick J, Aparicio O, Jennings E, Simon I, Zeitlinger J, Schreiber J, Hannett N, Kanin E, Volkert T, Wilson C, Bell S, Young R (2000) Genome-wide location and function of DNA binding proteins. Science 290:2306–2309.
19. Roth FP, Hughes JD, Estep PW, Chruch GM (1998) Finding DNA regulatory motifs within unaligned noncoding sequences clustered by whole-genome mRNA quantitation. Nature Bioteh 16:939–945.
20. Staden R (1984) Computer methods to locate signals in nucleic acid sequences. Nucl Acids Res 13: 505–519.
21. Stormo GD, Hartzell GW (1989) Identifying protein-binding sites from unaligned DNA fragments. Proc Natl Acad Sci, USA, 86:1183–1187.
22. Sinha S, Tompa M (2002) Discovery of Novel Transcription Factor Binding Sites by Statistical Overrepresentation. Nucleic Acids Res 30:5549–5560.
23. Sumazin P, Chen GX, Hata N, Smith AD, Zhang T, Zhang MQ (2004) DWE: Discriminating Word Enumerator. Bioinformatics 21:31–38
24. Thompson JD, Higgins DG, Gibson TJ (1994) ClustalW: improving the sensitivity of progressive multiple sequence alignment through sequence weighting, position-specific gap penalties and weight matrix choice. Nucleic Acids Res 22:4673–4680.
25. van Helden J, Andre B, Collado-Vides J (2000) Discovering regulatory elements in non-coding sequences by analysis of spaced dyads. Nucleic Acids Res 28:1808–1818
26. Wolfertstetter F, Frech K, Herrmann G, Werner T (1996) Identification of functional elements in unaligned nucleic acid sequences by a novel tuple search algorithm. Bioinformatics 12:71–81.
27. Zhang MQ, Marr TG (1993) A weight array method for splicing signal analysis. Computer Application in the Biosciences (CABIOS) 9(5):499–509.

28. Zhao XY, Huang HY, Speed T (2004) Finding short DNA motifs using permuted Markov models. Proceeding of RECOMB 04:68–75.

13

A Cross-species Topological Study of the Protein-protein Interaction Networks

Chien-Hung Huang, Po-Han Lee, Jywe-Fei Fang, and Ka-Lok Ng

Summary. We employed the random graph theory approach to analyze the protein-protein interaction database DIP, for seven species. Several global topological parameters were used to characterize the protein-protein interaction networks (PINs) for each species. The logarithm of the node degree cumulative distribution $P_{cum}(k)$ vs the logarithm of node degree k plots indicated that PINs are well describe scale-free networks ($P_{cum}(k) \sim k^{-\alpha}$). We also found that the logarithm of the average clustering coefficient $C_{ave}(k)$ scales with k (i.e. $C_{ave}(k) \sim k^{-\beta}$) for E. coli and the S. cerevisiae. In particular, we determined that the E. coli and the S. cerevisiae PINs are better represented by the stochastic and deterministic hierarchical network models respectively. These findings leaded us to conclude that, in contrast to scale-free structure, hierarchical structure model applied for certain species' PINs only. The current fruit-fly protein-protein interaction dataset does not has convincing evidence in favor of the hierarchical network model. We also demonstrated that PINs are quite robust when subject to random perturbation where up to 50% of the nodes were rewired. These suggested that network topological results are robust against experimental artifacts. Average node degree correlation study supported the fact that nodes of low connectivity are correlated, whereas nodes of high connectivity are not directly linked.

13.1 Introduction

Networks of interactions are fundamental to all biological processes; for example, the cell can be described as a complex network of chemicals connected by chemical reactions. Cellular processes are controlled by various types of biochemical networks [1]: (i) metabolic network; (ii) protein-protein interaction network (PIN), and (iii) gene regulatory network. In the last few years, we began to see much progress in analyzing biological networks using the random network approach. The random network approach had become a powerful tool for investigating different biological systems,

such as the yeast protein interaction network [2], food web [3] and metabolic network [4, 5]. Many studies indicated that there are underlying global structures of those biological networks. Below we highlight some of the current status of these results.

(I) Metabolic network
Metabolism comprises the network of interaction that provides energy and building blocks for cells and organisms. In many of the chemical reactions in living cells, enzymes act as catalysts in the conversion of certain compounds (substrates) into other compounds (products). Comparative analyses of the metabolic pathways formed by such reactions give important information on their evolution. The large-scale organization of the metabolic networks of 43 organisms are investigated and it is found that they all have the feature of a scale-free small-world network [5], and the diameter of the metabolic pathway is the same for the 43 organisms.

(II) Protein-protein interaction network
Proteins perform distinct and well-defined functions, but little is known about how in-teractions among them are structured at the cellular level. Recently, it was reported that [6] in the yeast organism, the protein-protein interactions are not random but well organized. It was found that, most of the neighbors of highly connected proteins have few neighbors, that is highly connected proteins are unlikely to interact with each other.

(III) Gene transcription regulatory network
A genetic regulatory network consists of a set of genes and their mutual regulatory interactions. The interactions arise from the fact that genes code for proteins that may control the expression of other genes, for instance, by activating or inhibiting DNA transcription [7]. It was reported that [8] there is a hierarchical and combinatorial organization of the transcriptional activity pattern in the yeast organism.
In this paper we reported topological and hierarchical structure study of protein-protein interaction by employing the random graph theory approach to analyze the protein-protein interacting database DIP (Oct. 2004), for seven species. Our analysis extended previous studies to a total of seven species, and it provided some evidence suggesting that there are underlying topological structures across different species.
In section 2, we give a detailed description of the input protein-protein interaction data [9, 10] and the topological parameters [11, 12] we used in this paper. Section 3 is the seven species' PINs topological structure study results. Section 4 is the discussion and summary.

13.2 Method

2.1 Input data - Database of Interacting Protein (DIP)
In our analysis we used the database DIP [9] (http://dip.doe-mbi.ucla.edu) as the

input data. DIP is a database that documents experimentally determined protein-protein interactions (a binary relation). We analyzed the DIP database, for seven different species, E. coli, H. pylori, C. elegans, D. melanogaster, H. sapiens, M. musculus and S. cerevisiae. Table 1 summarized the statistics of the number of proteins, and their number of interactions for the seven species in our analysis. It is evident from Table 1, only H. pylori, D. melanogaster and S. cerevisiae have more than 40% protein coverage, assuming each gene encodes one protein.

In order to obtain more reliable results we employed the CORE subset of DIP in our analysis, which contains the pairs of interacting proteins identified in the budding yeast, S. cerevisiae that were validated according to the expression profile reliability and paralogous verification method [10].

Table 1. DIP database statistics for E. coli, H. pylori, C. elegans, D. melanogaster, H. sapiens, M. musculus and S. cerevisiae

Organsims	Proteins	Interactions	Gene numbers
E. coli	336	611	~ 4000
H. pylori	702	1420	~ 1500
C. elegans	2629	4030	~ 19000
D. melanogaster	7057	20988	~ 13000
H. sapiens	1059	1369	~ 30000
M. musculus	327	286	~ 37000
S. cerevisiae(CORE)	2609	6574	~ 6300

2.2 Topological parameters of a complex network

The biological networks discussed above have complex topology. A complex network can be characterized by certain topological measurements [11]. Erdos and Renyi were the first to propose a model of a complex network known as a random graph [12]. In the graph theory approach, each protein is represented as a node and interaction as an edge. By analyzing the DIP database one constructs an adjacency matrix to represent the protein-protein interaction network. In the adjacency matrix a value of zero, one and infinity (for convenient a very large number is used in programming) is assigned to represent self-interacting, direct interacting and non-interacting protein respectively.

Node degrees distribution and power law

The first topological feature of a complex network is the node degrees distribution. From the adjacency matrix, one can obtain a histogram of k interactions for each protein. Dividing each point of the histogram with the total number of proteins provide $P(k)$. In a random network, the links are randomly connected and most of the nodes have degrees close to $< k >$. The degree distribution $P(k)$ of a random network with N nodes, can be approximated by the Poisson distribution for large N [11]. In many real life networks, the degree distributions have no well-defined peak

but have power-law distributions, $P(k) \sim k^{-\gamma}$, where γ is a constant. Such networks are known as scale-free networks. The power-law form of the degree distributions imply that the networks are extremely inhomogeneous. In the scale-free networks, there are many nodes with few links and a few nodes with many links. The highly connected proteins could possibly play a key role in the functionality of the networks.

To reduce fluctuations, we studied the logarithm of the node degree cumulative distribution $P_{cum}(k)$ verses the logarithm of k plot, where $P_{cum}(k)$ is defined as[13].

$$P_{cum}(k) = \sum_{k'=k}^{\infty} P(k') \tag{13.1}$$

It was shown that $P_{cum}(k) \sim k^{-\alpha}$ for scale-free networks [13] with $\gamma = -1$. In order to quantify the relationship between $P_{cum}(k)$ and k, we applied the correlation and regression method to analyze the $LogP_{cum}(k)$ vs $Logk$ plots, determined the coefficient of determination r^2 and regression coefficient.

Average network diameter and network diameter

The second topological measurement is the average network distance between two nodes, which is given by the number of links along the shortest path. The number of links by which a node is connected to the other nodes varies from node to node. The average network diameter, also known as the average path length, is the average of the distances between all pairs of nodes.

For all pairs of proteins, the shortest interaction path length, L (i.e. the smallest number of reactions by which one can reach protein 2 from protein 1) will be determined by using the Floyd algorithm [14]. The Floyd algorithm is an algorithm to find the shortest paths for each vertex in a graph. The algorithm represents a network having N nodes as an N by N square matrix M. Each entry (i, j) of the matrix gives the distance d_{ij} from node i to node j. If i is linked directly to j, then d_{ij} is finite, otherwise, it is infinite. The Floyd algorithm is based upon the idea that, given three nodes i, x and k, it is shorter to reach j from i by passing through x if $d_{ix} + d_{xj} < d_{ij}$.

The average network diameter d is given by the average of the shortest path lengths over all pairs of nodes,

$$d = \frac{\sum_L Lf(L)}{\sum_L f(L)} \tag{13.2}$$

where L is the shortest path length and $f(L)$ is the frequency of nodes have a path length of L. The network diameter D is a global topological parameter of the network, which is defined to be the maximal of all the shortest path lengths.

Clustering coefficient

The clustering coefficient for node i is defined by $C_i(k_i) = 2n_i/k_i(k_i - 1)$, where n_i is the number of links connecting the k_i neighbors of node i to each other, and $C_i(k_i)$ is equal to 1 for connected graph (also known as clique). The average clustering coefficient for nodes with node degree k is defined by

$$C_{ave}(k) = \sum_{k_i=k} \frac{C_i(k_i)}{n(k)} \tag{13.3}$$

where $n(k)$ denotes the total number of nodes with k links, and the summation sums over for all node i having the same node degrees k_i . The known properties of hierarchical networks are: scale-free distribution of node degrees, scaling of clustering coefficient of nodes with k links, and a large clustering coefficient. It was shown that in deterministic scale-free networks the clustering coefficient of a node with k links is governed by the scaling law [15, 16], that is $C_{ave}(k) \sim k^{-\beta}$, where β equals to 1. Several pieces of works had demonstrated that the hierarchical exponent can be tuned as one tunes some of the network parameters, such as p_a, which stands for fraction of the newly added nodes, therefore, a stochastic version of the hierarchical model was proposed [16, 17].

Robustness of network

There were concerns [18] that the experimental bias of the yeast two-hybrid experiment [19] could possibly spoil the topological parameters calculation, therefore, in order to test whether the interaction network is robust against errors, we perturbed the network randomly [6, 20]. First, we randomly select a pair of edges A-B and C-D. The two edges are then rewired in such a way that A connected to D, while C connected to B. Notice that this process will not change the degree of connectivity of each node. We repeated the above rewiring steps up to 50% of the total number of nodes, and lead to a randomized perturbation of the original networks. Multiple sampling of the randomized networks allowed us to calculate the ensemble average diameters of the perturbed networks $< d_{rew} >$, and compared the perturbed results with the unperturbed networks diameter, i.e. $\delta = \frac{(<d_{rew}>-d)}{d} * 100\%$.

Correlation profile of node connectivity

In the random graph models with arbitrary node degree distributions, node-node connectivity is uncorrelated [11]. In order to test for the node degree correlations, we employed the approach introduced by Maslov and Sneppen [6], and counted the frequency $P(K_1, K_2)$ that two proteins with node degrees K_1 and K_2 connected to each other by a link and compared it to the same quantity $P_R(K_1, K_2)$ measured in a randomized version of the same network. The average node degree for a fixed K_1 is given by,

$$< K_2 >= \sum K_2 \frac{P(K_1, K_2)}{< P_R(K_1, K_2) >} \tag{13.4}$$

where $< P_R(K_1, K_2) >$ is the multiple sampling average, and the summation sums for all K_2 with a fixed K_1. In the randomized version, the node degree of each protein is kept the same as in the original network, whereas their linking partner is totally random.

13.3 Results

In Table 2, we summarized the average node degree $< k >$, standard deviation of node degree σ_k, maximum node degree k_{max} , average network diameter d, average rewired diameter $< d_{rew} >$ and the δ results for the seven species. The average node degrees of PINs lie between 1.68 and 5.90. This means every protein has a few interactions on the average. On the other hand, the maximum node degrees are much larger than $< k >$ for the seven species, these results strongly indicated that PINs are not random networks. The average network diameter d of the networks lie between 3.57 and 6.80 for any two proteins.

One can also conclude from Table 2 that PINs are quite robust when subject to the random rewiring perturbation (up to 50% of the total number of nodes are rewired), that is $< d_{rew} >$ differs from d with $\delta < 12\%$. These results could be interpreted that PINs are robust against perturbation [6]. Due to the data availability, some of the species' PIN reconstructed from the data could have many isolated components, therefore, in order to obtain reliable results we considered networks with at least 90% of proteins are connected, which is valid for C. elegans, D. melanogaster, H. pylori and S. cerevisiae. In fact we had also demonstrated that PINs are quite robust when subject to failure, attack, edge deletion and random rewiring perturbations (to appeared at some international conferences or journals). These suggested that network topological results are robust against experimental artifacts, hence, it clarifies the false negative and false positive concerns.

Table 2. the average node degree $< k >$, standard deviation of node degree σ_k, maximum connectivity k_{max} , average network diameter d, average rewired diameter $< d_{rew} >$ and the δ results for the seven species.

Organsims	$< k > \pm \sigma_k$	k_{max}	d	$< d_{rew} > (\delta)$
E. coli	2.17± 3.31	54	5.63	
H. pylori	3.87± 5.42	54	4.14	4.02(-2.9%)
C. elegans	3.02± 7.19	187	4.81	4.39(-8.7%)
D. melanogaster	5.90± 9.37	178	4.46	4.01(-10.1%)
H. sapiens	1.68± 1.40	12	3.57	
M. musculus	2.49± 2.99	33	6.80	
S. cerevisiae(CORE)	4.87±6.07	111	5.01	4.42(-11.8%)

In Table 3 we sumarized results of the regression coefficient α, coefficient of determination r^2, p-value, network diameter D, total frequency of occurrence of D (f_D), length of the path with the highest frequency (L') and the percentage of cumulative frequency of paths have a length less than or equals to L' for the seven species. Regression analysis determined that α lie between 1.48 and 2.34 for the seven species. Correlation analysis provides very good evidence (p-value $\ll 10^{-6}$) supporting the fact that the seven PINs form scale-free networks ($Pcum(k) \sim k^{-\alpha}$).

In other words, proteins have multiple connections are rare. All the species have a r^2 value larger than 0.90, and the closer r^2 is to 1, the better it accounts for the correlation. The scale-free degree distributions conclusion had been reported for C. elegans [21] and S. cerevisiae [6, 22]. Here we extended previous studies to a total of seven species. Also, it was found that H. sapiens tends to have the largest diameter D. A larger D values mean that any two proteins can have indirect interaction via more successive chemical reactions. We also noticed that one could approximate the average network diameter d by the network's highest frequency path length L', that is, the L' values in Table 3 is approximately equal to the d values in Table 2.

Table 3. The regression coefficient α, coefficient of determination r^2, p-value, network diameter D, total frequency of occurrence of diameter, f_D, path length with the highest frequency L', and the percentage of cumulative frequency of paths have a length less than or equals to L' results for the seven species.

Organsims	α	r^2	$p-value$	D	f_D	$L'(\%)$
E. coli	1.67±0.14	0.93	$\ll 10^{-6}$	19	2	2(17%)
H. pylori	1.65±0.07	0.95	$\ll 10^{-6}$	9	26	4(40%)
C. elegans	1.48±0.02	0.99	$\ll 10^{-6}$	14	2	4(30%)
D. melanogaster	1.90±0.02	0.93	$\ll 10^{-6}$	11	52	4(39%)
H. sapiens	1.95±0.09	0.96	$\ll 10^{-6}$	21	10	7(15%)
M. musculus	2.34±0.16	0.96	$\ll 10^{-6}$	9	28	2(23%)
S. cerevisiae(CORE)	1.97±0.09	0.91	$\ll 10^{-6}$	13	8	5(33%)

To further characterize the network structures, we considered the logarithm of the average clustering coefficient $C_{ave}(k)$ verses the logarithm of node degree k distributions. The regression and correlation analysis results are depicted in Table 4.

Table 4. Regression and correlation results of the logarithm of $C_{ave}(k)$ verses the logarithm of k plots (β , r^2 and p-value), average clustering coefficient C, and the C values from Reference 24 for the seven species.

Organsims	β	r^2	$p-value$	C	C[24]
E. coli	1.70±0.28	0.86	$8.3*10^{-4}$	0.43	
H. pylori	0.49±0.13	0.37	$5.6*10^{-4}$	0.025	
C. elegans	0.63±0.13	0.36	$2.0*10^{-5}$	0.049	0.047
D. melanogaster	0.26±0.05	0.24	$8.2*10^{-6}$	0.015	0.014
H. sapiens	0.66±0.32	0.19	0.055	0.17	
M. musculus	0.60±0.28	0.43	0.077	0.10	
S. cerevisiae(CORE)	0.89±0.09	0.72	$\ll 10^{-3}$	0.30	
S. cerevisiae				0.13	0.12

Correlation analysis of the $LogC_{ave}(k)$ vs. $Logk$ plots indicated that the S. cerevisiae PIN is well described by the deterministic hierarchical network model ($Cave(k) \sim k^{-\beta}$) [16, 17], since the slope is consistent with model predication (i.e. β =0.89 $\pm$ 0.09), and r^2 is equal to 0.74 (p-value $\ll 10^{-3}$) which is rather statistically significant. The E. coli PIN has a higher r^2 value, that is 0.86, but the slope is not quite consistent with the deterministic hierarchical network model predication. One can interpret this finding in terms of the stochastic hierarchical network model; for β= 1.70, the E.coli PIN is better represented by the stochastic model with a p_a value approximately equal to 0.55, where we estimated it from Fig. 5b in Ref. [16]. These findings lead us to conclude that these two species' network structures could be described by the hierarchical network model.

From Table 4, we observed that besides E.coli and S. cerevisiae, the signature of the scaling behavior of $C_{ave}(k)$ for the other five species is not very strong (i.e.0.19 $\leq r^2 \leq$ 0.43), in particular, the fruit-fly PIN has a β value of 0.26, which is rather close to the scale-free behavior (i.e. $LogC_{ave}(k)$ is independent of $Logk$), hence, the hierarchical model description is not so convincing.

We had plotted $LogC_{ave}(k)$ verses $Logk$ for the five species C. elegans, D. melagonaster, H. pylori, H. sapiens and M. musculus (not shown due to space limitation). For D. melanogaster, we observed that $C_{ave}(k)$ exhibits a rather flat plateau for a large range of k, and it falls rapidly for large k. The clustering coefficient C for the fruit-fly is the smallest among the seven species, where one would expect a large C value for hierarchical network model. These results indicated that the modular structures are suppressed in the fruit-fly PIN, which is consistent with Ref. 24 results.

On the other hand, the current results indicated that all the species (perhaps except M. musculus) exhibit rather flat plateaus for small k (around 10). These seemed to suggest that the plots are better described by a scale-free model for small k and a hierarchical model for large k. Nevertheless, it is evident that $C_{ave}(k)$ decreases with k (i.e. 0.49 $\leq r \leq$0.66) for the four species (H. pylori, C. elegans, H. sapiens and M. musculus). These results provided some evidence suggesting that PINs' topology deviate from the scale-free behavior, there could be embedded modular structures in these four species too. At the present time, the datasets for these four species are quite limited, a more definite conclusion can be reach once larger datasets are available.

To study the node degree disributions correlation, we plotted the logarithm of the average node degree, $Log(< K_2 >)$ verse the logarithm of the node degree K_1, $LogK_1$, for the seven species (not shown due to space limintaion). These results indicated that there is a strong correlation between nodes of lower connectivity; that is the $Log(< K_2 >)$ to $LogK_1$ ratio is larger than 1 in the left region of every plot. In the large K_1 region of every plot, the ratio is smaller than or about 1, which suggested that nodes of high connectivity are link to nodes of lower connectivity, whereas nodes of high connectivity are not directly linked. In fact, the $< K_2 >$

values evaluated at K_1 =1 are of the order of 10 to 30 folds larger than $< K_2 >$ at $K_1 = k_{max}$ for the seven species. The absence of any structures in the large K_1 region of the figures strongly indicated that nodes of high connectivity are not directly linked. The same conclusion was obtained previously for yeast only [6, 23]. Our analysis extended the previous works to seven species, hence, these results provided some evidence suggesting such correlation relations might be a general feature of the PINs across different species.

13.4 Summary and Discussion

We employed the random graph theory approach to analyze the Oct. 2004 version of the protein-protein interacting database DIP, for seven different species (E. coli, H. pylori, C. elegans, D. melanogaster, H. sapiens, M. musculus, and S. cerevisiae). Several global topological parameters (such as node degrees, node degree cumulative distributions, average network distances, average clustering coefficients, node degree correlation profiles) were used to characterize PINs. The logarithm of the node degree cumulative distributions $Log(P_{cum}(k))$ vs. the logarithm of node degree $Logk$ plots indicated that PINs follow a power law ($Pcum(k) \sim k^{-\alpha}$) behavior, and correlation analysis provided very good evidence (p-value $\ll 10^{-6}$) supporting the fact that the seven PINs form scale-free networks.

The logarithm of the average clustering coefficient $C_{ave}(k)$ verses the logarithm of node degree k plots indicated that $C_{ave}(k)$ scales with k with good evidence for E.coli and S. cerevisiae only. These findings lead us to conclude that certain PINs can be described by the hierarchical network models quite well. In particular, the E.coli and S. cerevisiae PINs are well described by the stochastic and deterministic hierarchical network models respectively. On the other hand, the current fruit-fly protein-protein interaction data set does not has convincing evidence in favor of the hierarchical network model. For the other four species (H. pylori, C. elegans, H. sapiens and M. musculus) $C_{ave}(k)$ also scales with k, but with a less significant correlation coefficient. At the present time, the datasets for some of the species (C. elegans, H. sapiens and M. musculus) are quite limited, a more definite conclusion can be reach once larger datasets are available. In summary, our results suggesting that the hierarchical network model is a better description for certain species' PINs (E. coli and S. cerevisiae), and it may not be an universal feature across different species.

We also demonstrated that the interaction networks are quite robust when subject to random rewiring perturbation (at a 50% pertubed level), that is the average diameter for the perturbed case, $< d_{rew} >$ are slightly differ ($< 12\%$) from the unperturbed cases, d. These suggested that network topological results are robust against experimental artifacts.

Average node degree correlation study supports the earlier results that nodes of low con-nectivity are correlated, whereas nodes of high connectivity are not directly linked. Our analysis extended the previous work to seven species, hence, these results provided some evi-dence suggesting such correlation relations might be a general feature of the PINs across dif-ferent species.

Acknowledgment

One of the authors, Ka-Lok Ng, would like to thank the Institute of Physics, Academia Sinica to support this work through a summer visiting funding. This work is supported in part by the R.O.C. NSC grants NSC 93-2745-E-468-008-URD and NSC 93-2112-M-001-040.

References

1. Kanehisa M. Post-genome Informatics. Oxford University Press, Oxford (2000).
2. Wagner A. Mol. Biol. Evol .18(7), 1283, (2001).
3. Melian C. and Bascompte J. Ecology Letters 5, 705 (2002).
4. Ma Hongwu and Zeng An-Ping. Bioinformatics 19, 270 (2002).
5. Jeong H., Tombor B., Albert R., Oltvai Z.N., and Barabasi A.L.. Nature 407, 651 (2000).
6. Maslov S, and Sneppen K. Science, 296, 910 (2002).
7. Lewin B. Genes VII. Oxford University Press, Oxford (2000).
8. Farkas I., Jeong H., Viscek T., Barabasi A.L and Oltvai Z.N. Physica A, 318, 601(2003).
9. Xenarios I., Frenandez E., Salwinski L., Duan X., Thompson M., Marcotte E., and Eisenberg D. Nucl. Acid Res. 29, 239 (2001).
10. Deane CM, Salwinski L, Xenarios I, Eisenberg D. Mol. Cell Prot 1, 349 (2002).
11. Albert R. and Barabasi A.L. Rev. Mod. Phys. 74, 47 (2002).
12. Erdos P and Renyi A. Publ. Math. Inst. Hung. Acad. Sci. 5, 17 (1960).
13. Dorogovtsev S.N., Goltsev A.V., Mendes J.F.F. Phys. Rev. E, 65, 066122 (2002).
14. Floyd R. W. Communication of the ACM 5, no.6, 345 (1962).
15. Dorogovtsev S.N., Goltsev A.V., Mendes J.F.F. Phys. Rev. E, 65, 066122 (2002).
16. Ravasz, E. and Barabasi, A.-L. Phys. Rev. E, 67, 026112 (2003).
17. Szabo G, Alava M and Kertesz J. Phys. Rev. E 67, 056102 (2003)
18. Aloy P. and Russell R.B. FEBS Lett. 530,253 (2002).
19. Lodish H., Berk A., Zipursky S., Matsudaira P., Baltimore D. and Darnell J. Molecular Cell Biology, Fourth edition. W.H. Freeman, N.Y. (2001).
20. Sneppen K., Maslov S., and Eriksen K.A. (2003). Proc. Idea-Finding Symposium, Frankfurt Institute for Advanced Studies.
21. Siming Li, Christopher M. Armstrong,Nicolas Bertin, Hui Ge et al. Science, 303, 540 (2004).
22. Jeong H., Mason S., Barabasi A.-L. and Oltvai Z. N. Nature 411, 41 (2001).
23. Maslov S, and Sneppen K. FEBS Lett. 530, 255 (2002).
24. Goh K.I., Kahng B. and Kim B.. LANL archive, q-bio.MN/0502018 (2005).

14

The Stochastic Model and Metastability of Gene Network

Yuping Zhang and Minping Qian

Summary. There are large numbers of molecules, including proteins, DNA, RNA and so on with complicate motions in the living cells. The interactions between them constitute molecular networks to carry out various cellular functions. These molecular networks should be dynamically stable against various fluctuations which are inevitable in the living world. For such large complex systems, what is the mechanism to regulate them functioning reliably and stably? Many works have contributed to this problem, from dynamical point of view or probabilistic point of view. In this paper, we address it from a metastability point of view of a dynamical system perturbed by noises.

We model the network regulating the cell cycle of the budding yeast by a system of differential equations with noises, and explain how such system can be lead to a discrete model, a finite stationary Markov chain, which matches the observation by biologists well.

A continuous dynamical model of a system of ODEs can reasonably model the basic average dynamical behavior of the interacting system of particles. But a discrete model on n particles of "on" and "off" type meets the biological observation well. We explain how the dynamical system can be lead to a discrete state Markov chain on $\{0,1\}^n$, by metastability theory, with the behavior matching the biological observation well.

14.1 Introduction

Numerous molecules including proteins, DNA, RNA and small molecules, hold complex interactions in the cell. The emergence and development of many high-throughput data-collection techniques, such as microarrays [62], protein chips or yeast two-hybrid screens [84], automated RTPCR and 2-D gel electrophoresis help us to simultaneously obtain the expression profiles of a cell's components at any given time and find how and when these molecules interact with each other. It

presents an opportunity to construct the real gene networks from experimental observation. Gene network inference is a hot research field of contemporary molecular biology.

Complex interactions between the cell's numerous constituents not only determine the structure of biological networks, but also most other biological characteristics, such as complexity, versatility, dynamics, and robustness. [6, 7, 8, 9, 10, 41, 12, 42]. Another major challenge of contemporary molecular biology is to systematically investigate the complex molecular processes underlying biological systems – how these molecules and their interactions determine the functions of all kinds of complex living systems, as well as other system-scale biological characteristics of cellular networks. Many researches in network biology indicate that cellular networks, such as an organism's metabolic network and genetic interaction network, are driven by self-organizing processes and governed by universal laws [14, 15, 16, 17, 18, 19, 20, 21].

14.1.1 From Experiment Data to Gene Network

Increment and accumulation of biological data, such as, expression profiles data, CHIP-chip data and DNA sequences data, make it possible to infer gene network and understand the functioning of organisms on the molecular level. One should select candidate genes which show significant expression changes, because large amounts of data can be simultaneously routinely generated by large-scale gene screening technologies, such as mRNA hybridization micro-arrays and RT-PCR. To identify these genes of interest, the simplest methods are straightforward scoring methods, which e.g. according to whether a significant change exists at one or all conditions or whether the fluctuation pattern shows high diversity according to Shannon entropy [63].

Besides selecting genes which show significant expression changes, we sometimes need further find co-expression genes assuming is caused by co-regulation. We can use classify gene expression patterns to find co-expression genes for exploring shared functions and regulations. Many clustering methods can be used to accomplish classification. Before clustering the gene expression data, we should choose distance measure first, which is used to quantify the difference in expression profiles between two genes and may be as important as the choice of clustering algorithm. Different distance measures emphasize different regularities presented within the data. Distance measures can be divided into at least three classes, according to different types of regularities in the data [58]:

a) similarity according to positive correlations, which may identify similar or identical regulation;

b) similarity according to positive and negative correlations, which may also help identify control processes that antagonistically regulate downstream pathways;

c) similarity according to mutual information, which may detect even more complex relationships.

When distance measure has been chosen, one can choose preferable clustering method. Many clustering algorithms have been proposed. As a whole, clustering algorithms can be divided into hierarchical and non-hierarchical methods. Hierarchical methods return a hierarchy of nested clusters, where each cluster typically consists of the union of two or more smaller clusters. Non-hierarchical methods typically cluster N objects into K groups in an iterative process until certain goodness criteria are optimized, such as, [58]

a)The K-means algorithm [2] can be used to partition N genes into K clusters, where K is pre-determined by the user (see *Tavazoie et al.* [64] for an application to yeast gene expression);

b)The Self-Organized Map (SOM) method is closely related to K-means and has been applied to mRNA expression data of yeast cell cycles as well as hematopoietic differentiation of four well-studied model cell lines [65];

c)The Expectation-Maximization (EM) algorithm [66] for fitting a mixture of Gaussians (also known as Fuzzy K-Means; [3]) is very similar to K-means, and has been used by *Mjolsness et al.* [67] to cluster yeast data;

d)Autoclass is also related to EM, in that a mixed probability distribution has been found. In addition, Bayesian methods has been used to derive the maximum posterior probability classification, and the optimum number of clusters [4].

Different clustering methods can work well in different applications. It's hard to say which clustering method is the best.

Clustering of gene expression data can only help elucidate the regulation (or co-regulation) of individual genes, not what is regulating what. The eventual goal of gene network inference is to understand the integrated behavior of networks of regulatory interactions – construct a coarse-scale model of the network of regulatory interactions between the genes. To deduce the unknown underlying regulatory network from a large amount of data, one requires inference of the causal relationships among genes, that is, reverse engineering the network architecture from its activity profiles [58].

Reverse engineering is the process of elucidating the structure of a system by reasoning backwards from observations of its behavior [59]. In reverse engineering biological networks, a complex genetic network underlies a massive set of expression data, and the task is to infer the connectivity of the genetic circuit. Many methods can be used, such as directed graph, Bayesian network, Boolean network and their generalizations, ordinary and partial differential equations, qualitative differential equations, stochastic equations, and so on.

Complexity of the model used to infer a gene network determines the number of needed data points. Such as, the data requirement of a fully connected Boolean network model is $O(2^N)$, while a continuous fully connected model with additive restrictions requires at least $N + 1$ data points [85, 86].

Different models can help us to analyze the biological systems at different levels – from the very coast and abstract to the very concrete. One can choose models like Boolean networks to handle large-scale data in a global fashion with examination of very large systems (thousands of genes), or choose fine-grained quantitative stochastic models, such as, full biochemical interaction models with stochastic kinetics in *Arkin et al* [60], to analyze biological systems in the very concrete scale.

14.1.2 Topological Properties

Interactions between numerous molecules in cell produce various types of molecular interaction networks including protein-protein interaction, metabolic, signaling and transcription-regulatory networks. Most of these networks are proved have system-scale behavior.

In 1960, Paul Erdös and Alfrëd Rënyi, initiated the study of the mathematical properties of random networks [24]. The Erdös-Rënyi (ER) model of a random network starts with N nodes and connects each connects independently each pair of nodes with probability p. The node degrees follow a Poisson distribution, which indicates that most nodes have roughly the same number of links, approximately equal to the network's average degree. The clustering coefficient ($C_I = 2n_I/k(k-1)$, where n_I is the number of links connecting the k_I neighbours of node I to each other) is independent of a node's degree. The mean path length ($< l >$, represents the average over the shortest paths between all pairs of nodes and offers a measure of a networks overall navigability) is proportional to the logarithm of the network size, $< l > \sim \log N$, which indicates that it is characterized by the small-world property. Recently, a series findings indicate that many real networks share common architectural features deviated from random network. The most striking property is that, in contrast to the Poisson degree distribution, for many real networks, from social networks to cellular networks [15, 16, 17, 18, 19, 21, 25, 26, 27, 28, 29, 30], the number of nodes with a given degree follows a power law. That is, the probability that a chosen node has exactly k links follows $P(k) \sim k^{\gamma}$, where γ is the degree exponent,with its value for most networks being between 2 and 3 [23]. Networks with a power degree distribution are called scale-free [23, 32, 33], which are highly non-uniform: most of the nodes have only a few links, a few nodes have a very large number of links. Scale-free networks with degree exponents $2 < \gamma < 3$, a range that is observed in most biological and non-biological networks, are ultra-small [31, 33], with the average path length following $< l > \sim \log\log N$, which is significantly shorter than $\log N$ that characterizes random small-world networks. Gene duplication is likely to be a key mechanism for generating the scale-free topology [14, 34, 35, 36, 37, 38, 39, 40].

In contrast to the scale-free features of complex networks emphasizing the organizing principles that determine the network's large-scale structure, the concept of modularity is introduced to characterize specific networks, which starts from the bottom and looks for highly representative patterns of interactions. Small regulatory interaction patterns, called subgraphs and motifs, occupy distinct positions in and between organs, offering insights into their dynamical role in information processing [48]. Milo *et al.* identified small subgraphs (motifs) that appear more frequently in

a real network than in its randomized version [49]. In general, modularity refers to a group of physically or functionally linked molecules (nodes) working together to achieve a different function [6, 41, 42, 43]. Biological function are carried by discrete functional modules. For example, temporally coregulated groups of molecules are known to govern various stages of the cell cycle [44, 45, 46], or to convey extracellular signals in bacteria or the yeast pathways. Natural selection aims to maintain function, which, however, is rarely carried by single components, but rather by a network of interacting subunits. Therefore, we should see a tendency towards the evolutionary conservation of subnetworks that are capable of carrying biological function. Motifs aggregate into motif clusters. It is likely a general property of most real networks [47, 49]. However, modularity and scale-free property seem to be contradictory. The definition of modules seems to indicate the existence of some groups of nodes relatively isolated from the rest of the system. Whereas, in a scale-free network hubs are in contact with a high fraction of nodes, which makes the existence of relatively isolated modules unlikely [14]. Because of the coexistence of clustering and hubs, topological modules are not independent, but hierarchical. [43, 51]. In fact, many real biological systems including all examined metabolic [51] and protein interaction networks, demonstrate that hierarchical relationship among modules universally exists.

14.1.3 Robustness and Dynamics

Networks with power-law distributed degrees are robust to random perturbations: Upon removal of randomly chosen nodes, the mean distance (network diameter) between network nodes that can still be reached from each other increases only very little, while in graphs with other degree distribution, network diameter can increase substantially [52]. Cellular networks can be subject to random errors as a result of mutations or protein misfolding, as well as harsh external conditions eliminating essential metabolites [53]. Many real complex systems have a key feature of robustness, which refers to the system's ability to maintain relatively normal behaviour responding to changes in the external conditions or internal organization [14]. *Jeong et al.* found that metabolic network graphs with power-law distributed degrees are robust against perturbations [15]. Recently, a considerable amount of attention has been paid to the quantitative modelling and understanding of the budding yeast cell cycle regulation [25, 21, 68, 69, 70, 71, 72, 73, 74, 75, 76, 77], and similar robust results have been obtained for the protein network of yeast as well [25, 21].

On a molecular level, functions in time, i.e. causality and dynamics, are manifested in the behavior of complex networks. The dynamics of these networks resemble trajectories of state transitions, which corresponds to temporal gene expression. The concept of attractors is what really lends meaning to these trajectories, i.e. the attractors are the high dimensional dynamic molecular representations of stable phenotypic structures such as differentiated cells and tissues, either healthy or diseased [1, 55]. In higher metazoa, each gene or protein is estimated on average to interact with four to eight other genes [56], and to be involved in ten biological functions [57]. The global gene expression pattern is therefore the result of the collective

behavior of individual regulatory pathways. In such highly interconnected cellular signaling networks, gene function depends on its cellular context; thus understanding the network as a whole is essential [58].

One available method to research the principles of network behavior is to radically simplify the individual molecular interactions, and focus on the collective outcome. *Kauffman* represented Boolean networks [54], in which each gene is considered as a binary variable (either ON or OFF) and regulated by other genes through logical or Boolean functions [61]. Even the construction of Boolean network is very simple, the network behavior is already extremely rich [1]. Many useful concepts naturally emerge from such a simple mathematical model. Take example for the budding yeast cell cycle regulation system. Li *et al.* [70] introduced a deterministic Boolean network [54] model and investigated its dynamic and structural properties. Their main result is that the network is both dynamically and structurally stable. The biological stationary state is a big attractor of the dynamics; the biological pathway is a globally attracting dynamic trajectory. These properties are largely preserved with respect to small structural perturbations to the network, e.g. adding or deleting links.

Boolean networks provide a useful conceptual tool for investigating the principles of network organization and dynamics. We can study the role of various constraints on global behavior in terms of network complexity, stability and evolvability. Investigations into abstract models will help us understand the cybernetic significance of network features, and provide meaningful questions for targeted experimental exploration.

14.2 Discrete Stochastic Model

As referred in Sect. 14.1.3, Li *et al.* [70] introduced a deterministic Boolean network model and investigated its dynamic and structural properties. However, one crucial point left unaddressed in their study is the effect of stochasticity or noise, which inevitably exits in a cell and may play important roles [78]. We investigate the stochastic effect on the deterministic network model of Li *et al.* [79]. We found that both the biological stationary state and the biological pathway are well preserved under a wide range of noise level. When the noise is larger than a value of the order of the interaction strength, the network dynamics quickly becomes noise dominating and looses its biological meaning. In *Li et al.*, six attractors without biological meanings are produced. Our result indicates that other six attractors without biological meanings are unstable under real noisy environment. All states converge to the most stable state (stationary G1 state – the attractor with biological meaning in [70]).

In our model, the 11 nodes in the network shown in Fig. 14.1, namely, Cln3, MBF, SBF, Cln2, Cdh1, Swi5, Cdc20, Clb5, Sic1, Clb2, and Mcm1 are represented by variables $(s_1, s_2, ..., s_{11})$, respectively. Each node i has only two values: $s_i = 1$ and $s_i = 0$, representing the active state and the inactive state of the protein i,

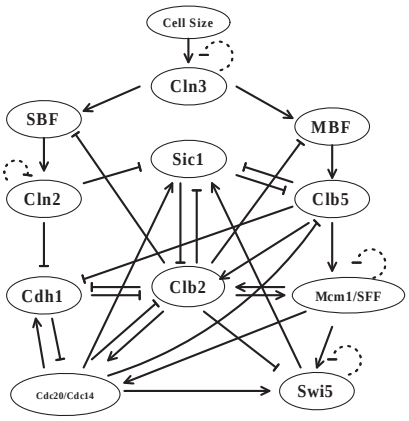

Fig. 14.1. The cell-cycle network of the budding yeast. Each node represents a protein or a protein complex. Arrows are positive regulation, "T"-lines are negative regulation, dotted "T"-loops are degradation.

respectively. Mathematically we consider the network evolving on the configuration space $S = \{0,1\}^{11}$; the $2^{11} = 2048$ "cell states" are labelled by $\{n = 0, 1, ..., 2047\}$. The statistical behavior of the cell state at the next time step is determined by the cell state at the present time step. That is, the evolution of the network has the Markov property [5]. The time steps here are logic steps that represent causality rather than actual times. The stochastic process is assumed to be time homogeneous. Under these assumptions and considerations, we define the transition probability of the Markov chain as follows:

$$\begin{aligned} &P_r(s_1(t+1), ..., s_{11}(t+1)|s_1(t), ..., s_{11}(t)) \\ &\quad = \prod_{i=1}^{11} P_r(s_i(t+1)|s_1(t), ..., s_{11}(t)), \end{aligned} \tag{14.1}$$

where

$$P_r(s_i(t+1) = \sigma_i|s_1(t), ..., s_{11}(t)) = \frac{\exp(\beta(2\sigma_i - 1)\sum_{j=1}^{11} a_{ij}s_j(t))}{\exp(\beta\sum_{j=1}^{11} a_{ij}s_j(t)) + \exp(-\beta\sum_{j=1}^{11} a_{ij}s_j(t))},$$

if $\sum_{j=1}^{11} a_{ij}s_j(t) \neq 0, \sigma_i \in \{0,1\}$; and

$$P_r(s_i(t+1) = s_i(t)|s_1(t), ..., s_{11}(t)) = \frac{1}{1+e^{-\alpha}}, \tag{14.2}$$

if $\sum_{j=1}^{11} a_{ij}s_j(t) = 0$. We define $a_{ij} = 1$ for a positive regulation of j to i and $a_{ij} = -1$ for a negative regulation of j to i. If the protein i has a self-degradation loop, $a_{ii} = -0.1$. The positive number β is a temperature-like parameter characterizing the noise in the system [80]. To characterize the stochasticity when the input to a node is zero, we have to introduce another parameter α. This parameter controls

the likeliness for a protein to maintain its state when there is no input to it. Notice that when β, $\alpha \to \infty$, this model recovers the deterministic model of Li *et al.* [70]. In this case, they showed that the G1 state ($n = 68$) is a big attractor, and the path $1092 \to 836 \to 964 \to 896 \to 904 \to 907 \to 155 \to 51 \to 55 \to 53 \to 116 \to 100 \to 68$ is a globally attracting trajectory. Our study focuses on the stochastic properties of the system.

We first study the property of the biological stationary state G1 and define an "order parameter" as the probability for the system to be in the G1 state, π_{G1}. Plotted in Fig. 14.2(a) is the value of the order parameter as a function of the control parameter β. At large β (low "temperature" or small noise level), the G1 state is the most probable state of the system and π_{G1} has a significant value. (Note that for a finite α there are "leaks" from the G1 state and the maximum π_{G1} is less than 1.) When β is lowered, one observes a sharp transition at around $\beta_c \approx 1.1$ where π_{G1} drops to a very small value, indicating a "high temperatures" phase in which the network dynamics cannot converge to the biological steady state G1. The system is, however, rather resistant to noise. The transition "temperature" is quite high–the value of $\beta_c \approx 1.1$ implies that the system will not be significantly affected by noise until when a fraction of $e^{-1.1}/(e^{1.1} + e^{-1.1}) \approx 0.1$ of the updating rules are wrong. r

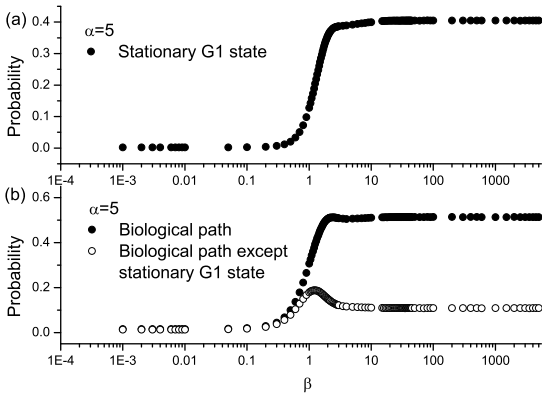

Fig. 14.2. The probability of the stationary G1 state and the biological pathway. (a) The order parameter π_{G1} as a function of β; (b)The sum of the probability for the states on the bio-pathway with and without G1 being included.

We next study the statistical properties of the biological pathway of the cell-cycle network. In Fig. 14.2(b), we plot the probability for the system to be in any of the biological states along the biological pathway, as a function of β. We also plot the same probability with the G1 state excluded. One observes a similar transition as before. The jump of the probability of the states along the biological pathway in the low temperature phase is due to the fact that in this phase the probability flux

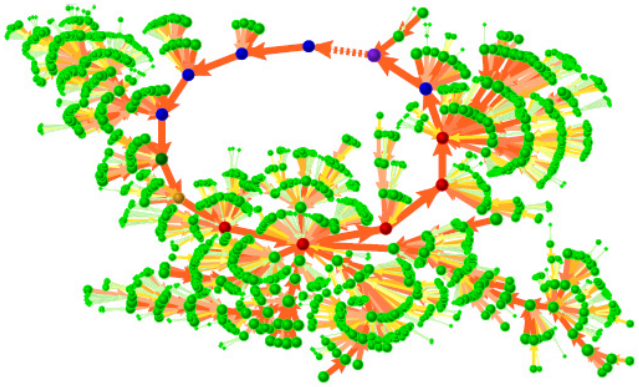

Fig. 14.3. The probability flux. For a node, only the largest flux from it is shown. The nodes on the biological pathway are denoted with different colors: purple, the stationary G1 state; blue, the other G1 states; olive-green, S state; dandelion, G2 state; and red, M states. All other states are noted in normal green. The simulations were done with $\alpha = 5$ and $\beta = 6$.

among different states in the systems is predominantly the flow along the biological pathway. To visualize this, we show in Fig. 14.3 an example of the probability flux among all 2048 states. Each node in Fig. 14.3 represents one of the 2048 states. The size of a node reflects the stationary distribution probability of the state. If the stationary probability of a state is larger than a given threshold value, the size of the node is in proportion to the logarithm of the probability. Otherwise, the node is plotted with the same smallest size. The arrows reflect the pure probability flux (only the largest flux from any node is shown). The probability flux is divided into seven grades, which are expressed by seven colors: light-green, canary, goldenrod, dandelion, apricot, peach and orange. The warmer the color is, the wider the arrow is, and the larger the probability flux. The width of an arrow is in proportion to the logarithm of the probability flux it carries. The arrow representing the probability flux from the stationary G1 state to the excited G1 state (the START of the cell-cycle) is shown in dashed lines. One observes that once the system is "excited" to the START of the cell cycle process (here by noise (α) and in reality mainly by signals like "cell size") the system will essentially go through the biological pathway and come back to the G1 state. Another feature of Fig. 14.3 is that the probability flux from any states other than those on the biological pathway is convergent to the biological pathway. Notice that this diagram is similar to the Fig. 2 of Ref. [70]. For $\beta < \beta_c$, this feature of a convergent high flux bio-pathway disappears.

we also define a "potential" function and study the change of the "potential landscape" as a function of β. Specifically, we define

$$S_n = -\log \pi_n = \beta E_n, \tag{14.3}$$

where E_n is the pseudo energy defined by:

$$E_n = -\frac{\log \pi_n}{\beta}. \tag{14.4}$$

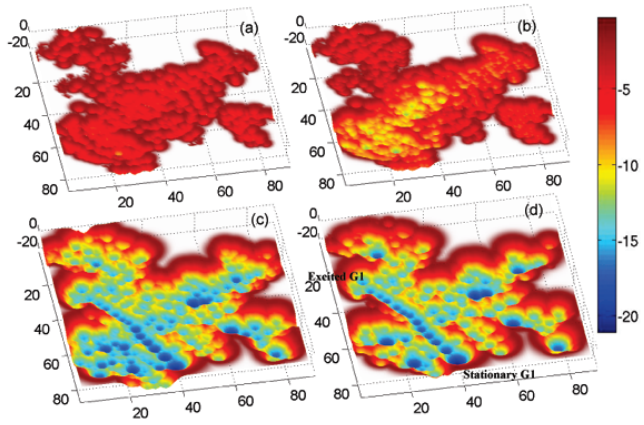

Fig. 14.4. The "potential" landscape of the system before and after the transition. (a) $\beta = 0.01$, (b) $\beta = 0.6$, (c) $\beta = 1.5$, (d) $\beta = 6.0$, all for $\alpha = 5$. The color code gives the relative value of the potential function.

Fig. 14.4 shows four examples of $\Delta S_n = S_n - S0$ distribution, where the reference potential $S0$ in each plot is set as the highest potential point in the system.

One observes that far from the transition point ($\beta = 0.01$, Fig. 14.4(a)), the potential values are high (around -4), and the landscape is flat. Near but below the transition point ($\beta = 0.6$, Fig. 14.4(b)), some local minima (blue points) become more pronounced, but the landscape still remains rather flat. We notice that these minimum points do not correspond to the biological pathway. Right after the transition point ($\beta = 1.5$, Fig. 14.4(c)), the system quickly condenses into a landscape with deep valleys. The state with the lowest potential value corresponds to the stationary G1 state. A linear line of blue dots from up-left to down-middle corresponds to the biological pathway, which forms a deep valley. Some deep blue dots out of the biological pathway are local attractors in Ref. [70]. Notice that although their potential values are low, they attract only a few nearby initial states–all these points are more or less isolated. After the transition point, the potential landscape does not change qualitatively (see Fig. 14.4(d) with $\beta = 6$). As β, $\alpha \to \infty$, the landscape becomes seven deep holes, each corresponding to an attractor of the system [70].

14.3 Continuous Stochastic Model

Although we have introduced stochastic noises into the discrete model and given a microscopic statistical understanding of the system. The model is still an "on-off" model, which does not meet very well to the real interaction between genes and proteins. The Boolean approximation assumes highly cooperative binding (very "sharp" activation response curves) and/or positive feedback loops to make the variables saturate in ON or OFF positions. However, examining real gene expression

data, it seems clear that genes spend a lot of their time at intermediate values: gene expression levels tend to be continuous rather than binary. We need to introduce variables, characterizing the quantities of each kind of genes and proteins, which are crucial for chance of binding.

14.3.1 Interacting Particle System Model

Assuming r kinds of proteins or genes in all. N_i^M is the total number of the i^{th} kind of particle. $N_i(t)$ $(0 \leq N_i(t) \leq N_i^M)$ is the number of i^{th} kind of particle in active at time t. Given that there are currently $\mathbf{N}$(t) particles in active in the system, as $h \to 0$, let

$$P(N_i(t+h) - N_i(t) = k|\mathbf{N}(t)) = \begin{cases} \lambda_i(\mathbf{N}(t))h + o(h) & , \text{ if } k = 1 \\ \mu_i(\mathbf{N}(t))h + o(h) & , \text{ if } k = -1 \\ o(h) & , \text{ if } |k| > 1 \end{cases}$$

where assumes only one increasing or decreasing event occur in a very small interval of time. While the probability is not exactly zero for more than one event, it is negligible. The above conditions imply that

$$P(N_i(t+h) - N_i(t) = 0|\mathbf{N}(t)) = 1 - \lambda_i(\mathbf{N}(t))h - \mu_i(\mathbf{N}(t))h + o(h). \tag{14.5}$$

We get a Markov chain to characterize the system. Transition probability of the Markov process is

$$P(\mathbf{N}(t+h)|\mathbf{N}(t)) = \prod_{i=1}^{r} P(N_i(t+h)|\mathbf{N}(t)). \tag{14.6}$$

The biological observation can only indicate which kind of particles is mostly in active or inactive.

14.3.2 Approximate SDE For Particle Systems

Set $X_t^i = \frac{N_i(t)}{N_i^M}$, $t \geq 0$. This system nests on $[0,1]^r$. $\mathbf{X_t}$ is the proportion of all kinds of particles in active or in working situation at time t. Each dimension X_t^i $(i \in [1,r])$ stands for the proportion of a kind of particles in active, which behaves like birth-death processes.

This can be approximated by a stochastic differential equations (SDE) taking value on $[0,1]^r$, where r is the number of kinds of particles.

$$dX_t^i = \varphi_i(\mathbf{X_t})dt + \varepsilon \Sigma_{i=1}^n X_t^i dw_t \tag{14.7}$$

In our system, the attractors in determinate model all locate at the vertices of points (or sets).

The motion of the system moving from one to the other metastable state can be approximated by the Markov chain on $\{0,1\}^r$, which likes the Markov chain of "on-off" model.

The biological path reported is the transition path between high level attractors, which can be reach in the real observation time scale.

14.4 Metastability

The metastability was a phenomenon first reported in the physics literature. Robert Schomann was first to bring the subject to the attention of probabilists, to discuss the metastable behavior of contact process and 2- dimensional Ising model. Chen, Feng and Qian introduced the large deviation method to solve this problem mathematically [80, 81].

Roughly speaking, metastability is a property of the system that persists in its existing equilibrium when undisturbed (or only slightly disturbed) but is able to pass to a more stable equilibrium when sufficiently disturbed.

14.4.1 Metastability of Markov Chain

Let the state space $\mathbf{S} = \{\xi_1, ..., \xi_N\}$ be finite. Consider a family of Markov chains on $\mathbf{S}$ with transition matrices $\{\mathbf{P}^\beta(\xi,\eta); \beta \in [0,\infty]\}$, satisfy

$$\lim p^\beta(\xi,\eta) = p^\infty(\xi,\eta), \forall \xi,\eta \in \mathbf{S} \tag{14.8}$$

as $\beta \to \infty$ (the temperature $\to 0$). Assume that the following limit exits:

$$\lim_{\beta\to\infty} -\frac{1}{\beta}\log p^\beta(\xi,\eta) = C_{\xi\eta}, \tag{14.9}$$

$$\text{if } p^\infty(\xi\eta) = 0 (\text{with convention that } \log 0 = -\infty), \text{then } C_{\xi\eta} > 0. \tag{14.10}$$

The family of Markov chains with transition probability matrices $\{\mathbf{P}^\beta(\xi,\eta); \beta \in [0,\infty]\}$ is an exponential perturbation of the Markov chain with transition probability matrix $\mathbf{P}^\infty$. If $\{\mathbf{P}^\infty(\xi,\eta)\}$ is degenerate and irreducible, the stochastic model becomes the deterministic dynamical system. In Qian *et al.* [81], metastability of exponentially perturbed Markov chains are exploited by following theorems. Before describing theorems, we give some definitions first. For a subset $K \subset S$, the exit time of Markov chain $\{X_n\}$ is denoted by

$$\tau(K) = inf\{n; X_n \notin K\}, \tag{14.11}$$

and the hitting time by

$$\sigma(K) = inf\{n; X_n \in K\}. \tag{14.12}$$

Let $\{A_1, ..., A_s\}$ be the set of all recurrent classes of $\mathbf{P}^\infty$. We assume that $\mathbf{P}^\infty_{A_i}$ is aperiodic with every $i \in \{1, ..., s\}$, while $\mathbf{P}^\infty_{A_i}$ is the transition probability matrix restricted to recurrent class A_i. For each A_i, which corresponds to an attractor of dynamical systems, define the attractive basin B_i to be

$$B_i = \{\xi | \mathbf{P}^\infty(\sigma(A_i) < \infty | X_0 = \xi) > 0\}). \tag{14.13}$$

Obviously $\cup_i B_i = S$. However, for the stochastic version we are considering now, $B_i \cap B_j \neq \emptyset$ is well possible. The behavior of Markov chain (such as exit time, exit distribution and ergodicity, etc.) with very large β is determined by $C_{\xi\eta}$. Define

$$T(B_i) = min\{\Sigma_{k=1}^{l} C_{\xi_{k-1}\xi_k} | l \geq 1, \xi_0 \in A_i, \xi_1, \xi_2, ..., \xi_{l-1} \in B_i, \xi_l \notin B_i\} \tag{14.14}$$

and for $\xi \in B_i, \eta \notin B_i$, $T_{\xi\eta}(B_i)$ can be similarly defined.

Theorem 1. *Suppose that $\{X_n\}$ is a Markov chain starting from $\xi \in B_i$.*
i) Exit time

$$\lim_{\beta\to\infty} \frac{1}{\beta} \log E^\beta_\xi \tau(B_i) = T(B_i). \tag{14.15}$$

ii) Exit distribution: For $\eta \notin B_i$,

$$\lim_{\beta\to\infty} \frac{-1}{\beta} \log P^\beta(X_{\tau(B_i)} = \eta | X_0 = \xi) = -T(B_i) + T_{\xi\eta}(B_i), \tag{14.16}$$

$$\lim_{\beta\to\infty} P^\beta_\xi(X_{\tau(B_i)} \in \{\eta \notin B_i : T_{\xi\eta}(B_i) = T(B_i)\}) = 1. \tag{14.17}$$

Theorem 2. *If the initial state $\xi \in B_i \setminus \cup_{j\neq i} B_j$, then $\frac{\tau(B_i)}{E^\beta_\xi \tau(B_i)}$ converges in distribution to the exponential random variable with mean 1, as $\beta \to \infty$. In particular, for $\delta > 0$ small enough, we have*

$$\lim_{\beta\to\infty} P^\beta_\xi(e^{(T(Bi)-\delta)\beta} < \tau(B_i) < e^{(T(Bi)+\delta)\beta}) = 1, \tag{14.18}$$

$$\lim_{\beta\to\infty} \frac{-1}{\beta} \log P^\beta_\xi(\sigma(\zeta) > e^{\delta\beta}) \geq \delta, \forall \zeta \in A_i. \tag{14.19}$$

Theorem 3. *Suppose that $\{\upsilon_i(\zeta)\}$ is the invariant measure of $\mathbf{P}^\infty_{A_i}$. For $\zeta \in A_i$, $\xi \in B_i \setminus \cup_{j\neq i} B_j$, $0 < \delta < T(B_i)$, then*

$$\lim_{\beta\to\infty} E^\beta_\xi [\frac{1}{N_\beta} \sum_{k=1}^{N_\beta} I_{\{\zeta\}}(X_k) - \upsilon_i(\zeta)]^2 = 0, \tag{14.20}$$

where I is the indicator function and N_β is the integral part of $e^{(T(B_i)-\delta)\beta}$.

Demonstration of above three theorems and more details can be seen in Qian *et al.* [81]. The phenomena characterized by the theorems are collectively called metastability. This kind of metastability can also be observed at higher levels. In Qian *et al.* [81], the higher level metastability is also described. The transition from one attractive basin to another attractive basin also exhibits metastability. Some attractive basins constitute attractive basin of second level. The Markov chain stays in a certain attractive basin of second level for an asymptotically exponential random time, and then enters another attractive basin of second level with a definite hitting probability. Repeating this process, we can get attractive basins of third level, and so on.

Let us explain the metastability of Markov chain with exponential perturbation more distinctly. For β is infinite, the state space of system breaks down into several subspaces. Every state of each subspace never gets to other subspaces. In other words, every state can only evolute in its' own subspace. If β is large, but finite, the system will be ergodic, the stable states (or sets) become "metastable" states (or sets). Noises make the attractors stronger or weaker. How hard to leave one attractor and reach to another attractor is also affected by noises level. The evolutional distance between different states will become closer or further compared to the situation when β is infinite. There is a hierarchical structure, like a pyramid, between these metastability states. Considering a metastable state b, the time that system stays it is in the order of $e^{\beta T(b)}$ (as $\beta \to \infty$), where $T(b)$ is a constant. In the time less than the scale of $e^{\beta T(b)}$, the state b looks like stable, when the time scale is larger than $e^{\beta T(b)}$, b becomes unstable, and goes to a metastable state of higher level. That's why we call b metastable state. As $\beta \to \infty$, the system spends most time at the "most stable" (the highest level of) metastable state(s), and spends less time in next level of metastable state(s). In a fixed short time scale, the system almost never reach to the metastable states of low enough levels [81]. Thus in biological observation these states never can be seen. When the system going from a metastable state to another metastable state, usually there is a most possible path, with almost probability 1 [81]. Therefore in observation we can only see the system going on those most possible path.

In our example [79], see Fig. 14.4, the states with cooler colors are metastable states of higher levels. When $\beta \to \infty$, system almost stays at the bluest state. Transition from one metastable state to another metastable state goes along the transition path of Fig. 14.3 (arrows), with almost probability 1.

14.4.2 Metastability of SDE

We introduced metastability theory of discrete Markov chain above. In fact, similar metastability theory of stochastic differential equation exits. Suppose that we have a stochastic differential equation as following:

$$dx_t = b(x_t)dt + \varepsilon dw_t \tag{14.21}$$

where $\varepsilon = \gamma/\beta$ and γ is independents of β. Then $\beta \to \infty$ corresponds to $\varepsilon \to 0$. When $\varepsilon \to 0$, the system become a deterministic dynamical system with several attractors. These attractors can also move from one to the others under the random perturbation. Attractors (points) are not stable sets (points) for ever, but become metastable sets (states) in different levels. A hierarchical structure like pyramid between these metastability states also exists.

14.5 Conclusion

In conclusion, we introduced some stochastic models for the yeast cell cycle network. In discrete stochastic model, we have found that there exists a transition point as the noise level is varied. With large noise, the network behaves randomly; it cannot carry out the ordered biological function. When the noise level drops below a critical value, which is of the same order as the interaction strength ($\beta_c \approx 1.1$), the system becomes ordered: the biological pathway of the cell cycle process becomes the most probable pathway of the system and the probability of deviating from this pathway is very small. So in addition to the dynamical and the structural stability [70], this network is also stable against stochastic fluctuations. Metastability theory makes continuous stochastic model connected with discrete stochastic model. By dint of meltability theory, we interpret why the simulation results of discrete model match with real biological situation well. We used a pseudo potential function to describe the dynamic landscape of the system. In this language, the biological pathway can be viewed as a valley in the landscape [82, 83]. This analogy to equilibrium systems may not be generalizable, but it would be interesting to see if one can find more examples in other biological networks, which are very special dynamical systems.

References

1. Kauffman, S.A. (1993) The Origins of Order, Self-Organization and Selection in Evolution. Oxford University Press
2. MacQueen J, (1967) Some methods for classification and analysis of multivariate observation. In *Proceedings of the Fifth Berkeley Symposium on Mathematical Statistics and Probability*. Vol. I. Ed. by L. M. Le Cam and J. Nyeman. University of California Press.
3. Bezdek J.C. (1981) Pattern Recognition with Fuzzy Objective Function Algorithms. Plenum Press, New York.
4. Cheeseman P. and Stutz J. (1996) Bayesian Classification (AutoClass): Theory and Results. in Advances in Knowledge Discovery and Data Mining, Fayyad U.M., Piatetsky-Shapiro G., Smyth P. and Uthurusamy R., Eds. AAAI Press/MIT Press. http://icwww.arc.nasa.gov/ic/projects/bayesgroup/images/kdd-95.ps
5. K. L Chung, Markov chains with stationary transition probability (Springer, New York, 1967).

6. L. H. Hartwell, J. J. Hopfield, S. Leibler and A. W. Murray (1999) Nature 402:47–52.
7. J. Hasty, D. McMillen, J. J. Collins (2002) Nature 420:224–230.
8. H. Kitano (2002) Nature 420:206–210.
9. E. V. Koonin, Y. I. Wolf and G. P. Karev (2002) Nature 420:218–223.
10. Z. N. Oltvai, A.-L. Barabsi (2002) Science 298:763–764.
11. M. E. Wall, W. S. Hlavacek, M. A. Savageau (2004) Nature Rev. Genet. 5:34–42.
12. D. Bray (2003) Science 301:1864–1865.
13. U. Alon (2003) Science 301:1866–1867.
14. Albert-Lszl Barabsi and Zoltn N. Oltvai (2004) Nature Rev. Genet. 5:101–113.
15. H. Jeong, B. Tombor, R. Albert, Z. N. Oltvai, and A. L. Barabasi (2000) Nature 407:651
16. Eisenberg E, Levanon EY (2003) Phys. Rev. Lett.
17. Jeong, Neda, A.-L. B (2003) Europhys. Lett.
18. Li et al. (2004) Science
19. Giot et al. (2003) Science
20. Haijun Zhou (2003) Phys. Rew. E 67:041908
21. B. Vogelstein, D. Lane,A. J. Levine (2000) Nature 408:307–310.
22. D.J. Watts and S.H. Strogatz (1998) Nature(London) 393:440.
23. A.-L. Barabasi and R. Albert (1999) Science 286:509.
24. P. Erdös and A. Rënyi (1960) Publ. Math. Inst. Hung. Acad. Sci. 5:17–61.
25. H. Jeong, S. P. Mason, A. -L. Barabási and Z. N. Oltvai (2001) Nature 411:41–42.
26. A. Wagner (2001) Mol. Biol. Evol. 18:1283–1292.
27. S. -H. Yook, Z. N. Oltvai and A. -L. Barabási (2004) Proteomics 4:928–42.
28. P. Uetz et al. (2000) Nature 403:623–627.
29. T. Ito et al. (2001) Proc. Natl Acad. Sci. USA 98:4569–4574.
30. D. E. Featherstone and K. Broadie (2002) Bioessays 24:267–274.
31. F. Chung and L. Lu (2002) Proc. Natl Acad. Sci. USA 99: 15879–15882.
32. A. -L. Barabási and E. Bonabeau (2003) Sci. A. 288:60–69.
33. R. Cohen and S. Havlin (2003) Phys. Rev. Lett. 90:058701.
34. A. Rzhetsky and S. M. Gomez (2001) Bioinformatics 17:988–996.
35. J. Qian, N. M. Luscombe and M. Gerstein (2001) J. Mol. Biol. 313: 673–681.
36. A. Bhan, D. J. Galas and T. G. Dewey (2002) Bioinformatics 18: 1486–1493.
37. R. Pastor-Satorras, E. Smith and R. Sole (2003) J. Theor. Biol. 222:199–210.
38. A. Vazquez, A. Flammini, A. Maritan and A. Vespignani (2003) ComPlexUs 1:38–44.
39. J. Kim, P. L. Krapivsky, B. Kahng and S. Redner (2002) Phys. Rev. E. Stat. Nonlin. Soft Matter Phys. 66:055101.
40. A. Wagner (2003) Proc. R. Soc. Lond. B 270:457–466.
41. M. E. Wall, W. S. Hlavacek and M. A. Savageau (2004) Nature Rev. Genet. 5:34–42.
42. U. Alon (2003) Science 301:1866–1867.
43. E. Ravasz, A. -L. Barabási (2003) Phys. Rev. E. Stat. Nonlin. Soft Matter Phys. 67:026112.
44. I. Simon et al. (2001) Cell 106:697–708.
45. J. J. Tyson, A. Csikasz-Nagy and B. Novak (2002) Bioessays 24: 1095–1109.
46. H. H. McAdams and L. Shapiro (2003) Science 301:1874–1877.
47. S. S. Shen-Orr, R. Milo, S. Mangan and U. Alon (2002) Nature Genet. 31:64C68.

48. G. Balázsi , A. -L. Barabási and Z. N. Oltvai (2005) PNAS 102:7841–7846.
49. R. Milo et al. (2002) Science 298:824.
50. U. S. Bhalla, P. T. Ram and R. Iyengar (2002) Science 297: 1018–1023.
51. E. Ravasz, A. L. Somera, D. A. Mongru, Z. N. Oltvai and A. -L. Barabási (2002) Science 297:1551–1555.
52. R. Albert, H. Jeong, A. -L. Barabasi (2000) Nature 406:378.
53. R. Albert and A. -L. Barabási (2002) Rev. Mod. Phys. 74:47–97.
54. S. A. Kauffman (1969) J Theoret. Biol. 22:437-467.
55. Somogyi R and Sniegoski C (1996) Complexity 1(6):45–63.
56. Arnone M.I. and Davidson E.H. (1997) Development 124:1851–1864.
57. Miklos G.L. and Rubin G.M. (1996) Cell 86:4 521–9.
58. P. D'haeseleer, S. Liang and R. Somogyi (2000) Bioinformatics 16(8):707–26.
59. Alexander J Hartemink (2005) Nat. Biotech. 23:554–555.
60. A. Arkin, J. Ross and H. H. McAdams (1998) Genetics 149:1633-1648
61. Yuh C.H., Bolouri H. and Davidson E.H. (1998) Science 279: 1896–902.
62. G. Zweiger (1999) Trends Biotech 17:429–436.
63. Fuhrman S, Cunningham MJ, Wen X, Zweiger G, Seilhamer JJ, and Somogyi R. (2000) Biosystems 55(1-3):5-14.
64. Tavazoie S., Hughes J.D., Campbell M.J., Cho R.J. and Church G.M. (1999) Nat. Genet. 22:281–285.
65. Tamayo, P., Slonim D., Mesirov J., Zhu Q., Kitareewan S., Dmitrovsky E., Lander E.S. and Golub T.R. (1999) Proc. Natl. Acad. Sci. USA 96:2907.
66. Dempster, A.P., Laird, N.M. and Rubin D.B. (1977) J. R. Stat. Soc. B 39:1–38.
67. E. Mjolsness, T. Mann, R. Castaño and B. Wold (1999) From Co-expression to Co-regulation: An Approach to Inferring Transcriptional Regulation among Gene Classes from Large-Scale Expression Data. Technical Report JPL-ICTR-99-4, Jet Propulsion Laboratory Section 365. http://www-aig.jpl.nasa.gov/public/mls/papers/emj/GRN99prprnt.pdf
68. K. C. Chen, A. Csikasz-Nagy, B. Gyorffy, J. Val, B. Novak and J. J. Tyson (2000) Mol. Biol. Cell 11:369 .
69. F. R. Cross, V. Archambault, M. Miller and M. Klovstad (2002) Mol. Biol. Cell 13:52.
70. F. -T. Li, T. Long, Y. Lu, Q. Ouyang and C. Tang (2004) Proc. Natl. Acad. Sci. 101:4781.
71. H. -C. Chen, H. -C. Lee, T. -Y. Lin, W. -H. Li and B. -S. Chen (2004) Bioinformatics 20:1914.
72. K. C. Chen, L. Calzone, A.Csikasz-Nagy, F. R. Cross, B. Novak and J. J. Tyson (2004) Mol. Biol. Cell 15:3841.
73. F. R. Cross, L. Schroeder, M. Kruse and K. C. Chen (2005) Mol. Biol. Cell 16:29
74. B. Futcher (2002) Curr. Opin. Cell Biol. 14:676.
75. A. W. Murray (2004) Cell 116:221.
76. N. T. Ingolia and A. W. Murray (2004) Curr. Biol. bf14:R771.
77. M. Tyers (2004) Curr. Opin. Cell Biol. 16:602.
78. C. V. Rao, D. M. Wolf and A. P. Arkin (2002) Nature 420:231.
79. Y. -P. Zhang, M. -P. Qian, Q. Ouyang, C. Tang et al. (To appear).
80. S. Albeverio, J. Feng and M. -P. Qian (1995) Phys. Rev. E 52:6593.
81. M. -P. Qian, D. -Y. Chen and J. -F. Feng (1996) Sci. in China, Ser.A 39:7.
82. P. Ao (2004) J. Phys. A 37:L25.

83. X. -M. Zhu, L. Lan, L.Hood and P. Ao (2004) Funct. Integr. Genomics 4:188.
84. T. Ito, T. Chiba, R. Ozawa, M. Yoshida, M. Hattori and Y. Sakaki (2001) Proc. Natl. Acad. Sci. 98(8):4569–4574.
85. P. D'haeseleer, X. Wen, S. Fuhrman and R. Somogyi (1999) *Linear modeling of mRNA expression levels during CNS development and injury.* Pacific Symposium on Biocomputing 4:41–52. http://www.smi.stanford.edu/projects/helix/psb99/Dhaeseleer.pdf
86. D. C. Weaver, C. T. Workman and G. D. Stormo (1999) *Modeling regulatory networks with weight matrices.* Pacific Symposium on Biocomputing 4:112–123. http://www.smi.stanford.edu/projects/helix/psb99/Weaver.pdf

15

Messenger RNA Information — its implication in protein structure determination and others

Liaofu Luo and Mengwen Jia

Summary. Three problems on mRNA information in protein-coding region are discussed. First, how the mRNA sequence information (tRNA gene copy number) is related to protein secondary structure. Second, how the mRNA structure information (stem/loop content) is related to protein secondary structure. Third, how the specific selection for mRNA folding energy is made among genomes. From statistical analyses of protein sequences for human and *E.coli* we have found that the m-codon segments (for m=2 to 6) with averagely high tRNA copy number (TCN) (larger than 10.5 for human or 1.95 for *E.coli*) preferably code for alpha helix and that with low TCN (smaller than 7.5 for human or 1.7 for *E.coli*) preferably code for coil. Between them there is an intermediate region without structure-preference. In the meantime, we have demonstrated that the helices and strands on proteins tend to be preferably "coded" by mRNA stem region, while the coil on proteins tend to be preferably "coded" by mRNA loop region. The occurrence frequencies of stems in helix and strand fragments have attained 6 standard deviations more than the expected. The relation between mRNA stem/loop content and protein structure can be seen from the point of mRNA folding energy. Both for *E.coli* and human, the mRNA folding energy in protein regular structure is statistically lower than that in randomized sequence, but for irregular structure (coil) the Z scores are near their control values. In the last part we have studied the folding energy of native mRNA sequence in 28 genomes from a broad view. By use of the analysis of covariance, taking the co-variable G+C content or base correlation into account we demonstrate that the intraspecific difference of the mRNA folding free energy is much smaller than the interspecific difference. The distinction between intraspecific homogeneity and interspecific inhomogeneity is extremely significant ($P < 0.0001$). This means the selection for local mRNA structure is specific among genomes. The high intraspecific homogeneity of mRNA folding energy as compared with its large interspecific inhomogeneity can be explained by concerted evolution. The above result also holds for the folding energy of native mRNA relative to randomized sequences. This means the robustness of the distinction between intraspecific homogeneity and interspecific inhomogeneity of mRNA folding under the perturbation of sequential and structural variation.

DNA, RNA and Protein are three basic elements of life system. A Chinese ancient philosopher Laozhi said: One generates two, two generates three and three generates all things in the Universe. So, three means infinity. The interaction network of these three elements makes the genetic language complex enough to represent the life. Although the importance of DNA and protein interaction is well known the role of RNA in the network has not been analyzed thoroughly. We shall discuss some aspects of mRNA information in the determination of protein structure and in the specific selection among genomes.

15.1 mRNA sequence information (tRNA gene copy number) related to protein secondary structure

There have been three generations in the empirical prediction of protein secondary structure. The first generation of the empirical prediction is based on single-residue statistics. The second generation is based on segment statistics (typically 11-21 adjacent residues were taken from a protein). In the third generation of prediction the evolutionary information is used through the method of multiple sequence alignment. A typical example is the particular neural network-based method PHD. Up to now the highest prediction accuracy currently attained is about 76% by use of support vector machine method. So, "the dinosaurs of secondary structure prediction are still alive" [1]. We feel that the relatively low accuracy of secondary structure prediction has its deep origin in the formation of secondary structure. The problem is twofold. The first is related to the importance of long-range information and environmental information in determining the secondary structure. The second is the possible role of mRNA sequence on the formation of protein structure. The latter is more fundamental since it is a challenge to Anfinsen's sequence-structure principle [2]. The possible structural signals in mRNA sequence were analyzed by several authors [3][4][5][6]. Based on di-peptide frequencies we have studied the influences of codon usage on protein secondary structure [7]. It is demonstrated that for human, the structural preferences of codons in 45 (or 79) di-peptides are different from those of amino acids and they could not be explained by stochastic fluctuations at 95% (or 90%) confidence level, and for *E.coli*, the number is 36 (or 60). So the codon usage may influence protein secondary structure at the level of 10% or lower for different species, from higher mammals to prokaryotes. Apart from the possible structural signal in mRNA sequence the influence of messenger RNA on protein secondary structure may occur through two other approaches, namely, the codon tRNA abundance and the stem-loop structure of mRNA [8][9][10].

Since the regular secondary structure (alpha helix and beta strand) occurs in the very early epoch of protein folding and the tRNA molecule is the adaptor of mRNA sequence to amino acid sequence we ask if the tRNA molecule can exert some influence on the formation of protein secondary structure? Consider m-codon segment, m=2, 3 ,4, 5, or 6 (hereafter called m-mer). The average of tRNA gene copy number (TCN) values over codons in an m-mer is denoted as v [9]. Consider a sliding window of width of m codons shifted along the mRNA sequence by 1 codon each step and count the number of m-codons segments corresponding to a definite

protein secondary structure α, β or c (the m-mer that corresponds to two structures will not be taken into account). The m-mer frequency in the k-th interval of v which codes for protein secondary structure α, β or c is denoted as n_k^j ($j = \alpha$, β or c). The total number of m-mers in the k-th interval is denoted by n_k, $n_k = \sum_j n_k^j(obs)$. Set

$$q_j = \frac{\sum_k n_k^j(obs)}{\sum_{kj} n_k^j(obs)} \qquad (j = \alpha,\ \beta\ or\ c) \tag{15.1}$$

Theoretically, the distribution n_k^j ($j = \alpha$, β or c) in three structures is a stochastic variable, obeying multinomial distribution

$$n_k^j(exp) = n_k \cdot q_j \tag{15.2}$$

and the corresponding deviation

$$\sigma_k^j = \sqrt{n_k \cdot q_j \cdot (1 - q_j)} \tag{15.3}$$

Calculating the parameter of codon preference for protein secondary structure

$$F_k^j = \frac{n_k^j(obs) - n_k^j(exp)}{\sigma_k^j} \tag{15.4}$$

in each interval of v we obtain $F_k^j - v$ relations for three structures α, β and c.

We count the number of m-mers in a window of width v_0 , $v_0 = (v_{max} - v_{min})/20$, and shift the window by steps of $v_0/10$. The resulted $F_k^j(m) - v$ relations for human and *E.coli* are shown in scattered point diagram, Figure 1 and Figure 2. The data have been filtered by $|F_k^j| \geq 3$.

From Figure 1 and Figure 2 we find that

1. The mRNA sequences consisting of m-codons ($m = 2$ to 6) with averagely high copy number of tRNA, namely v larger than around 10.5 for human or v larger than around 1.95 for *E.coli*, preferably code for α helix but less code for coil.
2. The structural preference/avoidance turns out contrary to the codons with low tRNA copy number. As average TCN v smaller than around 7.5 for human or v smaller than around 1.7 for *E.coli* the m-mers preferably code for coil but less code for α helix.
3. There exists a clear transition region between high v and low v regions of different preferences. Detailed studies show that the location of the intermediate region slightly shifts for different m.
4. For beta strand the preference/avoidance tendency is not obvious. In most cases $-2 < F_k^\beta < 2$.

All strong preference/avoidance modes with $F_k^j(m) \geq 3$ and $\leq$ -3 in non-overlapping TCN intervals are listed in Table 1 and 2 for human and *E.coli* respectively These modes are arranged in a line following the order of TCN. The

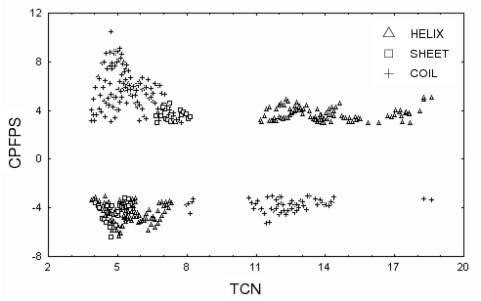

Fig. 15.1. F_k^j(m) – v relations for Human
m=2, . . . , 6. The interval number between v_{max} and v_{min} is supposed to be 20

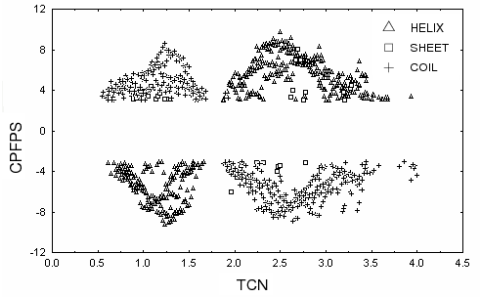

Fig. 15.2. F_k^j(m) – v relations for *E.coli*
m=2, . . . , 6. The interval number between v_{max} and v_{min} is supposed to be 20

mode notation, for example, kc,Nhe means in the *k-th* interval of average TCN the *m-mer* preferably code for random coil (denoted as c) but less code for α helix (denoted as h) and β strand (denoted as e), *etc.*

The preference of TCN for protein secondary structure is essentially a problem of the existence of mutual interaction between two factors. That is, the stochastic variable n_k^j, the number of m-mer in the k-th TCN interval coding for protein structure j (j=1, . . . , a; k=1, . . . , b), depends on two factors, factor A – protein secondary structure and factor B – the interval of codon TCN v. Define Q_A is A-induced deviation, and Q_B is B-induced deviation. The total deviation Q_{tot} can be put into

$$Q_{tot} = Q_A + Q_B + Q_{A\times B} \tag{15.5}$$

where $Q_{A\times B}$ describes mutual effect of two factors. Decompose $Q_{A\times B}$ into two parts, Q_N(1 degree of freedom) and Q_{error}((a-1)(b-1)-1 degrees of freedom). Define

$$Q_R = \frac{Q_N}{Q_{error}}((a-1)(b-1)-1) \tag{15.6}$$

Q_R for Hum and *E.coli* are calculated and listed in Table 3. Tukey [11] proved that there exists mutual interaction between two factors – factor A and B at significance level α if $Q_R > F_{1-\alpha}(1, df)$ where $F_{1-\alpha}(1, df)$ is 100(1-α)-th percentiles of the F

distribution with numerator degree of freedom 1 and denominator degree of freedom df=(a-1)(b-1)-1. From Table 3 we find Q_R always much larger than $F_{0.999}$ (1, df) for all m-mers in human and *E.coli*. Therefore, the mutual interaction between protein secondary structural type and codon TCN is very marked.

Table 15.1. Strong structure-preference/avoidance modes of codon TCN (human) (9 TCN intervals) ($F(m) \geq 3$ or $\leq$ -3)

m-mers	low TCN region			high TCN region				
2mers	1c	2c,Nhe	3e,Nc				7h	8h
3mers	1c,Nh	2c,Nhe	3e			6h	7h	
4mers		2c,Nhe	3Nh		5h	6h,Nc		
5mers		2c,Nh	3c,Nh		5h,Nc	6h		
6mers		2c,Nh	3c,Nh		5h,Nc	6h,Nc		

Table 15.2. Strong structure-preference/avoidance modes of codon TCN (*E.coli*) (19 TCN intervals) ($F(m) \geq 3$ or $\leq$ -3)

m-mers	low TCN region					high TCN region							
2mers	1c	2Nh	3c,Nh	4c,Nh	5c	7Ne	8h	9h,Nc	10h,Nc	11h,Nc	12h,Nc		15Nc
3mers		2c,Nh	3ec,Nh	4c,Nh	5c,Nh	7h	8h,Nc	9h,Nc	10h,Nc	11h,Nc	12h,Nc	13h,Nc	15Nc
4mers	1c	2c,Nh	3c,Nh	4c,Nh	5c,Nh	7h,Nc	8h,Nc	9h,Nc	10h,Nc	11h,Nc	12h,Nc	13h	
5mers		2c,Nh	3c,Nh	4c,Nh	5Nh	7h,Nc	8h,Nc	9h,Nc	10h,Nc	11h,Nc			
6mers	1c	2c,Nh	3c,Nh	4c,Nh	5Nh	7h,Nc	8h,Nc	9h,Nc	10h,Nec	11h			

Finally, to study the origin of structure preference we compare

$$|\frac{n_k^{\alpha}(obs)}{n_k} - q_{\alpha}| + |\frac{n_k^{\beta}(obs)}{n_k} - q_{\beta})| + |\frac{n_k^{c}(obs)}{n_k} - q_{c}| = R_k \tag{15.7}$$

with

$$|\frac{n_k^{\alpha}(stoch)}{n_k(stoch)} - q_{\alpha}| + |\frac{n_k^{\beta}(stoch)}{n_k(stoch)} - q_{\beta})| + |\frac{n_k^{c}(stoch)}{n_k(stoch)} - q_{c}| = R_k^{stoch} \tag{15.8}$$

where stoch means the quantity calculated in codon-randomized sequence. If the structure preference results from amino acid sequence then one should have $R_k = R_k^{stoch}$. However, by direct statistics we find

$$(1 - \frac{R_k^{stoch}}{R_k}) > 0.5 \quad or < -0.5 \tag{15.9}$$

for more than half TCN intervals. So the contribution to the structural preference does not come from amino acid sequence alone. Accompanying amino acid sequence the non-uniform codon usage gives important contribution to the structural preference.

Table 15.3. Assessment of mutual interaction between protein secondary structure and codon TCN

		3-mers	4-mers	5-mers	6-mers
Human	df	29	25	21	19
	Q_R	90.11	82.27	63.76	62.83
	$F_{0.999}$	13.39	13.88	14.59	15.08
E.coli	df	23	19	17	15
	Q_R	84.00	53.50	50.30	50.18
	$F_{0.999}$	14.19	15.08	15.72	16.59

The average TCN (v) of m-mer is divided into 21 intervals for human and 19 intervals for *E.coli*. df=(a-1)(b-1)-1= 2b-3 (a=3, b=effective interval number). $F_{0.999}(1,df)$ is the percentile of F distribution which gives the threshold of Q_R at significance level 0.001. Q_R is a measure of mutual interaction between two factors – protein secondary structure and codon TCN, which is calculated from their statistical deviations. It shows $Q_R > F_{0.999}(1,df)$ for all m-mers in human and *E.coli*. So, the mutual interaction between two factors does exist.

15.2 mRNA structure information (stem-loop content) related to protein secondary structure

The mRNA econdary structure is deduced from nucleotide sequence by use of RNAstructure 3.6 [12]. We fold the mRNA sequence through base pairing by use of RNAstructure3.6 in a window of 100 nucleotides, and shift the window along the sequence. The un-pairing part in the tail of the first 100 nucleotides is put into the shifted window and participates in the next folding. Based on the above model we postulate the secondary structure of mRNA as a number of hairpins or more complex units, constructed by loops and stems (pairing bases). The nucleotide in loop is denoted by 0 and that in stem by 1. So, the secondary structure of an mRNA is depicted by a sequence written by two symbols, 0 and 1.

To study the relation between mRNA structure and protein secondary structure we align amino acid sequence for given secondary structure (helix, denoted as H; extended strand, denoted as E; turn, denoted as T; or coil, denoted as C) [13] and corresponding mRNA sequence written by 0 and 1. Set the observed base number of mRNA structure j occurring in the k-th protein secondary structure denoted by $n_k^j(obs)$. Define F_k^j as Eq(4) but with its meaning changed. It gives a measure of preference- avoidance of protein secondary structure k for the mRNA structure j.

Based on IADE database which contains 2269 protein sequences [8], we calculate the mRNA folding and study the relation between RNA stem-loop frequencies and protein secondary structure. We find the regular secondary structures – helices and strands – on proteins are strongly related to the stems of the corresponding mRNA structure. These regular structures tend to be preferably "coded" by mRNA stem

region, while the coil on proteins tend to be preferably "coded" by mRNA loop region (Table 4).

Table 15.4. Preference of protein secondary structural types for the mRNA stems

	k=H(helix)	k=E(strand)	k=T(turn)	k=C(coil)
F_k^1	3.40	4.21	3.43	-9.25
σ_k^1	186	136	104	169

$(F_k^0 = -F_k^1)$

To obtain a better statistics we define four-amino-acid-fragment that shows pronounced secondary structural propensity as "structural word"(SW). We study the following types of SW: H-type, the secondary structures corresponding to four-amino-acid-fragment are HHHH; E-type, the secondary structures corresponding to four-amino-acid-fragment are EEEE; T-type, the secondary structures corresponding to four-amino-acid-fragment are TTTT; and boundary type, the secondary structures corresponding to four-amino-acid-fragment are T and other structures (H,E,C), for example, HHHT, TTEE, TCCC, HHTC, *etc.* An i-type structural word means that the occurrence of the word in structure i is not at random with 95% confidence level and this word is a characteristic word of the structure i.

Based on SWs we are able to manifest the relation between protein secondary structure and mRNA stem-loop structure more clearly. We calculate the occurrence frequency of stem or loop in each kind of SW. In calculation the double count should be avoided. For successive SWs of same type the overlapping part should be counted only once. We deduce the preference of protein secondary structures for the mRNA stems/loops and find the tendencies are more obvious if we observe the structural words. The preferences of the H-type SWs (H) and E-type SWs (E) for the mRNA stem structure are very marked. As seen from Table 5 the occurrence frequencies of stems in H and E-words have attained 6 standard deviations more than the expected. The result is understandable since H and E-words are amino acid fragments characteristic of helix and strand. Their preferences for stems more clearly reflect the essential connections of helix and strand to the stem structure of mRNA.

Table 15.5. Preference of protein structural words for the mRNA stems

	H-type word	E-type word	T-type word	T-related boundary word
F_k^1	5.73	6.83	-1.52	9.21
σ_k^1	151	109	77	132

$(F_k^0 = -F_k^1)$

The n-nucleotide fragment analyses (up to n=6) further prove the above conclusion. All n-mers sorely composed of loops very scarcely occur in helices and strands (H-type and E-type words) with a high confidence level, but they tend to code for non-regular secondary structures. However, the strands (E-type SWs) preferably tend to be coded by n-mers sorely composed of stems. The H-type words also preferably tend to be coded by n-mers mainly composed of stems but the tendency is not so obvious as in E-type words (Table 6).

Note: The secondary structures of protein are usually classified into three categories, namely, helix, strand and coil. The class of coil includes all structures not assigned as helix or strand [13]. But we have found in coil the turns and turn-related boundaries are of special interest. They are preferably coded by stems, different from other coils. So, we have separated them as an independent class, different from the other coils, in the stem-loop preference analysis.

The relation between mRNA stem/loop content and protein structure can be seen from the point of mRNA folding energy. The folding energy is calculated by use of the RNAfold program from Vienna RNA package [12][14][15]. The energy Z-score is defined by

$$Z = \frac{E_{native} - \langle E_{random} \rangle}{STD} \tag{15.10}$$

where $\langle E_{random} \rangle$ means the energy of codon-randomized sequence averaged over a large number of samples (larger than 50) generated from the native sequence and STD means its standard deviation. Simultaneously, we define

Z^{reg} — when the regular secondary structure segments are randomized
Z^{coil} — when the coil segments are randomized
Z^{reg}_{ctrl} — when part codons randomized with same percentage as regular structure in native sequence, which is served as a control of Z^{reg}
Z^{coil}_{ctrl} — when part codons randomized with same percentage as coil segments, which is served as a control of Z^{coil}

The above Z scores are free energy Z score. If energy E is changed to the percentage of nucleotides in stem then the score calculated is called stem-loop score Z_{SL}. The energy Z score is oppositely correlated with stem content Z score. Figure 3 gives an example.

The Z scores for mRNA sequences in different protein secondary structures are calculated and shown in Table 7. It gives the average energy Z scores of 107 *E.coli* genes and 125 human genes. From Table 7 we find for *E.coli* the mean Z score of regular structure is -1.38 with control -1.01 (difference 0.37), and for human, the two values are -1.71 and -1.24 respectively (difference 0.47). So, both for *E.coli* and human, the Z scores of regular structure are explicitly lower than their control values. However, the case is different for coil region. For *E.coli*, the average Z score of coil region is -0.93, very near the control value -0.86 (difference 0.07), and for humans, the Z score of coil is -1.03, even slight larger than its control -1.20 (difference -0.17). So, we conclude the mRNA folding energy in protein regular structure (helix and strand)

Table 15.6. Preference of protein structural words (a) and structural types (b) for the stem-loop structure in mRNA oligo-nucleotide fragments (n-mers with $n \leq 6$) (All modes with $F_k^j \geq 3$ or $\leq$ -3 are listed)

a

Strc	0	1	00	11	000	101	111	0000	1011	1111	00000
H.W.	-5.7	5.7	-6.9	3.8	-7.7	3.2	—	-8.6	3.1	—	-9.5
E.W	-6.8	6.8	-6.9	6.5	-6.6	—	7.7	-6.0	—	8.4	-5.0
B.W.	-9.2	9.2	-10.3	7.6	-12.1	—	6.8	-13.2	—	5.7	-13.6
T.W.	—	—	—	—	—	—	—	—	—	—	—

Strc	00111	10000	10111	11101	11111	000000	100000	100001	110000	111101	111111
H.W.	—	—	3.1	—	—	-10.1	—	—	—	—	—
E.W.	—	-3.1	—	3.1	8.9	-3.6	-3.4	—	-3.7	3.9	8.5
B.W.	3.3	—	—	—	4.9	-13.9	—	3.3	—	—	4.0
T.W.	—	—	—	—	—	—	—	—	—	—	—

b

Strc	0	1	00	11	000	001	111	0000
helix	-3.4	3.4	-4.2	—	-4.9	—	—	-5.7
strand	-4.2	4.2	-4.0	4.6	-3.6	—	6.0	-3.2
turn	-3.4	3.4	—	—	-3.3	4.2	—	—-
other	9.2	-9.2	8.8	-6.1	8.5	—	-6.1	7.9

Strc	0011	1111	00000	00111	11111	000000	000110	111111
helix	—	—	-6.0	—	—	-6.5	—	—
strand	—	6.3	—	—	6.4	—	—	6.5
turn	3.6	—	—	4.2	—	—	3.1	—
other	—	-4.5	7.0	—	-3.0	6.8	—	—

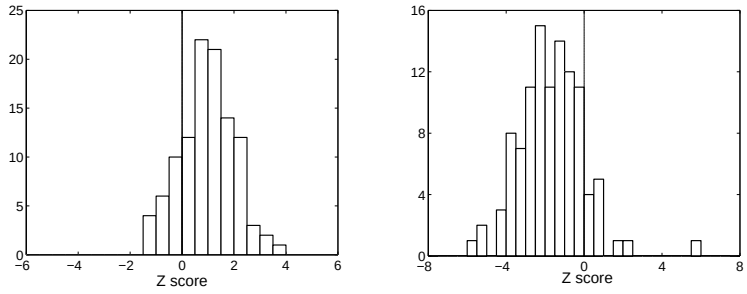

Fig. 15.3. The histograms of stem-loop and energy Z score distribution (*E.coli*) The left figure gives the stem-loop Z score (Z_{SL}) distribution for 107 *E.coli* genes, and the right figure the energy Z score distribution for 107 *E.coli* genes.

is statistically lower than that in randomized sequence, but for irregular structure (coil) no such conclusion can be deduced. The Z scores for irregular structure are near their control values.

The detailed difference between Z scores in regular and irregular structures can be plotted in a diagram. We study the distributions of Z^{reg} - Z^{reg}_{ctrl} and Z^{coil} - Z^{coil}_{ctrl} for 107 *E.coli* and 125 human genes. The results are shown in Figure 4. Evidently, both for *E.coli* and human the maximum distributions of Z score difference in regular structure are located at some values smaller than zero, that is, the distributions shifted towards left as compared with those of irregular structure. Note that in spite of the maximum of Z score difference for coil taking a value slightly larger than zero its average value (the average Z^{coil} minus its control) is near zero due to the bias-to-left of the shape of coil distribution curve. These results indicate obviously that the mRNA sequence coding for protein regular structure has more negative free energy (relative to randomized samples) than sequence segment coding for coil.

A more detailed comparison of Z scores for regular structure and irregular structure can be established through statistical test. Consider 107 (125) Z^{reg}'s and Z^{reg}_{ctrl}'s for *E.coli* (human) as two sets of variables separately. By use of Aspin-Welch t test we find the Z scores of regular structure, Z^{reg}, are significantly different from the control set both for *E.coli* and human. So the folding free energy of native mRNA sequence segment coding for protein regular structure (relative to the energy of randomized sequence) is significantly different from the control set . But for irregular structure, the difference between two Z scores, Z^{coil} and Z^{coil}_{ctrl}, is not significant.

Table 15.7. The dependence of energy Z-score on protein structure

	Z^{reg}	Z^{reg}_{ctrl}	Z^{coil}	Z^{coil}_{ctrl}
E.coli	-1.38	-1.01	-0.93	-0.86
Human	-1.71	-1.24	-1.03	-1.20

We have indicated in previous paragraphs that stems tend to code for protein regular structure while loops tend to code for irregular structure. So, the mRNA sequence coding for protein regular structure has more negative folding energy due to the hydrogen bonds existed between stems that decrease the folding energy. The conclusion is consistent with the present energy Z score analysis. We studied Z score in protein regular structure and that in irregular structure separately. We have deduced the Z score in protein regular structure (Z^{reg}) is more negative than that in coil (Z^{coil}). This shows again the mRNA sequence coding for protein regular structure has more negative folding energy.

Two factors – tRNA gene copy number and stem/loop content – are coupled

We have proposed a phenomenological model on the relation between structure-preference and translational accuracy [9]. The model assumes the protein structure-

Table 15.8. Aspin-Welch t test and F test for the difference of Z scores

	t test				F test			
	regular struc		irregular struc		regular struc		irregular struc	
	t-value	df	t-value	df	F-value	df_1, df_2	F-value	df_1, df_2
Human	-2.0^*	240	1.02	247	1.43^+	124	1.10	124
E.coli	-2.04^*	200	-0.44	193	1.66^+	106	1.91^+	106

$*$ means the calculated t-value (absolute value) $> t_{0.975}$ and the difference of average Z scores very significant between Z^{reg} and Z^{reg}_{ctrl}. $+$ means the calculated F-value $> F_{0.975}$ and the difference of deviations of Z scores very significant between Z^{reg} and Z^{reg}_{ctrl} (or Z_{coil} and Z^{coil}_{ctrl}). df = degree of freedom. When F-value is large enough Aspin-Welch t-test for average Z scores should be used (as shown in the left panel).

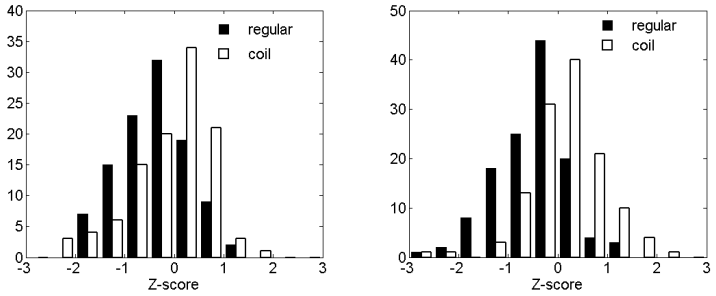

Fig. 15.4. The histograms for the distribution of Z^{reg}-Z^{reg}_{ctrl} and Z^{coil}-Z^{coil}_{ctrl} for *E.coli* and human. The left figure gives the distribution of Z^{reg}-Z^{reg}_{ctrl} and Z^{coil}-Z^{coil}_{ctrl} for 107 *E.coli* genes and the right figure gives the distribution of Z^{reg}-Z^{reg}_{ctrl} and Z^{coil}-Z^{coil}_{ctrl} for 125 human genes.

preference of codons dependent on translational accuracy. Then the translational accuracy is assumed to be proportional to tRNA abundance (tRNA copy number, TCN). Apart from TCN we introduce R to describe other translational accuracy-related factors that influence structure-preference. R factor is a matrix which, on the one hand, depends on three protein structural types and on the other hand, depends on three TCN regions of codons. We have established equations which should be satisfied by R matrix elements and demonstrated that the stem/loop content of mRNA is a possible solution for R factor. The result suggests that there may exist an adjusting factor on translation accuracy which is expressed in three TCN regions and correlates with stem/loop distribution. This factor plays a role of positive regulation for helix but negative regulation for random coil. So, the interaction between mRNA structure and tRNA abundance may play an important role in an associated way in protein secondary structure formation.

15.3 mRNA folding energy – specific selection among genomes

In the last part of the paper the mRNA folding energy of genes will be studied in a wider range of species (28 genomes including 8 archaea, 14 eubacteria and 6 eukaryota) from a broad view which will give us some new insights into the role of mRNA local folding in the genome evolution. For each species about 120 genes (coding regions) are chosen stochastically. Using the RNAfold program from Vienna RNA package [14][15] we fold each mRNA sequence in a local window pattern, namely, the sequence is folded in short regions of 50 bases and shifted by 10 bases [16]. The averaged local folding energy E_{native} of the j-th native mRNA sequence in the i-th genome is denoted by y_{ij}. We study the statistical property of folding energies by use of the analysis of covariance. Set $y_{ij} = (E_{native})_{ij}$ (i=1, ..., t treatments or classes and for each treatment i, j=1, ..., n_i observations). In the General Linear Model one assumes y_{ij} depending on another set of co-variables x_{ij} and these two sets of variables obeying a regression equation in the form of

$$y_{ij} \approx a + bx_{ij} \tag{15.11}$$

for each class. Set

$$\begin{aligned} x_{ij} &= (G+C)\% \qquad (Model\ GC) \\ &= D_1 + D_2 \qquad (Model\ D_1 + D_2) \end{aligned} \tag{15.12}$$

D_1 and D_2 are informational redundancies and D_1+D_2 describes the base correlation in a DNA sequence [17]. Define the error sum of squares

$$\begin{aligned} SSe &= \sum_{ij}(y_{ij} - a - bx_{ij})^2 \\ &= \sum_{ij}(y_{ij} - \overline{y}_i)^2 - b^2\sum_{ij}(x_{ij} - \overline{x}_i)^2 \\ b &= \frac{\sum_{ij}(y_{ij} - \overline{y}_i)(x_{ij} - \overline{x}_i)}{\sum_{ij}(x_{ij} - \overline{x}_i)^2} \end{aligned} \tag{15.13}$$

(where $\overline{y}_i$ ($\overline{x}_i$) is the average of y_{ij} (x_{ij}) in a given class i) and the mean error sum of squares

$$MESS = \frac{SSe}{df(SSe)} = \frac{SSe}{\sum_i n_i - t - 1} \tag{15.14}$$

Define the class sum of squares

$$CLS = \sum_{ij}(\ (y_{ij} - \overline{y})^2 - b'^2(x_{ij} - \overline{x})^2\ ) - \sum_{ij}(\ (y_{ij} - \overline{y}_i)^2 - b^2(x_{ij} - \overline{x}_i)^2\ )$$

$$b' = \frac{\sum_{ij}(y_{ij} - \overline{y})(x_{ij} - \overline{x})}{\sum_{ij}(x_{ij} - \overline{x})^2} \tag{15.15}$$

(where $\overline{y}$ ($\overline{x}$) is the overall average of y_{ij} (x_{ij})) and the mean class sum of squares

$$MCSS = \frac{CLS}{df(CLS)} = \frac{CLS}{t-1} \tag{15.16}$$

The covariant F-test is defined by

$$F = \frac{CLS/(t-1)}{SSe/(\sum_i n_i - t - 1)} \tag{15.17}$$

which gives a criterion for examining the difference between classes. Evidently, it includes usual F-test as a special case when x variable vanishes. We put 28 species into three classes. For class 1 (archaea) t=8, for class 2 (eubacteria) t=14 and for class 3 (eukaryota) t=6. Through the analysis of covariance we obtain mean error sum of squares ($MESS$) and mean class sum of squares ($MCSS$) of folding free energy of native mRNA. The former describes the square deviation of mRNA folding energy in a genome and the latter describes the square deviation of this energy among genomes. By comparing the calculated F value with F-distribution the significance level (P-value) is deduced. The results are summarized in Table 9.

The results in Table 9 are given in two regression models (Model GC and Model D_1+D_2). All results show $MCSS$ much larger than $MESS$ at significance level $<$ 0.0001. So, the square deviation of mRNA folding energy among genomes is definitely higher than that within a genome. Simultaneously, the results show that the linear relation between energy variable y_{ij} and co-variable x_{ij} (GC content or D_1+D_2) existed.

To understand its meaning we study the energy difference between native and randomized sequence. That is, we set

$$y_{ij} = (E_{native} - \langle E_{random} \rangle)_{ij} \tag{15.18}$$

Three types of random sequences are produced based on different randomization methods. The first procedure, called Codonrandom (CODRAN), preserves the same encoded amino acid sequence of mRNA sequence under the random codon choice. The second procedure, called Codonshuffle (CODSHU), shuffles synonymous codon in given mRNA sequence and preserves the same encoded amino acid sequence and codon usage (base composition) of mRNA sequence. The third procedure called Dicodonshuffle (DICODSH) was developed by Katz and Burge [16]. This procedure preserves the di-nucleotide composition, codon usage and encoded amino acid sequence of mRNA sequence.

By use of the same method we find the extremely significant difference between $MCSS$ and $MESS$ also existed for folding energy of native sequence relative to randomized sequence (Table 10). This is a universal law: whether the folding energy of native sequence is lower or higher than the randomized sequence [16][18][19], whether the folding is energy-favorable or not, all species exhibit the same trend — the energy deviation in different genomes always higher than that in a genome. Further, the above law is irrespective of the kingdoms of species and irrespective of the randomization method which has been adopted [16][18][19]. Another important

Table 15.9. Square sum of folding energy of native mRNA sequence

	$MCSS$	(df_1)	$MESS$	(df_2)	F	P value	$\|R\|$
Model GC							
CLS 1	14.61	7	1.120	949	13.04	<0.0001	0.959
CLS 2	16.66	13	0.602	1652	27.66	<0.0001	0.940
CLS 3	19.75	5	0.883	705	22.37	<0.0001	0.941
Model D_1+D_2							
CLS 1	1295.1	7	3.336	949	388.2	<0.0001	0.873
CLS 2	178.5	13	1.541	1652	115.8	<0.0001	0.861
CLS 3	440.4	5	2.614	705	168.5	<0.0001	0.814

$MCSS$=mean class sum of squares, $MESS$=mean error sum of squares, df=degree of freedom, df_1 =t-1, df_2 = $\sum n_i$ - t -1 (t, number of species; n_i, sequence number taken in this study for species i), F= $MCSS/MESS$, R = correlation coefficient in linear regression, CLS1 including 8 archaea — *A.fulgidus* (sequence number 120), *A.pernix* (119) , *H.sp.*(119), *M.thermoautotropicum* (120), *P.abyssi* (120), *S.solfataricus* (120), *S.tokodaii* (120), and *T.volcanium* (120), CLS2 including 14 eubacteria — *A.aeolicus* (120), *B.burgdorferi* (120), *B.subtills* (120), *C.acetobutylicum* (120), *E.coli* (107), *H.influenzae* (120), *H.pylori* (120), *M.pneumoniae* (120), *R.prowazekii* (120), *S.pcc*6803 (120), *S.typhi* (120), *T.maritima* (120), *T.pallidum* (120), and *V.cholerae* (120), CLS3 including 6 eukaryota — *A.thaliana* (120), *C.elegans* (114), *D.melanogaster* (120), *Homosapiens* (125), *S.cerevisiae* (120), and *P.falciparum* (113). The P-value column gives the significance level.

result summarized in two tables is the approximate linear relation between energy variable y_{ij} and co-variable x_{ij} (GC content or D_1+D_2). The correlation coefficients $|R|$ are always large in CODRAN randomization procedure both in model GC and model D_1+D_2. But in DICODSH randomization the linear relation between energy variable and co-variable (G+C)% or D_1+D_2 does not exist.

The above results show that the selection for mRNA folding is specific among genomes. From the point of evolution the large interspecific difference occurs due to the rapid accumulation of mutations. However, if we assume that, by certain mechanisms of concerted evolution (coincidental evolution) the mutation, and in turn, the change of mRNA folding energy can spread horizontally to all gene members in the same genome, then the high intraspecific homogeneity of mRNA folding energy as compared with its large interspecific inhomogeneity can be explained naturally. Numerous examples of concerted evolution of multigene families have been proposed. A large body of data obtained by restriction enzyme analysis and DNA sequencing techniques has attested to the generality of concerted evolution [20]. We suggest that the concept of concerted evolution of multigene families may be generalized to mRNA folding of genes in whole genome. Under this assumption the high specific selection for mRNA folding among genomes compared with high intraspecific homo-

Table 15.10. Square sum of folding energy of native mRNA relative to randomized sequence

	$MCSS$	(df_1)	$MESS$	(df_2)	F	P value	$\|R\|$
CODRAN	Model GC						
CLS 1	14.27	7	0.981	949	14.55	<0.0001	0.896
CLS 2	14.06	13	0.540	1652	26.05	<0.0001	0.812
CLS 3	50.17	5	0.943	705	53.22	<0.0001	0.803
CODRAN	Model D_1+D_2						
CLS 1	420.9	7	1.395	949	301.8	<0.0001	0.849
CLS 2	64.20	13	0.860	1652	94.36	<0.0001	0.755
CLS 3	192.4	5	1.187	705	162.1	<0.0001	0.744
DICODSH	Model GC						
CLS 1	1.16	7	0.206	949	5.62	<0.0001	0.268
CLS 2	1.76	13	0.160	1652	10.95	<0.0001	0.291
CLS 3	0.79	5	0.130	705	6.09	<0.0001	0.204
DICODSH	Model D_1+D_2						
CLS 1	1.866	7	0.208	949	8.96	<0.0001	0.252
CLS 2	1.827	13	0.160	1652	11.40	<0.0001	0.292
CLS 3	0.704	5	0.131	705	5.37	<0.0001	0.192

(see table legend given below Table 9)

geneity is a result of concerted evolution. The deeper meaning of gene interaction in a genome at RNA level and the evolutionary conservation of mRNA folding should be clarified in future investigation.

The intraspecific homogeneity and interspecific inhomogeneity of mRNA folding can be visualized as the clustering of folding free energy of genes in energy space for each species. To study the relation between folding energy of the native sequence (E_{native}) and the corresponding relative energy we have made linear regression analysis and find there exists a good linear relation between these two energies for each genome (in 27 genomes for CODRAN case and 24 genomes for DICODSH case). Further, setting the folding free energy averaged over genes of species i as

$$\langle (E_{native})_{ij} \rangle_j = E_i \tag{15.19}$$

and the energy difference averaged over genes as

$$\langle (E_{native} - \langle E_{random} \rangle)_{ij} \rangle_j = D_i \tag{15.20}$$

we find E_i and D_i linearly related to each other for 28 species with correlation coefficient R=0.963 in CODRAN and 0.386 in DICODSH randomization. These R values explicitly exceed the critical correlation coefficient at significance 0.05 ($R_{0.05}$

= 0.374). So the clustering of genes in energy space leads to the clustering of genes in relative energy space. Therefore, the assumed concerted evolution may lead to not only the homogeneity of mRNA folding energy among genes in a genome, but also the homogeneity of folding free energy of native mRNA relative to randomized sequence. Since the randomization can be regarded as a perturbation applied to the native mRNA sequence the above result shows that the homogeneity of folding energy among genes in a genome should remain valid even under certain perturbation of mRNA sequence and structure. This means the robustness of the distinction between intraspecific homogeneity and interspecific inhomogeneity of mRNA folding free energy.

References

1. Rost B, Sander C (2000) Third generation prediction of secondary structure. In: Webster DM (eds) Methods in Mol. Biol. V.143. Humena Press. New Jersey.
2. Anfinsen CB (1973) Science 181, 223-230
3. Brunak S, Engelbrecht J (1996) Proteins 25: 237-252.
4. Oresic M, Shalloway D (1998) J. Mol. Biol. 281: 31-48.
5. Adzhubei IA, Adzhuhei AA, Neidle S (1998) Nucleic Acids Res. 26: 327-331.
6. Xie T, Ding DF (1998) FEBS Lett. 434: 93-96.
7. Li XQ, Luo LF, Liu CQ (2003) Chinese J Biochem Mol Biol. 19(4), 441-444 (in Chinese).
8. Jia MW, Luo LF, Liu CQ (2004) Biopolymers 73: 16-26.
9. Luo LF, Jia MW, Li,X.Q (2004) Biopolymers 74: 432-447.
10. Luo LF (2004) Theoretic-Physical Approach to Molecular Biology. Shanghai Sci. Tech. Publishers, Shanghai.
11. Tukey JW (1949) Biometrics 5:232-242.
12. Mathews DH, Sabina J, Zucker M, Turner H (1999) J. Mol. Biol. 288: 911-940.
13. Kabsch,W, Sander C(1983) Biopolymers 22: 2577-2637.
14. Hofacker IL, Fontana W, Stadler PF, Bonhoeffer S, Tacker M, Schuster P (1994) Monatsh. Chem. 125: 167-188.
15. Zuker M, Stiegler,P (1981) Nucleic Acid Res. 9: 133-148.
16. Katz L, Berge CB (2003) Genome Res. 13: 2042-2051.
17. Luo LF, Lee WJ, Jia LJ, Ji FM, Tsai L (1998) Phys. Rev. E. 58: 861-871
18. Seffens W, Digby D (1999) Nucleic Acid Res. 27: 1578-1584
19. Workman C, Krogh A (1999) Nucleic Acid Res. 27: 4816-4822
20. Li WH (1997) Molecular Evolution. pp. 309-334. Sinauer Associates, Massachusetts, and references cited therein.